

**MODELING AND SIMULATION OF A NOVEL INTERNAL
CIRCULATING FLUIDIZED BED REACTOR FOR SELECTIVE
CATALYTIC REDUCTION OF NITROGEN OXIDES**

by

Xingxing Cheng

M. Sc., Southeast University, Nanjing, 2008

B. Eng., Southeast University, Nanjing, 2006

A THESIS SUBMITTED IN PARTIAL FULFILLMENT OF
THE REQUIREMENT FOR THE DEGREE OF
DOCTOR OF PHILOSOPHY

in

THE FACULTY OF GRADUATE AND POSTDOCTORAL STUDIES
(CHEMICAL AND BIOLOGICAL ENGINEERING)

The University of British Columbia

(Vancouver)

October 2013

©Xingxing Cheng, 2013

Abstract

The internal circulating fluidized bed (i-CFB) reactor exhibits an ability to overcome the negative impact of excessive O_2 present in the flue gas on selective catalytic reduction of NO_x with hydrocarbons as the reductant (HC-SCR) by decoupling NO_x adsorption and reaction into two separate zones. A mathematical model has been developed in this study, which includes three sub-models: hydrodynamics, adsorption and reaction kinetics. Each sub-model was developed separately and validated by experimental data before they were integrated into the i-CFB model.

For the hydrodynamics of i-CFB, solids circulation rates, which were later used for model parameter fitting, were measured using optical fibre probe. The hydrodynamics model was then developed based mass and pressure balance. Adsorption isotherm and $deNO_x$ reaction kinetics were developed based on a series of fixed bed experimental data: O_2 adsorption, NO_x adsorption and NO_x reaction. The kinetic model was further evaluated by fluidized bed adsorption and reaction experiments.

The simulation results of the integrated i-CFB model showed good agreement with the experimental data. It is observed from the model that the performance of the current laboratory scale i-CFB reactor was dominated by the catalyst reactivity, rather than the catalyst adsorption rate, because of too short a solids residence time in the reduction zone for the $deNO_x$ reaction. Simulation results for i-CFBs with different cross sectional areas of the adsorption and reduction zones showed that a large reduction zone could significantly enhance the overall $deNO_x$ efficiency, and there existed an optimal reduction zone to adsorption zone area ratio at which NO_x conversion is maximized at a given operating condition. It was also observed that the performance of i-CFB reactors with a larger reduction zone is less sensitive to gas bypass from reduction zone to adsorption zone.

Overall, the i-CFB model developed in this study can be used as a tool to assist reactor design and scale up, and to provide guidance on how to further improve the NO_x reduction efficiency. The simulation

results showed that it is possible to achieve a higher deNO_x efficiency higher while avoiding the negative effects of flue gas O₂.

Preface

Chapter 2 is based on a literature review which was submitted for publication: Xingxing Cheng and Xiaotao T. Bi, “A review of recent advances in selective catalytic NO_x reduction reactor technologies”. Xingxing Cheng was responsible for all the literature review and the manuscript preparation. Dr. Bi provided feedback and insight throughout this process and edited the manuscript.

Chapter 3 is based on the experimental and modeling work conducted in a hot model i-CFB reactor. Xingxing Cheng was responsible for the experimental design, data collection and analysis, model development and manuscript preparation. Dr. Zhiwei Chen (postdoctor fellow in UBC), Dr. Jun Xu (a former visiting student from China), and Dr. Chuigang Fan (a former postdoctor fellow in UBC), kindly helped with the experimental work on solids circulation rate measurement. A manuscript based on Chapter 3 will be published: Xingxing Cheng and Xiaotao T. Bi, “Hydrodynamics of an i-CFB deNO_x reactor”, Powder Technology. Dr. Bi provided feedback throughout this process and edited the manuscript. Similar but different to the work in Chapter 3, another hydrodynamic model was developed for coarse bed materials and the performance of different distributors was compared. The work was presented in the Conference of Fluidization 2013 and has been published in the conference proceeding: Xingxing Cheng and Xiaotao Bi, (2013), “Gas bypass and solids circulation rate of an i-CFB reactor with coarse particles”, Fluidization 2013. Xingxing Cheng was responsible for the model development and manuscript preparation. Dr. Bi provided feedback and insight throughout this process, edited the manuscript and presented the work in the conference.

Chapter 4 is based on the modeling work conducted by Xingxing Cheng, who carried out all the model development, program coding, data analysis and manuscript preparation. The part of adsorption modeling in fixed bed has been published: Xingxing Cheng and Xiaotao T. Bi, “Modeling NO_x adsorption onto Fe/ZSM-5 catalysts in a fixed bed reactor”, International Journal of Chemical Reactor

Engineering, Volume 11, Issue 1, Pages 1-12. For this part, Xingxing Cheng carried out all the model development, program coding, data analysis and paper preparation. Dr. Xiaotao T. Bi provided feedback throughout this process and edited the manuscripts. An earlier version of the kinetic modeling part has been published: Xingxing Cheng and Xiaotao T. Bi, (2012), "Reaction Kinetics of selective catalytic reduction of NO_x by propylene over Fe/ZSM-5", Chemical Engineering Journal, Volume 211-212, Pages 453-462. In this part, Xingxing Cheng carried out all the model development, program coding, data analysis and paper preparation. Dr. Xiaotao T. Bi provided feedback throughout this process and edited the manuscripts. Most of the experimental data used for the modeling was obtained by Terris Tianxue Yang, who conducted the experiment in a fixed bed unit. A paper has also been published: Terris T. Yang, Hsiaotao T. Bi, Xingxing Cheng, (2011), "Effects of O₂, CO₂ and H₂O on NO_x adsorption and selective catalytic reduction over Fe/ZSM-5", Applied catalysis B: Environmental. Volume 102, Issue 1-2, Pages 163-171. For this paper, Terris T. Yang carried out all the experimental design, data collection and analysis and paper preparation. Dr. Xiaotao T. Bi provided feedback and insight throughout this process and edited the manuscripts. Xingxing Cheng helped with the revision of the paper, conducted part of the literature review and data analysis.

Chapter 5 is based on experimental and modeling work in a fixed bed unit and a fluidized bed unit. Xingxing Cheng was responsible for the experimental design, data collection and analysis, model development, program coding and manuscript preparation. Dr. Zhiwei Chen and a former visiting student from China, Dr. Luning Tian, kindly helped with the experimental setup and running. A paper based on Chapter 5 has been published: Xingxing Cheng and Xiaotao T. Bi, (2013), "Modeling and simulation of nitrogen oxides adsorption in fluidized bed reactors", Chemical Engineering Science, Volume 96, Pages 42-54. Dr. Xiaotao T. Bi provided feedback and insight throughout this process and edited the manuscript.

Chapter 6 is based on the modeling work conducted by Xingxing Cheng, who was responsible for the model development, program coding and manuscript preparation. The work will be submitted to a journal for publication: Xingxing Cheng, Xiaotao T. Bi, "Modeling catalytic reduction of NO_x in the

reaction zone of an i-CFB reactor”. Dr. Xiaotao T. Bi provided feedback and insight throughout this process and edited the manuscript. An earlier version of the fluidized bed model, together with a different kinetic model was published in a conference proceeding: Xingxing Cheng, Xiaotao Bi, (2010), “Modeling of fluidized bed hydrocarbon catalytic deNO_x reactors”, Proceedings of 10th China-Japan Symposium on Fluidization. Xingxing Cheng carried out all the model development, program coding, data analysis and manuscript preparation. Dr. Bi provided feedback and insight throughout this process, edited the manuscript and presented the work in the conference.

Chapter 7 is based on the modeling work conducted by Xingxing Cheng, who was responsible for the model development, program coding and manuscript preparation. The work will be submitted to a journal for publication: Xingxing Cheng, Xiaotao T. Bi, “Modeling catalytic reduction of NO_x in a novel i-CFB reactor”. Dr. Xiaotao T. Bi provided feedback and insight throughout this process and edited the manuscript.

Table of contents

Abstract	ii
Preface	iv
Table of contents	vii
List of tables.....	xiii
List of figures.....	xiv
List of abbreviations	xix
Nomenclature.....	xxi
Acknowledgements.....	xxxvi
Chapter 1 Introduction	1
1.1 Background.....	1
1.2 Previous research results summary on i-CFB.....	4
1.3 A review on fluidized bed reactor models	6
1.4 Research objective of this study	8
1.5 Thesis layout.....	9
Chapter 2 Literature review: SCR reactors	10
2.1 SCR technologies: reaction mechanisms and catalysts	10
2.1.1 NH ₃ -SCR.....	10
2.1.2 HC-SCR	12

2.1.3 NO _x storage reduction (NSR).....	14
2.2 SCR reactors.....	15
2.2.1 Structured reactors.....	15
2.2.2 Fluidized bed reactors.....	20
2.2.3 Moving bed reactors.....	22
2.3 Multifunctional SCR reactors.....	24
2.3.1 Decoupled adsorption-reaction.....	24
2.3.2 Combined SCRs.....	35
2.4 Summary.....	36
Chapter 3 Hydrodynamics in i-CFB: experiments & modeling.....	38
3.1 Introduction.....	38
3.2 Experiment details.....	38
3.2.1 Experimental setup.....	38
3.2.1 Bed expansion.....	42
3.2.2 Gas bypass.....	42
3.2.3 Solids circulation rate.....	43
3.3 Hydrodynamics model of i-CFB.....	46
3.3.1 Mass and pressure balance equations.....	46
3.3.2 Pressure drop calculation.....	47
3.3.3 Effective bed height.....	48
3.4 Results and discussion.....	52

3.4.1 Bed expansion characteristics	52
3.4.2 Gas bypass.....	54
3.4.3 Measured solids circulation rates	56
3.4.4 Prediction of solids circulation rate.....	62
3.5 Summary.....	66
Chapter 4 Development of deNO _x reaction kinetics	67
4.1 Introduction	67
4.2 Experiments.....	69
4.2.1 Experimental setup.....	69
4.2.2 Adsorption performance of Fe/ZSM-5.....	72
4.3 Adsorption and reaction modeling in fixed bed.....	74
4.3.1 Kinetics of adsorption	74
4.3.2 NO _x reduction kinetics model	76
4.3.3 Governing equations of the fixed bed reactor model	77
4.4 Modeling results and discussion.....	80
4.4.1 Fitting of adsorption isotherm curves.....	80
4.4.2 Model parameters for the fixed bed adsorption model.....	82
4.4.3 Simulations of NO _x adsorption in fixed bed.....	86
4.4.4 deNO _x reaction kinetics for Fe/ZSM-5 catalyst	88
4.5 Summary.....	90
Chapter 5 Modeling NO _x adsorption in fluidized bed reactors.....	92

5.1 Introduction	92
5.2 Experiment.....	93
5.3 Fluidized bed adsorption model.....	94
5.3.1 Adsorption isotherm.....	94
5.3.2 Governing equations for fluidized bed.....	94
5.3.3 Hydrodynamics	96
5.3.4 Mass transfer	97
5.3.5 Gas and solids mixing	97
5.4 Experimental results	98
5.4.1 Fixed bed.....	98
5.4.2 Fluidized bed.....	99
5.5 Modeling results	100
5.5.1 Parameter fitting.....	100
5.5.2 Simulation of fluidized bed NO _x adsorption	104
5.5.3 Simulation of adsorption zone in an i-CFB deNO _x reactor	109
5.6 Summary.....	115
Chapter 6 Modeling NO _x reduction in fluidized bed reactors.....	117
6.1 Introduction	117
6.2 Fluidized bed reactor model	117
6.2.1 Model governing equations.....	117
6.2.2 Model parameters.....	119

6.3 Fluidized bed modeling results.....	119
6.3.1 Model verification.....	119
6.3.2 Fluidized bed simulation.....	122
6.3.3 Simulation of reduction zone of an i-CFB.....	126
6.4 Summary.....	135
Chapter 7 Modeling catalytic NO _x reduction in i-CFB reactors.....	136
7.1 Introduction.....	136
7.2 i-CFB experiment.....	136
7.3 i-CFB model.....	138
7.3.1 Reaction zones.....	139
7.3.2 Governing equations.....	141
7.3.3 Hydrodynamics.....	144
7.4 Modeling results and comparison with experimental data.....	145
7.4.1 Model verification.....	145
7.4.2 Sensitivity analysis.....	150
7.5 Simulation of i-CFB: design and optimization.....	153
7.5.1 Solids back-mixing.....	153
7.5.2 Solids circulation rate.....	156
7.5.3 i-CFB configurations.....	158
7.6 Summary.....	166
Chapter 8 Conclusions and recommendations for future work.....	168

8.1 Conclusions	168
8.1.1 Hydrodynamics model	168
8.1.2 Adsorption model.....	169
8.1.3 Reaction model.....	170
8.1.4 i-CFB model.....	171
8.2 Recommendations for future work	172
References.....	174
Appendix A More discussions on solids circulation rate.....	186
Appendix B Derivation of adsorption isotherm.....	188
Appendix C Detailed discussion on k_f	192
Appendix D Details of adsorption experiments	195
D.1 Experimental procedure of fixed bed adsorption.....	195
D.2 Experimental details of fluidized bed adsorption	196
D.3 Experimental results of fixed bed adsorption	197
D.4 Experimental results of fluidized bed adsorption	198
Appendix E Sensitivity analysis of fluidized bed adsorption model	200
Appendix F MATLAB codes for i-CFB model	201

List of tables

Table 1.1 Inlet conditions of experiments conducted by Yang [11]	5
Table 1.2 Submodels and data sources used for the modeling of the i-CFB reactor	9
Table 3.1 Dimensions of the cold model i- CFB unit	40
Table 3.2 Fine Fe/ZSM-5 particle properties.....	42
Table 3.3 Calculation procedures for effective bed heights.....	51
Table 4.1 Inlet conditions of fixed bed adsorption experiments.....	72
Table 4.2 Fitted parameters for adsorption model	81
Table 4.3 Comparison of fitted and estimated mass transfer parameters.....	85
Table 4.4 Fitted kinetic model parameters (T=350 °C).....	89
Table 5.1 Experimental conditions of NO _x adsorption	94
Table 5.2 Parameters used in the fluidized bed adsorption model.....	103
Table 6.1 Inlet conditions for different fluidized bed used for simulation	129
Table 7.1 i-CFB equations and boundary conditions.....	142

List of figures

Figure 1.1 Schematic of the integrated NO _x adsorption-reduction process	3
Figure 2.1 Schematics of wire gauze structured reactor [50].....	17
Figure 2.2 Wire-mesh honey comb reactor [50]	18
Figure 2.3 Schematics of ceramic foam [51]	19
Figure 2.4 Schematics of MOC's low-pressure-drop deNO _x fluidized bed reactor [5]	21
Figure 2.5 Fluidized bed reactor for simultaneous SO ₂ /NO _x removal [57]	22
Figure 2.6 Moving bed SCR reactors, (a), MMC design [58], (b), BWPGG design [59]	23
Figure 2.7 Mechanism of decoupled deNO _x process, (a), HC-SCR; (b), direct NO decomposition	25
Figure 2.8 Schematic of NOXSO's IFB reactor [64].....	27
Figure 2.9 Schematics of a temperature swing adsorption (TSA) process [69].....	30
Figure 2.10 Working principle of loop reactor [73].....	32
Figure 2.11 Reverse flow reactor	33
Figure 2.12 Countercurrent internal recirculation reactor [75]	33
Figure 2.13 Schematics of the rotating reactor	34
Figure 3.1 Schematics of the i-CFB reactor.....	39
Figure 3.2 Schematics of the i-CFB system.....	41
Figure 3.3 Schematics of the gas bypass between the draft tube and the annulus.....	43
Figure 3.4 Details of the tip of the optical fibre probe for particle velocity measurement	44
Figure 3.5 Voidage calibration of the optical probe (Symbols: experimental data, line: correlation)	45
Figure 3.6 Schematic of four i-CFB flow modes and the effective bed height.....	51
Figure 3.7 Measured voidage data for ZSM-5 powders and comparison with the Cai correlation (Symbols: experimental data, line: correlation)	53

Figure 3.8 Gas bypass ratios at different U_{d0} . (a), from draft tube to annulus, R_{d-a} ; (b), from annulus to draft tube, R_{a-d} (Symbols: experimental data, lines: correlation)	55
Figure 3.9 Measured radial profiles of (a) voidage and (b) particle velocity at different U_{a0} , ($U_{d0}=1$ m/s, bed loading=2.275 kg. Symbols: experimental data, lines: connection of symbols)	58
Figure 3.10 Measured radial profiles of (a) particle velocity and (b) voidage at different U_{a0} , ($U_{d0}=1$ m/s, bed loading=3.3 kg. Symbols: experimental data, lines: connection of symbols)	59
Figure 3.11 Measured radial profiles of (a) axial particle velocity and (b) voidage at $U_{a0}=0.1$ m/s (Symbols: experimental data, lines: connection of symbols).....	60
Figure 3.12 Net solids circulation rate at different U_{d0} , with bed solids loadings of (a), 2.275 kg, and (b), 3.3 kg. Symbols: experimental data, lines: connection of symbols)	61
Figure 3.13 Calculated (a) voidage and (b) effective bed height at a bed solids loading of 3.3 kg (Symbols: calculated data points, lines: connection of symbols)	63
Figure 3.14 Fitted C_D values as a function of Re_p (Symbols: experimental data, lines: connection of symbols).....	64
Figure 3.15 Predicted (a) $C_{O_2,d}$ and (b) G_s as a function of U_{a0}	65
Figure 4.1 Fixed bed reaction system	70
Figure 4.2 Adsorption capacity of (a) O_2 at different temperatures and (b) NO_x at different O_2 concentrations (Symbols: experimental data, lines: connection of symbols)	73
Figure 4.3 Schematics of NO_x adsorption mechanism onto the catalyst surface	78
Figure 4.4 Adsorption capacities as a function of the feed concentration at different temperatures (Symbols: experimental data; lines: isotherm model).....	81
Figure 4.5 Comparison of fitted and experimental adsorption curves in the fixed bed reactor at 325°C with $NO=600$ ppm	82
Figure 4.6 Comparison of model fitted and experimental adsorption curves at different (a) NO_x concentrations and (b) temperatures. (Symbols: experimental data; lines: model fitting).....	86

Figure 4.7 (a): gas phase concentration along the reactor length; (b): effluent concentration as a function of time at different temperatures	87
Figure 4.8 Effluent NO _x concentration as a function of time at different GHSV	88
Figure 4.9 Modeled and simulated conversions at different HC:NO ratios in fixed bed, (a), NO _x conversion; (b), HC conversion. (Symbols: experimental data; lines: model fitting).....	90
Figure 5.1 Schematic of mass transfer (a) in the fluidized bed and (b) around particles.....	95
Figure 5.2 Adsorption capacity at different feed NO _x concentrations. (Symbols: experimental data; lines: fitted isotherm model).....	99
Figure 5.3 Breakthrough curves at (a) different NO _x inlet concentrations at 250 °C; and (b) different gas velocities at 300 °C.....	100
Figure 5.4 Comparison of model-fitted and experimental breakthrough curves at different (a) velocities and (b) temperatures (Symbols: experimental data; lines: model fitting).....	102
Figure 5.5 Model evaluation at different temperatures (Symbols: experimental data; lines: model fitting)	104
Figure 5.6 (a) Outlet NO _x concentrations in different phases as a function of time; (b), dimensionless NO _x concentration as a function of dimensionless bed height, (t=170 s)	106
Figure 5.7 Influence of particle size on outlet NO _x concentrations	107
Figure 5.8 Influence of superficial gas velocity on outlet NO _x concentration	109
Figure 5.9 Gas and solids flow in (a) conventional fluidized bed and (b) continuous fluidized bed decoupled from the i-CFB reactor	110
Figure 5.10 NO _x adsorption performance as a function of G_s^*	113
Figure 5.11 NO _x adsorption performance as a function of $C_{s,feed}/C_s^*$	115
Figure 6.1 Modeled NO _x and HC conversion as a function of superficial gas velocity in the fluidized bed (Symbols: experimental data; lines: model fitting).....	122
Figure 6.2 NO _x conversion at different U_g in fixed and fluidized bed reactors	123
Figure 6.3 Dimensionless axial profiles of NO _x concentration in different phases	124

Figure 6.4 NO _x conversion at different gas dispersion and interphase mass transfer coefficient as a function of U _g	125
Figure 6.5 Dimensionless solids phase NO _x concentration along the reactor at different settings	126
Figure 6.6 Flow diagram of fluidized bed and decoupled i-CFB	127
Figure 6.7 Dimensionless NO _x concentration as a function of U _g for different reactors	131
Figure 6.8 X _r as a function of U _g in different reactors.....	132
Figure 6.9 Overall efficiency, X _r , and slip ratio, SI, as a function of G _s /G _{s0}	133
Figure 6.10 X _r and SI values at different solids circulation rate.....	135
Figure 7.1 Schematics of i-CFB model.....	139
Figure 7.2 Schematics of the flow regions of i-CFB studied.....	140
Figure 7.3 (a) NO _x and (b) HC conversion as a function of U _{a0} (O ₂ =4%, U _{d0} =0.6 m/s. Symbols: experimental data; lines: model fitting)	147
Figure 7.4 NO _x conversion as a function of U _{a0} at O ₂ =4%, a), U _{d0} =0.75 m/s, b), U _{d0} =0.9 m/s (Symbols: experimental data; lines: model fitting)	148
Figure 7.5 NO _x conversion as a function of U _{a0} at a), U _{d0} =0.6 m/s , b), U _{d0} =0.75 m/s (Symbols: experimental data; lines: model fitting)	149
Figure 7.6 Comparison of NO _x conversion in an i-CFB and a regular fluidized bed (Symbols: experimental data; lines: model fitting)	150
Figure 7.7 Sensitive of NO _x conversion in i-CFB to gas bypasses	152
Figure 7.8 Sensitivity of NO _x conversion to variations in NO _x adsorption capacity and reduction rate constant	153
Figure 7.9 Profile of dimensionless NO _x concentration along bed height	155
Figure 7.10 Axial profiles of dimensionless solids phase NO _x concentrations at different G _s	157
Figure 7.11 NO _x conversion as a function of solids circulation rate G _s	158
Figure 7.12 Schematics of the simulated i-CFB	160
Figure 7.13 NO _x conversion as a function of A _R /A _{total}	162

Figure 7.14 NO _x concentration change as a function of A _R /A _{total} at different zones.....	163
Figure 7.15 Sensitivity of NO _x conversion to NO _x adsorption capacity for i-CFBs with different configurations	165
Figure 7.16 Sensitivity of NO _x concentration change to catalyst NO _x adsorption capacity	165
Figure A.1 Experimental and modeled solids circulation rates at a bed solids loading of 2.275 kg. (Symbols: experimental data; lines: modeling results.)	187
Figure D.1 Schematics of fluidized bed set-up	196
Figure D.2 Fixed bed NO _x adsorption breakthrough curves at 250 °C	198
Figure D.3 Repeated breakthrough curves in the fluidized bed (T=300 °C, NO=900 ppm)	198
Figure D.4 Breakthrough curve of different NO _x inlet concentrations at (a) 300 °C and (b) 350 °C.	199
Figure E.1 Model sensitive analysis	200

List of abbreviations

BWPGG	Babcock & Wilcox Power Generation Group
CSTR	Continuously stirred tank reactors
deNO _x	NO _x reduction
ESP	Electrostatic precipitator
FCC	Fluidized catalytic cracking
Fe(AA) ₃	Iron(III) acetylacetonate
GHSV	Gas hourly space velocity, h ⁻¹
HC	Hydrocarbon
HC-SCR	Selective catalytic reduction with hydrocarbon
I.D.	Inner diameter
i-CFB	Internal circulating fluidized bed
IFB	Interconnected fluidized bed
IMPO	Impregnation in organic solution
LNP	Lean NO _x traps
MMC	Mitsui Mining Company
MOC	Mobile Oil Company
NH ₃ -SCR	Selective catalytic reduction with ammonia
NSR	NO _x storage-reduction
NTP	Non-thermal plasma
O.D.	Outer diameter
PUC	China University of Petroleum (Beijing, China)

SCR	Selective catalytic reduction
SNCR	Selective non-catalytic reduction
VOC	Volatile organic compound
ZSM-5	One type of zeolite

Nomenclature

A	Reactor cross area, m^2
A_a	Cross sectional area of the annulus, m^2
A_A	Cross sectional area of the adsorption zone, m^2
a_b	Contacting area of bubbles in unit volume, m^{-1}
A_d	Cross sectional area of the draft tube, m^2
A_i	Arrhenius pre-exponential coefficient of reaction i, $mol/s.m^3$
A_{or}	Area of orifice, m^2
A_R	Cross sectional area of the reduction zone, m^2
A_{total}	Total cross sectional area, m^2
b	Adsorption coefficient in Langmuir isotherm, -
B	Lumped coefficient for site coverage on the catalyst, -
b_0	Adsorption coefficient in Langmuir isotherm, -
b_{NO_2}	Adsorption coefficient in Langmuir isotherm of NO_2 , -
C_0	Initial concentration, mol/m^3
$C_{a,H}$	Concentration in the dense (high) phase of the annulus, mol/m^3
$C_{a,in}$	Inlet concentration of the annulus, mol/s

$C_{a,L}$	Concentration in the bubble (low) phase of the annulus, mol/m ³
$C_{a,out}$	Concentration at the outlet of the annulus, mol/m ³
C_D	Discharging coefficient of the orifice, -
$C_{d,H}$	Concentration in the dense (high) phase of the draft tube, mol/m ³
$C_{d,in}$	Inlet concentration of the draft tube, mol/s
$C_{d,L}$	Concentration in the bubble (low) phase of the draft tube, mol/m ³
$C_{d,out}$	Concentration at the outlet of the draft tube, mol/m ³
$C_{feeding}$	Feeding concentration, mol/m ³
C_g	Concentration in gas phase, mol/m ³
C_{g^*}	Gas phase concentration in equilibrium with solids phase, mol/m ³
$C_{g,in}$	Inlet concentration in gas phase, mol/m ³
$C_{g,out}^*$	Outlet gas phase NO _x concentration in equilibrium with solids phase inlet NO _x concentration, mol/m ³ .cat
C_{gi}	Concentration in gas phase of species i, mol/m ³
C_H	Concentration in high (dense) phase, mol/m ³ . cat
$C_{HC,a}$	Hydrocarbon concentration in the annulus, mol/m ³
$C_{HC,a0}$	Hydrocarbon concentration in the flue gas fed into the annulus, mol/m ³
$C_{HC,d}$	Hydrocarbon concentration in the draft tube, mol/m ³

$C_{HC,d0}$	Hydrocarbon concentration in the reductant gas fed into the draft tube, mol/m ³
C_i	Concentration of species i, mol/m ³
$C_{in,NOx-A}$	NO _x concentration at the inlet of the adsorption zone, mol/m ³
$C_{in,NOx-R}$	NO _x concentration at the inlet of the reduction zone, mol/m ³
C_L	Concentration in low (bubble) phase, mol/m ³ . cat
c_m	Total number of active on the catalyst, mol/kg cat
C_{NO}	NO concentration, mol/m ³
$C_{NO,a}$	NO concentration in the annulus, mol/m ³
$C_{NO,a0}$	NO concentration in the flue gas fed into the annulus, mol/m ³
$C_{NO,d}$	NO concentration in the draft tube, mol/m ³
$C_{NO,d0}$	NO concentration in the reductant gas fed into the draft tube, mol/m ³
C_{O_2}	O ₂ concentration, mol/m ³
$C_{O_2,a}$	Oxygen concentration in the annulus, mol/m ³
$C_{O_2,a0}$	Oxygen concentration in the flue gas fed into the annulus, mol/m ³
$C_{O_2,d}$	Oxygen concentration in the draft tube, mol/m ³
$C_{O_2,d0}$	Oxygen concentration in the reductant gas fed into the draft tube, mol/m ³
C_{out}	Outlet concentration, mol/m ³
$C_{out,NOx-A}$	NO _x concentration at the outlet of the adsorption zone, mol/m ³

$C_{\text{out,NO}_x\text{-R}}$	NO_x concentration at the outlet of the reduction zone, mol/m^3
C_s	Concentration in solids phase, $\text{mol/m}^3 \cdot \text{cat}$
C_s^*	Solids phase NO_x concentration in equilibrium with gas phase inlet NO_x concentration, $\text{mol/m}^3 \cdot \text{cat}$
$C_{s,\text{feeding}}$	Concentration in feeding solids, $\text{mol/m}^3 \cdot \text{cat}$
$C_{s,\text{in}}$	Inlet concentration in solids phase, mol/m^3
$C_{s,\text{out}}^*$	Outlet solids phase NO_x concentration in equilibrium with gas phase inlet NO_x concentration, $\text{mol/m}^3 \cdot \text{cat}$
$C_{\text{XNO}_x\text{-A}}$	NO_x concentration change in the adsorption zone, %
$C_{\text{XNO}_x\text{-R}}$	NO_x concentration change in the reduction zone, %
D	Diameter, m
D_a	Diameter of the annulus zone, m
D_b	Bubble diameter, m
D_d	Diameter of the draft tube, m
D_e	Effective diffusivity, m^2/s
D_g	Gas axial dispersion coefficient, m^2/s
D_H	Axial dispersion coefficient of high (dense) phase, m^2/s
D_L	Axial dispersion coefficient of low (bubble) phase, m^2/s

D_m	Molecular diffusivity, m^2/s
d_p	Particle diameter, m
D_s	Axial dispersion coefficient of solids phase, m^2/s
E	Overall efficiency, -
E_{ai}	Activation energy of reaction i, J/mol
E_r	Reduction efficiency, %
F	Gas flow rate at room temperature, m^3/s
F_A	Flow rate in the adsorption zone, m^3/s
F_{a0}	Flow rate of feeding gas in the annulus, m^3/s
F_{a-d}	Flow rate of gas bypass from the annulus to the draft tube, m^3/s
F_b	Gas flow rate in bubble phase, m^3/s
F_d	Gas flow rate in the draft tube, m^3/s
F_{d0}	Flow rate of feeding gas in the draft tube, m^3/s
F_{d-a}	Flow rate of gas bypass from the draft tube to the annulus, m^3/s
$F_{flue-gas}$	Flow rate of flue gas, m^3/s
F_{fw}	Gas-wall friction force per unit volume of the column, N/m^3
F_{pw}	Particle-wall friction force per unit volume of the column, N/m^3
Fr	Froude number,-

F_R	Flow rate in the reduction zone, m^3/s
g	Acceleration due to gravity, $9.8 m/s^2$
G_s	Solids circulation rate, $kg/m^2.s$
G_s^*	Dimensionless solids circulation rate
$G_{s,0}$	Minimum solids circulation rate, $kg/m^2.s$
H	Bed height, m
H_a	Bed height in the annulus, m
H_{CA}	Hydrocarbon molar flow rate in the adsorption zone, mol/s
H_{CR}	Hydrocarbon molar flow rate in the reduction zone, mol/s
HC_t	Total hydrocarbon molar flow rate, mol/s
H_d	Bed height in the draft tube, m
$H_{draft-tube}$	Height of the draft tube, m
H_f	Expanded bed height, m
H_G	Gap distance in the distributor, mm
H_{mf}	Bed height at minimum fluidization, m
H_s	Bed height, m
k	Overall mass transfer coefficient, s^{-1}
K	Adsorption equilibrium in linear adsorption isotherm, -

k_1	Reaction rate coefficient of reaction 1 (forward), -
k'_1	Intraphase mass transfer coefficient, s^{-1}
k_{-1}	Reaction rate coefficient of reaction 1 (reversed), -
k_2	Reaction rate coefficient of reaction 2 (forward), -
k'_2	Intraphase mass transfer coefficient, s^{-1}
k_{-2}	Reaction rate coefficient of reaction 2 (reversed), -
k_3	Reaction rate coefficient of reaction 3, -
k_4	Reaction rate coefficient of reaction 4, -
k_c	External mass transfer coefficient, m/s
k_f	Intraphase mass transfer coefficient, s^{-1}
k_F	Freundlich adsorption constant related to sorption capacity, -
k'_f	Modified intraphase mass transfer coefficient, s^{-1}
k_{f0}	Intraphase mass transfer coefficient, s^{-1}
k_{Fi}	Freundlich adsorption constant related to sorption capacity of species i, -
k_{FNO_2}	Freundlich adsorption constant related to sorption capacity of NO_2 , -
k_{FO_2}	Freundlich adsorption constant related to sorption capacity of O_2 , -
k_{HL}	Interphase mass transfer coefficient, m/s
k_i	Reaction rate coefficient of reaction i, -

K_i	Adsorption equilibrium of species i, -
k_{i0}	Reaction rate coefficient of reaction i, -
K_{i0}	Adsorption equilibrium of species i, -
K_{NO_2}	Adsorption equilibrium of NO_2 , -
k'_{NO_2}	Lumped Freundlich adsorption constant related to sorption capacity of NO_2 , -
k''_{NO_2}	Freundlich adsorption constant related to sorption capacity of NO_2 lumped with O_2 , -
K_{O_2}	Adsorption equilibrium of O_2 , -
L	Reactor length, m
L_a	Effective bed length in the annulus, m
L_{a0}	Initial effective bed length in the annulus, m
L_d	Effective bed length in the draft tube, m
L_{d0}	Initial effective bed length in the draft tube, m
L_e	Effective distance of optical fibre, m
L_j	Jet penetration depth, m
m_1	Reaction order, -
m_2	Reaction order, -
m_3	Reaction order, -
m_4	Reaction order, -

m_5	Reaction order, -
M_a	Catalyst weight in the annulus, kg
M_d	Catalyst weight in the draft tube, kg
M_{loading}	Catalyst loading in i-CFB, kg
M_{NO}	Molecular weight of NO, 30 g/mol
n	Freundlich adsorption constant related to sorption intensity, -
$N(Q)$	Number of sites having adsorption energy Q , -
n_i	Constant in Freundlich adsorption equations of species i , -
n_{NO_2}	Constant in Freundlich adsorption equations of NO_2 , -
n_{NO_x}	Constant in Freundlich adsorption equations of NO_x , -
n_{O_2}	Constant in Freundlich adsorption equations of O_2 , -
P	Operation pressure, Pa
Pe_c	Correlated Péclet number, -
Pe_f	Fitted Péclet number, -
Pe_H	Péclet number of high (dense) phase, -
Pe_s	Péclet number of solids phase, -
Q	Adsorption energy, J/mol
q	Adsorbate loading, $\text{mol/m}^3 \text{ cat}$

q	Average adsorbate loading, mol/m ³ cat
q^*	Adsorbate loading in equilibrium, mol/m ³ cat
Q_b	Volumetric gas flow rate in bubble phase, (m ³ /s)
q_e	Adsorption capacity, mol/m ³ . cat
$q_{e,i}$	Adsorption capacity of species i, mol/m ³ . cat
q_{eNO_x}	Adsorption capacity of NO _x , mol/m ³ . cat
q_{eO_2}	Adsorption capacity of O ₂ , mol/m ³ . cat
$Q_{NO_x,d-a}$	Molar flow rate of NO _x returned from the annulus to the draft tube, mol/s
$Q_{NO_x,feeding}$	Molar flow rate of NO _x in the feeding flue gas, mol/s
$Q_{NO_x,slip}$	Molar flow rate of NO _x slipping out of the reduction zone, mol/s
R	Ideal gas constant, 8.314 J/Pa.K
r	Radius, m
R_0	Radius of fluidized bed, m
r_1	Reaction rate of reaction 1, mol/s.m ³
r_2	Reaction rate of reaction 2, mol/s.m ³
r_3	Reaction rate of reaction 3, mol/s.m ³
r_4	Reaction rate of reaction 4, mol/s.m ³
R_a	Radius of the annulus, m

R_{a-d}	Gas bypass ratio from the annulus to the draft tube, %
R_d	Radius of the draft tube, m
R_{d-a}	Gas bypass ratio from the draft tube to the annulus, %
Re	Reynolds number, -
Re_c	Reynolds number at transition velocity, -
Re_p	Reynolds number around particles, -
r_{HC}	Reaction rate of HC, mol/s.m ³
$R_{HC:NO}$	Molar ratio of HC:NO, -
R_i	Reaction rate of species i, mol/s.m ³
r_{NO_x}	Reaction rate of NO _x , mol/s.m ³
r_{O_2}	Reaction rate of O ₂ , mol/s.m ³
R_p	Radius of particles, m
S	Integrated area of the adsorption curve, s
Sc	Schmidt number, -
Sh	Sherwood number, -
Sl	NO _x slip ratio from reduction zone, %
t	Time, s
T	Temperature, K

T_0	Ambient temperature, °C
$t_{1/2}$	Breakthrough time, s
U	Superficial gas velocity, m/s
U_a	Real gas velocity in the annulus, m/s
$U_{a,H}$	Gas velocity of the dense (high) phase in the annulus, m/s
$U_{a,L}$	Gas velocity of the bubble (low) phase in the annulus, m/s
U_{a0}	Feeding gas velocity in the annulus, m/s
U_b	Bubble rise velocity, m/s
U_c	Transition velocity at which standard deviation of pressure fluctuation reaches a maximum, m/s
U_d	Gas velocity in the draft tube, m/s
$U_{d,H}$	Gas velocity of the dense (high) phase in the draft tube, m/s
$U_{d,L}$	Gas velocity of the bubble (low) phase in the draft tube, m/s
U_{d0}	Feeding gas velocity in the draft tube, m/s
U_g	Gas velocity, m/s
U_H	Gas velocity in high (dense) phase, m/s
U_L	Gas velocity in low (bubble) phase, m/s
U_{mf}	Minimum fluidization velocity, m/s

U_{out}	Gas velocity at the outlet, m/s
U_p	Particle velocity, m/s
$U_{p,a}$	Particle velocity in the annulus, m/s
$U_{p,d}$	Particle velocity in the draft tube, m/s
U_s	Solids velocity, m/s
U_t	Terminal velocity, m/s
V_{catalyst}	Volume of catalyst, m^3
V_g	Gas volumetric flow rate, m^3/s
V_s	Solids volumetric flow rate, m^3/s
W_{cat}	Catalyst loading, g
X	Conversion, %
x	Fraction, -
X_r	NO_x conversion in reduction zone, %
Y	Dimensionless coefficient, -
z	Axial position in the reactor, m
ΔP	Pressure drop, Pa
ΔP_a	Pressure drop in the annulus, Pa
ΔP_{a0}	Initial pressure drop in the annulus, Pa

ΔP_d	Pressure drop in the draft tube, Pa
ΔP_{d0}	Initial pressure drop in the draft tube, Pa
ΔP_{or}	Pressure drop through the orifice, Pa
α	Pre-exponential coverage coefficient, -
ε	Voidage, -
ε_a	Voidage in the annulus, -
ε_b	Bubble fraction, -
ε_d	Voidage in the draft tube, -
ε_{mf}	Voidage at minimum fluidization, -
ε_s	Solids fraction, -
Θ	Coverage on the catalyst, -
Θ_T	Total coverage on the catalyst, -
κ	Coefficient for Freundlich constant related to temperature, -
μ	Dynamic viscosity, Pa.s
ρ_g	Gas density, kg/m ³
ρ_p	Density of catalyst particles, kg/m ³
τ	Time lag, s
$\Phi_{a,H}$	Fraction of high (dense) phase in the annulus, -

$\Phi_{a,L}$	Fraction of low (bubble) phase in the annulus, -
$\Phi_{d,H}$	Fraction of high (dense) phase in the draft tube, -
$\Phi_{d,L}$	Fraction of low (bubble) phase in the draft tube, -
Φ_H	Fraction of high (dense) phase, -
Φ_L	Fraction of low (bubble) phase, -
ψ	Slip factor, -
ϕ_s	Spherical coefficient, -

Acknowledgements

I would like to take this opportunity to express my sincere gratitude to my supervisor, Dr. Xiaotao Bi, for his immense guidance and financial assistance during my research. I give utmost appreciation to my research committee members, Dr. Jim Lim and Dr. W. Kendal Bushe, for their valuable suggestions at the start of this work.

Many individuals who contribute to this research would be greatly acknowledged. Dr. Terris Tianxue Yang, a former PhD student in our group, who carried out the preliminary research work on i-CFB catalytic reduction of NO_x by hydrocarbon in our group, provided very used suggestions on the experimental work. Dr. Chuigang Fan, a former postdoctor fellow in our group, contributed a lot to the setup of the fixed bed and i-CFB units. Dr. Zhiwei Chen, a postdoctor fellow from Dr. Bi's group, helped a lot with the model development, program coding, solids circulation rate measurement and fluidized bed setup. Dr. Jun Xu, a former visiting student from China, provided help with the i-CFB reactor setup and solids circulation rate measurement. Dr. Luning Tian, a former visiting student from China, helped with the experimental work of fluidized bed adsorption investigation. I also appreciate the hard work of the technical and administrative staff in the department stores, offices and workshop.

This research was financially supported by the Canada Foundation for Innovation (CFI) and the Natural Science and Engineering Research Council of Canada (NSERC). I'm also grateful to a CSC Scholarship from China.

Last but not least, I am sincerely grateful to my family for their endless support and encourage throughout my whole life.

Chapter 1 Introduction

1.1 Background

Growing environmental awareness in recent years has resulted in the introduction of more rigorous and stringent environmental laws and regulations. The term ‘air pollutant’ covers all substances which may harm humans, animals, vegetation and material [1, 2]. The main sources of air pollution are the combustion processes of fuels used in power plants, vehicles and other incineration processes. Key combustion-generated air contaminants are sulfur oxides (principally SO_2), particulate matter, carbon monoxide, hydrocarbons and nitrogen oxides (NO_x). NO_x are considered as the primary pollutants of the atmosphere, since they are responsible for the formation of photochemical smog, acid rain and ground level ozone, the destruction of stratosphere ozone layer and even global warming (mainly associated with N_2O) [1-3].

There are two major sources of NO_x : mobile combustion engines and stationary sources, such as power plants [1-4]. The abatement of NO_x emission can be generally classified into three categories: pre-combustion control, combustion modification and post-combustion control [2]. Pre-combustion control can be achieved by fuel purification to reduce the nitrogen content in the fuel. Combustion modification alters operational conditions to reduce the NO_x formation. Both pre-combustion and combustion controls are helpful, but can only achieve a modest reduction in NO_x emissions, usually less than 50% [3, 5]. For applications required to achieve high NO_x reduction, post combustion control is needed. Post-combustion control, as the term suggests, deals with nitrogen oxides in exhaust gases from combustion or incineration processes. The most commonly used technologies are selective non-catalytic reduction (SNCR) and selective catalytic reduction (SCR) of NO_x [3, 4].

SNCR reactors are typically operated at 870-980 °C, with urea or ammonia as the reductant to reduce NO_x to N₂ [3, 4]. Capital costs are moderately low because no catalyst is required. A drawback of this approach is that the maximum level of NO_x reduction achievable is only about 50% [5]. The SCR process is a proven technology for NO_x emission control [4, 5]. It operates at moderate temperatures, with a higher capital and operating costs than SNCR. It adds reducing agent to a NO_x containing flue gas stream and relies on a catalyst, usually honeycomb monoliths, to promote the reduction of NO_x by reducing agent. It is the only single method which can achieve more than 75% NO_x control efficiency for the flue gases emitted from stationary combustion sources with a high selectivity toward N₂ [6]. A well-designed SCR reactor could reach an efficiency of 94% and tolerable ash contents up to a maximum of 50 g/m³ [6].

The NH₃-SCR offers a practical approach for NO_x abatement, and has been commercialized [6, 7]. However, it has the following drawbacks: the handling of large quantities of NH₃ is a concern because NH₃ is toxic and corrosive. Furthermore, un-reacted NH₃ may potentially be discharged to the environment (ammonia slippage) [3, 4]. It could also react with SO₃ and H₂O to form ammonium sulphate, causing the fouling of downstream equipment. Vanadium emissions and high operating costs are also obstacles for this technology [3, 8]. Taking the drawbacks of the NH₃-SCR process into account, hydrocarbons instead of NH₃ have been considered as the most promising alternate reducing agents for the SCR process.

As a technology under development, most studies have focused on the development of catalysts, the selection of reducing agents, or the understanding of the reaction mechanisms of the process [9]. In order for such a technology to be used in industrial processes, engineering aspects still need to be considered to address technical challenges in the reactor design and scale-up for the HC-SCR process.

To avoid the negative impact of the poisoning components and excess O₂ in the flue gas, Yang and Bi [10] proposed a new concept of an integrated NO_x adsorption-reduction process, where the NO_x

adsorption and reduction are carried out in two separate zones of the reactor, as shown in Fig. 1.1. The flue gas is passed into the adsorption zone where NO_x is adsorbed by the catalyst. The NO_x -adsorbed catalyst particles then move into the reaction zone where NO_x is reduced by injected hydrocarbons at controlled oxygen concentrations, and at the same time, other adsorbed flue gas contaminants are also stripped from the catalyst. The regenerated catalyst particles are then recirculated back to the adsorption zone to establish a continuous operation. The hypothesis has then been validated in a novel internal circulating fluidized bed (i-CFB) reactor and the work was presented in Yang's PhD thesis [11].

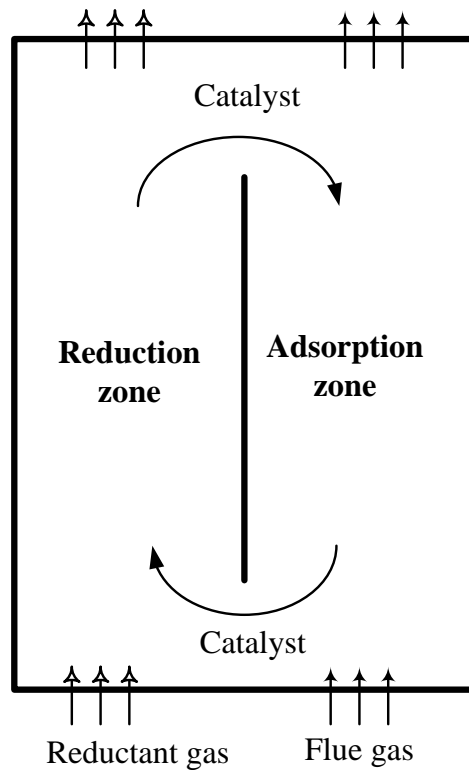


Figure 1.1 Schematic of the integrated NO_x adsorption-reduction process

1.2 Previous research results summary on i-CFB

The main objective of Yang's work [11] was to evaluate the potential application of the integrated adsorption-reduction process for the selective catalytic reduction of NO_x with hydrocarbons in the internal circulating fluidized bed (i-CFB) reactor.

The catalyst used by Yang [11] was Fe/ZSM-5, which showed a good performance. The catalyst support was H/ZSM-5 (BET surface area of $171 \text{ m}^2/\text{g}$), which was obtained as a free sample from Albemarle Corporation. The fine Fe/ZSM-5 catalyst was prepared by wet impregnation in organic solution (IMPO) of toluene. The prepared fine Fe/ZSM-5 catalyst has an iron content of 5% and a BET surface area of $163 \text{ m}^2/\text{g}$, which is slightly lower than the original ZSM-5 catalyst support. The reducing agent used for the HC-SCR process was propylene, which also showed good NO_x reduction activity over ZSM-5 catalysts in other researches [12, 13].

Three experiment units were built by Yang [11]: a fixed bed unit to test the adsorption performance and reaction kinetics of the catalyst; a cold model i-CFB unit to investigate the hydrodynamics, mainly gas bypass; and a hot model i-CFB, with the same dimension of cold model i-CFB, to study the deNO_x performance.

The hypothesis of i-CFB was validated by Yang [11] by a series of experiments. In the fixed bed reactor, the catalyst was tested at different inlet conditions for its adsorption and reaction performances. The hydrodynamics of i-CFB, mainly gas bypass between the annulus and draft tube, was investigated in the cold model i-CFB unit. Then the deNO_x reaction was studied in the hot model i-CFB reactor. The results showed that the catalyst exhibited promising NO_x reduction performance and a strong ability to inhibit the negative impact of excess O_2 in the i-CFB reactor, proving that adsorption-reduction two-zone reactor is effective for the NO_x removal from oxygen-rich combustion flue gases. For different experiments, the different reaction conditions and parameters investigated are summarized in Table 1.1. Details of the data could be found in [11]. It should be noted that another catalyst Fe/ZSM-5 (PUC),

which was prepared from a different ZSM-5 support, was also tried by Yang [11]. But its performance for deNO_x is much worse. Similarly, some other i-CFB configurations with different distributors were also tested, but finally dropped due to the unsatisfactory hydrodynamic characteristics. These results won't be used for the modeling. In this thesis, only the selected results are discussed.

Table 1.1 Inlet conditions of experiments conducted by Yang [11]

Unit	Experiment	Inlet condition	Parameters investigated
Fixed bed	NO adsorption	O ₂ =4% NO=200, 400, 600, 800, 1000 ppm GHSV=5000 h ⁻¹	NO _x adsorption breakthrough curves NO _x adsorption capacity
	NO _x reaction	O ₂ =0.5, 1, 2, 4, 8 % NO=600 ppm HC:NO= 0.5, 1, 2, 4 GHSV=5000 h ⁻¹	NO _x conversion HC conversion
Cold model i-CFB	Hydrodynamics	U _{a0} =0.2~0.45 m/s U _{d0} =0.4~0.9 m/s	Gas bypass ratios: R _{a-d} , R _{d-a}
Hot model i-CFB	NO _x reaction	NO=600 ppm HC:NO=1, 2 O ₂ =1, 4, 8, 12 % U _{a0} =0.2~0.5 m/s U _{d0} =0.6~0.9 m/s	NO _x conversion HC conversion
Regular fluidized bed	NO _x reaction	NO=600 ppm HC:NO=1, 2 O ₂ =1, 4, 8 % U _g =0.2~0.6 m/s	NO _x conversion HC conversion

1.3 A review on fluidized bed reactor models

For the modeling of fluidized bed reactors, two types of models have been proposed: mechanistic models and computational fluid dynamic (CFD) models.

Mechanistic modeling is an interactive process of representing a system found in nature by an abstract mathematical description based on physical and chemical principles in order to make prediction and gain insights about the system's underlying phenomena. This process attempts to match observations with a set of equations describing and explaining what is observed and/or measured in nature, and predicting the behaviour of a system [14]. Mechanistic models are the most traditional method used for fluidized bed modeling since 1950s [15]. They incorporate the key factors, such as dispersion, convection, mass transfer, mass and molar balance equations, leaving out factors of lesser importance. These models could provide rational approaches for predicting key features of fluidized beds while keeping the calculation simple.

The other type is the computational fluid dynamic (CFD) model, which is established based on fundamental continuity, momentum and energy equations (Navier-Stokes equations). CFD codes have had great success in recent decades in simulating single-phase flows. Similar approaches have been attempted by a number of research groups for multiphase flows. With the fast development of high speed computers, CFD models have become an expanding subject and are playing an important role in fluidization applications. There are two categories of CFD models for gas-solids flows: Lagrangian-Eulerian models and Eulerian-Eulerian models. While multiphase CFD models will no doubt make valuable future contributions to predicting the performance of fluidized bed reactors, they are currently unable to make reliable predictions [16]. Comparing to CFD models, mechanistic models are currently more reliable, while also being much easier to be used [16]. In the current study, the mechanistic model is selected.

The conversion in gas-solids fluidized bed reactors has been observed to be lower than those with the gas flow being assumed as in plug flow or well-mixed flow [17]. Historically, two classes of mechanistic models have been proposed to describe the performance of fluidized bed reactors: one is based on a pseudo-homogeneous approach and the other on a two-phase approach [18]. The pseudo-homogeneous approach, where the existence of more than one phase is not taken into account, applies the conventional single phase flow models, such as dispersion models, CSTR-in-series models, to fluidized bed reactors.

The two-phase approach, however, considers the fluidized reactor to consist of at least two phases, a bubble phase and an emulsion/dense phase, and proposes separate governing equations for each phase with a term describing mass interchange between the two phases. The concept of two-phase fluidization [15] and the first two-phase fluidized-bed reactor model [19] dated back to the 1950s. Since then, various two-phase reactor models have been developed for different fluidization regimes. Those models, which incorporate solid fractions, mixing and interphase exchange, have been used for modeling and scale-up of fluidized bed reactors. Such models include the Grace [20] two-phase model, the Kunii and Levenspiel [21] three-phase model, the Kato and Wen [22] bubble assemblage model and the Partridge and Rowe [23] cloud model, just to list a few. These models have either been derived or comprehensively summarized by Grace [20, 24], Kunii and Levenspiel [25] and more recently by Marmo et al. [26] for bubbling bed. Bi et al. [27] summarized models developed for turbulent fluidized bed reactors, accounting for interchange of gas between low- and high-density phases, axial dispersion, gas convection and reaction. Recently, generalized comprehensive models were further developed by Abba [28] and Mahecha-Betero [14], which are applicable across the flow regimes most commonly encountered in industrial scale fluidized bed reactors.

1.4 Research objective of this study

The possible application of the integrated adsorption-reduction process for the selective catalytic reduction of NO_x with hydrocarbons was identified and demonstrated by Yang [11] in an internal circulating fluidized bed. The i-CFB reactor exhibited the ability to overcome the negative impact of excessive O_2 in the flue gas using Fe/ZSM-5 as the de NO_x catalyst. In order to scale up this process and to understand the underlying fundamental mechanism of this novel i-CFB reactor system, a mathematical reactor model is needed. Furthermore, the NO_x conversion in the current i-CFB design was less than 80%, which needs to be further optimized in order to improve the de NO_x efficiency. Modeling is an effective and efficient approach to systematically examine the i-CFB reactor at low-cost. The objective of this research is to develop a mathematical model for the i-CFB reactor to predict, simulate and ultimately improve the performance of the i-CFB reactor, assisting the design and scale up of pilot and commercial i-CFB de NO_x reactors.

Before developing the i-CFB model, three different parts will be studied first: hydrodynamic, adsorption kinetics and reaction kinetics. Key hydrodynamic parameters of an i-CFB include gas bypass and solids circulation rate. An adsorption isotherm of the investigated catalyst will be developed based on fixed bed adsorption experimental data and then evaluated by fluidized bed adsorption experimental data. Similarly, reaction kinetics of the catalyst will be developed from fixed bed reaction experiment data and then evaluated by the fluidized bed performance data. Finally, the hydrodynamic, adsorption and reaction kinetics models are integrated to simulate the performance of i-CFB reactors. Data in Yang's thesis [11] will be used to fit model parameters and evaluate the model predictions. Additional experiments are also carried out to measure the model parameters not investigated in the previous studies. Different parts of the i-CFB model, together with the experimental data sources, are listed in Table 1.4.

Table 1.2 Submodels and data sources used for the modeling of the i-CFB reactor

Models	Sub-models	Experimental data source
Hydrodynamics	Gas bypass rate	Yang [11]
	Solids circulation rate	This study
Adsorption	Fixed bed adsorption: adsorption isotherm	Yang [11] and this study
	Fluidized bed adsorption performance	This study
Reduction	Fixed bed reaction: kinetics	Yang [11]
	Fluidized bed reaction performance	Yang [11]
i-CFB model	i-CFB reaction performance	Yang [11]

1.5 Thesis layout

Chapter 1 provides the background of the project, a summary of previous work conducted in our group and the objectives of this study. A literature review is then presented in Chapter 2 to summarize the development of SCR technologies and novel reactors. Hydrodynamics of i-CFB, including gas bypass and solids circulation rate, is studied by both experiment and modeling in Chapter 3. Adsorption breakthrough curves and reaction kinetics are developed based on fixed bed test data in Chapter 4. Then adsorption isotherms and kinetics are used to model adsorption performance in fluidized beds, together with the performance of the adsorption zone in an i-CFB, in Chapter 5. NO_x reaction kinetics is applied to investigate the NO_x reduction performance in a fluidized bed reactor in Chapter 6. Finally, the NO_x reaction in the i-CFB is modeled and simulated in Chapter 7 by integrating the hydrodynamic, adsorption and reaction kinetics models in Chapters 3 to 6. Recommendations are also made on how to improve the design and performance of the i-CFB for catalytic NO_x reduction. Conclusions drawn from this study and recommendations for future studies are given in Chapter 8.

Chapter 2 Literature review: SCR reactors¹

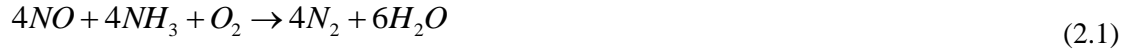
To date, SCR technology has been reviewed extensively [2, 8, 9, 29, 30], with a special focus on the reaction mechanism and catalyst development. Only limited efforts have been made to address the knowledge and advancement of reactor design and process optimization. The main focus of this chapter is to review and examine the recent development of SCR reactors and processes. First, SCR mechanism and catalyst development will be briefly reviewed for different reducing agents: NH_3 /urea, hydrocarbons and hydrogen. Then the SCR reactors developed for different purposes will be discussed. Some non-SCR reactors, such as non-selective reduction (NSR) and direct NO decomposition, will also be examined, since they show either a high similarity with the SCR technology or have been used in combination with SCR for NO_x removal.

2.1 SCR technologies: reaction mechanisms and catalysts

2.1.1 NH_3 -SCR

Currently, NH_3 -SCR is the most widely used technology for its high efficiency and wide operating temperature window [3]. This method involves the reaction of NO_x with NH_3 within a catalytic bed at appropriate temperature ranges (200-400 °C). NO_x species react with NH_3 according to several reactions, with the dominant ones being [3]:

¹ A version of this chapter has been submitted for publication: Xingxing Cheng and Xiaotao T. Bi, A review of recent advances in selective catalytic NO_x reduction reactor technologies.



Ammonia is first chemisorbed onto the active sites of the catalyst surface, where it reacts with adsorbed NO_x from the flue gases. Depending on applications there are different possible ammonia sources, *e.g.* liquefied ammonia, ammonium carbamate, urea dissolved in water and solid urea.

The catalyst is of primary importance for the process, and much of the on-going research has been focused on improving the catalyst performance. The catalysts for NH_3 -SCR processes are normally metal or metal oxides supported on SiO_2 , TiO_2 , carbon-based materials or zeolites [9]. The selection of catalyst depends on the efficiency of NO_x removal, operating temperatures and catalyst regeneration. Almost all metals and their combinations have been tested in SCRs of NO_x reduction by NH_3 . Among metal oxides studied, pure vanadium and oxidized vanadium on oxide supports such as alumina, silica, zirconia and titania have been extensively investigated. Additionally, catalysts based on pure, supported and/or mixed metal oxides of iron, copper, chromium and manganese were also extensively tested. Particular interest has been placed on V_2O_5 mixed with WO_3 and/or MoO_3 supported on TiO_2 because of their robustness to SO_2 poisoning and their high reactivity at temperatures around 300 °C [31]. However, vanadium is a pollutant to the environment and is difficult to dispose of.

Catalysts with metals supported on zeolites have become popular for their comparable efficiencies and lower prices than TiO_2 . The most studied catalysts are Cu/ZSM-5 and Fe/ZSM-5. Cu/ZSM-5 is well known as the best low temperature SCR catalyst [32]. It is favored for configurations where the exhaust gas temperature is below 450 °C. Fe/ZSM-5 has also been studied extensively for NH_3 -SCR [33-37]. Fe/ZSM-5 SCR catalysts are preferred at higher temperatures, from 450 °C to 600 °C [37, 38]. To expand the temperature window, combinations of Cu-zeolite and Fe-zeolite have been tested, and it was reported that the temperature range could be widened for this combined catalyst system [38]. Other metals have

also been added to the zeolite to widen the temperature window. Kim [9] added Mn to Fe/ZSM5 catalyst and demonstrated excellent low-temperature SCR activity.

2.1.2 HC-SCR

NH₃-SCR offers a practical approach for NO_x abatement, and has been commercialized [7]. However, it has the following drawbacks: the handling of large quantities of NH₃ is a concern because NH₃ is toxic and corrosive. Furthermore, un-reacted NH₃ may potentially be discharged to the environment (ammonia slippage). It could also react with SO₃ and H₂O to form ammonium sulphate, causing the fouling of downstream equipment. Vanadium emissions and high operating costs are also obstacles for this technology [8]. Taking the drawbacks of NH₃-SCR process into account, hydrocarbons instead of NH₃ have been considered as the most promising alternate reducing agents for the SCR process. The first study on SCR of NO_x with hydrocarbons was reported by Iwamoto et al. [39]. Thereafter, SCR of NO_x by hydrocarbons (HC-SCR) has attracted considerable attention as an alternative to ammonia or urea process for the treatment of oxygen-rich flue gases, and various types of catalysts and reducing agents have been widely investigated [40].

Three types of catalyst have been studied for HC-SCR reaction: metal oxides (represented by Ag/Al₂O₃), ion-exchanged zeolites (Cu/ZSM-5) and noble metal catalysts (Pt). The metal oxide catalysts for the reduction of NO_x by hydrocarbons have attracted attention due to its high activity and hydrothermal stability [9, 41]. Zeolite based catalysts have received much attention due to its high activity and relatively wide temperature window. So far, the most extensively studied catalysts are Cu and Fe supported on zeolite, especially ZSM-5 [9]. Cu/ZSM-5 might be the most studied catalyst for its high NO conversion over a wide temperature window (300-550 °C) using various reducing agents. However, deactivation of zeolite catalyst by H₂O and SO₂ in the flue gas is still an obstacle in the practical applications. Comparing to Cu/ZSM-5, Fe/ZSM-5 shows better resistance against water vapour at lower

reaction temperatures 250-400 °C [11]. Compared to metal oxides and ion exchanged zeolites, noble metal catalysts are active at low temperature regions. Moreover, they show relatively better resistance against SO₂ [9]. The major issue with Fe/ZSM-5 is its low selectivity toward N₂ (typically 30%).

There are two main mechanisms for selective catalytic reduction of NO_x by hydrocarbons. One is the adsorption/dissociation mechanism [9], which involves the adsorption of NO on the active metal sites and then dissociation into N(ads) and O(ads). The O(ads) reacts with hydrocarbon to form CO₂, and two N(ads) combine to produce N₂. The reactions on noble metal are usually regarded as following the adsorption /dissociation mechanism. The other one is the oxidation-reduction mechanism [9]. NO first reacts with oxygen to produce some initial reactive intermediates such as NO₂, NO₃(ads). At the same time, hydrocarbon is activated to hydrocarbon oxygenates. The intermediates can differ for different catalysts and reducing agents. In recent years evidence has been generated to support the adsorption/reduction mechanism, at least in principle, although full details at the elementary reaction level on the catalyst surface remain to be established [42]. More about the catalysts and mechanism of HC-SCR can be found in earlier review papers [9, 41].

One of the obstacles for HC-SCR is its lower NO_x conversion than that in NH₃-SCR at a given reductant to NO_x stoichiometric ratio, because of the poor selectivity of HC toward NO_x. The utilization efficiency of hydrocarbons is quite poor with less than one-tenth of injected hydrocarbon being used for NO_x reduction, if the oxidant is taken as NO, and less than one in five if it is NO₂. The remainder is wasted through combustion. The overall removal of NO_x under practical conditions in vehicles tests is low, less than 30%, due to many factors including inhibition by the high steam content, the interactions within hydrocarbon mixtures and a poor temperature match [42].

Recently, selective catalytic reduction of NO_x by H₂ (H₂-SCR) has attracted more and more attention for the NO_x removal [8]. When H₂ is used as the reducing agent, NO_x can be effectively reduced at low temperatures (T<200 °C). Moreover, that the combustion of H₂ in air produces water without any

CO₂ formation makes it environmentally benign. Nobel metals, and particularly supported Pt and Pd catalysts, exhibited higher NO_x conversion. But the cost is very high compared to the catalysts used for NH₃- and HC-SCR. Moreover, only a few catalysts have been tested on their water and SO₂ resistance for the H₂-SCR reaction. More information on the mechanism and factors controlling the performance of H₂-SCR catalyst can be found in [8].

2.1.3 NO_x storage reduction (NSR)

NO_x storage reduction (NSR), also known as lean NO_x traps (LNP), was first developed by Toyota and is generally regarded as a leading deNO_x technology for lean burn vehicle engines. NSR catalysts usually consist of a NO_x storage component (typically BaO) and a precious metal (Pt and Rh) supported on gamma-alumina. Under the lean-conditions NO was adsorbed onto the BaO surface and oxidized to NO₂ over the catalyst which was then stored in a form of nitrate at the BaO surface. After changing periodically to short cycles of fuel-rich conditions the stored NO_x was released from the BaO surface and reduced to N₂ by HC, CO, and H₂ generated from incomplete combustion of fuels over the noble metal catalyst, resulting in the regeneration of the BaO catalyst. The NO_x reduction efficiency could reach essentially up to 100%.

Generally speaking, NSR is not classified as an SCR technology, but an independent NO_x control technology. However, all aspects of this technology, no matter its application, catalysts or reaction kinetics, show a high similarity with SCR technology, especially HC-SCR. To some extent, it can be considered as an SCR process with NO_x adsorption and reduction decoupled. There is also a trend to combine the NSR and SCR technologies for deNO_x of lean burn engines.

2.2 SCR reactors

2.2.1 Structured reactors

2.2.1.1 *Monolith reactors*

The conventional configuration of SCR reactors is the catalytic monolith reactor, with the catalysts pre-formed into two shapes, plate-type and honeycomb-type [6]. The catalytic monolith reactor has been widely used as a pollution abatement device because of its structural integrity and unique advantages such as high heat and mass transfer rates per unit of pressure drop, high specific interfacial area, and ease of scale-up compared to packed bed or ceramic foam reactors [43]. It consists of a matrix of a large number of parallel channels of about 1 mm in hydraulic diameter. The catalyst is deposited in the form of a washcoat (of typical average thickness of 10-50 μm) on the inner walls of the channels. As the reacting fluid flows along the channel, the reactants diffuse transverse to the flow direction from the bulk gas phase into the washcoat where they diffuse and react on the active catalyst sites. There are also some disadvantages of this reactor, such as the absence of radial mixing, low interphase mass and heat transfer rates and low contact areas. In a typical monolith reactor, only 10% of the volume is occupied by the catalytically active ‘washcoat’, with the rest being the monolith itself and the empty channels [44]. Moreover, the NO_x removal efficiency may gradually decrease due to the plugging by fly-ash in the straight channels of the monolith honeycomb catalyst.

The conventional monolithic catalyst works the best with flue gases from furnaces and engines, which contain moderate amounts of NO_x and other gaseous pollutants, but are relatively free of particulates. It could not work well for flue gases with a high dust load. Several modified configurations were proposed for SCRs to be operated with high dust loadings. Kraftanlagen [45] proposed the use of a rotating basket or rotating honeycomb element. Exhaust gases containing NO_x would flow over a segment in rotation, so that incoming air, flowing in the opposite direction, could dislodge some of the particulates

from the catalyst. Kittrell and Herman [46] tested the reduction of nitric oxide in a dust laden gas with ammonia in a reactor with the gas passing near, but not through, the catalyst bed. The only way for NO_x to reach the catalyst bed was via diffusion from a plurality of centrally located tubes containing fine perforations. Dust laden gas passed through the tubes, but never impinged directly on the catalyst bed.

2.2.1.2 Metal wire reactors

As an alternative to monolith reactors, metal wire gauzes as catalyst supports and structured reactor internals were recently studied by Odłowski [47] for NH_3 -SCR as schematically shown in Fig. 2.1. This new structure was also investigated by the same group on its hydrodynamics [48] and other applications, such as for the combustion of VOCs [49]. It was reported that this new type of structured catalytic reactors possesses high mass transfer rates and moderate flow resistances [48]. When used for NH_3 -SCR, wire gauze internals decreased reactor length by 10 times comparing to monolith [47] because of the enhanced heat and mass transfer rates. Furthermore, even for a moderately fast reaction such as NH_3 -SCR of NO_x , the catalyst loading and activity play less important roles than the catalyst distribution inside the reactor. The support structure determines the external and the internal diffusional resistances, and thus, reactor yield as well as the overall flow resistance.

Although proven to be highly efficient for NO_x reduction, problems could arise during operation since the layers of weaved metal wires could be plugged by fly ash more easily than the monolith reactor. Cleaning the plugged ash could also be more difficult than the monolith because of the lack of straight channels inside the reactor.

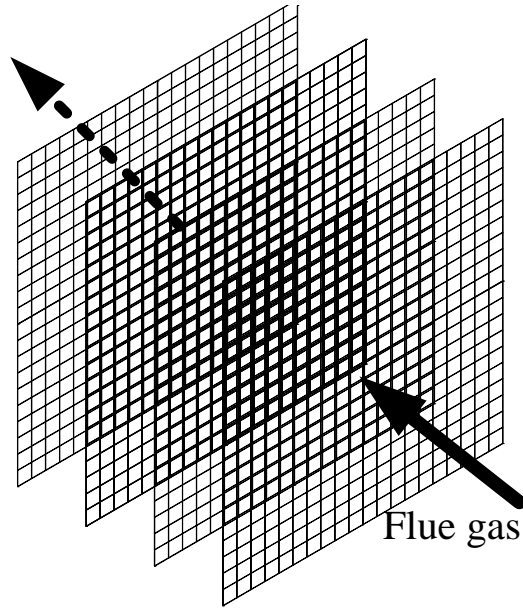


Figure 2.1 Schematics of wire gauze structured reactor [50]

In a further study of Sun [50], a wire-mesh honeycomb was manufactured by stacking alternatively corrugated and plain wire-mesh sheets, as shown in Fig. 2.2, which combined the characteristics of wire-mesh and monolith catalysts. This structure was found to not only enhance the external mass-transfer rate but also provide a more uniform fluid flow distribution across the entire cross section of the bed, which offered better efficiencies of gas-solid contact. Since gas could pass through the straight channels, dust tolerance of this reactor could also be better than the wire gauze structured reactor. The wire-mesh honeycomb, compared to the ceramic monolith with a similar cell density, had a higher geometric surface area, larger open frontal area, lower pressure-drop and also a higher NO_x conversion efficiency, as evidenced from HC-SCR experiments [50].

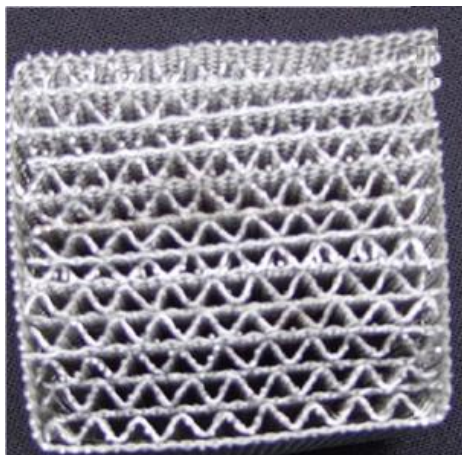


Figure 2.2 Wire-mesh honey comb reactor [50]

Conventional packed bed reactors were also investigated as a comparison to the gauze reactor and monolith reactor by Jodłowski [47]. The catalyst loading and the flow resistance of the three types of reactors followed such an order: packed bed reactor > gauze reactor > monolith. Based on the results, the conventional packed bed reactor appears to be ineffective for high-efficiency exhaust gas cleaning applications because of its high flow resistance and the high diffusional resistance (especially internal diffusion) that gives a very low effectiveness factor of the catalyst pellet.

2.2.1.3 Ceramic or metal foam reactors

Another packed structure, monolith ceramic or metal foam, as shown in Fig. 2.3, has attracted increasing attention because of its unique structure and morphology which offers the potential for having a low pressure drop and high heat and mass transfer rates, which is different from other packed bed reactors [51]. Foam monoliths can be made of ceramic or metal. The open cell foams consist of a network of interconnected solid struts building cavities (=cells) that communicate through windows. Ceramic foams and metallic foams have open porosities of about 75-85% and 95%, respectively. The open structure of foams allows the fluid to pass through with low-pressure drops while maintaining good radial mixing and

enhanced turbulence in the tortuous flow paths. The heat transport to the walls occurs not only by conduction, as in honeycombs, but also by convection and radiation. Patcas [51] showed that catalytic foam packings combine a high permeability to gas flow with good mass and heat transfer characteristics. The pressure drop and mass transfer coefficient are between those of packed bed and honeycomb monoliths. Compared to honeycomb monoliths, foams offer the advantage of radial mixing and more efficient heat transfer. Although never tested for SCR application, the feasibility of its application should be investigated in the future by coating SCR catalysts onto the foam support. The foam reactor could be a potential alternative to a monolith reactor, especially in the applications where heat transfer and mass transfer are of greater importance. Due to the tortuous flow paths, the dust load is expected to be more problematic than both monolith and metal wire structure reactors.

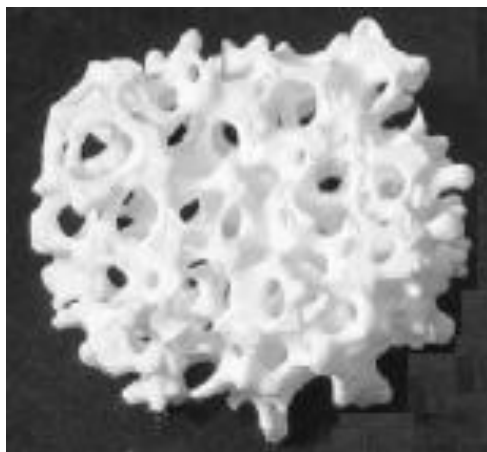


Figure 2.3 Schematics of ceramic foam [51]

2.2.1.4 Combined NO_x and PM capture

Unlike the above reactors, an integrated SCR-ESP reactor with the catalyst coated on collector plates of the electrostatic precipitator (ESP), was constructed to capture particulate and reduce NO_x [52]. Ammonia injected either directly into the ESP or upstream catalytically reduces NO_x to N_2 . An excess amount of ammonia also helps the capture of particulates in the ESP because of the increased particle surface

conductivity. This could also prevent problems of ammonia slippage. In another study [53], high-temperature fabric filters were coated with a layer of a proprietary vanadium/titanium (V/Ti) catalyst. The catalyst-coated fabric filters are targeted for simultaneous NO_x and particulate control in power plants or industrial facilities installed with high temperature baghouses. Issues pertaining to the successful development and marketing of this technology, such as catalyst and filter durability, NO_x and particulate control efficiencies, ammonia slip levels, and catalyst deactivation have also been addressed [52].

2.2.2 Fluidized bed reactors

Fluidized beds have been extensively explored for NO_x removal. Small Fe particles supported on silica sand (139-400 μm) were fluidized in a bubbling bed for NO reduction with CO as a reducing agent at high temperatures, i.e., 700-900 °C [54]. Alumina particles or CuO_x/Al₂O₃ were also used as catalysts for the reduction of NO in bubbling fluidized bed reactors [55, 56]. Irfan et al. [56] evaluated NO removal over CuO/γ-Al₂O₃ catalyst in a bubbling fluidized bed and investigated the effects of fluidizing gas velocity, NH₃ to NO molar ratio, and the static bed height on the reduction of NO at various reactor temperatures. It was observed that bubble size increase with increasing gas velocity led to a decrease in NO conversion. Therefore, there is a need to decrease the bubble size and solids back-mixing in the fluidized bed in order to improve the reactor performance. Another major issue concerning fluidized beds is excessive sorbent attrition, requiring mechanically strong catalysts to minimize attrition losses. However, the mechanical strength of SCR catalysts has seldom been investigated. CuO/γ-Al₂O₃ prepared by Rahmaninejad [31] was reported to have a high attrition resistance based on the durability test. After 25 regeneration cycles, the catalytic activity for NO_x reduction did not decrease noticeably.

Fluidized beds also show advantages over fixed beds for treating flue gases with high dust loadings. The fluidized bed reactor was applied by Mobile Oil Company [5] (MOC) for high dust flue gas treatment from the FCC process. Gas containing NO_x and entrained catalyst fines pass up through a bed

of catalyst at a sufficient velocity to expand and fluidize the catalyst bed. Particulates deposited on the catalyst are dislodged or elutriated by fluidizing gases, preventing fouling of the deNO_x catalyst. A reduction efficiency of up to 90% could be reached, while the pressure drop through such a bed was reasonably low although higher than that through a honeycomb. An improved reactor design was developed to lower the pressure drop by allowing side entry of gases into the fluidized bed to lower the superficial gas velocity, as presented in Fig. 2.4.

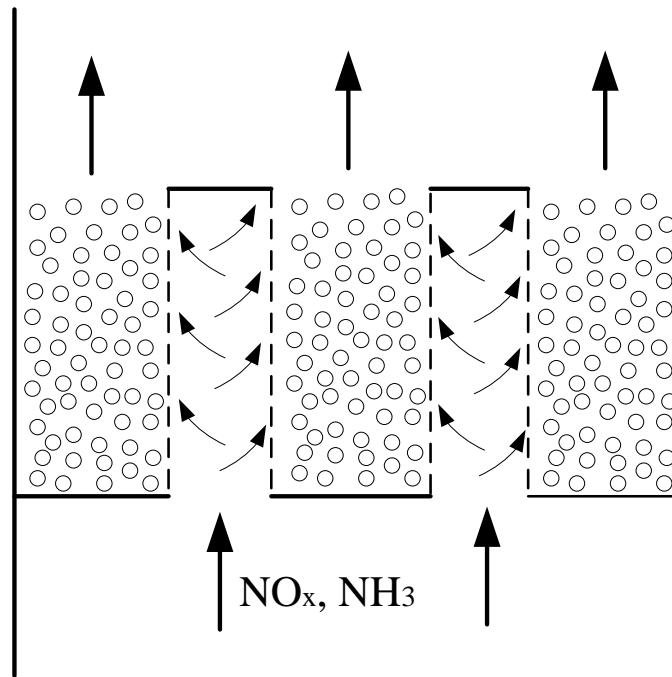


Figure 2.4 Schematics of MOC's low-pressure-drop deNO_x fluidized bed reactor [5]

Gao [57] used a fluidized bed for simultaneous removal of NO_x and SO₂, in which NO_x was reduced by NH₃ over coarse WO₃/TiO₂ particles and SO₂ was adsorbed onto fine particles consisting of CuO, ZnO and dust. Both fine and coarse particles were fluidized, with only fine particles being entrained from the bed continuously for regeneration. The schematic of the unit is shown in Fig. 2.5. The reaction temperature was tested from 300 °C to 600 °C and it was found that at 600 °C the highest efficiency was achieved with 100% NO_x reduction and 80% SO₂ capture.

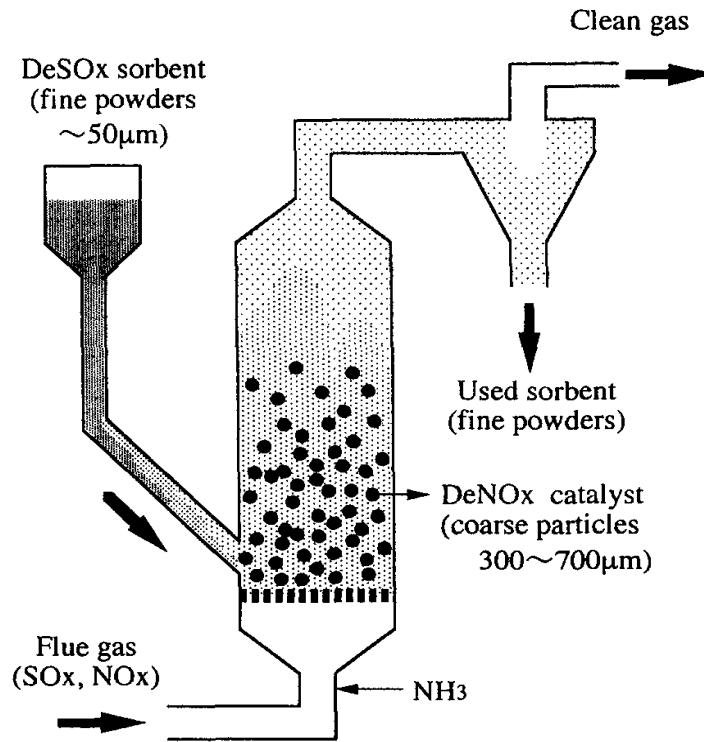


Figure 2.5 Fluidized bed reactor for simultaneous SO₂/NO_x removal [57]

The fluidized bed configuration offers a number of advantages over the honeycomb structure, including a better gas solid contact, less chance for dust clogging, and a more compact reactor size, as well as facilitation of in-situ regeneration of the catalyst. Further effort is still needed to investigate catalyst attrition in the fluidized bed. Careful design is also required to improve the reaction performance by decreasing bubble size and solids back-mixing.

2.2.3 Moving bed reactors

Moving beds, which can prevent dust clogging and has low solids back-mixing, has also been applied for NO_x control. A moving bed technology invented by Mitsui Mining Company (MMC) in the 1980s [58]

and shown in Fig. 2.6 (a) could be used for either NO_x adsorption or reaction. The catalyst particles move from the top to the bottom and are then regenerated and recirculated to the top feeding chamber. Flue gases flow horizontally through the reactor to have the NO_x reduced by the catalysts. Various baffles with different shapes are installed in the reactor to control the gas distribution and solid movement.

Another configuration of moving beds, which also permits continuous introduction of refreshed catalysts, was applied for NO_x reduction recently by Babcock & Wilcox Power Generation Group (BWPGG) [59], as shown in Fig. 2.6(b). Similar to the configuration in Fig. 2.6(a), solids move downward in the reactor while the flue gas flows horizontally through the catalysts. The configurations of baffles installed in the reactor could ensure a good distribution of gas and solids and also a good contact between gas and solids. The continuous operation mode of a moving bed makes the regeneration of catalysts more convenient, which is particularly important for the low sulfur-resistance catalysts, such as Cu and Fe on zeolite. But the continuous recirculation of solids may increase the operation cost of the reactor.

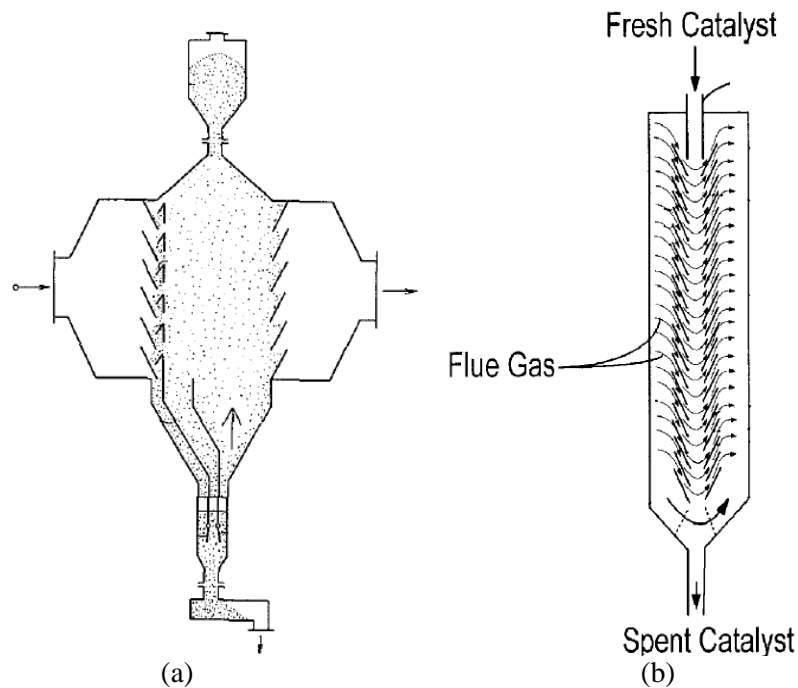


Figure 2.6 Moving bed SCR reactors, (a), MMC design [58], (b), BWPGG design [59]

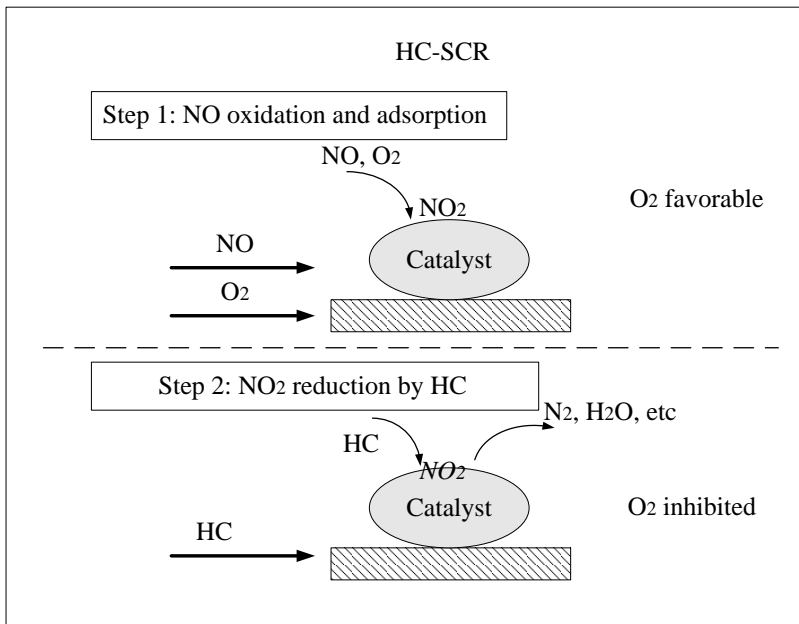
2.3 Multifunctional SCR reactors

2.3.1 Decoupled adsorption-reaction

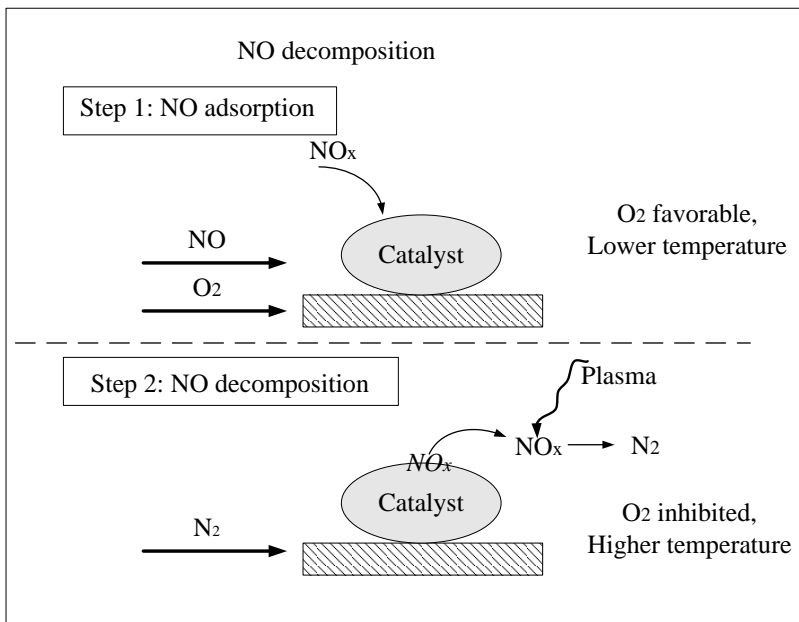
2.3.1.1 Mechanism

For a heterogeneous catalytic reaction, reactants are first adsorbed onto the surface of the catalyst and then reaction takes place. DeNO_x reactor performance could be improved if the adsorption and reaction can take place in different regions of the reactor in order to avoid the negative effects of other gas species on the catalyst performance or to concentrate the NO_x for high-efficiency destruction. This may also offer an opportunity for the adsorption and reaction to be optimized independently. This constitutes the basic principle of the decoupled SCR process, with a single reactor serving multiple functions.

For HC-SCR, as discussed in section 2.1.2, one of the major problems is the low selectivity of hydrocarbon toward NO_x, especially with flue gases of a high O₂ concentration. There has been strong experimental evidence [60-63] that NO_x conversion could be seriously suppressed by the high O₂ concentration in the flue gas because of its competitive oxidation reaction with the reducing agent. Therefore, the deNO_x performance can be potentially improved if the direct contact of HC and O₂ can be avoided, see Fig. 2.7(a). In the direct NO decomposition process, NO_x in the flue gas could be first adsorbed onto the catalyst. The adsorbed NO_x is then desorbed from the catalyst by a separate inert gas stream, usually N₂ or Ar. The inert gas stream, which now contains concentrated NO_x, could then be treated to decompose NO_x into N₂ at a high efficiency, often assisted by plasma, as illustrated in Fig. 2.7(b). Usually, the flue gas temperature is controlled to be low during NO_x adsorption and high during desorption. Many different reactor configurations have been designed to facilitate these decoupling processes, which will be reviewed next.



(a)



(b)

Figure 2.7 Mechanism of decoupled deNO_x process, (a), HC-SCR; (b), direct NO decomposition

2.3.1.2 SCRs with catalyst swing

In order to separate adsorption and reaction in a bi-functional reactor, catalysts saturated with one reactant in the adsorption zone could move to another zone to react with reducing agent or other reactants. The circulating fluidized bed is the most widely used reactor to continuously move particles between different zones of the reactor.

An internal circulating fluidized bed, i-CFB (UBC) was proposed by Yang and Bi [10] for an integrated NO_x adsorption-reduction process of HC-SCR. The aim was to avoid the negative impact of the excess O_2 and poisoning components in the flue gas. The NO_x adsorption and reduction are carried out in two separate zones of the reactor, as illustrated in Chapter 1. The flue gas passes through the adsorption zone where NO_x is absorbed by the catalyst. The NO_x -adsorbed catalyst particles then move into the reaction zone where NO_x is reduced by injected hydrocarbons at controlled oxygen concentrations, and, at the same time, other adsorbed flue gas contaminants can also be stripped from the catalyst. The regenerated catalyst particles are then circulated back to the adsorption zone to establish a continuous operation. The feasibility of this design was validated by experiments on an i-CFB. The catalyst used was Fe/ZSM-5 and reducing agent is C_3H_6 . The goal of avoiding negative impact of O_2 was further demonstrated by comparing the performance of the i-CFB and a regular fluidized bed loaded with the same amount of catalysts [10].

With the catalyst particles circulating between a reduction zone and an oxidizing zone, it is also expected that the flue gas contaminants such as dusts could be stripped from the catalyst, minimizing fouling and catalyst deactivation caused by the deposit of carbon and other contaminants. Those features can potentially prolong the catalyst life in treating flue gases of high dust loading, although experimental validation is still needed.

An interconnected fluidized bed (IFB) was also proposed for simultaneous removal of SO_2 and NO_x by NOXSO corporation [64] in 1990s, as shown schematically in Fig. 2.8. The IFB consists of multiple

compartments, with the flow of solids between compartments being induced and controlled by means of the difference in gas aeration rates. The solids flow from one compartment to the other over a weir or through an orifice which connect the respective compartments. The compartments with upflowing solids act as the adsorber and regenerator and the solids downflow compartments serve as stripper and cooler between two reactors. NO_x and SO_2 were first adsorbed onto the adsorbents in the adsorber at about 120 °C. Then NO_x was removed from the adsorbent in the stripper and SO_2 was removed in the regenerator at 680 °C. Hot sorbent was then cooled down to 130 °C and returned to the adsorber.

The adsorption-regeneration concept was investigated extensively by the NOXSO corporation in the 1990s in a series of regular fluidized beds. It was reported that the system could remove 70-90% NO_x and 90% SO_2 [64]. However, the NO_x control efficiency in the integrated IFB unit was never reported. The IFB reactor was further investigated in Delft University of Technology [65, 66], with a focus on the hydrodynamics and its potential applications for biomass combustion [66].

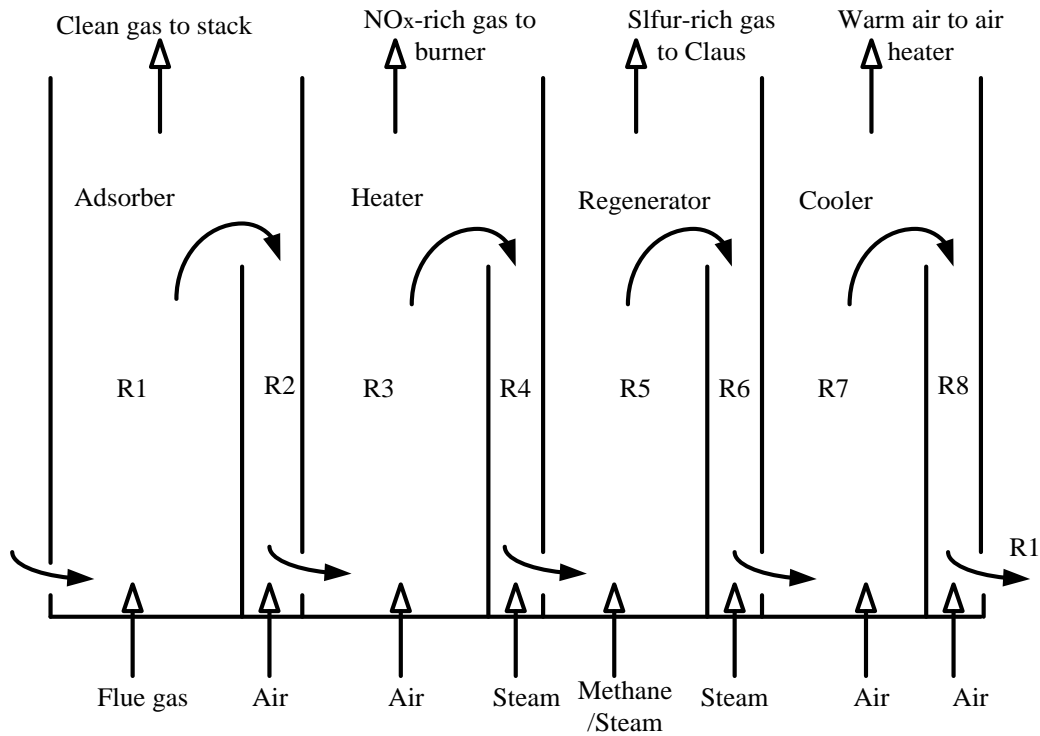


Figure 2.8 Schematic of NOXSO's IFB reactor [64]

This adsorption-reduction process in a circulating fluidized bed could be further extended to NH₃-SCR. V₂O₅-based catalyst could only adsorb NH₃ on the surface and the SCR reaction takes place between adsorbed NH₃ species and gaseous NO [67]. In the application of CFB, NH₃ could be adsorbed onto the catalysts and then used to reduce NO, avoiding the direct contact of NH₃ with SO₂ to decrease sulfur poisoning. This method is similar to the rotary bed reactor proposed by Riekert et al. [45], in which it was proven that ammonia bisulfate could be prevented when NH₃ was first adsorbed on to the catalyst before contacting flue gas. This feature is especially important for NH₃-SCR with zeolite as the catalysts, which have a lower sulfur tolerance. Moreover, zeolite could adsorb both NO and NH₃ [67]. The adsorption zone could be designed to adsorb either NO or NH₃, depending on the specific requirement of the system.

2.3.1.3 SCRs with gas switching

In fluidized beds, catalysts can move from one zone to another to decouple the adsorption and reaction. Such a decoupling could also be realized by switching different gas streams from one zone to another, with one zone operated in the adsorption mode while the other operated in the NO_x reduction mode.

A combined adsorption-discharge plasma catalytic process for removing low-concentration NO_x from flue gases was proposed by Yu [68]. NO_x in an oxygen-rich gas stream is first adsorbed by the catalyst in the reactor operated in the adsorption mode (plasma off). Then in the plasma discharge mode, flue gases are switched off while Ar or N₂ is turned on to the reactor as the plasma carrier gas to decompose NO_x adsorbed on the catalysts by plasma, with the negative effect of flue gas O₂ being avoided. To improve the decomposition of adsorbed NO_x in N₂ plasma, solid carbon as a scavenger for oxygen species was mixed to the catalyst. The decomposition efficiency of adsorbed NO_x was observed, and the carbon was progressively burned off, providing a possibility for the simultaneous removal of NO_x and unburned carbon particles at a low energy consumption.

A continuous NO_x reduction process, which combines non-thermal plasma (NTP) and temperature swing adsorption (TSA), was proposed and tested by Yoshida [69-71] for diesel engine exhaust gas NO_x treatment. As shown in Fig. 2.9, the system comprises of two adsorption chambers, 1 and 2, which operate in series. Hot exhaust gas from an engine first indirectly heats up adsorption chamber 1, in which the adsorbent is regenerated by thermal desorption, and the exhaust gas subsequently enters adsorption chamber 2, where NO_x is removed by adsorption. A small amount of N₂ or low-O₂ gas (containing less than a few percent O₂) is supplied to chamber 1 to elute desorbed NO_x from the chamber. This concentrated NO_x stream passes to an NTP reactor and is subsequently reduced. The gas exiting the NTP reactor still contains NO_x, and is injected to the air intake of the engine. The adsorbent used is a mixture of CuO and MnO_x. It was claimed that both high energy efficiency and high NO_x-removal efficiency could be achieved with this system, but the compact design of the adsorption chambers to fit diesel engines will be a challenge. The advantage of this system is that no additional fuel injection (for CO/H₂ generation) or urea injection is needed. However, an additional system to produce low O₂ gas stream is required. One possible way to produce the low O₂ gas is to pass a small amount of air through a particulate-matters (PM) collection unit where the unburned hydrocarbons or carbon particles are reacted with O₂ in the air.

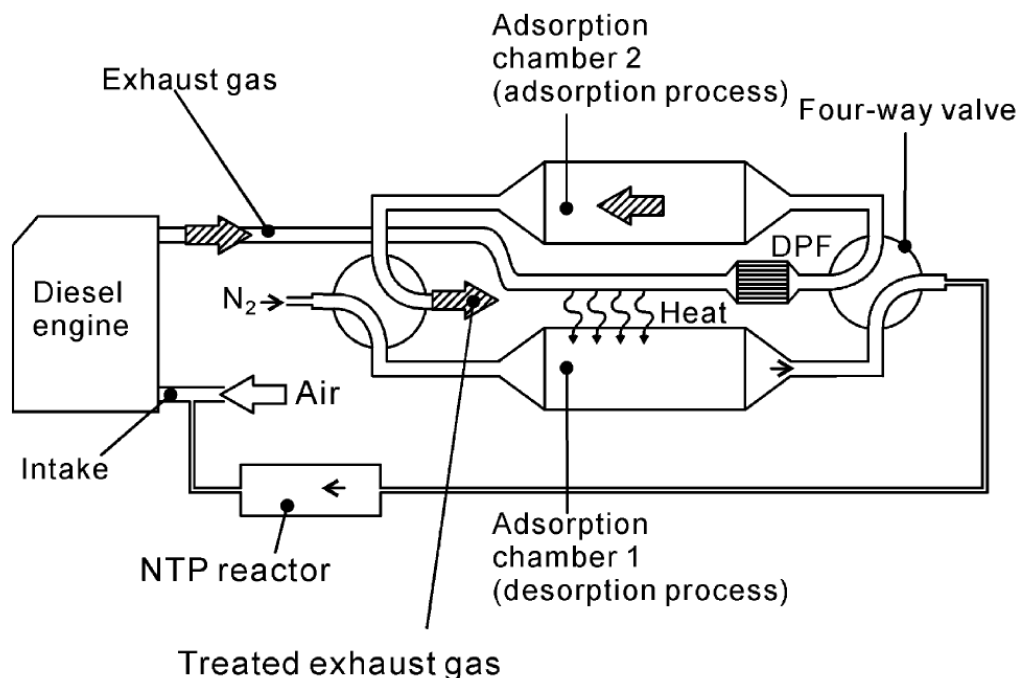


Figure 2.9 Schematics of a temperature swing adsorption (TSA) process [69]

The above configuration consists of two reactors, one for adsorption and the other one for reaction. Adsorption and reaction take place alternately between these two reactors, which thus requires the two reactors to be exactly identical in order to maintain a stable operation. However, usually the reaction rates of adsorption and reaction are not the same, requiring different reaction time and reactor size. For example, Yoshida [69] pointed out that a bigger adsorption chamber is needed, but not the desorption chamber. Although this unsymmetrical requirement could be balanced by adjusting flow rates in the two reactors, the system could be much simpler for design and operation if identical reactors are adopted.

Another problem associated with the swing-reactor system is the discontinuous alternation between the reactors. Taking the adsorption-reduction system as an example, flue gases and reducing agent are switched alternately between the two reactors. The adsorption time is determined by the breakthrough characteristics of the catalyst. In order to ensure the high capture efficiency, adsorbate concentration must be controlled at a low level. Therefore, most of the catalysts along the reactor are far away from being

saturated with NO_x . This leads to a very low utilization efficiency of the total adsorption capacity. Comparing to the gas swing reactor, internal circulating bed (i-CFB) offers a higher utilization efficiency of the catalyst adsorption capacity. In i-CFB, highly saturated catalysts are continuously recirculated into the reduction zone and the size of the adsorption and reduction zones can be optimized independently.

A more advanced gas switching system, loop reactors, has been proposed for the NH_3 -SCR process [72-74]. Loop reactors use a network of reactors with periodical switching of the feeding position from one reactor to the next one in sequence. In the reactor, a set of valves allows for the change of the feeding position, thus achieving a sustained dynamic behavior. The working principle is illustrated in Fig. 2.10. The proposed loop reactors take the advantage of the catalysts that could strongly adsorb NH_3 in the NH_3 -SCR process to avoid the ammonia slip while fulfilling the required high NO_x conversion. It should be noted that in the loop reactor of Fissore [72], adsorption and reaction are not completely separated although the main purpose of the reactor is to use the high capacity of NH_3 adsorption. NH_3 and the flue gas were fed to the reactor together. A network of three reactors was built to simulate the behavior of a moving bed [72], which contains commercial zeolite catalysts supported on a monolith. Five three-way valves are required to change the feed position along the sequence of the three reactors: from initial 1-2-3 to 2-3-1 and finally to 3-1-2. The feasibility of the reactor was demonstrated by both numerical simulations and experiments [72], where NO_x reduction efficiency was maintained at more than 90% and ammonia emission was decreased to about 1/10 of the emission from a regular reactor. It was also evidenced that the adsorption capacity can play a role even more important than the catalytic activity [74]. Recent research in Barresi's group [73] showed the possibility of using an industrial-scale loop reactor to carry out NH_3 -SCR. The advantages have been highlighted in a case study, where a substantial reduction in energy consumption (65kW vs.130 kW) and the complete avoidance of NH_3 slip were achieved.

The main drawback of loop reactors is represented by the reactor configuration, whose piping is much more 'complex' than in the conventional system. Loop reactors were also extensively studied in

Sheintuch's group [75-79], with a main focus on improving the thermal efficiency of the reactor, as well as the design and control technology.

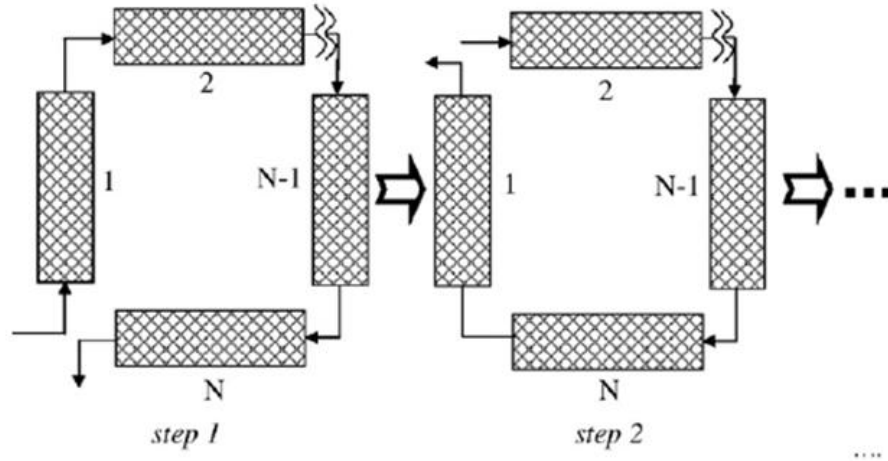


Figure 2.10 Working principle of loop reactor [73]

Another alternative design, which serves a similar function as the loop reactor, is the reverse flow reactor, where sustained dynamic behaviour is obtained by periodically reversing the flow direction, as shown in Fig. 2.11. The reverse flow reactor was first applied for NH_3 -SCR by Agar [80] in the 1980s. Similar to the loop reactor proposed in Barresi's group, this reactor also takes advantage of the high NH_3 adsorption capacity of catalysts by trapping NH_3 in the catalyst. The feasibility of the process was demonstrated by experiments and detailed kinetic modeling. It was reported that this type of reactor design offered high NO_x removal efficiency without ammonia slip and ameliorated problems associated with the fluctuations and distribution of the flue gas. However, the reverse flow reactor has a serious drawback, namely the wash-out, i.e. the emission of unconverted reactants when the flow direction is reversed [73].

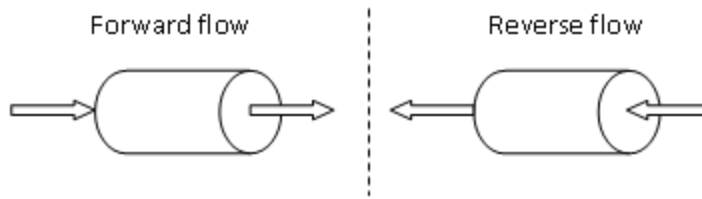


Figure 2.11 Reverse flow reactor

Countercurrent internal recirculation reactor, as shown in Fig. 2.12, is another design that performs similar to the reverse flow reactor and loop reactor. The main feature of countercurrent internal recirculation reactor is good heat exchanging. In the reactor, the feed gas enters through one (say, inner) tube and then turns around and flows out through (the outer) another. Attaching two such mirror-imaged reactors will form an arrangement similar to the heat-exchanging reactor with countercurrent flow. This reactor is attractive for the NO_x -SCR application only when heat released from the reaction is of great significance. Sheintuch [75] compared the performance of a loop reactor, a reverse flow reactor and an internal recirculation reactor in terms of temperature distribution for ethylene oxidation. The results showed that the simpler inner–outer internal-recycle reactor may perform better at low flow rates than that with a flow reversal, but the conclusion is reversed at high flow rates. The performance of loop reactor depends on the switching frequency, reaction/adsorption/desorption kinetics and the reactor length, while the performance of the other two reactors mainly depends on the thermal conductivity of the catalyst bed.

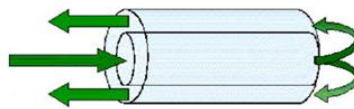


Figure 2.12 Countercurrent internal recirculation reactor [75]

Rotating reactors have also been used for NO_x -SCR, which behave between a swing reactor and a loop reactor. As shown in Fig. 2.13, the reactor is divided into an adsorption zone and a reduction zone. The catalyst is rotating between the two zones. The rotation of catalyst could also be achieved by switching the feeding gas. Every sector along the axial direction (say, a fan-shaped sector) could be considered as a swing reactor, swinging between the adsorption zone and the reduction zone. However, from the viewpoint of cross section, the reactor could be considered as a loop reactor.

Kraftanlagen [45] used a rotary basket reactor where reducing agent NH_3 and flue gas pass through the catalyst bed alternately. For catalysts with a higher NH_3 storage capacity, NH_3 could be first stored onto the catalyst surface before reacts with NO_x . The advantage of the NH_3 storage-reduction process is the avoided undesired secondary reactions, which form ammonium bisulfate before flue gas and ammonia are introduced onto the catalysts. It was found that the formation of ammonium bisulfate was almost completely prevented. The process could effectively exclude the undesirable deposits onto the catalyst surfaces and the downstream equipment.

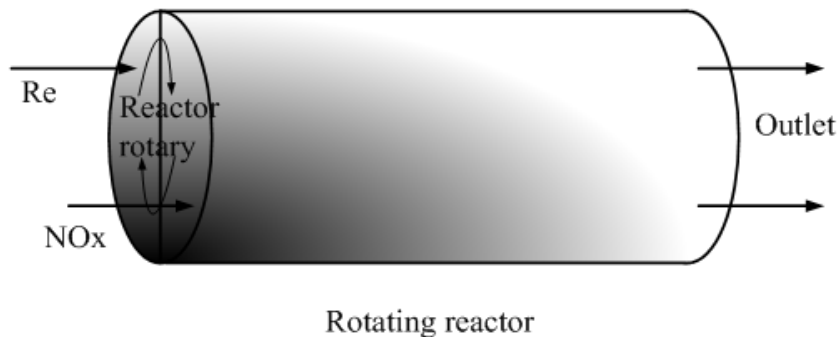


Figure 2.13 Schematics of the rotating reactor

2.3.2 Combined SCRs

2.3.2.1 Combined NSR-SCR

NH₃-SCR and NO_x storage and reduction (NSR) technologies have been commonly used for controlling NO_x in exhaust gases from lean-burn engines. Studies have also been conducted on the combined NSR and SCR system [81-86]. The coupling between a NO_x-trap catalyst and a NH₃-SCR catalyst located downstream or as a second layer in a monolith was first patented by Ford in 2004 [86]. The emission control system is used for the treatment of exhaust streams from diesel engines and lean burn gasoline engines to enhance the NO_x removal efficiency [81-84].

A typical NSR-SCR system has an NSR catalyst and an SCR catalyst located downstream of the NSR catalyst [85]. While the reduction of NO and NO₂ to N₂ occurs in the presence of NSR catalyst during the fuel-rich periods, ammonia can also form as a by-product from the NSR catalyst, e.g.:



The generated NH₃, a regulated air pollutant, must also now be controlled before the exhaust is vented to the atmosphere, which is accomplished in the SCR catalyst bed where NH₃ is used as the NO_x reducing agent. This method combines the advantages of NSR and SCR catalysts. Nitrogen oxides are intermediately stored during lean operation, and released during rich operation to form NH₃ and stored on either the adsorbent or the SCR catalyst. The stored NH₃ can be released to reduce nitrogen oxides during a subsequent fuel-lean operation. The combined system showed a superior NO_x removal efficiency (as high as 99.5% at 300 °C) and a lower ammonia slip compared to the single NSR catalyst at all temperatures examined [81]. The highest activity could be obtained during the rich pulse with both CO and H₂ as reductants [84]. Cu-ZSM-5 [84, 87] and Fe-ZSM-5 [88-90] are usually used as the SCR catalyst for this combined SNR/SCR process. It was also reported that a mixture of NSR and SCR catalysts gives

better performances than the dual bed system [91]. More details on the development and mechanism of such a combined NSR-SCR system could be found in a recent review [91].

2.3.2.2 Combined HC-SCR and NH₃-SCR

Beside combined NSR and NH₃-SCR systems, combined HC-SCR and NH₃-SCR systems have also been proposed recently in a dual bed system [92]. The first bed is a single layer (layer A) catalyst bed and the second bed is a double layer (layers A and B) catalyst bed including a first layer catalyst and a second layer catalyst to reduce the nitrogen oxides to N₂. The layer A catalyst is selected from the group consisting of Ag/Al₂O₃, Ag/Y, Ag/ZSM-5, Ag/Ba/Y, or a combination thereof; and the layer B catalyst comes from the group of Pt/Al₂O₃, Pt/Ba/Al₂O₃, Cu/ZSM-5, CuCo/Y, Pd/Al₂O₃, or a combination thereof. The first bed reduces NO_x initially through the (HC+OHC)/SCR process to N₂, meanwhile also producing NH₃ as a byproduct over layer A in the first bed. The NH₃ subsequently reduces NO_x over layer A and layer B through the NH₃/SCR process, producing more N₂ and thereby enhancing the NO_x reduction efficiency of the hybrid catalyst system.

2.4 Summary

SCR technology has been extensively studied in recent decades. Most of the research mainly focuses on reaction mechanisms and catalyst development. To date, the most widely used SCR technologies include NH₃-SCR, HC-SCR and NSR. Among these technologies, NH₃-SCR offers the highest NO_x reduction efficiency, the best sulfur tolerance and moderate catalyst and operation cost. Ammonia slip is the main obstacle of this technology. As an ammonia-free process, HC-SCR also has high NO_x reduction efficiencies. The catalyst cost could be even lower than NH₃-SCR. But most of the HC-SCR catalysts tend to be easily poisoned by sulfur in the flue gas. Another problem of this process is hydrocarbon combustion by oxygen presented in the flue gas. NSRs are been developed for lean-burn engines.

Although the deNO_x efficiency of current SCR technologies is generally high enough to meet the stringent requirements, there still exist drawbacks such as the high cost of the noble metal catalyst. It is expected that proper selection and design of the SCR reactor could alleviate these problems and accelerate the wide application of these technologies. Moreover, catalyst regeneration, which could keep the catalyst activity and prolong the life of catalyst, also impose special requirements for the reactor design.

Monolith reactors are simple and the most widely used reactor for its low pressure drop, relatively high interfacial area and ease of scale-up. Other structural reactors, e.g., metal wire reactors and foam reactors, show some advantages over monolith reactors with better mass transfer and heat transfer properties. The major concern for their applications is ash plugging. Comparing to fixed bed reactors, fluidized bed reactors offer a better gas-solid contact and smaller reactor size, as well as easier catalyst regeneration. But further investigation is required to improve the attrition resistance of catalysts and decrease solids back-mixing. Moving bed reactors, which have less solids back-mixing than fluidized beds, were also applied for SCR process.

Besides the basic reactors, various multifunctional reactors were also developed for SCR process based on the specific reaction mechanism. These reactors allow for coupling several operations (chemical reaction, separation, and/or heat exchange process) into a single equipment, thus improving yield and selectivity, and reducing investment and operation costs, in comparison to traditional reactor configurations. In these reactors, SCR reactions could be either decoupled or coupled. Adsorption and reaction could be decoupled in the reactor by either catalyst circulation or gas switching to provide better reaction conditions for each step. Different SCR technologies could also be combined to take advantage of each other. Multifunctional reactors should be further investigated since they could potentially enhance the deNO_x performance significantly.

Chapter 3 Hydrodynamics in i-CFB: experiments & modeling²

3.1 Introduction

The performance of the i-CFB reactor is expected to be impacted significantly by the hydrodynamics in the i-CFB, including both the gas bypass between the draft tube and the annulus regions and the internal solids circulation, which should be well studied in order to properly design the reactor and select suitable operating conditions as well as to provide data for modeling such a reactor. Several studies have been reported on the hydrodynamics of i-CFB reactors, mainly focused on the measurement of solids circulation rates [93, 94] and the development of correlations for predicting the solids circulation rate [95, 96]. These empirical or semi-empirical models could not be applied directly to i-CFBs with different configurations. In this chapter, the performance of the reactor is investigated both experimentally and analytically. Gas bypassing, bed expansion and solids circulation rate in a deNO_x i-CFB reactor are tested in a cold model unit. The solids circulation rate is then predicted based on pressure and mass balance equations.

3.2 Experiment details

3.2.1 Experimental setup

The i-CFB reactor was constructed by Yang [11], with the configuration shown in Fig. 3.1. The dimensions of the model unit are listed in Table 3.1. There was a draft tube in the reactor. The distance of

² A version of this chapter will be published: Xingxing Cheng and Xiaotao T. Bi, Hydrodynamics of an i-CFB deNO_x reactor, Powder technology.

the opening gap between the draft tube and distributor was selected as 10 mm by Yang [11] through a series of experiments. Gas was fed to both the draft tube and annulus at different flow rates and the bed particles circulated between the draft tube and annulus. If the draft tube is taken out, the i-CFB could be operated as a regular fluidized bed. Bed expansion was tested in such a regular fluidized bed.

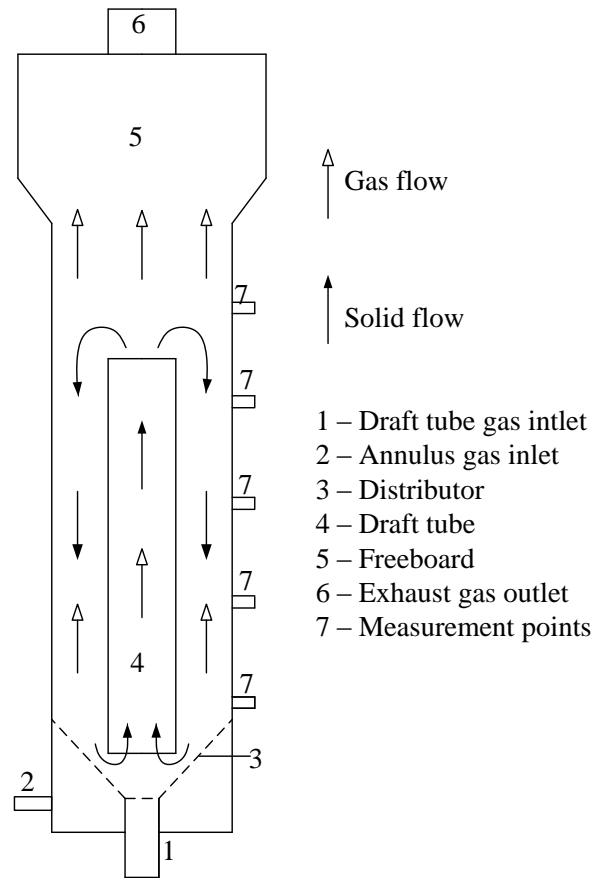


Figure 3.1 Schematics of the i-CFB reactor

Table 3.1 Dimensions of the cold model i- CFB unit

Item	Dimension
Draft tube diameter, mm	50.8 (I.D.), 63.5 (O.D.)
Draft tube length, mm	1016
Column diameter, mm	101.6 (I.D.), 114.3 (O.D.)
Column height, mm	1092
Freeboard diameter, mm	254.0 (I.D.), 266.7 (O.D.)
Freeboard height, mm	508
Annulus gas distributor opening ratio	2.1%
Holes on the distributor	52 holes of 1.6mm diameter
Gas nozzle diameter, mm	34.9 (I.D.), 38.1 (O.D.)

The i-CFB system is shown schematically in Fig. 3.2. For the experiments of solids circulation rate, building air was fed to both the annulus and draft tube as the fluidizing gas. For the measurement gas bypass ratio, CO₂ was also fed into the draft tube or annulus as a tracer. The bed material used in the experiment was zeolite particles which were the same as the catalyst tested by Yang [11] in the i-CFB reaction experiment. Some properties of the particles are given in Table 3.2. In the table, U_c is transition velocity from bubbling to turbulent fluidization and was determined based on the maximum standard deviation of pressure fluctuations as described in [97].

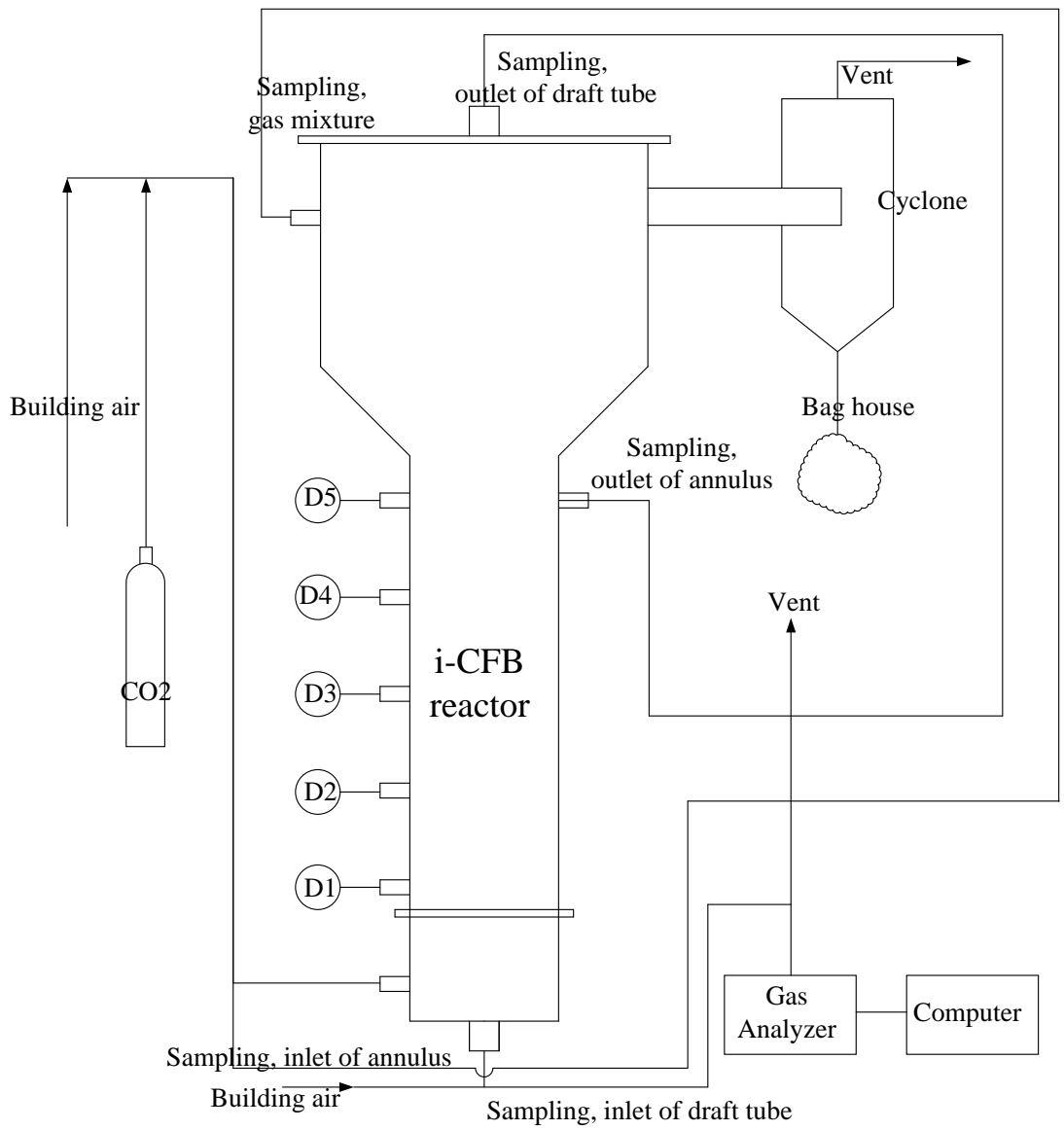


Figure 3.2 Schematics of the i-CFB system

Table 3.2 Fine Fe/ZSM-5 particle properties

Material	Bulk density (kg/m ³)	Average particle diameter (mm)	U _{mf} ^{*a} (m/s)	U _c ^{*b} (m/s)	U _t ^{*c} (m/s)
Fe/ZSM-5	968	0.155	0.01	0.38	0.90

Note: *a: measured; *b: measured. *c: calculated from correlation: $U_t^* = \left[\frac{18}{(d_p^*)^2} + \frac{0.591}{(d_p^*)^{0.5}} \right]^{-1}$,

$$d_p^* = d_p \left[\frac{\rho_g (\rho_p - \rho_g) g}{\mu^2} \right]^{1/3}, U_t = U_t^* \left[\frac{\rho_g^2}{\mu (\rho_p - \rho_g) g} \right]^{1/3} \quad [25]$$

3.2.1 Bed expansion

Bed voidage is an important flow structure parameter which determines the pressure drop in i-CFB. Here, bed expansion was investigated in a fluidized bed with the same dimension of the i-CFB reactor as shown in Fig. 3.1 but with a flat perforated plate as the distributor and the absence of the draft tube. Building air was used as the fluidizing gas, and zeolite powders were used as the bed material. Pressure drop was measured between points D1 and D3 at different gas inlet velocities and voidage was calculated according to Eq. (3.1) by neglecting frictional losses between gas/particle mixture and wall surfaces.

$$\Delta P = \rho_p g (1 - \varepsilon) H \quad (3.1)$$

where, ΔP is the pressure drop between the two points, ρ_p is the density of tested particles, ε is the voidage in the bed, and H is height of the bed between the two measurement points.

3.2.2 Gas bypass

The gas bypass between the draft tube and annulus was studied by Yang [11] using CO₂ tracer method with the bed loaded with 3.3 kg zeolite powders. At a given steady state operating condition, continuous

CO₂ tracer was injected into the inlet gas flow of the annulus, with CO₂ concentrations at the outlet of the draft tube and the annulus, and the inlet of the draft tube and the annulus being monitored. The schematics of gas bypass is shown in Fig. 3.3. Gas bypass ratios, R_{d-a} and R_{a-d} , which are defined in Eq. (3.2), were then calculated based on the mass balance of CO₂ tracer.

$$R_{d-a} = \frac{F_{d-a}}{F_{d0}}, \quad R_{a-d} = \frac{F_{a-d}}{F_{a0}} \quad (3.2)$$

where F_{d0} , F_{a0} , F_{d-a} and F_{a-d} are the flow rates of the gas fed to the draft tube, fed to the annulus, bypassing from the draft tube to the annulus and bypassing from the annulus to the draft tube, respectively.

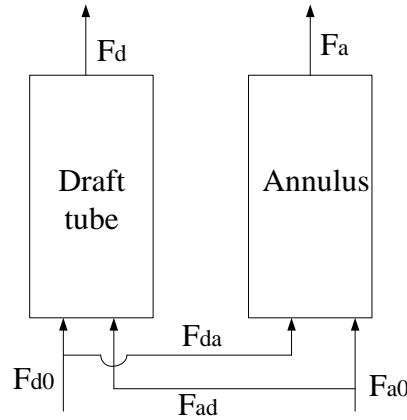


Figure 3.3 Schematics of the gas bypass between the draft tube and the annulus

3.2.3 Solids circulation rate

Experimentally, solids circulation rate can be determined from the vertical flux of particles passing through one or more of the regions using a number of methods [98] such as multi-fiber optical probes, radioactive tracer particles, and hot solids tracer techniques. In the current study, optical fiber probes were used to measure solids flux for fine catalyst particles. A particle velocity analyzer (PV-4A) manufactured by the Institute of Process Engineering, Chinese Academy of Sciences, was used for the measurement,

which included an optical fibre probe, a light conversion box, a data acquisition board and a program for sampling and recording data into the computer for analysis. This technique has been widely applied to determine particle velocity and voidage in fluidized beds [99, 100].

The optical fibre probe used in the current work is shown in Fig. 3.4. There are three bundles of fibres of 15 microns in diameter. Each bundle has a diameter of about 0.8 mm. The measurement volume of the probe employed in this work is less than 2 mm^3 , and is very small compared to the size of bubbles. Thus, this probe is sensitive to the local flow pattern but does not impose significant interference on the passing bubbles. The central bundle of fibres is for light projection, whereas the other two act as light receivers, corresponding to two sampling channels A and B. The basic mechanism to measure the velocity is to calculate the time lag, τ , between the moments when the particles pass the two light receivers by cross-correlation method. The particle velocity, U_p , can then be calculated by: $U_p = L_e / \tau$.

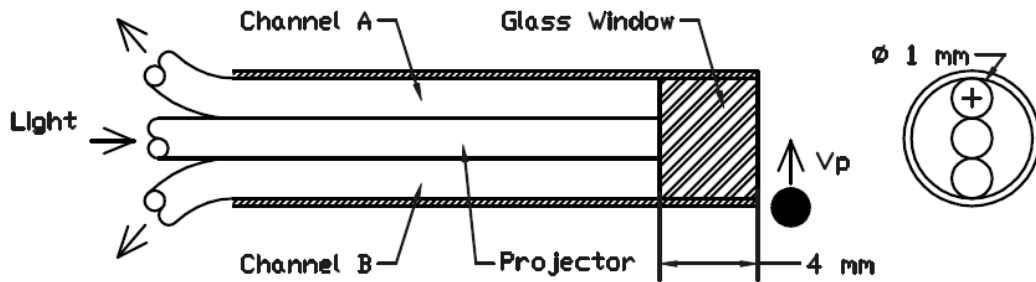


Figure 3.4 Details of the tip of the optical fibre probe for particle velocity measurement

The probe was calibrated employing the zeolite particles used in this study. A rotating plate with glued particles was driven by a motor. Particles rotated together with the rotating plate, at a preset particle velocity, U_p , and the time lag, τ , between the two channels of the probe was measured by the cross-correlation of the signals from the two channels. The effective distance was then calculated by multiplying the particle rotating velocity and the time lag. In a typical measurement, two series of signals were recorded from the system, which represent the intensity of the reflected light through the two

channels. These data series were divided into several groups, with cross-correlation being carried out on each group to find the time lag between the two channels.

For the measurement of local bed voidage, the optical fibre probe was calibrated in a packed bed. It is practically very challenge to create homogeneous gas-solid suspensions over a sufficiently wide range of solids concentrations. Black coke particles can absorb light and give no reflection back to the receicing tip of the probe. Therefore, these particles can not be ‘seen’ by the probe. Here, a mixture of bed particles and coke particles at different volume fractions of coke was used to simulate packed bed with different voidages, represented by black coke particles. However, one should note that the property of coke particles is not exactly the same as the ‘void’ between particles since these particles could affect light penetration throug the bed, leading to inaccuracy of the calibration, especially when there is a large light penetration depth of the probe. The calibration curve is shown in Fig. 3.5. The local voidage was then correlated with the probe reading by an exponential equation (see Fig. 3.5). Details on the optical fibre probe calibration by the mixture of two particle components can be found in [99, 101].

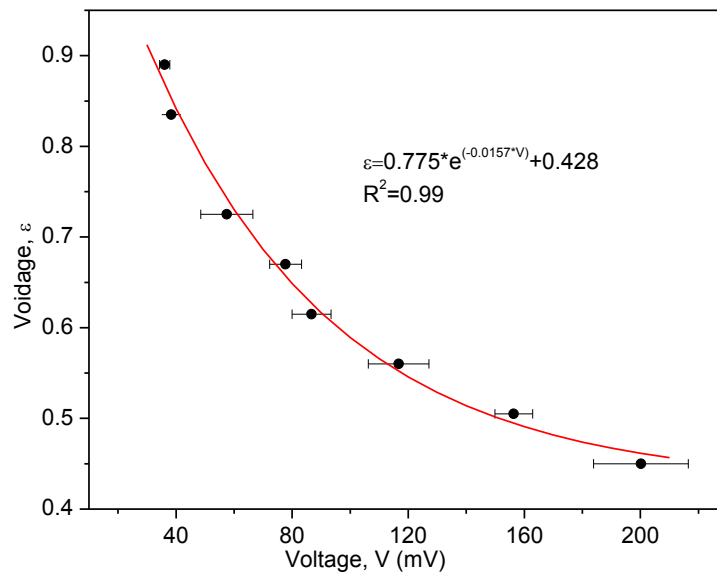


Figure 3.5 Voidage calibration of the optical probe (Symbols: experimental data, line: correlation)

The measurement was conducted at point D4 in the annulus, 950 mm above the bottom. Both solids velocity and local voidage were measured along the radial direction at an interval of 2.5 mm. The average solids flux in the annulus G_s could be calculated by the integration of local solids flux along the radial direction:

$$G_s = \rho_p \cdot \int_{R_d}^{R_a} \pi(1 - \varepsilon)U_p 2rdr \quad (3.3)$$

The particle back-mixing in fluidized beds can affect the particle velocity measurement, and also its influence is difficult to be determined. In this work, the instantaneous particle velocity signals were obtained over a period of time, which then were averaged to give the average solids velocity, avoiding the effect of the particle back-mixing on the particle velocity measurement [102].

3.3 Hydrodynamics model of i-CFB

3.3.1 Mass and pressure balance equations

In an i-CFB, the internal circulation of solids is created by the pressure difference between the draft tube and the annulus operating at different superficial gas velocities. The solids circulation rate dictates both the gas and solids residence time in each region and hence the extent of NO_x adsorption and catalytic NO_x reduction. There are several correlations in the literature, which link the bed hydrodynamics to the solids circulation rate [93, 95, 103]. Because the solids circulation rate is influenced by the bed geometry in addition to fluid and particle properties and gas velocity, those correlations from the literature could not be used directly when the geometry of the reactor is changed. In this research, the solids circulation rate is estimated based on the mass and momentum balances in the i-CFB reactor.

Solids mass balance equations include the conservation of total solids inventory in the system and solids circulation rate balance between the draft tube and the annulus:

$$M_{loading} = M_a + M_d = \rho_p(1 - \varepsilon_a)A_a H_a + \rho_p(1 - \varepsilon_d)A_d H_d \quad (3.4)$$

$$G_s = \rho_p \cdot U_{p,a} \cdot (1 - \varepsilon_a) = \rho_p \cdot U_{p,d} \cdot (1 - \varepsilon_d) \cdot \frac{A_a}{A_d} \quad (3.5)$$

where $M_{loading}$, M_a and M_d are total bed loading, mass of bed material in the annulus and mass of bed material in the draft tube, respectively. H_a , H_d , ε_a , ε_d , A_a , A_d , $U_{p,a}$ and $U_{p,d}$ are the bed heights, voidage, cross-sectional area and particle velocity in the annulus and the draft tube, respectively.

The driving force of the solids circulation is the pressure difference between the annulus and the draft tube, subtracting the pressure drop across the orifice connecting them. The pressure balance in the whole system is

$$\Delta P_a = \Delta P_d + \Delta P_{or} \quad (3.6)$$

where ΔP_a , ΔP_d and ΔP_{or} are the pressure drop in the annulus, in the draft tube and through the orifice, respectively.

3.3.2 Pressure drop calculation

In a fluidized state, the pressure drop could be expressed by Eqs. (3.7) and (3.8), which consist of the pressure drops due to gravity, solids acceleration, fluid-wall friction and particle-wall friction.

$$\Delta P_a = L_a(1 - \varepsilon_a)\rho_p g - 0.5(1 - \varepsilon_a)\rho_p U_{p,a}^2 + H_{draft-tube} F_{gw} - H_{draft-tube} F_{pw} \quad (3.7)$$

$$\Delta P_d = L_d(1 - \varepsilon_d)\rho_p g + 0.5(1 - \varepsilon_d)\rho_p U_{p,d}^2 + H_{draft-tube} F_{gw} + H_{draft-tube} F_{pw} \quad (3.8)$$

where L_a and L_d are the effective bed heights in the annulus and draft tube, respectively. F_{gw} and F_{pw} are the gas-wall and the particle-wall frictional force per unit volume of the column, respectively. In the case of gas velocities lower than 6 m/s, and straight column with diameter in excess of 4 cm, the contribution

of gas-wall friction F_{gw} could be neglected [104]. Konno and Saito's equation [105], which was developed for relatively low concentration of solids in vertical column, was used to calculate the solid-wall friction.

$$F_{pw} = 0.057 \cdot G_s (g / D_d)^{0.5} \quad (3.9)$$

The pressure drop across the orifice between the bottoms of annulus and draft tube could be correlated with solids circulation rate G_s . For mechanical valves like slide valves where the solids flow is controlled by changing the opening area, the pressure drop across the control valve and solids flux can be related by [106]:

$$G_s = C_D \frac{A_{or}}{A_a} \sqrt{\frac{2\rho_p(1-\varepsilon_a)\Delta P_{or}}{1-\left(\frac{A_{or}}{A_a}\right)^2}} \quad (3.10)$$

The discharge coefficient C_D in Eq. (3.10) has values typically between 0.2 and 0.6 with an average value of 0.4, although it depends on the geometrical configuration, orifice edge parameters and the D_{or}/d_p ratio. So C_D needs to be fitted from the experimental data for specific configurations.

3.3.3 Effective bed height

To obtain the effective bed height for Eqs. (3.7) and (3.8), the flow in the i-CFB was categorized into four different operating modes as shown in Fig. 3.6. It should be noted that the flow mode is classified here in such a way to facilitate the calculation of effective bed height and is different from the flow patterns reported in the literature [107].

- If there is not sufficient bed solids loading and the gas velocity inside the draft tube is lower than the particle transport velocity, the draft tube could not be fully filled with particles and a flow pattern in

Fig. 3.6(a) will be created without internal solids circulation. The initial pressure drops in the two zones could be obtained by

$$L_{d0} = H_{draft-tube} \quad (3.11)$$

$$L_{a0} = \frac{M_{loading} - \rho_p(1 - \varepsilon_d)L_{d0}A_d}{\rho_p(1 - \varepsilon_a)A_a} \quad (3.12)$$

$$\Delta P_{a0} = \rho_p(1 - \varepsilon_a)gL_{a0} \quad (3.13)$$

$$\Delta P_{d0} = \rho_p(1 - \varepsilon_d)gL_{d0} \quad (3.14)$$

If $\Delta P_{a0} < \Delta P_{d0}$, there is no solids circulation. This regime is of little interest in the operation of i-CFB.

But this procedure could be used to identify whether there is solids circulation or not. It should be noted that if the gas velocity in the annulus is bigger than that in draft tube, particles could be entrained to the annulus, forming solids circulation reversely. This case is not considered for the i-CFB yet and will not be discussed here.

- When the solids loading and/or the gas velocity in the draft tube are increased, particles fill up the draft tube and start to circulate to the annulus region. This corresponds to flow pattern (b) in Fig. 3.6. In this mode, the effective bed height in the draft tube is the same as the draft tube height, and the effective annulus bed height could be calculated by overall mass balance.

- If the particle loading and/or gas velocity are further increased, the annulus bed height could exceed the height of the draft tube and flow pattern (c) is established. In this case, the effective annulus bed height can still be calculated by mass balance and the effective draft tube bed height is equal to the effective annulus bed height. An initial guessed value of effective draft tube height should be taken to start the mass balance calculation, and the mass balance equations are then iterated to obtain the final bed height values.

$$L_d = L_{a0} \quad (3.15)$$

$$L_a = \frac{M_{loading} - \rho_p(1 - \varepsilon_d)L_d A_d}{\rho_p(1 - \varepsilon_a)A_a} \quad (3.16)$$

- When the bed loading or gas velocity is further increased, the annulus dense bed becomes too high and the gas jet on top of the draft tube becomes unstable or can no longer penetrate through. As a result, flow pattern (d) is formed. The vertical jet penetrate length L_j could be estimated in the same way as jet penetration depth in spout-fluid bed [108].

$$\frac{L_j}{D_a} = 11.52 \left(\frac{\rho_g}{\rho_p - \rho_g} \frac{U_d^2}{gD_d} \right)^{0.1966} \quad (3.17)$$

The effective draft tube bed height, L_d , is the sum of draft tube length and jet height, and the effective annulus bed height L_a equals L_d . The detailed criteria and calculation procedures for each of the four flow patterns are given in Table 3.3.

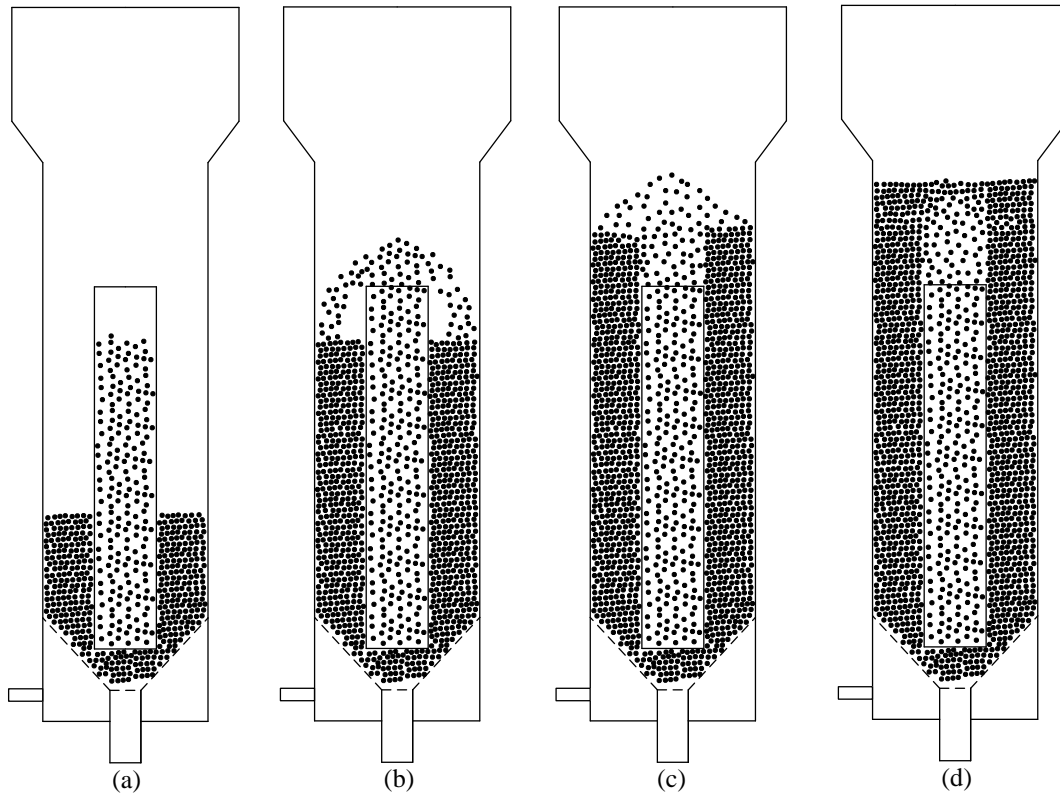


Figure 3.6 Schematic of four i-CFB flow modes and the effective bed height

Table 3.3 Calculation procedures for effective bed heights

Flow patter	$\Delta P_{a0} > \Delta P_{d0} ?$	$L_{a0} < L_{d0} ?$	$L_j > L_{a0} - L_{d0} ?$	L_a	L_d
(a)	N	--	--	Calculated from mass and pressure balance	Calculated from mass and pressure balance
(b)	Y	Y	--	Calculated from mass balance	$L_d = H_{draft-tube}$
(c)	Y	N	Y	Calculated from mass balance	$L_d = L_a$
(d)	Y	N	N	$L_a = L_d$	$L_d = H_{draft-tube} + L_j$

3.4 Results and discussion

3.4.1 Bed expansion characteristics

The bed voidage at different inlet gas velocities was measured in a cylindrical fluidized bed and plotted in Fig. 3.7. The experimental data were fitted to obtain correlations for the modeling of bed voidage in the i-CFB reactor.

Cai [109] modified Babu's correlation [110] to fit their bed expansion data obtained in both bubbling and turbulent fluidization regimes. The bubble size and bubble rise velocity are estimated, respectively, by,

$$D_b = 0.21H_f^{0.8} P^{0.06} (U - U_{mf})^{0.42} \exp\left[-1.4 \times 10^{-4} P^2 - 0.25(U - U_{mf})^2 - 0.1P(U - U_{mf})\right] \quad (3.18)$$

$$U_b = U - U_{mf} + 0.71(gD_b)^{0.5} \quad (3.19)$$

Gas flow rate in the bubble phase is calculated as

$$F_b = U_b \varepsilon_b A = Y(U - U_{mf})A \quad (3.20)$$

with Y being correlated to

$$Y = 0.108H_s^{0.26} (U - U_{mf})^{0.09} d_p^{-0.48} \rho_p^{-0.19} \quad (3.21)$$

where $H_s = H_{mf} / (1 - \varepsilon_{mf})$.

By assuming no particles inside the bubble phase, the bubble phase fraction (δ_b) and the bed voidage in the fluidized bed could then be calculated by

$$\delta_b = \frac{Y(U - U_{mf})}{U_b} \quad (3.22)$$

$$\varepsilon = \delta_b + (1 - \delta_b)\varepsilon_{mf} \quad (3.23)$$

When the Cai correlation was compared with our experimental data, it was found that the correlation gave a good agreement with experimental data with an error within 3.24%. To further improve the bed expansion prediction, the correlation of Y in Cai's correlation is slightly modified to

$$Y = 0.116H_s^{0.26}(U - U_{mf})^{0.09}d_p^{-0.48}\rho_p^{-0.19} \quad (3.24)$$

The calculated values from modified Cai correlation was plotted in Fig. 3.7, which has an error less than 2.44%. This correlation will be applied to both the annulus and draft tube zones of the i-CFB reactor.

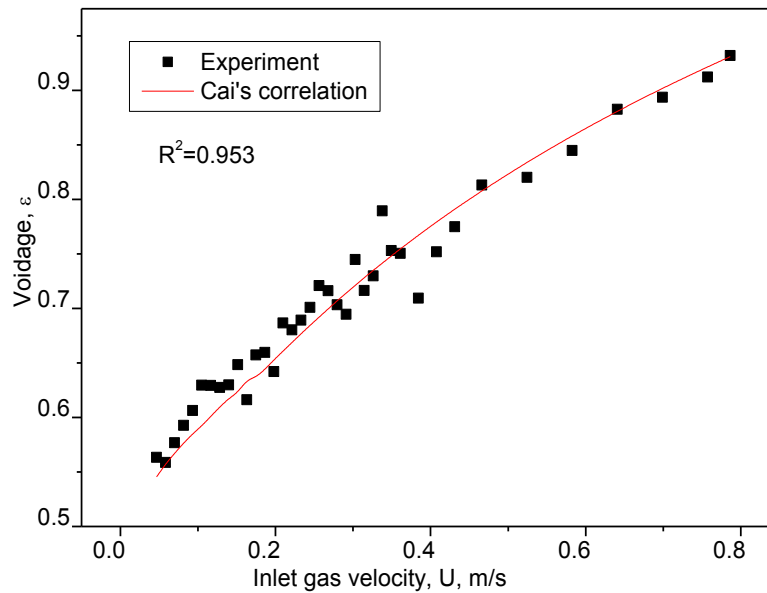


Figure 3.7 Measured voidage data for ZSM-5 powders and comparison with the Cai correlation (Symbols: experimental data, line: correlation)

It should be noted that the Cai correlation can only be used for bubbling and turbulent regimes. If the gas velocity exceeds U_t , the draft tube is operated as a transport riser. The Pugsley correlation [111], which was developed for transport risers with diameters of 0.05 to 1 m and for particles with diameters of 50 to 350 μm , could be used for the estimation of voidage:

$$\varepsilon = \frac{U\rho_p}{G_s\psi + U\rho_p} \quad (3.25)$$

where G_s is the solids circulation rate and U is the superficial gas velocity inside the draft tube. The slip factor was defined as the ratio of gas interstitial velocity to the average particle velocity and correlated to the Froude number.

$$\psi = \frac{U}{\varepsilon U_p} = 1 + \frac{5.6}{Fr} + 0.47Fr_t^{0.41} \quad (3.26)$$

where Fr and Fr_t are Froude number and particle Froude number, respectively.

$$Fr = \frac{U}{(gD_d)^{0.5}}, \quad Fr_t = \frac{U_t}{(gD_d)^{0.5}} \quad (3.27)$$

3.4.2 Gas bypass

Gas bypass is very important for the design and operation of i-CFB, which determines both the gas velocities and actual reactant concentrations in the annulus and draft tube. The measured gas bypass data from Yang [11] were shown in Fig. 3.8, where R_{d-a} is the gas bypass ratio from draft tube to the annulus and R_{a-d} is from the annulus to draft tube.

It can be seen from Fig. 3.8(a) that R_{d-a} increases with increasing U_{d0} , gas feed rate to the draft tube. It is seen that more gas leaks to the annulus as the gas velocity in the draft tube increases. However, when

the gas velocity in the annulus is higher, less gas leaks from draft tube to the annulus, leading to a lower R_{d-a} . Also, the effect of feed gas velocity in the annulus is less significant at lower U_{d0} , as evidenced from the slopes of R_{d-a} at different U_{d0} . At $U_{d0}=0.45$ m/s, R_{d-a} is almost unaffected by U_{d0} .

Comparing to R_{d-a} , R_{a-d} data are much more scattered and show no obvious trend. The change in both U_{a0} and U_{d0} has almost no effect on R_{a-d} , which fluctuates in the range of 5~9%, as shown in Fig. 3.8(b).

It should be noted that the net gas exchange is mostly from draft tube to the annulus based on calculated gas flow rate both from the annulus to draft tube and from draft tube to annulus (results are not shown here), which is in opposite to the net solids flow from the annulus to the draft tube. The low gas bypass from annulus to draft tube can limit the oxygen concentration buildup in the NO_x reduction zone in an i-CFB, leading to potential improvement of the overall de NO_x efficiency.

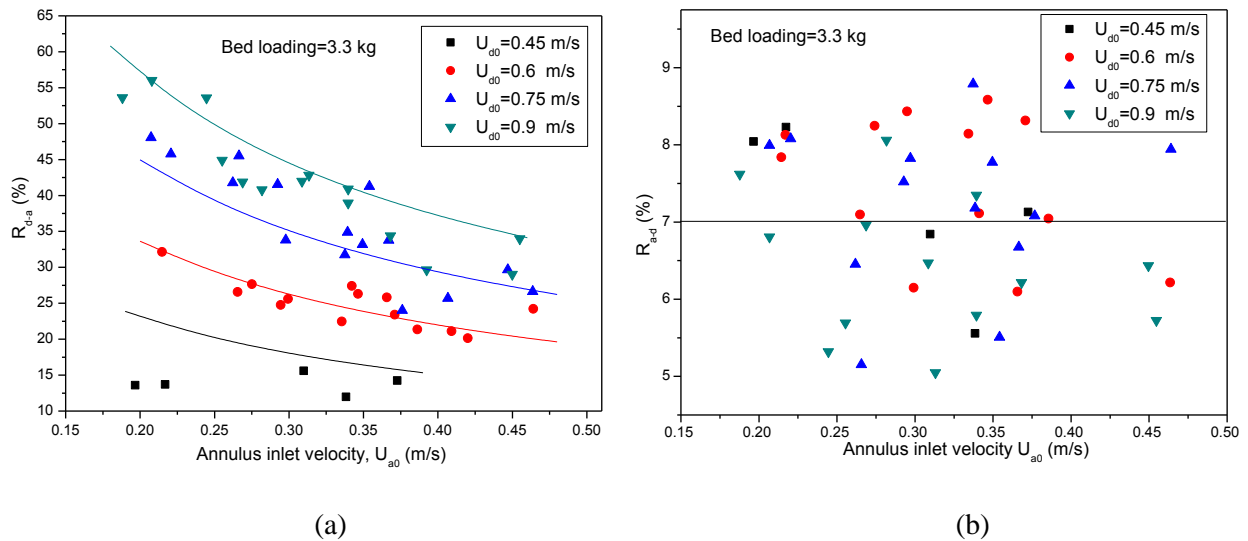


Figure 3.8 Gas bypass ratios at different U_{d0} . (a), from draft tube to annulus, R_{d-a} ; (b), from annulus to draft tube, R_{a-d} (Symbols: experimental data, lines: correlation)

For modeling the hydrodynamics of the i-CFB, the gas bypass R_{d-a} data are correlated to U_{a0} and U_{d0} by

$$R_{d-a} = 1.039 \left(\frac{U_{a0}}{U_{mf}} \right)^{-0.616} \left(\frac{U_{d0}}{U_{mf}} \right)^{1.300} \quad (R^2=0.865) \quad (3.28)$$

Since R_{a-d} is much scattered across a narrow range, an average value of 7% was used.

$$R_{a-d}=7\% \quad (3.29)$$

It should be noted that the equations are only valid within the experimental range, $0.45 \text{ m/s} < U_{d0} < 0.9 \text{ m/s}$ and $0.2 \text{ m/s} < U_{a0} < 0.475 \text{ m/s}$. If $U_{d0} > 0.9 \text{ m/s}$, R_{d-a} is predicted to be more than 100% and is unrealistic. The same problem also happens when U_{a0} is smaller than 0.2 m/s .

It is observed that at a higher U_{d0} , the increase in R_{d-a} slows down with increasing U_{d0} . The difference between the values of R_{d-a} at $U_{d0}=0.75 \text{ m/s}$ and $U_{d0}=0.9 \text{ m/s}$ is very small. So, when U_{d0} is higher than 0.9 m/s , the values of R_{d-a} at $U_{d0}=0.9 \text{ m/s}$ is taken in the modeling. Also, when U_{a0} is smaller than 0.2 m/s , the R_{d-a} values at $U_{a0}=0.2 \text{ m/s}$ is used. It should be warned that this assumption could potentially lead to errors in the modeling, since these values have not been confirmed experimentally.

The real gas velocities in the annulus and draft tube can now be calculated as:

$$U_a = U_{a0} - R_{a-d} \cdot U_{a0} + R_{d-a} \cdot U_{d0} \cdot (A_d / A_a) \quad (3.30)$$

$$U_d = U_{d0} - R_{d-a} \cdot U_{d0} + R_{a-d} \cdot U_{a0} \cdot (A_a / A_d) \quad (3.31)$$

3.4.3 Measured solids circulation rates

The solids circulation rate in the i-CFB reactor was measured at two different particle loadings, 2.275 kg and 3.3 kg . The packed bed heights are 0.29 m and 0.42 m , respectively. The particle velocity and voidage in the annulus were measured at different radial positions by the optical fibre probe. Fig. 3.9(a) shows the particle velocity as a function of dimensionless radial positions at different annulus gas velocity

U_{a0} with a particle bed loading of 2.275 kg. The value of r is referred to the distance from the axis of the i-CFB to the measurement point and R_0 is the column radius. The annulus zone is from $r/R_0=0.5$ to $r/R_0=1$. The positive values of the particle velocity indicate a downflow of particles while negative values indicate an upflow of particles. It can be seen that the particle velocity increases with decreasing U_{a0} . However, this does not necessarily mean that the solids circulation rate is higher, since the solids circulation is determined by both particle velocity and the local voidage. For most of the curves in Fig. 3.9(a), especially at lower U_{a0} , local particle velocity is higher at the outer side of the annulus than at the inner side. For a particle loading of 2.275 kg at a low annulus gas velocity, the flow pattern (b) in Fig. 3.6 is expected, in which solids falls down fast near the outer wall of the annulus. At a higher U_{a0} , particle velocities in the middle of the annulus are very small, and sometimes the solids even move upward there. Most of the solids flow down the annulus along both the inner and outer walls of the annulus. The reactor may be operated at the flow pattern (c) in Fig. 3.6 at a higher annulus gas velocity, in which some solids from the jet above the draft tube fall down along the outer side wall, and some solids penetrate through the jet to the dense annulus zone and then fall down along the inner wall.

The measured radial voidage profile is shown in Fig. 3.9(a). The voidage is seen to be very low near both inner and outer walls of the annulus, and reaches a peak around the middle of the annulus, indicating the presence of fewer particles in the middle region of the annulus. The voidage decreases with increasing the annulus gas velocity, which is contradictory to that commonly observed in the fluidized bed which increases with increasing the inlet gas velocity. One likely explanation is that the optical probe at point D4 in Fig. 3.3 is located in the dilute region well above the upper surface of the dense fluidized bed. In the freeboard region of a fluidized bed or in the downcomer with countercurrent gas-solids flow, the voidage decreases with increasing the inlet gas velocity.

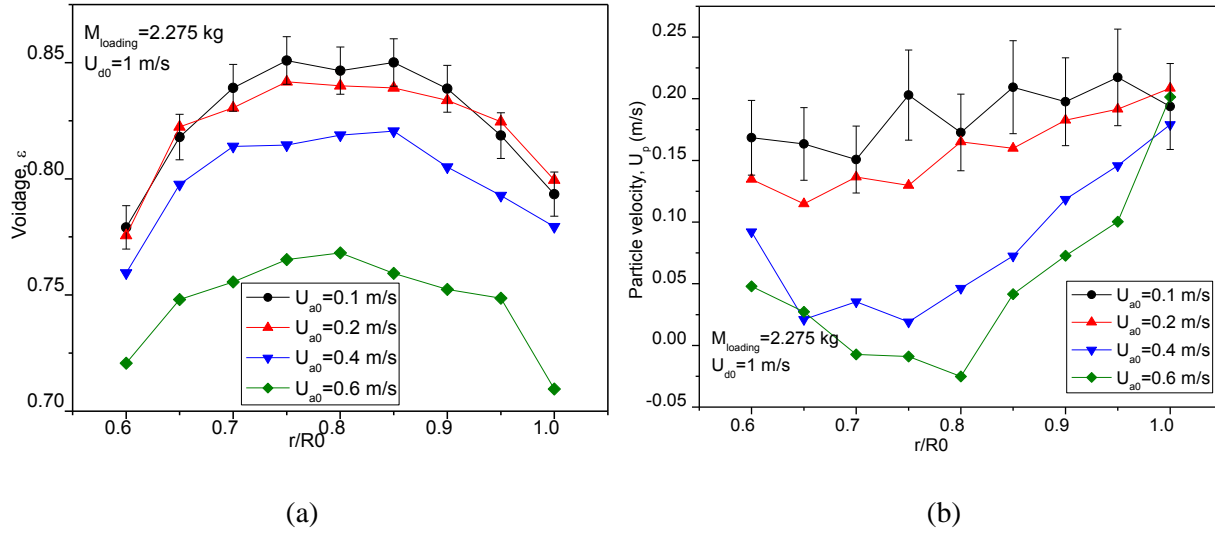


Figure 3.9 Measured radial profiles of (a) voidage and (b) particle velocity at different U_{a0} , ($U_{d0}=1$ m/s, bed loading=2.275 kg. Symbols: experimental data, lines: connection of symbols)

When particle loading is increased to 3.3 kg, the radial distribution of axial particle velocity in the annulus varies only slightly in the middle section, as shown in Fig. 3.10(a). The particle velocity increases slowly from the inner wall toward the middle of the annulus. Close to the column wall, the velocity increases substantially. The particle velocity decreases first when U_{a0} increases from 0 to 0.4 m/s and then increases a lot when U_{a0} is further increased to 0.6 m/s.

The radial voidage profile at a solids loading of 3.3 kg, as shown in Fig. 3.10(b), is also different from that at a solids loading of 2.275 kg. At a low U_{a0} , the voidage is almost flat along the radial direction, especially near the draft tube, indicating a uniform solids distribution in the annulus. At a high U_{a0} , voidage begins to decrease along the radial direction, leading to a denser region near the outer wall of the annulus. A valley appears on all profiles near the column wall. Combining with the radial particle velocity distribution, it can be concluded that more particles move downward near the column wall. Similar to Fig. 3.9(a) at the solids loading of 2.275 kg, the overall voidage decreases with increasing gas velocity. However, the voidage increases when U_{a0} further increases to 0.6 m/s. This can be explained by the bed expansion at different U_{a0} . It is likely that the optical probe is already immersed in the dense

section of the fluidized bed at $U_{a0}=0.4$ m/s. So if U_{a0} further increases, the measured voidage increases in the same way as the overall bed voidage.

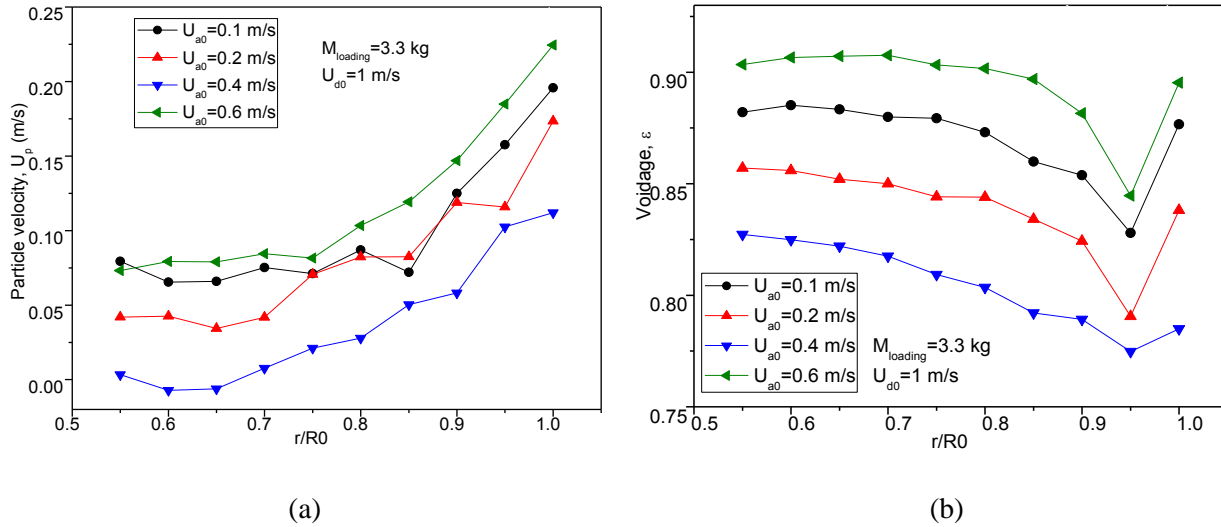


Figure 3.10 Measured radial profiles of (a) particle velocity and (b) voidage at different U_{a0} , ($U_{d0}=1$ m/s, bed loading=3.3 kg. Symbols: experimental data, lines: connection of symbols)

Fig. 3.11 shows the measured radial profiles of particle velocity and voidage at different U_{d0} . The particle velocities show a similar trend at different U_{d0} , but the effect of U_{d0} is not very clear. Comparing to particle velocity, the voidage in Fig. 3.11(b) is greatly influenced by U_{d0} , decreasing with increasing U_{d0} . Combining the solids velocity and voidage in the annulus, it can be inferred that the solids circulation rate increases with increasing U_{d0} .

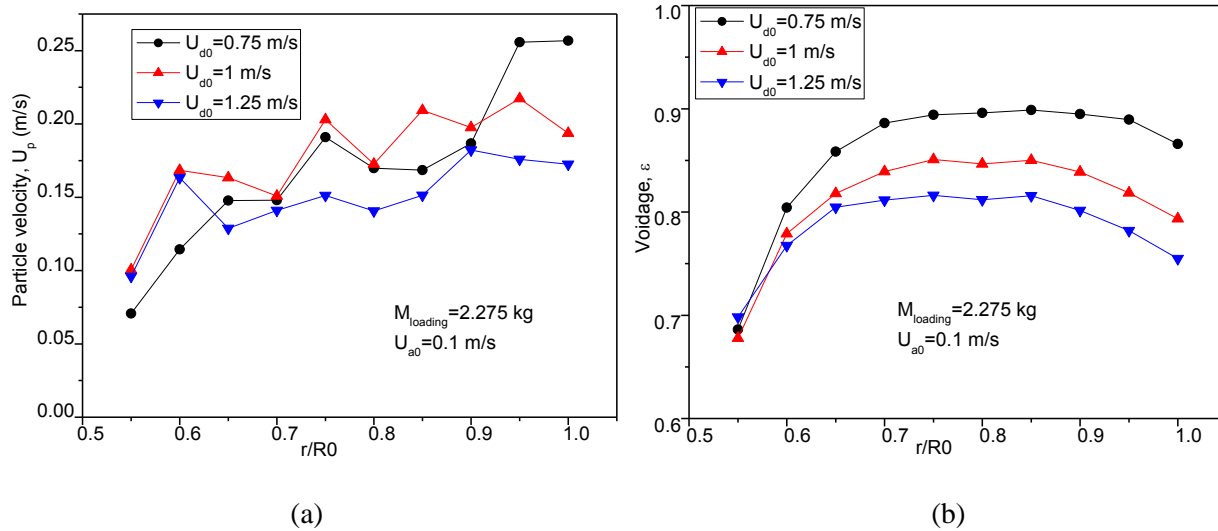


Figure 3.11 Measured radial profiles of (a) axial particle velocity and (b) voidage at $U_{a0}=0.1 \text{ m/s}$ (Symbols: experimental data, lines: connection of symbols)

The overall net solids flux in the annulus, G_s , is calculated from the integration of the local solids flux across the cross section of the annulus. Fig. 3.12(a) shows G_s as a function of U_{a0} at different draft tube velocities with a solids loading of 2.275 kg. As discussed above, the solids circulation rate mostly increases with increasing the draft tube gas velocity U_{d0} , but decreases with increasing U_{a0} . This can be explained by the pressure balance over the i-CFB reactor. When the draft velocity increases at a constant annulus velocity, solids circulation is increased because of the increased pressure difference between the draft tube and the annulus. On the other hand, at a constant draft tube gas velocity, the increase of annulus gas velocity increases the bed expansion in the annulus, which lowers the pressure buildup in the annulus and the pressure difference between the draft tube and the annulus, leading to the reduced solids circulation rate. G_s at a high bed solids loading of 3.3 kg is not sensitive to the annulus gas velocity at high draft tube gas velocities. At a low draft tube velocity, $U_{d0}=0.5 \text{ m/s}$, G_s increases from $U_{a0}=0$ to $U_{a0}=0.1 \text{ m/s}$ but decreases to less than $15 \text{ kg/m}^2 \cdot \text{s}$ when U_{a0} is increased from 0.1 to 0.4 m/s. This is likely caused by the small gas velocity difference between the draft tube and annulus, which can lead to loss of

pressure difference between these two zones. Also, G_s is less sensitive to U_{d0} at 3.3 kg solids loading than at a bed solids loading of 2.275 kg.

It is seen from those two figures that G_s is a strong function of bed solids loading and inlet gas velocities. At low bed solids loadings and low U_{d0} , G_s decreases as the annulus gas velocity increases. However, the trend changes and tends to be reversed at high bed solids loadings and high U_{d0} .

Many factors may influence the solids circulation rate of the i-CFB at different solids loadings. The trends of these curves cannot be simply explained by the differences of the inlet gas velocities. Gas bypass at different bed solids loading and inlet gas velocities could directly influence the actual gas velocity in both the annulus and draft tube, which determines the voidage in each zone. Effective bed heights in both zones are also influenced by operating conditions. These influencing factors will be further discussed in the modeling section.

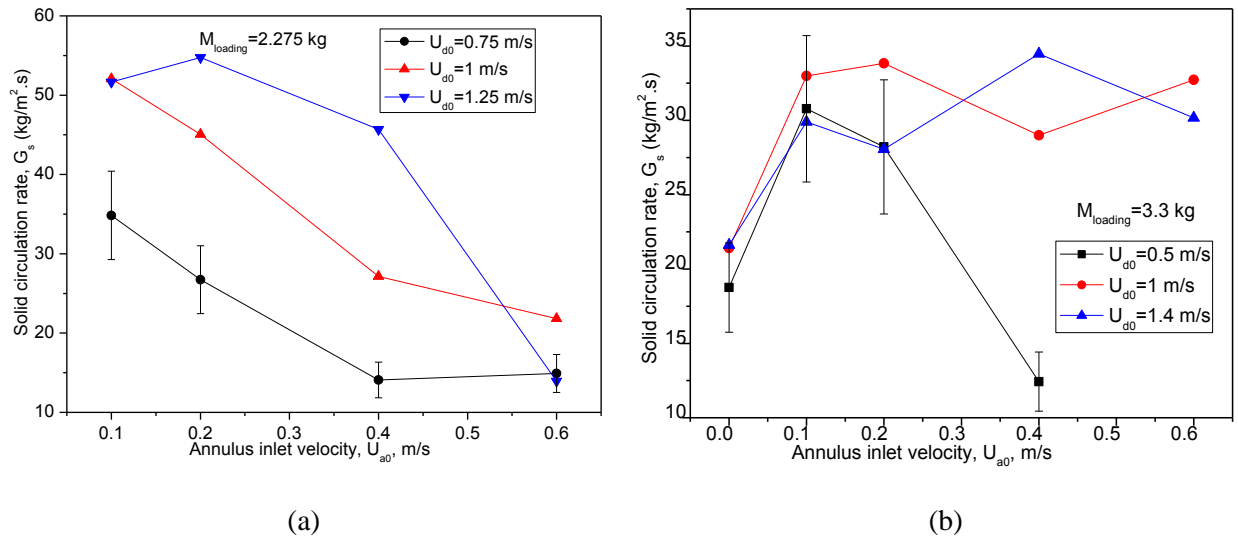


Figure 3.12 Net solids circulation rate at different U_{d0} , with bed solids loadings of (a), 2.275 kg, and (b), 3.3 kg. Symbols: experimental data, lines: connection of symbols)

3.4.4 Prediction of solids circulation rate

The solids circulation rate at a bed solids loading of 3.3 kg is modeled by mass and pressure balance equations. The real gas velocities in the annulus and draft tube are adjusted by the gas bypass ratios. Then voidage in both zones is calculated using Cai's correlation.

Fig. 3.13(a) shows the estimated voidage, with the closed symbols corresponding to the voidage in the annulus and the open symbols for the voidage in the draft tube. It can be seen that the voidage in the draft tube is always higher than the voidage in the annulus, since the velocity in the draft tube is always higher than in the annulus. From the bed expansion characteristics shown in Fig. 3.7, voidage is expected to increase from 0.6 to 0.85 when the gas velocity increases from 0.1 m/s to 0.6 m/s. The curves of annulus voidage ϵ_a seem to be quite different from expected without gas bypass. The voidage in the annulus increases with increasing the draft tube inlet gas velocity because more gas passes from the draft tube through the orifice to the annulus zone at higher U_{d0} . At the same U_{d0} , the slopes of most ϵ_a vs. U_a curves are lower than the slope in Fig. 3.7, due to smaller R_{d-a} values at higher U_{a0} . It can be concluded that the voidage in both zones of the i-CFB reactor is substantially changed by gas bypass.

Following the procedure given in Table 3.3, effective bed heights in the two zones are estimated through mass balance and plotted in Fig. 3.13(b). In the figures, 'a' is annulus and 'd' denotes draft tube. At low U_{a0} and U_{d0} , type (b) flow pattern is expected with $L_d=H_d$ and $L_a < H_d$. But at higher U_{a0} and U_{d0} , the flow patterns are expected to be either type (c) or type (d), with the effective heights of annulus and draft tube being the same and larger than the length of draft tube. It can be seen that the effective bed height increases with increasing both U_{d0} and U_{a0} . At low U_{d0} , the slope of the curves is steep, because increasing inlet gas velocity can significantly increase the expansion of the fluidized bed. But at higher U_{d0} and U_{a0} , the top of the annulus dense bed exceeds the height of the jet above the draft tube and flow patterns (c) or (d) are formed. Further increasing the inlet gas velocity has little effect on the effective bed height.

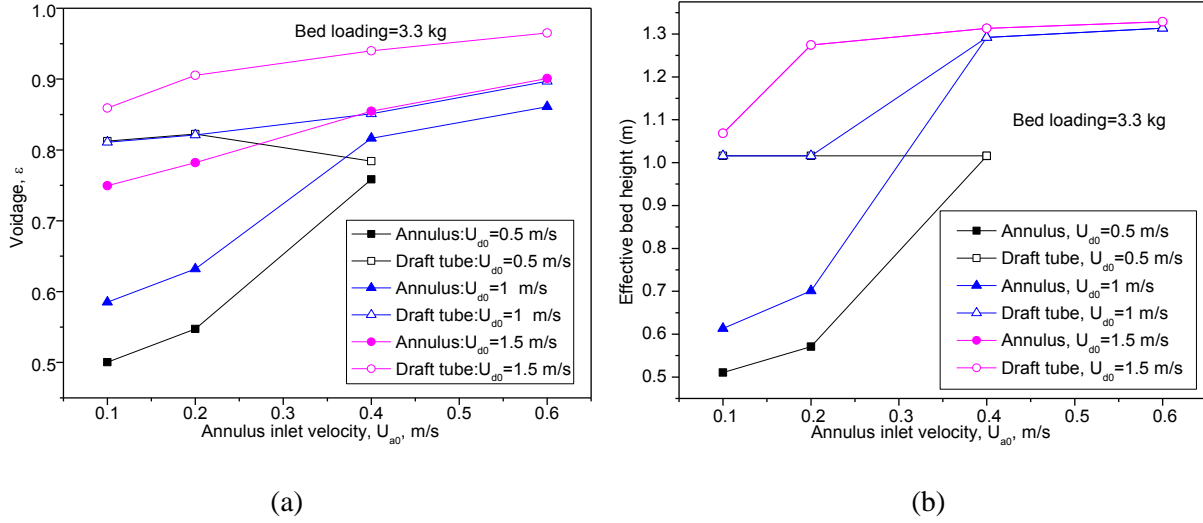


Figure 3.13 Calculated (a) voidage and (b) effective bed height at a bed solids loading of 3.3 kg (Symbols: calculated data points, lines: connection of symbols)

Pressure drop across the annulus and draft tube is estimated based on the estimated voidage and effective bed height, and the pressure drop across the orifice ΔP_{or} is obtained based on the pressure difference between the annulus and the draft tube. The values of ΔP_{or} are further fitted into Eq. (3.10) to obtain the discharge coefficient C_D at each operating condition. The calculated C_D data are shown in Fig. 3.14 as a function of Reynolds number of the particles passing through the orifice, Re_p , defined as:

$$Re_p = \frac{\rho_g d_p U_{p,a}}{\mu} \quad (3.32)$$

The fitted C_D values are quite scattered and varied from 0.13 to 0.21, which falls reasonably into the range as reported in the literature [106]. Since no obvious trend with Re_p was observed, an average C_D value of 0.167 is taken for further simulation.

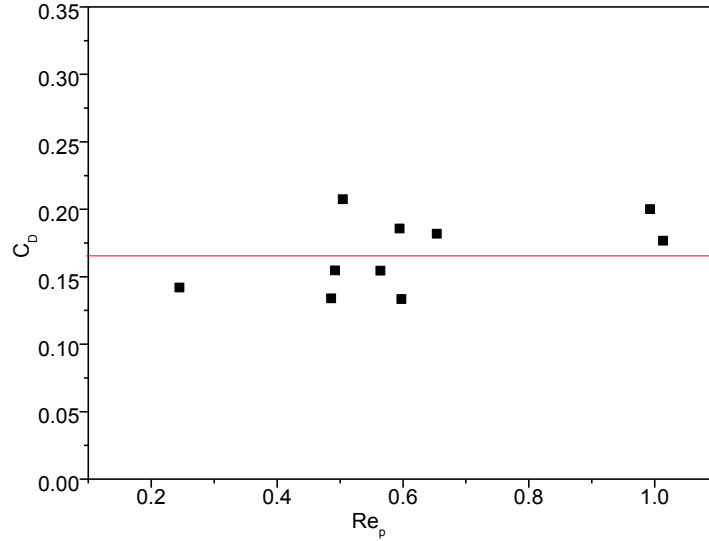


Figure 3.14 Fitted C_D values as a function of Re_p (Symbols: experimental data, lines: connection of symbols)

Using the current model, hydrodynamics at a bed solids loading of 3.3 kg is further investigated for the design of an i-CFB reactor. In an i-CFB deNO_x reactor, flue gas is fed into the annulus and NO_x in the flue gas will be adsorbed onto the catalyst surface. The oxygen concentration in the flue gas is always high in lean combustion of fuels, and the presence of high level oxygen favours the NO_x adsorption. In the draft tube, NO_x adsorbed on the catalyst surface is reduced by hydrocarbons. The reduction reaction is inhibited by O₂ because hydrocarbon reductant is consumed by oxygen. Therefore, careful control of the oxygen concentration inside the draft tube is of great importance to achieve the high deNO_x efficiency of the deNO_x reactor. Here, the actual O₂ concentration in the draft tube is estimated based on the gas bypass ratios and the gas flow rate into the draft tube using 3. (33). It is assumed that O₂ only exists in the gas fed into the annulus with a concentration of 8%.

$$C_{O_2,d} = C_{O_2,a0} \cdot \frac{F_{a-d}}{F_d} = C_{O_2,a0} \cdot R_{a-d} \cdot \frac{U_{a0}}{U_d} \quad (3.33)$$

Fig. 3.15(a) shows the predicted O_2 concentration in the draft tube, $C_{O_2,d}$, at various inlet gas velocities. All the values of $C_{O_2,d}$ are very low, ranging from 0.25% to 0.5%. This is due to the low gas bypass ratios from annulus to draft tube. The predicted low oxygen concentration in the draft tube can thus achieve a high NO_x reduction efficiency.

The overall NO_x abatement efficiency is determined by both the adsorption in the annulus, which directly removes NO_x from the flue gas, and the reduction in the draft tube. The NO_x adsorption efficiency in the annulus is strongly affected by the solids circulation rate, which represents how the NO_x can be efficiently transferred to the reduction zone and also determines the contact time between gas and catalyst. Fig. 3.15(b) shows the predicted solids circulation rate at different inlet gas velocities. It is seen that G_s is smaller at lower U_{d0} , e.g. 0.6 m/s. But further increasing U_{d0} from 0.75 m/s to 0.9 m/s has little effect on G_s and even leads to lower values of G_s . The broad width of the peak also indicates that the i- CFB can be well operated over a wide range of U_{a0} , with the optimal annulus velocities between 0.25 to 0.45 m/s.

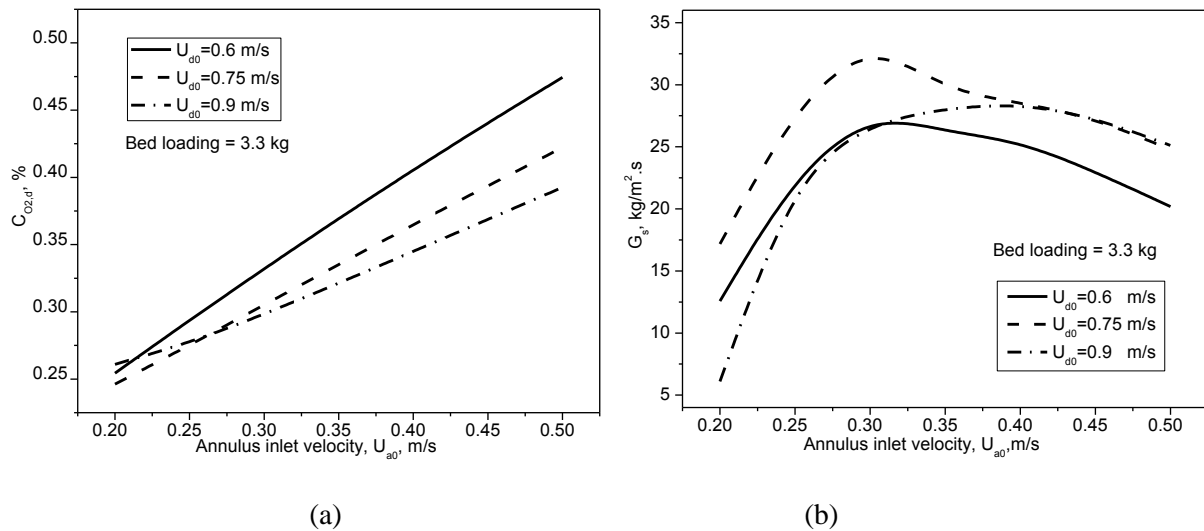


Figure 3.15 Predicted (a) $C_{O_2,d}$ and (b) G_s as a function of U_{a0}

3.5 Summary

The hydrodynamics of an i-CFB deNO_x reactor have been studied by both experiment and modeling. Gas bypass was investigated by a CO₂ tracer method, and the solids circulation rate was measured using an optical fibre probe at bed solids loadings of 3.3 kg and 2.275 kg. It was found that the solids circulation rate was a strong function of bed loading and feeding gas velocities. At low bed loading and low draft tube velocity, the solids circulation rate decreased as the annulus gas velocity increased. However, this trend could be reversed at high bed loading and high draft tube velocity. A hydrodynamic model was then developed based on mass and pressure balances. The discharging coefficient C_D was extracted from fitting the experimental data and an average value of 0.167 was taken for model simulation. The model captures the characteristics of the solids flow and gas flow distribution, and could serve as a useful tool for the design and simulation of the i-CFB deNO_x reactor system. However, modeling at different bed solids loadings requires the gas bypass characteristics being measured. With data on both the gas bypass and solids circulation rate, the hydrodynamic behavior could be coupled with the reaction kinetics to simulate the i-CFB performance for NO_x reduction.

Chapter 4 Development of deNO_x reaction kinetics³

4.1 Introduction

In order to model the i-CFB deNO_x reactor, the NO_x reduction kinetics of the selected catalyst needs to be developed first. Different from the conventional catalytic reactor where adsorption and reaction take place at the same time and at the same zone, adsorption and reduction take place in two different zones of the i-CFB reactor. Adsorption and reaction kinetics therefore should be decoupled and modeled separately for the adsorption zone and reduction zone and the performance of the adsorption and reduction zones is then linked by the solids circulation between the two zones. Although there are several kinetic models that separate adsorption and reduction for NSR catalyst [112], most of them are developed for Pt/Ba/Al catalyst and are based on intricate element reactions. These models are not applicable for the i-CFB reactor, in which both hydrodynamics and kinetics are very complex. In this chapter, a kinetic model will be proposed, consisting of two simplified sub-models, one adsorption model and one reduction model. The adsorption isotherm and kinetic parameters are fitted by the corresponding fixed bed experimental data.

For governing equations of kinetic model, surface reaction and surface adsorption are usually embedded into the gas phase mass balance equation, even with NO_x storage being considered [113, 114]. For the modeling of NSR (non-selective reduction) reaction, NO_x adsorption onto the catalyst surface in

³ A version of the adsorption modeling in this chapter has been published: Xingxing Cheng and Xiaotao T. Bi, Modeling NO_x adsorption onto Fe/ZSM-5 catalysts in a fixed bed reactor, *International Journal of Chemical Reactor Engineering*, 11(1): 1-12. An earlier version of the kinetics development part in this chapter has been published: Xingxing Cheng, Xiaotao Bi, (2012), Reaction kinetics of selective catalytic reduction of NO_x by propylene over Fe/ZSM-5. *Chemical Engineering Journal*, 211-212: 453-462.

the fuel-lean cycle and then be reduced in the fuel-rich cycle were modeled separately. For example, Lindholm [112] modeled NO_x storage and reduction with hydrogen as the reducing agent over Pt/Ba/Al catalyst in a monolith reactor. The reactor was treated as a series of continuously stirred tank reactors (CSTR). Reaction takes place on the catalyst surface between adsorbed NO_x and reduction agent during the fuel-rich cycle. The mass transport to the catalyst is modeled for adsorption, desorption, and reaction on the catalyst surface stages, separately, over a lean and rich cycle. The same model was also used for the modeling of NO_x adsorption and NO oxidation over Cu/ZSM-5 monolith catalyst [115], and a similar model was used [116, 117] for NO_x storage/reduction on Pt/Ba/Al monolith catalysts. Instead of CSTR, axial dispersion was considered in the gas phase mass balance equation. At the same time, less sophisticated reactions have also been proposed. Metkar et al. [118] recently developed a kinetic model for NH_3 -SCR over Fe- and Cu-zeolite monolith catalyst in which gas diffusion in the washcoat was considered. It was also reported by [118] that diffusion is very important in the SCR reactor and should be included in the reactor model. These models could work well with the monolith reactors where there is a distinct boundary between the gas phase and washcoat and reactants diffuse through the layer of the washcoat. However, gas flow and mass transfer in the packed bed could be different, where the gas species diffuses into the pores of each particle. Also, model developed for monolith reactor could not be extended to fluidized bed reactors, where both diffusion inside the particles and the mixing of the solids need to be considered.

To model the adsorption-reduction process, solids phase mass balance should be considered in the adsorption model in which the reaction term should be incorporated into the solids phase to account for catalytic reaction of adsorbed NO_x on the solids surface. In this chapter, kinetic model will be developed by fitting into the data obtained from a fixed bed reactor. Mass transfer between solids and gas phase is incorporated into the model, with the mass transfer coefficients being obtained from fitting fixed bed adsorption breakthrough curves. Both solids and gas phase mass balance equations were considered with the reaction term embedded into the solids phase mass balance equation.

4.2 Experiments

4.2.1 Experimental setup

Fixed bed experimental data of O₂ adsorption, NO_x adsorption and NO_x reaction are needed for the development of reaction and adsorption kinetics. Data for reaction kinetics are taken from the fixed bed reaction experiments of Yang [11]. NO_x adsorption was also tested by Yang [11] at different inlet NO concentrations and temperatures, with the inlet O₂ concentration being kept at 4%. NO_x adsorption at different inlet O₂ concentrations, as well as O₂ adsorption, is thus studied here in the same experimental setup as shown in Fig. 4.1, which consists of a tubular reactor, a gas supply and flow rate control unit, a gas preheating unit, a gas heating unit (furnace), a gas analysis unit and a data acquisition system. A stainless steel tubular reactor with an inner diameter of 13.5 mm was used in this experiment, and the catalyst packing height was maintained at 50.8 mm throughout all the tests.

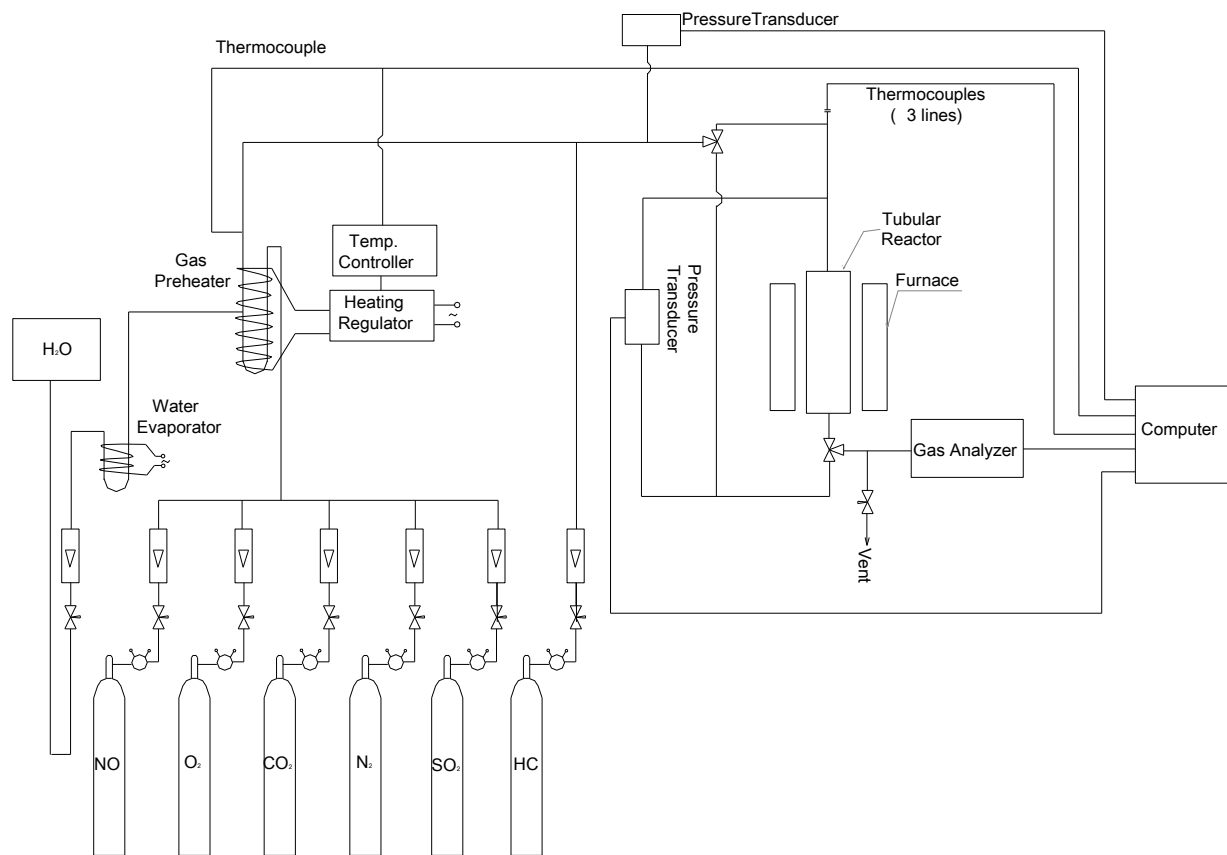


Figure 4.1 Fixed bed reaction system

Fe/ZSM-5 catalyst, which shows good performance in the previous i-CFB study of Yang [11], was tested in the adsorption experiment. The catalyst support is H/ZSM-5 (average particle size of 155 μm , apparent bulk density of 968 kg/m^3 , and BET surface area of 171 m^2/g), which was obtained as a free sample from Albemarle Corporation. The method to prepare the fine Fe/ZSM-5 catalyst was described in [63]. The prepared fine Fe/ZSM-5 catalyst has an iron content of 5% and a BET surface area of 163 m^2/g , which is slightly lower than the original ZSM-5 catalyst support.

The model flue gas used in the experiment was a mixture prepared from several gas cylinders: 50% O_2 balanced with N_2 , 0.6% NO balanced with N_2 and pure N_2 gas cylinders from Praxair Products Inc.

The compositions (NO_x and O_2) of the effluent gases were analyzed by a Horiba PG-250 flue gas analyzer.

Before the start up of the experiment, the reactor was first heated to the desired temperature with pure N_2 gas passing through the catalyst bed. After the reactor temperature was stabilized, the flow of a gas mixture at a preset composition was turned on to start the experiment, with the gas mixture inlet composition determined by the same gas analyzer.

In the NO_x adsorption experiment, the model flue gas was pre-mixed with pure N_2 as the balancing gas according to the preset flow rate and concentrations of NO and O_2 . The mixed flue gas was then preheated to $150\text{ }^\circ\text{C}$ by the preheating system, with the composition being measured by the gas analyzer. After stable readings of the analyzer were reached, which corresponded to the inlet model flue gas concentrations, the three-way valves switched the flow to the reactor inlet and the time was recorded as the starting point of the adsorption. During the adsorption process, the gas composition at the reactor's outlet was continuously monitored until the NO_x concentration became stable, with the final NO_x concentration defined as the equilibrium NO_x concentration. Thereafter, the NO flow from the gas cylinder was turned off and, at the same time, HC (i.e. propylene) at the same flow rate of NO was added into the $\text{O}_2 + \text{N}_2$ flow to start the catalytic reduction process by reacting propylene with the adsorbed NO_x on the catalyst. After 45 minutes, the HC flow was turned off and the gas composition passing through the catalyst bed was adjusted to 10% $\text{O}_2 +$ balanced N_2 at a flow rate of 500 ml/min to further remove the adsorbed HC or other intermediate species produced in the reduction process. This stripping process took 30~45 minutes or even longer to lower the outlet CO concentration to below 5 ppm. Afterward, pure N_2 was used to purge the catalyst bed for another 45 minutes to remove all adsorbed CO_x and O_2 from the catalyst.

To investigate the O_2 adsorption performance, which would be later used for the modeling of NO_x reduction kinetics, the O_2 adsorption experiment was also conducted. Similar procedures as the NO_x

adsorption were followed for the O₂ adsorption experiment. The only difference is that the reactor was purged with pure N₂ after adsorption. Inlet O₂ concentrations were set to be 0.4% and 1%, which is lower than most of the inlet O₂ concentrations in the NO_x adsorption test. This is because O₂ adsorption capacity is much lower than NO_x. When inlet O₂ concentration is higher than 1%, adsorption breakthrough time will become shorter than the measurement system response time, leading to significant experimental errors.

Four to eight repeated runs were used to obtain the standard deviation, with two times of standard deviations corresponding to 95% of confidence level.

Different experiments and experimental conditions are summarized in Table 4.1. The gas hourly space velocity (GHSV) was set to 5000 h⁻¹. It should be noted that only experimental data at 350 °C are used for the kinetic development. This is because 350 °C was found to be the optimum reaction temperature for Fe/ZSM-5 catalyst, and deNO_x reaction in the i-CFB was only tested at 350 °C by Yang [11].

Table 4.1 Inlet conditions of fixed bed adsorption experiments

Experiment	NO inlet, ppm	Inlet HC:NO	Inlet O ₂ , %	Gas velocity
Fixed bed O ₂ adsorption	N/A	N/A	0.4, 1	GHSV=5000 h ⁻¹
Fixed bed NO _x adsorption	200, 400, 600, 800, 1000	N/A	4	GHSV=5000 h ⁻¹
Fixed bed reduction	600	0.5, 1, 2, 4	0.5, 1, 2, 4, 8	GHSV=5000 h ⁻¹

4.2.2 Adsorption performance of Fe/ZSM-5

The NO_x adsorption curves at different NO concentrations are given in [11]. The adsorption capacity could be calculated by

$$q_e = \frac{P \times C_{feeding} \times 10^{-3} \times F \times M_{NO}}{R \times (T_0 + 273)} \times \frac{S}{W_{cat}} \quad (4.1)$$

where S is the area under the adsorption curve, calculated from integration of the adsorption curve:

$$S = \int_0^t \left(1 - \frac{C_{out}}{C_{feeding}} \right) dt \quad (4.2)$$

The adsorption capacities at different temperatures and 4% O_2 were reported in [11]. The adsorption of NO_x at different O_2 concentration and O_2 adsorption were tested following the same procedure, with the obtained adsorption capacities being shown in Fig. 4.2. As expected, O_2 adsorption capacities are much smaller than the NO_x adsorption capacity in Fig. 4.2(b) and decrease with increasing temperature. The NO_x adsorption was significantly promoted by the presence of O_2 , which increased about 7 times when O_2 concentration increased from 1% to 8%. This is because NO is first oxidized to NO_2 before adsorbed onto the catalyst surface. At higher O_2 concentrations, more NO is oxidized to NO_2 , leading to a higher adsorption capacity of NO_x .

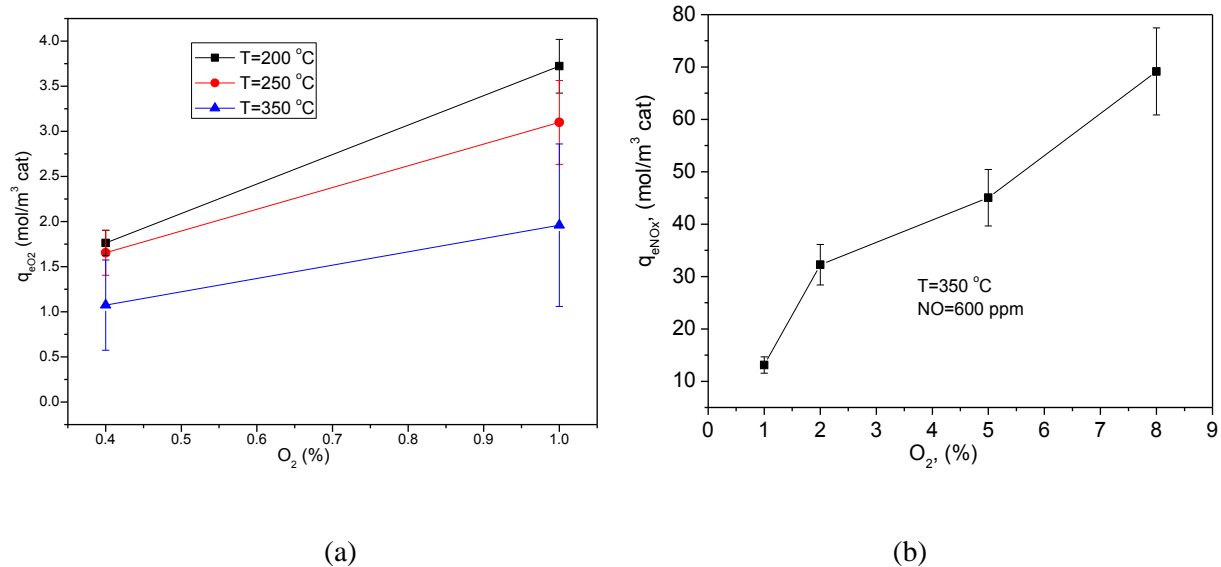


Figure 4.2 Adsorption capacity of (a) O_2 at different temperatures and (b) NO_x at different O_2 concentrations (Symbols: experimental data, lines: connection of symbols)

4.3 Adsorption and reaction modeling in fixed bed

The detailed kinetic model was divided into two sub-models, i), NO_x oxidation and adsorption, ii), NO_x reduction. These two sub-models describe the steps occurring over Fe/ZSM-5 catalyst during the NO_x adsorption and reduction, which could be used for the modeling of the i-CFB deNO_x reaction.

4.3.1 Kinetics of adsorption

The Fe-zeolite includes a number of different sites and it has been reported that the Fe/ZSM-5 catalysts contain three different Fe species: aggregated α -Fe₂O₃, Fe_xO_y, oligomer in the extra-framework, and oxo-Fe³⁺ at ion-exchanged sites [36]. It was further suggested that the ion-exchanged oxo-Fe³⁺ are the active sites for the SCR reaction, and that these sites only represent a small fraction of the total Fe content. However, due to the uncertainty in the actual nature of these active sites, and in order to keep the model as simple as possible, only a single type of sites was considered in this study for the NO_x adsorption, denoted as *.

Detailed Langmuir-Hinshelwood and Eley-Rideal models have been reported in the literature [115]. In this work, we emphasize on global kinetics that is simple enough to be integrated into the NO_x adsorption-reduction model. NO adsorption experiments at zero O₂ concentration showed that only a small amount of NO was adsorbed on the catalyst surface. Therefore, NO adsorption was ignored. Furthermore, NO_x adsorption is highly promoted by O₂ concentration, which was confirmed in Fig. 4.2(b), leading to the assumption that the main component of NO_x adsorbed on the catalyst surface is NO₂. Since the adsorption of NO₂ on the Fe/ZSM-5 catalyst is more favorable than that of NO, it is assumed that NO is first oxidized by adsorbed O₂ and then adsorbed onto the catalyst surface as NO₂. The kinetics of NO_x adsorption is proposed here as





The equilibrium constants of adsorption are

$$K_{O_2} = k_1 / k_{-1}, \quad K_{NO_2} = k_2 / k_{-2} \quad (4.3)$$

The net adsorption rates for oxygen and NO_x could be expressed as

$$r_1 = k_1 \cdot C_{O_2} \cdot [^*]^2 - k_{-1} \cdot [O^*]^2 = k_1 \cdot \left(C_{O_2} \cdot [^*]^2 - \frac{1}{K_{O_2}} \cdot [O^*]^2 \right) \quad (4.4)$$

$$r_2 = k_2 \cdot C_{NO} \cdot [O^*] - k_{-2} \cdot [NO_2^*] = k_2 \cdot \left(C_{NO} \cdot [O^*] - \frac{1}{K_{NO_2}} \cdot [NO_2^*] \right) \quad (4.5)$$

At equilibrium, $r_1 = 0$, $r_2 = 0$, so,

$$[O^*] = K_{O_2}^{1/2} \cdot C_{O_2}^{1/2} \cdot [^*] \quad (4.6)$$

$$[NO_2^*] = K_{NO_2} \cdot C_{NO} \cdot [O^*] \quad (4.7)$$

where, [^*] represents the number of vacant sites on the surface of the catalyst, [NO₂^{*}] is the number of sites occupied by NO₂, since NO₂ is the only form of NO_x adsorbed on the catalyst surface, which represents the adsorbed NO_x. At equilibrium, [O^{*}] and [NO₂^{*}] are the adsorbed oxygen and NO₂ concentrations on the surface of the catalyst and, therefore, represent the adsorption capacity of these species.

$$[O^*] = 2 \cdot q_{eO_2} \quad mol/m^3 cat \quad (4.8)$$

$$[NO_2^*] = q_{eNO_x} \quad mol/m^3 cat \quad (4.9)$$

The adsorbed O₂ and NO₂ could be expressed into Freundlich equations with the derivations shown in Appendix B:

$$q_{eO_2} = k_{FO_2} \cdot C_{O_2}^{n_{O_2}} \quad (4.10)$$

$$q_{eNO_x} = k_{FO_2} \cdot C_{O_2}^{n_{O_2}} \cdot k_{FNO_2} \cdot C_{NO}^{n_{NO_2}} \quad (4.11)$$

4.3.2 NO_x reduction kinetics model

The NO_x reduction kinetics model consists of two simplified reactions, hydrocarbon combustion (4.R3) and NO_x reduction (4.R4). Here, both oxygen and NO₂ are assumed to be adsorbed on the catalyst surface already, with their molar concentration being obtained from the adsorption model above. Adsorption was assumed to be at equilibrium, so [O*] and [NO₂*] were the saturated concentrations on the catalyst surface, calculated from Eqs. (4.10) and (4.11).



The power law kinetic model is applied for reactions (4.R3) and (4.R4).

$$r_3 = k_3 \cdot C_{HC}^{m_1} \cdot [O^*]^{m_2} \quad (4.12)$$

$$r_4 = k_4 \cdot [NO_2^*]^{m_3} \cdot C_{HC}^{m_4} \cdot [O^*]^{m_5} \quad (4.13)$$

The reaction rates of NO_x, hydrocarbon and oxygen are then expressed as

$$r_{NO_x} = -2r_4 \quad (4.14)$$

$$r_{HC} = -r_3 - r_4 \quad (4.15)$$

$$r_{O_2} = -4.5r_3 - 2.5r_4 \quad (4.16)$$

4.3.3 Governing equations of the fixed bed reactor model

Besides adsorption capacity, breakthrough behaviour is also very important for the design of NO_x adsorbers. Based on the gas dispersion, the dynamic adsorption has been modeled with the gas phase being assumed as in plug flow [119, 120], continuously stirred tanks in series with each tank perfectly mixed [115, 121], or axial dispersion [122-124].

Olsson et al. [115] considered the HC-SCR monolith reactor as a series of continuously stirred tank reactors. This approach is suitable for models with intricate adsorption kinetics, because only reaction and mass transfer between the gas and solids phase were considered in each tank. Also, the number of tanks could be easily adjusted. In this study where the simple adsorption kinetics is considered, an axial dispersion model is developed to fit the breakthrough curve in the fixed bed reactor. The differential mass balance equations provide the starting point for the development of a mathematical model to describe the dynamic adsorption behavior of the system.

A general approach to model the adsorption in the fixed bed needs to consider the following steps: 1, the external diffusion; 2, the diffusion inside the catalyst pores; 3, the adsorption at the surface of the catalyst. Although rigorous this approach is often over-sophisticated, because it involves too many adjustable parameters. Also the effect of these processes on the shape of the breakthrough curves is almost identical and can't be determined independently from the macroscopic experiments [121]. Thus simplified models are required for application purposes. The simplest and most frequently used model for

the external transport is the film model, introduced by Whitman [125]. Here it is considered that NO_x is adsorbed onto the catalyst surface and the pores of the catalyst after it diffuses through a thin film, with the porous solids being seen as a pseudo-homogeneous medium. All mass transfer resistances are located across the film adjacent to the particle surface as shown in Fig. 4.3. The NO_x concentration in the film is in equilibrium with the NO_x concentration in the gas phase. The same method is applied for O_2 adsorption and hydrocarbon transferring into the solids phase. For hydrocarbon, the concentration in the film is assumed to be the same as in the bulk, because hydrocarbon is only transferred to the solids. Mass transfer constant of the film, k_f , represents both inter-phase and intra-phase mass transfer resistances of the particle. The reaction term is embedded in the solids phase mass balance equation, representing the catalytic surface reaction.

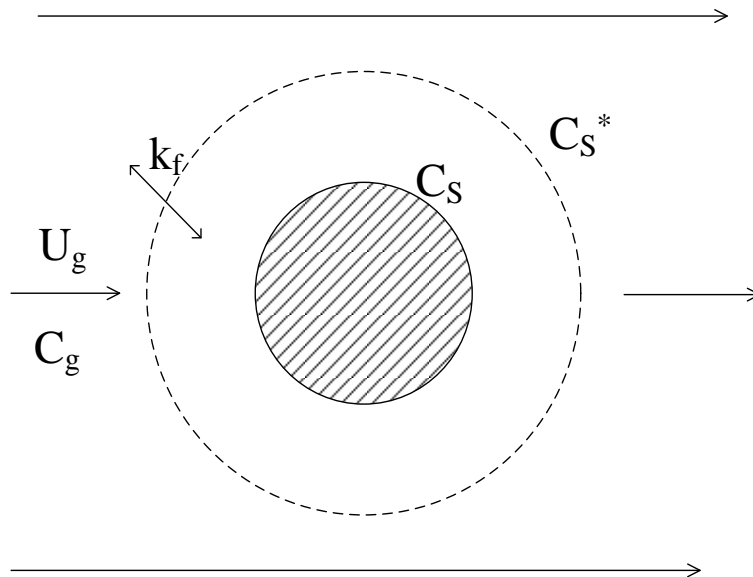


Figure 4.3 Schematics of NO_x adsorption mechanism onto the catalyst surface

General assumptions for the system include:

1. Since the NO_x concentrations were at ppm levels, the exothermic heat of adsorption was negligible and isothermal condition was assumed.

2. The pressure drop through the bed is negligible, and thus the gas velocity is considered constant.
3. Thermal equilibrium exists between the bulk gas phase and the solids surface.
4. All mass transfer resistances are limited to the film around the particle.
5. The radial concentration gradients in the reactor are negligible in both gas and solids phases.

The following governing equations are derived for each species:

$$\text{Solids phase:} \quad \frac{\partial C_s}{\partial t} - D_s \frac{\partial^2 C_s}{\partial z^2} - U_s \cdot \frac{\partial C_s}{\partial z} = -k_f (C_s - C_s^*) + R_i \quad (4.17)$$

$$\text{Gas phase:} \quad \frac{\partial C_g}{\partial t} - D_g \cdot \frac{\partial^2 C_g}{\partial z^2} + U_g \cdot \frac{\partial C_g}{\partial z} = \frac{\epsilon_s}{1 - \epsilon_s} \cdot k_f \cdot (C_s - C_s^*) \quad (4.18)$$

Since in the fixed bed particles are in stationary, the particle velocity and dispersion coefficients are zero. The solids phase equation becomes:

$$\frac{\partial C_s}{\partial t} = -k_f (C_s - C_s^*) + R_i \quad (4.19)$$

Initial and boundary conditions are:

$$z = 0, \quad C_g = C_{g,in}, \quad \frac{\partial C_s}{\partial z} = 0$$

$$z = L, \quad \frac{\partial C_g}{\partial z} = 0, \quad \frac{\partial C_s}{\partial z} = 0$$

$$t = 0, \quad C = C_0$$

where, C_s^* is the equilibrium concentration of the catalyst, determined by the solids phase concentration and the adsorption equilibrium of each species. For the reduction in fixed bed, only steady state is considered.

4.4 Modeling results and discussion

4.4.1 Fitting of adsorption isotherm curves

In order to fit Eq. (4.11) into experimental adsorption capacity, it is assumed that

$$k'_{NO_2} = k_{FO_2} \cdot k_{FNO_2} \quad (4.20)$$

So,

$$q_{eNOx} = k'_{NO_2} \cdot C_{O_2}^{n_{O_2}} \cdot C_{NO}^{n_{NO_2}} \quad (4.21)$$

If O_2 concentration is set to be constant, $k'_{NO_2} \cdot C_{O_2}^{n_{O_2}}$ could be lumped to k''_{NO_2} .

$$k''_{NO_2} = k'_{NO_2} \cdot C_{O_2}^{n_{O_2}} \quad (4.22)$$

And Eq. (4.11) becomes

$$q_{eNOx} = k''_{NO_2} \cdot C_{NO}^{n_{NO_2}} \quad (4.23)$$

So, n_{NO_2} could be obtained by first fitting the data at a constant O_2 concentration by taking natural logarithm (ln) of Eq. (4.23).

$$\ln(q_{eNOx}) = \ln(k''_{NO_2}) + n_{NO_2} \cdot \ln(C_{NO}) \quad (4.24)$$

Then k_{NO_2} was calculated for each data point at different oxygen concentrations.

$$k''_{NO_2} = q_{eNOx} / C_{NO}^{n_{NO_2}} \quad (4.25)$$

k'_{NO_2} and n_{O_2} were then fitted by taking ln of Eq. (4.22).

$$\ln(k''_{NO_2}) = \ln(k'_{NO_2}) + n_{O_2} \cdot \ln(C_{O_2}) \quad (4.26)$$

Finally, k_{FO_2} could be obtained from the O_2 adsorption experiment. The derived isotherm was fitted into the experimental capacities at different inlet NO concentrations and temperatures, as shown in Fig. 4.4. It could be seen that the fitting values, plotted as lines, agree well with experimental data, which are presented as symbols in the figure. The fitted isotherm parameters were given in Table 4.2.

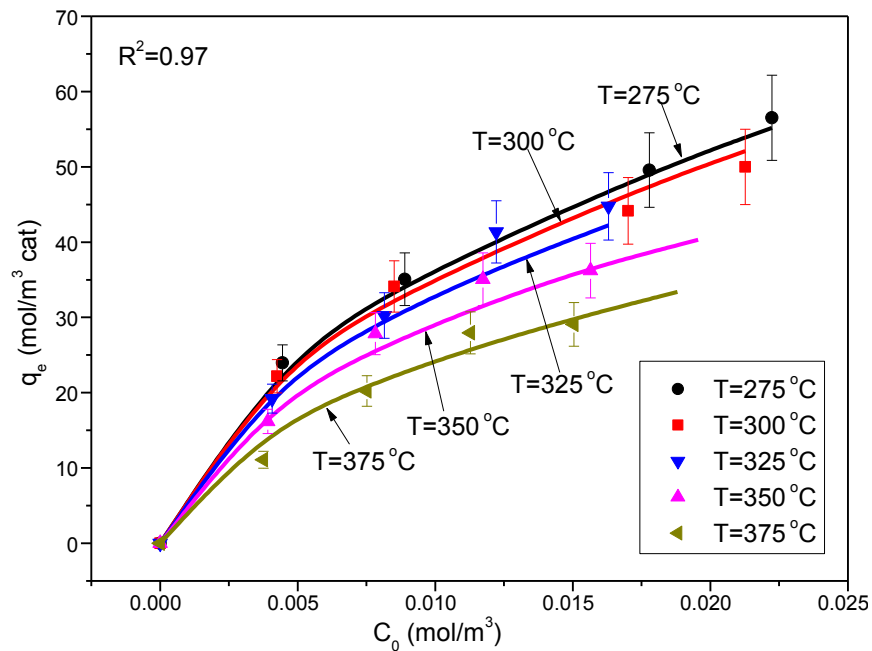


Figure 4.4 Adsorption capacities as a function of the feed concentration at different temperatures (Symbols: experimental data; lines: isotherm model)

Table 4.2 Fitted parameters for adsorption model

O_2 adsorption		NO_2 adsorption	
Parameter	Value	Parameter	Value
n_{O_2}	0.7356	n_{NO_2}	0.5539
k_{O_2}	$-0.0206T + 19.712$	k'_{NO_2}	$-0.0314 \times T^2 + 36.107 \times T - 9876$

4.4.2 Model parameters for the fixed bed adsorption model

Gas mixing coefficient D_g and mass transfer coefficient k_f were obtained by fitting the fixed bed model to the adsorption curve at 325°C with NO=600 ppm. The fitted values for D_g and k_f are $1.2 \times 10^{-4} \text{ m}^2/\text{s}$ and $1.776 \times 10^{-3} \text{ s}^{-1}$, respectively, with the fitted adsorption curve and the experimental data shown in Fig. 4.5.

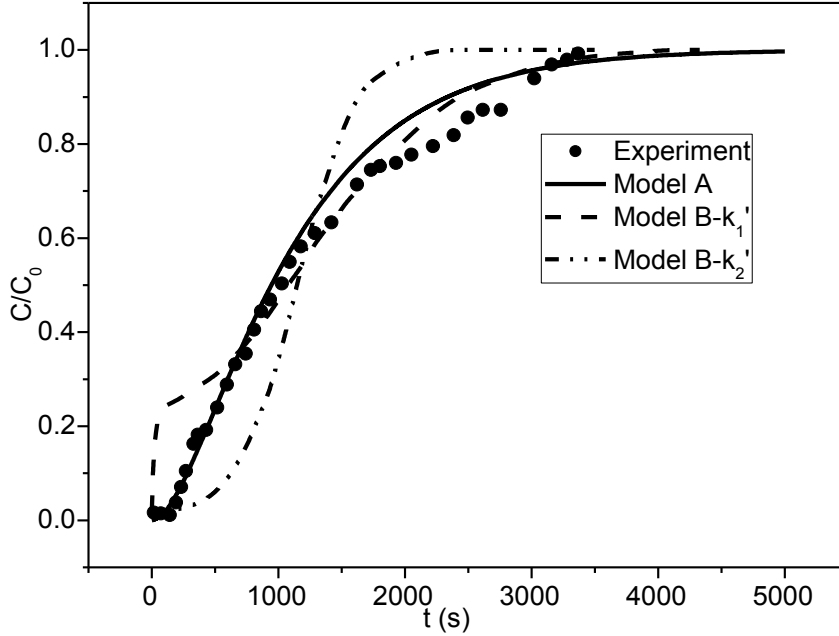


Figure 4.5 Comparison of fitted and experimental adsorption curves in the fixed bed reactor at 325°C with NO=600 ppm

The fitted mass transfer coefficient k_f and gas mixing coefficient D_g are compared with those estimated from correlations in the literature. The Pe number fitted in this model, Pe_f , is calculated as

$$Pe_f = \frac{L \cdot U_g}{D_g} = 20.02 \quad (4.27)$$

The Pe is estimated by the Wen and Fan [126] correlation

$$Pe_c = \frac{17.5}{Re^{0.75}} + 11.4 = 12.14 \quad (4.28)$$

The fitted value is seen to be in reasonable agreement with the literature value.

The classic linear driving force model for mass transfer [127] is

$$\frac{\partial \bar{q}}{\partial t} = k(q^* - \bar{q}) = kK(C_g - C_g^*) \quad (4.29)$$

where q^* is the adsorbate loading in equilibrium with the solute concentration, C_g , in the bulk fluid; C_g^* is the concentration in equilibrium with the average loading \bar{q} ; k is the overall mass transfer coefficient, which includes both external and internal transport resistances; and K is the adsorption equilibrium constant for a linear adsorption isotherm of the form $q=KC_g$.

The factor kK is related to internal and external diffusions by,

$$\frac{1}{kK} = \frac{R_p}{3k_c} + \frac{R_p^2}{15D_e} \quad (4.30)$$

where the second term on the right side represents the internal resistance and the first term represents the external mass transfer resistance. For the estimation of the external mass transfer coefficient k_c in fixed beds, the correlation of [128] could be used:

$$Sh = \frac{k_c d_p}{D_m} = 2.0 + 1.1Sc^{1/3} Re^{1/2} \quad 3 < Re < 10^4 \quad (4.31)$$

For the term $kK(C_g - C_g^*)$ in Eq.(4.25), it is assumed that the adsorption follows a linear isotherm, $q=KC_g$ [127]. However, the adsorption of NO_x on Fe/ZSM-5 follows the Freundlich type isotherm. The model with mass transfer treated as $kK(C_g - C_g^*)$ could not well capture the adsorption characteristics of Fe/ZSM-5. So the mass transfer term was modified to capture the Freundlich type adsorption performance. In our model, the mass transfer term $k_f(C_s - C_s^*)$ is comparable to the term $k(q^* - \bar{q})$ in Eq.

(4.29). Similar modification of the model was also adopted by Dasgupta [123] to enable the Langmuir form of isotherm to be used. But in Dasgupta's model, only intra-phase mass transfer resistance was considered. Since there is no correlation available in the literature for k , Eqs. (4.17) and (4.19) were slightly modified to equations (4.32) and (4.33) in order to evaluate k_f .

$$\frac{\partial C_g}{\partial t} - \frac{D_g}{1-\varepsilon_s} \cdot \frac{\partial^2 C_g}{\partial z^2} + \frac{U_g}{1-\varepsilon_s} \cdot \frac{\partial C_g}{\partial z} = -k'_f (C_g - C_g^*) \quad (4.32)$$

$$\frac{\partial C_s}{\partial t} = k'_f (C_g - C_g^*) \quad (4.33)$$

where C_g^* is the concentration in the gas phase in equilibrium with local solids phase NO_x concentration, which could be calculated by

$$C_g^* = \left[\frac{C_s}{k'_{\text{NO}_2} \cdot C_{\text{O}_2}^{n_{\text{O}_2}}} \right]^{1/n_{\text{NO}_2}} \quad (4.34)$$

Denoting this model as Model B and the model in section 4.3.3 as Model A, it is noted that the difference between these two models is that Model B is based on the gas phase concentration while Model A is based on the solids phase concentration. Following equations (4.30) and (4.31), k_f' ($=kK$) was calculated to be 9.49 s^{-1} with an effective diffusivity D_e of $3.97 \times 10^{-9} \text{ m}^2/\text{s}$.

Model B was then fitted to the same experimental data with the same D_g value as Model A and the best-fit value of k_f' is 3.55 s^{-1} (named as k_1'). The model-fitted results were also plotted in Fig. 4.5. However, Model B did not fit the experiment very well, since it over-estimated the outlet concentration at the beginning when $k_f'=k_1'$. When k_f' was increased to $k_2'=11.84 \text{ s}^{-1}$, the model, as shown in Fig. 4.5, under-estimated the experiment at the beginning and over-estimated outlet concentration at the end. It could thus be concluded that the best fitted value of k_f' is in the range of 3 s^{-1} to 12 s^{-1} , which is

reasonable since the k_f' value estimated from literature correlation is 9.49 s^{-1} as shown above. This result suggests that the fitted value of k_f in Model A is reasonable. Table 4.3 summarizes the Pe number and k_f' at different temperatures obtained from data fitting and correlations. It is seen that both parameters do not vary significantly in the range of the tested temperatures, which are from $275 \text{ }^\circ\text{C}$ to $375 \text{ }^\circ\text{C}$, and can be assumed to be constants in the simulation.

The model and the selected parameters are further evaluated with other experimental data at different temperatures and inlet concentrations. The model prediction and experimental data at different inlet NO concentrations at 325°C are compared in Fig. 4.6(a). It can be concluded that the model can well predict the experiment at different NO concentrations. Fig. 4.6(b) compares model and experiment at different temperatures at inlet NO=400 ppm. Again, the model can well capture the trend that the breakthrough time is longer at a lower temperature, although the modeling curves do not exactly match the experimental data. The experimental curve is not as smooth as the model because of temperature fluctuations ($\pm 2^\circ\text{C}$) during the adsorption experiment. The mass transfer and dispersion coefficients could change with temperature. In this model, however, they were assumed to be independent of temperature. The comparison of the model and experimental data at different temperatures shows that this assumption works reasonable for the NO adsorption process in our research. So it could be concluded that the model could well capture the adsorption process at different conditions. It also confirms that the fitted values of k_f and D_g , which are assumed to be constants and independent of temperature, work well over this tested temperature range.

Table 4.3 Comparison of fitted and estimated mass transfer parameters

T (°C)	Fitted Pe	Pe from correlation	Fitted k_f', s^{-1}	k_f' from correlation, s^{-1}
275	20.02	12.07	3.55	9.49
325	20.02	12.14	3.55	9.91
375	20.02	12.22	3.55	10.32

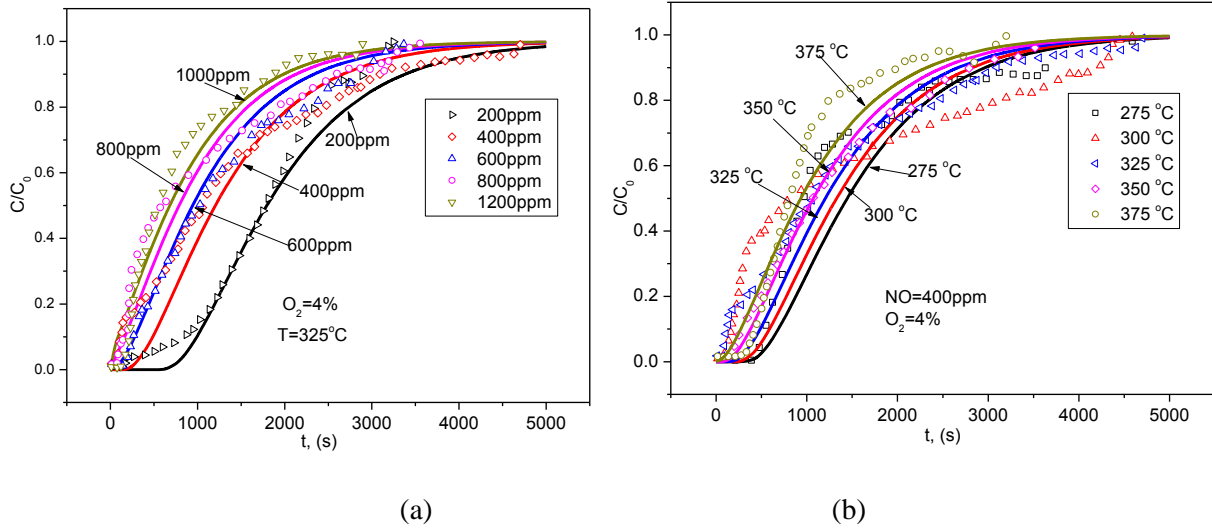


Figure 4.6 Comparison of model fitted and experimental adsorption curves at different (a) NO_x concentrations and (b) temperatures. (Symbols: experimental data; lines: model fitting)

4.4.3 Simulations of NO_x adsorption in fixed bed

The model was used to simulate the NO_x adsorption at other conditions. Fig. 4.7(a) presents the gas phase NO_x concentration along the reactor length. The curves show the concentrations at different time, ranging from 500 s to 3000 s. The NO gas adsorbs onto the catalyst surface along the reactor and the concentration decreases along the reactor. The axial profile of NO_x concentration is almost linear, suggesting that mass transfer between solid and gas phase might be the rate-limiting step in overall NO_x adsorption process. At the early stage of adsorption, $t=300$ s, most of the catalysts are unsaturated and the NO_x was adsorbed onto the surface of the catalyst all along the reactor. As time passes more catalysts are saturated and the gas phase NO concentration increases with time all along the reactor. At $t=3000$ s, most of the catalyst in the reactor is saturated and the NO concentration is close to the inlet concentration even at the outlet of the reactor. Breakthrough time $t_{1/2}$, which represents the time when effluent concentration reaches half of the initial (feed) concentration, was calculated from the simulated adsorption curves. For $t=500$ s, $L_1=26.5$ mm when $C/C_0=0.5$, which means that the minimum catalyst bed length is 26.5 mm in order to achieve a breakthrough time $t_{1/2}=500$ s. Also, if $t_{1/2}=700$ s, the minimum catalyst bed length

increases to $L_2=34$ mm. The required catalyst bed length is larger when longer breakthrough time $t_{1/2}$ is desired.

One advantage of modeling is that the model can simulate the process at the conditions which are not measured in the experiment. Fig. 4.7(b) shows the effluent NO_x concentration as a function of time at different temperatures. For $T=500^\circ\text{C}$, the breakthrough time is reached soon after the start of the adsorption process. When the temperature is lowered, the breakthrough time becomes longer. The breakthrough time increases about 400 s when the temperatures decrease from 300°C to 200°C .

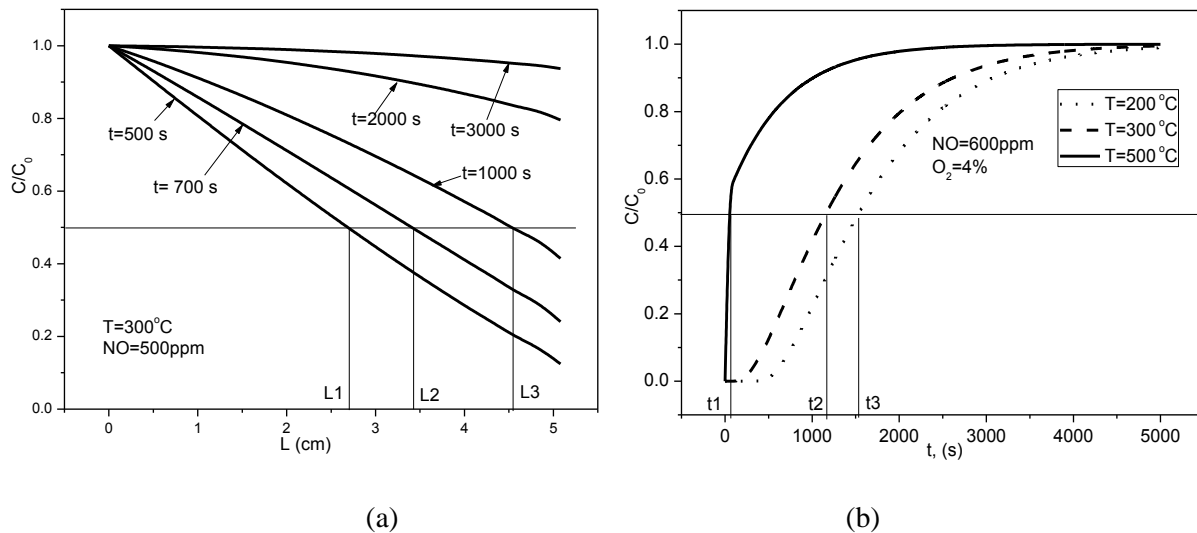


Figure 4.7 (a): gas phase concentration along the reactor length; (b): effluent concentration as a function of time at different temperatures

The adsorption performance was also simulated at different inlet gas velocities. The feed gas velocity is represented by the gas hourly space velocity (GHSV). Fig. 4.8 shows the effluent concentrations as a function of time at different GHSVs. It is quite obvious that the outlet concentration is higher when GHSV is higher, which means that there is a shorter residence time for the gas to be adsorbed onto the catalyst surface, leaving more NO gas escaped. At a lower gas velocity, e.g., $\text{GHSV}=1000\text{ h}^{-1}$, the effluent concentration increases slowly. There is no NO_x shown at the outlet until

after 2700 s. But at $\text{GHSV} > 6000 \text{ h}^{-1}$, NO_x could be detected at the outlet immediately and the concentration increases very fast. Intercepting the curves at $C/C_0=0.5$, breakthrough time $t_{1/2}$ can be obtained at different GHSV. From Fig. 4.8, for $\text{GHSV}=2000, 3000, 4000, 5000$ and $6000, 7000 \text{ h}^{-1}$, the corresponding $t_{1/2}$ s are 3000, 2000, 1500, 1200, 950 and 750 s, respectively. Breakthrough time decreases very fast at higher GHSV. There is nearly a linear relationship between $1/\text{GHSV}$ and breakthrough time, with the deviation most likely related to the gas axial dispersion.

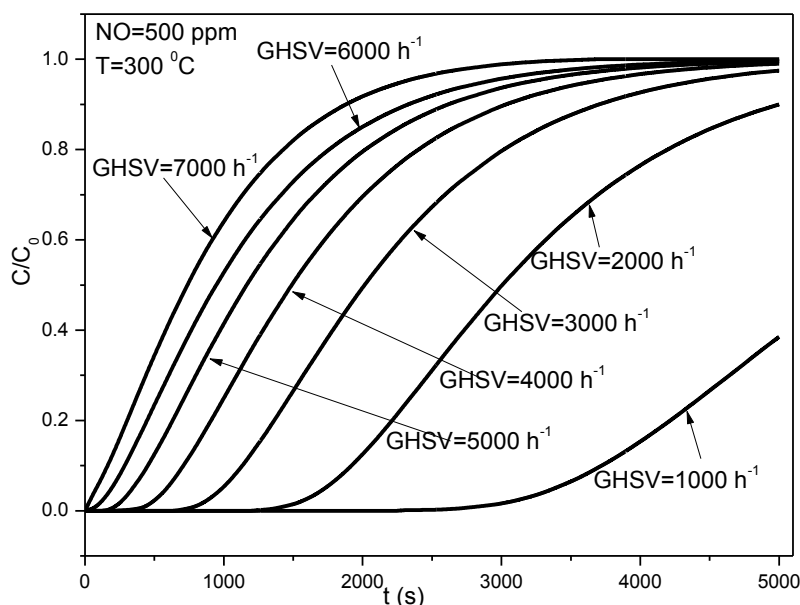


Figure 4.8 Effluent NO_x concentration as a function of time at different GHSV

4.4.4 de NO_x reaction kinetics for Fe/ZSM-5 catalyst

To develop the de NO_x reaction, the same gas mixing coefficient D_g and mass transfer coefficient k_f were used as the ones obtained by fitting the adsorption model to fixed bed adsorption breakthrough curves. It should be noted that k_f was fitted from fixed bed NO_x adsorption breakthrough curves at inlet $\text{O}_2=4\%$, $\text{NO}=600 \text{ ppm}$. However, values of k_f are dependent on the adsorption capacity of each reactant. Here the fitted k_f value is denoted as k_{f0} . k_f will be adjusted in the model for different reactants and different

reaction condition by Eq. (4.35) using adsorption equilibrium constant K , in which i denotes different reactants and 0 represents the reaction condition at the fitting condition. Detailed discussion of k_f is shown in Appendix C.

$$k_f = k_{f0} K_{i0} / K_i \quad (4.35)$$

deNO_x reaction kinetic model was coded into Matlab and fitted with experimental data. The best-fitting parameters were found by using the function of ‘fminsearch’ (unconstrained nonlinear optimization) in Matlab and shown in Table 4.4.

Table 4.4 Fitted kinetic model parameters (T=350 °C)

Sub-model	Model and Parameter	Fitted experiment (fixed bed)
Adsorption	$0.5[O^*] = qe_{O_2} = 6.88C_{O_2}^{0.736}$	O ₂ adsorption
	$[NO_2^*] = qe_{NO_x} = 350C_{O_2}^{0.736}C_{NO}^{0.505}$	NO _x adsorption
Reduction	$r_3 = 2.5C_{HC}^{0.8}[O^*]^{0.7}$	NO _x reduction
	$r_4 = 0.0155[NO_2^*]^{0.012}C_{HC}^{0.1}[O^*]^0$	NO _x reduction

Figs. 4.9(a) and (b) present the NO_x and HC conversion at different O₂ and hydrocarbon concentrations, with the symbols representing the experimental data and lines for the modeled values. Experimental data at O₂=0.5%, 4%, and 8% were used for the fitting of kinetic parameters and data at O₂=1% and 2% were used for verification. The model shows a good fitting to the experiment for most of the data points with an average error of about 7% for NO_x conversion and about 5% for HC conversion. But poor agreement was observed for HC conversion at inlet HC:NO=4. It is interpreted to be due to the catalyst deactivation at higher HC concentrations since unreacted HC tends to deposit on the catalyst surface. At a given O₂ concentration, NO_x conversion is seen to increase with increasing the inlet hydrocarbon concentration or inlet HC to NO_x molar ratio. NO_x reduction increased as O₂ increased from

0.5 to 1%, but then decreased with further increase in O_2 concentration. This is because that small amount of O_2 is required to oxidize NO to NO_2 , but higher O_2 concentration in the flue gas leads to the hydrocarbon oxidation, leaving less HC reductant for NO_x reduction and thus decreasing the NO_x conversion. The i-CFB is designed to solve this negative effect of excess O_2 in the flue gas.

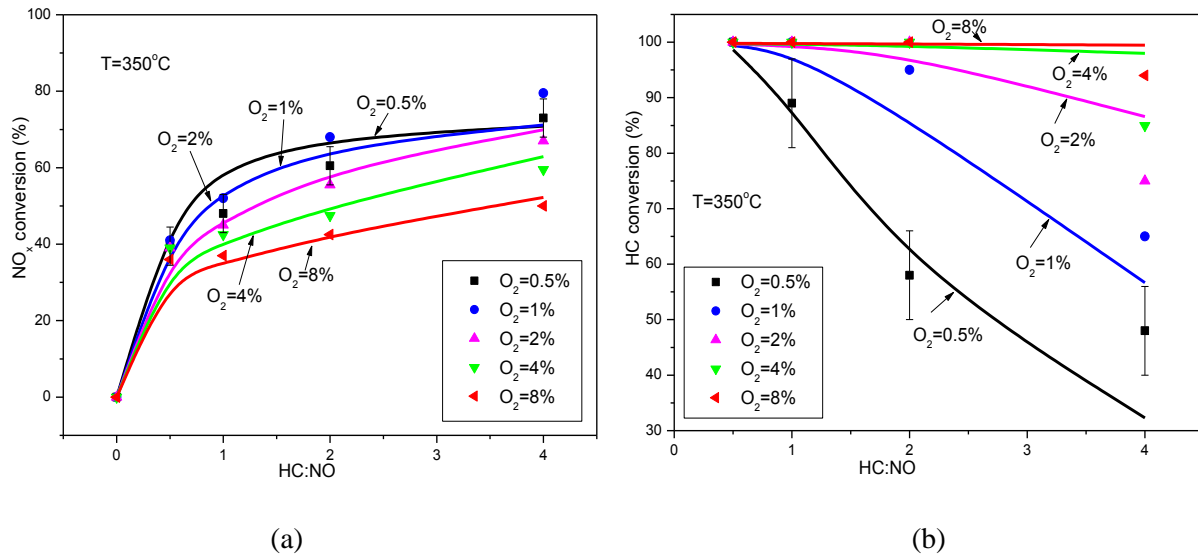


Figure 4.9 Modeled and simulated conversions at different HC:NO ratios in fixed bed, (a), NO_x conversion; (b), HC conversion. (Symbols: experimental data; lines: model fitting)

4.5 Summary

A simplified de NO_x reaction kinetic model was proposed, consisting of an adsorption sub-model and a reduction sub-model. To develop the adsorption model, the kinetics of NO oxidation and adsorption was considered, following the Freundlich type isotherm. The isotherm parameters were then obtained by fitting equations to the adsorption capacities experimental data obtained from a fixed bed unit. The de NO_x reaction kinetics includes NO_x reduction and hydrocarbon oxidation. Kinetic parameters were successfully extracted by fitting the model equations to NO_x reduction experimental data.

In applying the model to a fixed bed reactor, mass transfer between solids and gas phase was also considered in the governing equations. The mass transfer and axial dispersion coefficients are fitted from

the measured NO_x breakthrough curve. The reaction term was embedded into the solids phase mass balance equation. The model could be further extended for the modeling of deNO_x reactions in fluidized bed reactors.

Chapter 5 Modeling NO_x adsorption in fluidized bed reactors⁴

5.1 Introduction

NO_x adsorption kinetics was derived from experimental data obtained in a fixed bed reactor in Chapter 4. However, NO_x adsorption takes place in the fluidized bed in an i-CFB reactor, which behaves quite differently from the fixed bed reactor. There is thus a need to investigate the NO_x adsorption characteristics in fluidized beds in order to develop a reactor model for the novel i-CFB reactor.

In this chapter, NO_x adsorption is first tested experimentally in a fluidized bed reactor using Fe/ZSM-5 catalyst, prepared by the same method as described in Chapter 1. One should note that minor difference in the preparation procedure could lead to significant variation of the catalyst performance. In Chapter 4, the adsorption isotherm was developed for the catalyst prepared by Yang [11], which showed some difference in the adsorption performance from the catalyst prepared in this study. To keep consistency, adsorption characteristics is also investigated in the fixed bed to develop new adsorption isotherms for this newly prepared catalyst.

A number of fluidized bed models have been reported in the literature [129, 130]. Water vapor adsorption was modeled and simulated in a fluidized bed reactor for thermo-chemical energy conversion by Darkwa [131]. The gas phase moisture concentration was investigated. Voidage in the column was assumed to be constant without consideration of the presence of gas bubbles. A simple model derived from mass balance was used by Hamed [132] for the adsorption and desorption of water vapor in a fluidized bed loaded with silica gel particles. The voidage in the bed was assumed to be constant and the

⁴ A version of this chapter has been published: Xingxing Cheng and Xiaotao T. Bi, (2013), Modeling and simulation of nitrogen oxides adsorption in fluidized bed reactors, Chemical Engineering Science, 96: 42-54.

adsorbent in the reactor was treated as a CSTR, with outlet gas phase concentrations being investigated for the designing purpose. Axial dispersion models were also developed to investigate both liquid and solids phase concentrations [133, 134]. In all of these models, bubbles, which are quite important for the mass transfer, were not considered. On the other hand, the two phase model, consisting of bubble phase and dense phase, was used widely for the modeling of chemical reactions in fluidized beds [20, 28]. Few studies have examined the solids phase concentration of adsorbed gases in fluidized bed catalytic reactors. To our knowledge, there has been no model developed specifically for NO_x adsorption in fluidized bed reactors.

In this study, NO_x concentration profiles in both gas phase and solids phase are investigated, since solids saturated with NO_x in the adsorption zone would be circulated to the reduction zone for catalytic reduction in the i-CFB reactor. Bubbles are also an important factor in determining the mass transfer rate from the bubble phase to the dense phase. Different from other adsorption models in the literature, the current model considers the existence of adsorbing gas in three phases: solids phase with adsorbed species, gas in the bubble phase and gas in the dense phase. NO_x adsorption isotherms were obtained from a fixed bed reactor for Fe/ZSM-5 catalyst, and then used in the fluidized bed adsorption model to assess and evaluate the NO_x adsorption performance in a fluidized bed reactor using the same catalyst.

5.2 Experiment

The adsorption characteristics of Fe/ZSM-5, prepared by the method described in [11], is investigated in both fixed and fluidized bed (hot model unit) reactors. The configuration of the fixed bed reactor has already been given in detail in Chapter 4 and will not be repeated here. The details of the experiments are given in Appendix D. Other experimental conditions are summarized in Table 5.1.

Table 5.1 Experimental conditions of NO_x adsorption

	Fixed bed experiment	Fluidized bed experiment
Temperature, °C	250, 300, 350	250, 300, 350
NO inlet concentration, ppm	200, 400, 600, 800, 1000	300, 600, 900
Gas velocity, m/s	0.07	0.04, 0.06, 0.08

5.3 Fluidized bed adsorption model

5.3.1 Adsorption isotherm

The Freundlich equation, which was found to give a good fit to our experimental data, is also used to model the adsorption isotherm of NO_x on Fe/ZSM-5.

$$q_e = k_F \cdot C_0^{n_{NO_x}} \quad (5.1)$$

5.3.2 Governing equations for fluidized bed

A bubbling fluidized bed consists of two phases, bubble phase and dense phase. The mass transfer of NO_x not only takes place between the bubble phase and dense phase, but also between gas and particles in the dense phase, as shown in Fig. 5.1(a). Three phases were thus considered in the current study, particles in the dense phase, gas in the dense phase and the bubble phase. It is assumed that there are no solids particles in the bubble phase and adsorption takes place only in particles of the dense phase.

The gas film model was used to describe the mass transfer between particles and the gas in the dense phase, which assumes that a film in equilibrium exists at the surface of the particles as shown in Fig. 5.1(b). Here it is considered that NO_x is first adsorbed onto the external surface of the catalyst particle and then diffuses into the catalyst, with the porous particles being treated as a pseudo-

homogeneous medium. Mass transfer constant of the film, k_f , represents both inter-phase and intra-phase mass transfer resistances of the particle.

Other general assumptions for the modeled system include:

1. The pressure drop throughout the bed is negligible, and thus the gas velocity is considered constant.
2. Thermal equilibrium exists between the bulk gas phase and the solids surface.
3. All mass transfer resistances are limited to the film around the particle.
4. The concentration gradients are negligible in both gas and solids phases.

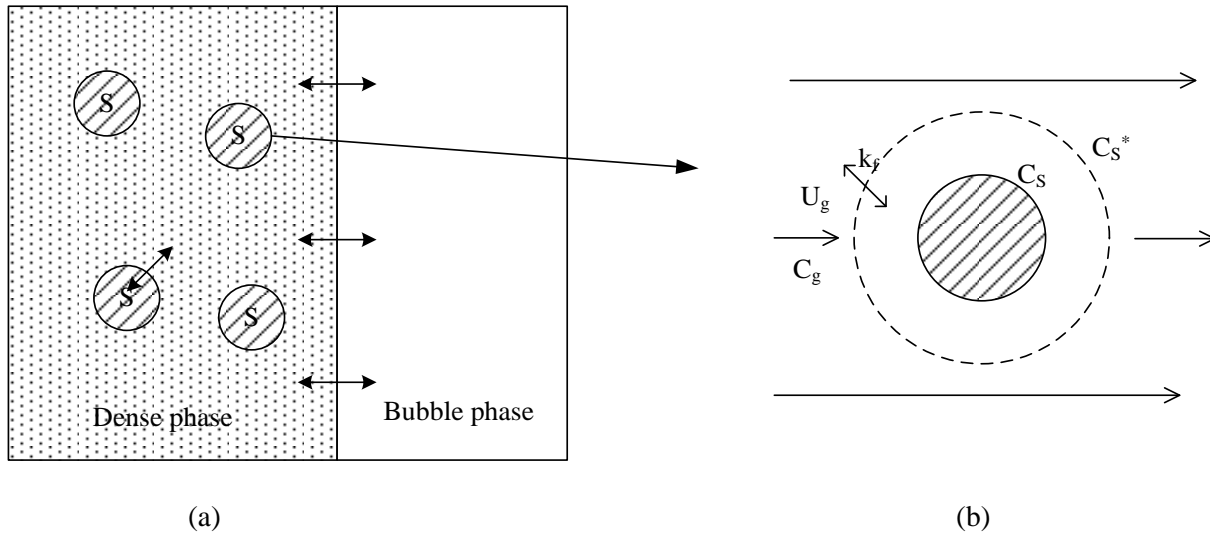


Figure 5.1 Schematic of mass transfer (a) in the fluidized bed and (b) around particles

Differential mass balance equations for an element of the adsorption column provide the starting point for the development of a mathematical model to describe the dynamic adsorption behavior of the system. Governing equations are:

$$D_s \varepsilon_s \frac{\partial^2 C_s}{\partial z^2} \pm U_s \varepsilon_s \frac{\partial C_s}{\partial z} - \frac{\varepsilon_s}{1 - \varepsilon_s} k_f \cdot (C_s - C_s^*) = \varepsilon_s \frac{\partial C_s}{\partial t} \quad (5.2)$$

for particles in the dense phase,

$$D_H \Phi_H (1 - \varepsilon_s) \frac{\partial^2 C_H}{\partial z^2} - U_H \Phi_H (1 - \varepsilon_s) \frac{\partial C_H}{\partial z} + k_f \cdot (C_s - C_s^*) + k_{HL} a_b (C_L - C_H) = \Phi_H (1 - \varepsilon_s) \frac{\partial C_H}{\partial t}$$

(5.3)

for the dense phase, and

$$D_L \Phi_L \frac{\partial^2 C_L}{\partial z^2} - U_L \Phi_L \frac{\partial C_L}{\partial z} - k_{HL} a_b (C_L - C_H) = \Phi_L \frac{\partial C_L}{\partial t} \quad (5.4)$$

for the bubble phase.

Initial and boundary conditions are:

$$z = 0, \quad C_H = C_{g,in}, \quad \frac{\partial C_s}{\partial z} = 0, \quad C_L = C_{g,in}$$

$$z = H, \quad \frac{\partial C_H}{\partial z} = 0, \quad \frac{\partial C_s}{\partial z} = 0, \quad \frac{\partial C_L}{\partial z} = 0$$

$$t = 0, \quad C_H = 0, \quad C_s = 0, \quad C_L = 0$$

where C_H , C_L and C_s^* are the NO_x gas concentrations in the dense phase, the bubble phase, and the equilibrium concentration in the dense phase, respectively, with the same unit, mole/m³ gas. C_s is the average concentration in the particles per unit catalyst volume with a unit of mole/m³ cat. C_s^* could be calculated from the adsorption isotherm fitted from fixed bed experiments. Φ_H and Φ_L are the fractions of dense phase and bubble phase, respectively, with Φ_L equal to bubble fraction ε_b and $\Phi_H = 1 - \Phi_L$. Parameter a_b is the specific dense-bubble phases contacting surface area, defined as

$$a_b = \frac{6\varepsilon_b}{d_b} \quad (5.5)$$

5.3.3 Hydrodynamics

The total voidage consists of two parts, voidage in the dense phase and the bubble fraction. The voidage in the dense phase is assumed to equal the voidage at minimum fluidization, ε_{mf} , and the gas velocity is assumed to remain at the minimum fluidization velocity u_{mf} . The estimation of other parameters, such as bed height and bubble velocity, are calculated in the same way as shown in Chapter 3.

5.3.4 Mass transfer

Interphase mass transfer coefficient is estimated by Sit and Grace's equation [135] for three-dimensional freely bubbling beds:

$$k_{HL} = \frac{U_{mf}}{3} + 2 \left[\frac{D_m \cdot \varepsilon_{mf} \cdot U_b}{\pi \cdot D_b} \right]^{0.5} \quad (5.6)$$

Intra-phase mass transfer coefficient between the solids phase and gas phase k_f consists of external mass transfer and internal mass transfer and was correlated to be Eqs. (4.29) to (4.31) as shown in Chapter 4.

In fitting the models to the experimental breakthrough curves, interphase mass transfer coefficient k_{HL} was estimated from the correlation shown above, while intra-phase mass transfer coefficient k_f was fitted by the experimental data and checked against the literature.

5.3.5 Gas and solids mixing

For axial solids dispersion in bubbling beds, there are several correlations in the literature [136, 137]. The correlation of Morooka [138] was selected in this study due to its similar experimental settings, with $U_g \geq 0.02$ m/s, $D=32 \sim 195$ mm, $H_{bed}=1 \sim 3$ m with FCC particles as the bed material, $d_p=80$ μ m.

$$Pe_s = \frac{U_g \cdot D}{D_s} = 19 \cdot (D + 0.23) \cdot \frac{U_g}{\sqrt{g \cdot D}} \left[1 + 6.5 \cdot \left(\frac{U_g}{\sqrt{g \cdot D}} \right)^{0.8} \right] \quad (5.7)$$

There are several correlations in the literature for gas dispersion, either vertical or radial, in fluidized beds [27]. However, the dispersion coefficients correlated in the literature are the overall

dispersion, different from D_L and D_H in Eqs. (5.3) and (5.4) for dense and dilute phases, separately. Therefore, the literature correlations are not directly applied in the model.

Dispersion in the bubble phase was assumed to be 0, $D_L=0$, according to the two-phase model of [20]. Gas mixing coefficient in the dense phase D_H was obtained by fitting the adsorption breakthrough curves at different gas velocities and temperatures. Since gas dispersion in the dense phase is caused mainly by the movement of solids, D_H is expected to be similar to the solids dispersion coefficient D_s . This assumption was also confirmed by the study of [28], who measured both the solids dispersion and dense phase gas dispersion and found the values were similar. However, no correlation was reported by Abba [28] due to the scarcity of data points. So the fitted D_H from the current study was compared with D_s calculated from Eq. (5.7).

5.4 Experimental results

5.4.1 Fixed bed

Adsorption breakthrough performances on Fe/ZSM-5 were tested at different temperatures and inlet NO_x concentrations. A series of adsorption breakthrough curves were obtained, as shown in Appendix D, and used to calculate the adsorption capacities.

The calculated adsorption capacities are plotted in Fig. 5.2 and fitted to the Freundlich isotherm equation, giving:

$$qe = (0.01345 \times T^2 - 17.19 \times T + 5551) \cdot C_0^{0.4786} \quad R^2 = 0.989 \quad (5.8)$$

This equation will later be used in the simulation of fluidized bed adsorption.

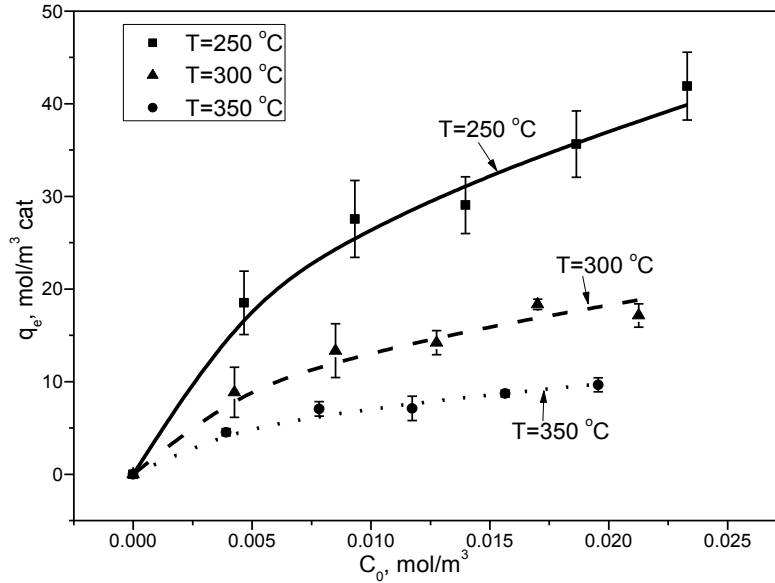


Figure 5.2 Adsorption capacity at different feed NO_x concentrations. (Symbols: experimental data; lines: fitted isotherm model)

5.4.2 Fluidized bed

Some typical breakthrough curves at different inlet NO_x concentration and gas velocities are presented in Fig. 5.3, with more results given in Appendix D. Unlike the breakthrough curves in the fixed bed where an initial period with almost zero NO_x concentration exists, there is no time delay in the fluidized bed breakthrough curves. This is caused by the gas bypassing from the bubble phase and will be further discussed in the modeling section. Although fluctuations also exist and the curves are not very smooth, it is quite clear that the slopes are bigger at higher inlet NO_x concentrations, which is consistent with the fixed bed adsorption results. The outlet NO_x concentration also increases slower at lower superficial gas velocities, as shown in Fig. 5.3(b), due to longer contacting time with the catalyst.

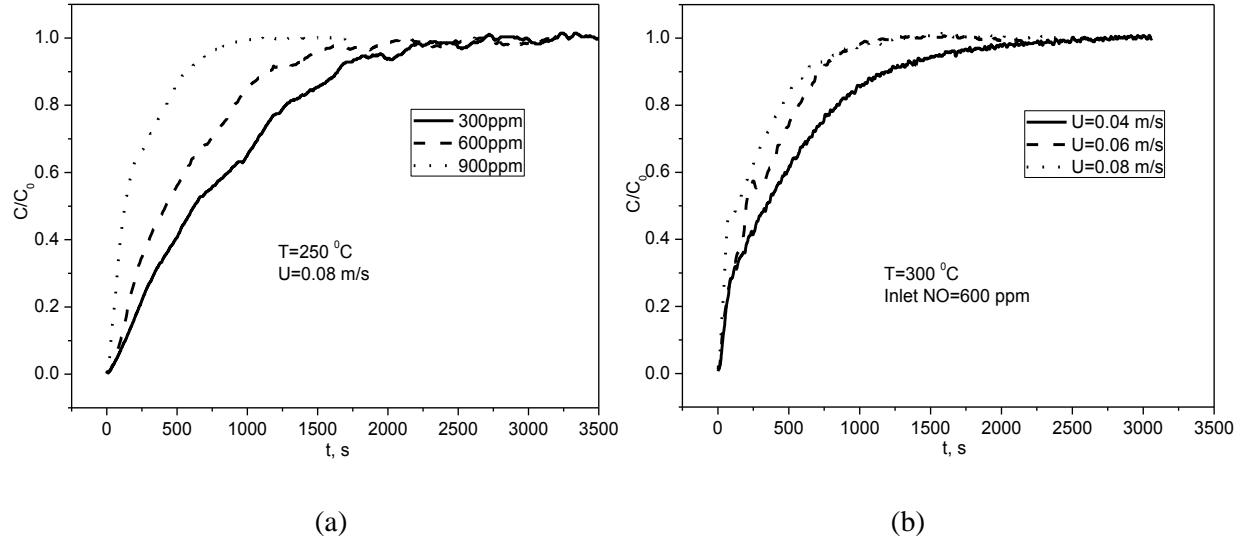


Figure 5.3 Breakthrough curves at (a) different NO_x inlet concentrations at 250 °C; and (b) different gas velocities at 300 °C

5.5 Modeling results

5.5.1 Parameter fitting

The model was coded into MATLAB with the partial differential equations differentiated with Crank-Nicolson method. The fluidized bed model was first fitted to the measured adsorption breakthrough curves of the fluidized bed with both gas dispersion coefficient in the gas phase, D_H , and gas-particle mass transfer coefficient, k_f , as the fitting parameters. The outlet gas concentration was calculated from both the predicted dense phase and bubble phase gas concentrations as:

$$C_{out} = \frac{\Phi_H U_H C_H + \Phi_L U_L C_L}{\Phi_H U_H + \Phi_L U_L} \quad (5.9)$$

The best-fitted parameters at different temperatures and superficial gas velocities are shown in Table 5.2, and Fig. 5.4 shows a good agreement between measured and fitted adsorption breakthrough curves.

The fitted parameters were further compared to the values from literature data and correlations. The k_f values calculated from literature correlations were also shown in Table 5.2. It should be noted that the literature correlation is based on the linear driving force model for mass transfer as indicated by Eq. (4.29) in Chapter 4. The k_f' from correlation and shown in Table 5.2 is equivalent to kK in Eq. (4.29). However, the fitted k_f value in this study is based on the equivalent term of $k(q^* - \bar{q})$ according to the mass balance equation, Eq. (5.2). To make the fitted value comparable with that estimated from the correlation, further treatment is required. In Table 5.2, fitted k_f values are multiplied by K , the adsorption equilibrium constant for a linear adsorption isotherm in the form of $q = Kc$, with each K being calculated for the given specific condition. It can be seen from the table that the values of the fitted k_f' are in the same order as the values estimated from correlations, implying that the fitted values are quite reasonable. The difference between these values could be caused by the inaccurate calculation of NO_x diffusivity. Only diffusivity of NO was considered in the calculation. But in fact, NO_2 , from the oxidation of NO , is also very important for the NO_x adsorption. This factor was not considered for the calculation of literature value, leading to the inaccuracy of the calculation. Different adsorption isotherm could also contributor to the variation between literature and fitted values.

The estimated values of the first and second terms of Eq. (4.30), which represent the external and internal mass transfer respectively, are also shown in Table 5.2. The internal mass transfer resistance is seen to be much higher than the external one, suggesting that the internal mass transfer is the rate-limiting step.

Both fitted and calculated k_f' values show a similar trend, increasing with increasing reactor temperature, likely associated with the increased gas diffusivity at higher temperatures. However, fitted k_f' increases with increasing the gas velocity while calculated k_f' remains at a constant. It is anticipated that the external mass transfer rate will increase with increasing the gas velocity but its contribution to the overall intra-phase mass transfer coefficient is almost negligible.

The fitted Pe_H values are very close to the literature values of Pe_s calculated from Eq. (5.7), confirming that solids dispersion is well correlated with gas dispersion in the dense phase. Fitted Pe_H decreases with increasing temperature while Pe_s from correlation remains at a constant at different temperatures. It is noticed [138] that the correlation was developed based on data obtained at constant temperatures without temperature effect being considered. In lack of reliable correlations, the fitted values will be used in the simulation of adsorption in the fluidized bed reactors in this study. The sensitivities of the model to these parameters are shown in Appendix D.

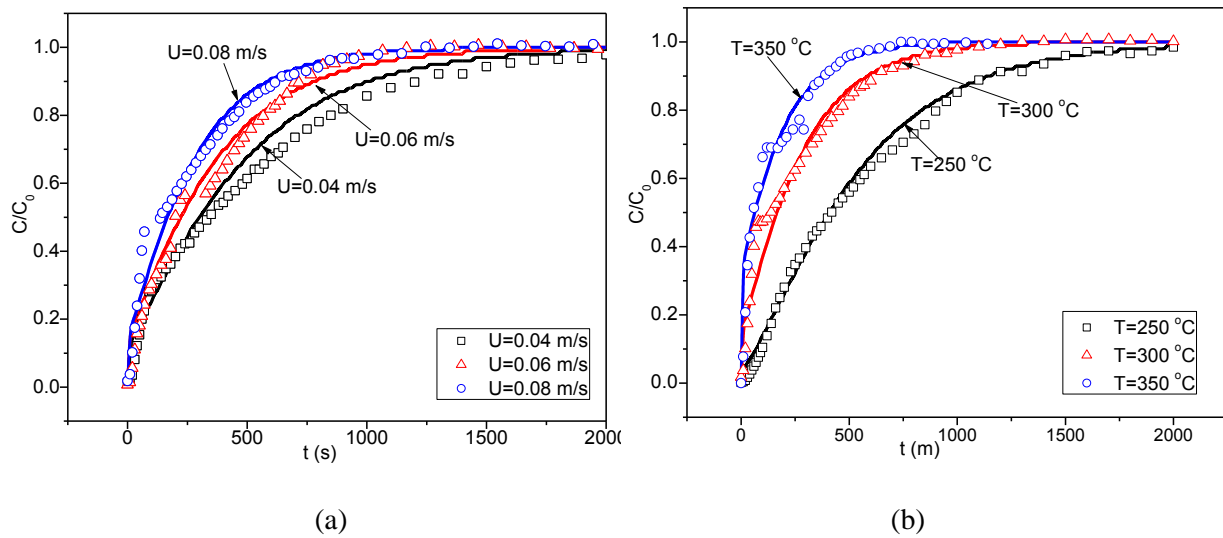


Figure 5.4 Comparison of model-fitted and experimental breakthrough curves at different (a) velocities and (b) temperatures (Symbols: experimental data; lines: model fitting)

Table 5.2 Parameters used in the fluidized bed adsorption model

T, (°C)	300	300	300	250	300	350
Gas velocity, (m/s)	0.04	0.06	0.08	0.08	0.08	0.08
D_H, fitted, (m²/s)	0.0107	0.0133	0.0173	0.013	0.0173	0.019
Pe_H, fitted	0.4037	0.4872	0.4994	0.6646	0.4997	0.4547
Pe_s, literature	0.3704	0.6252	0.9201	0.9201	0.9201	0.9201
k_f fitted, (s⁻¹)	0.0019	0.0023	0.0031	0.0021	0.0031	0.0036
K, (linear)	1112.7	1112.7	1112.7	1954.5	1112.7	605.9
k_f'= k_f*K, (s⁻¹)	2.11	2.56	3.45	4.1	3.45	2.18
k_f' literature, (s⁻¹)	9.70	9.70	9.70	9.27	9.70	10.12
R_p/(3k_c) (×10⁵), (s)	2.65	2.56	2.49	2.89	2.49	2.17
R_p²/(15D_e), (s)	0.103	0.103	0.103	0.108	0.103	0.0988

The current model was evaluated using the breakthrough curves that were not used for the parameter fitting. As shown in Fig. 5.5, the model-predicted adsorption curves could well represent the experimental adsorption performance at different temperatures and inlet gas conditions, indicating that the current model could be used for the simulation of bubbling fluidized bed adsorption. The sensitive analysis of the model is shown in Appendix E.

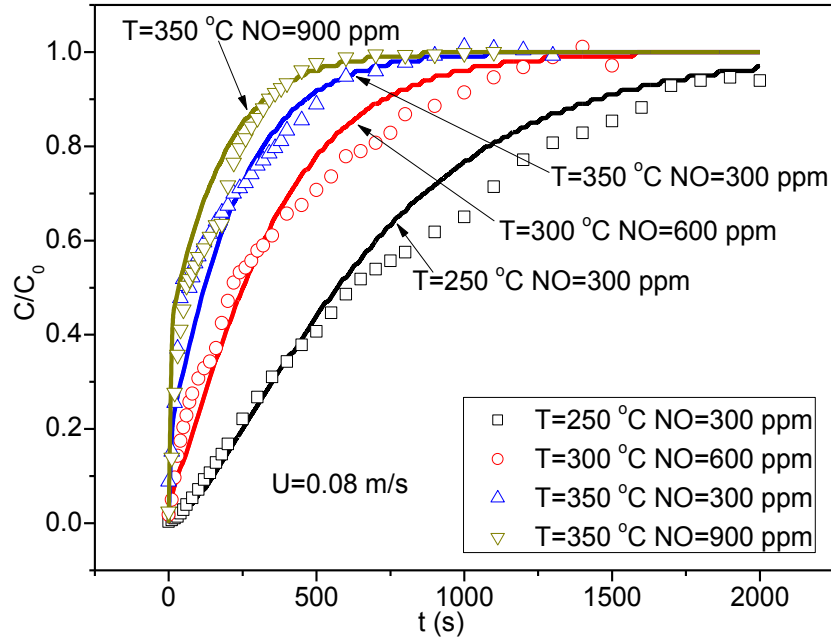


Figure 5.5 Model evaluation at different temperatures (Symbols: experimental data; lines: model fitting)

5.5.2 Simulation of fluidized bed NO_x adsorption

To further examine the adsorption performance of fluidized beds, the current adsorption model is applied to study those parameters not measured in the experiment. The outlet NO_x concentrations of the three phases are plotted as a function of time in Fig. 5.6(a) for a typical adsorption condition with T=300 °C, U=0.08 m/s and 4% inlet oxygen concentration. The concentrations are normalized by the corresponding saturation values in each phase. It is seen that the concentration in the solids phase increases steadily from 0 at the start of adsorption. The concentrations in the dense phase and bubble phase are generally higher than zero because of the gas bypass from the bubble phase. Due to high interphase mass transfer between the bubble phase and the dense phase, the difference in the gas phase NO_x concentration between the dense phase and the bubble phase is quite small. Comparing with interphase mass transfer, the mass transfer between the particles and gas in the dense phase is much smaller and rate limiting, reflected by the large difference between the solids phase NO_x concentration curve and the other two curves. As time

passes, NO_x concentration on the particle surface builds up gradually. The three curves converge after about 300 s, indicating the approach to saturation.

Fig. 5.6(b) shows the axial concentration profiles under the same operating conditions at $t=170$ s which corresponds to the breakthrough time, $t_{1/2}$, when effluent concentration reaches half of the initial (feed) concentration. It is seen again that the dense phase and bubble phase NO_x gas concentrations are very close to each other due to the fast interphase mass transfer, but they are quite different from the solids phase concentration. The concentration difference between the particles and gas in the dense phase decreases along the reactor height due to the transfer of NO_x from the gas to the particles. It should also be noted that the NO_x concentration in the particles is almost constant along the reactor, indicating strong solids mixing in the fluidized bed.

Solids mixing is not desirable for gas-solids reactions in a fluidized bed reactor, since too much back-mixing could lower the reaction rate. The effect of solids mixing on the adsorption performance was further examined by treating solids as plug flow (PFR) as in a moving or fixed bed, where the axial dispersion of particles is neglected. The simulated results were shown in Fig. 5.6(b) as dash lines. Comparing with the normal fluidized bed with strong solids mixing, NO_x concentration in solids phase decreases along the bed height in plug flow reactors. The gas phase NO_x concentration also confirms that less solids mixing could give a better NO_x capture efficiency, as reflected by the low outlet NO_x concentration.

The i-CFB de NO_x reactor is expected to perform better if the solids back-mixing is reduced because of the higher de NO_x capture efficiency and higher NO_x concentration on solids at the bottom of the adsorption zone which will be circulated to the reduction zone to be reduced by hydrocarbon reductant. A higher adsorbed NO_x concentration on catalyst surfaces passed to the reduction zone will likely improve the NO_x reduction and thus the overall performance of the whole i-CFB reactor. To reduce solids back-

mixing in the i-CFB reactor, one can consider the use of internals/baffles or division of the adsorption zone into multiple stages.

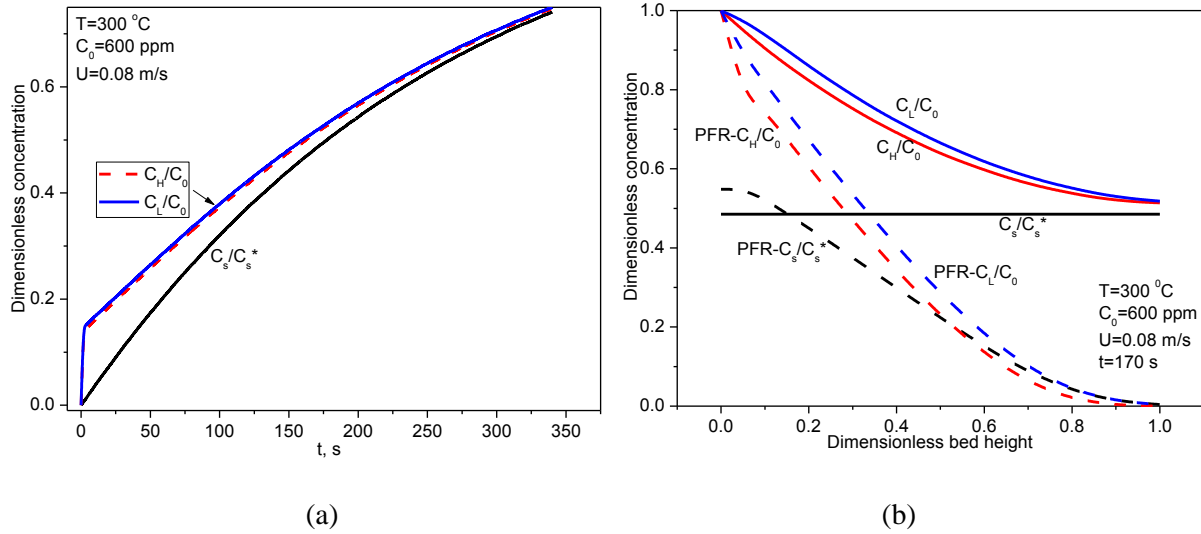


Figure 5.6 (a) Outlet NO_x concentrations in different phases as a function of time; (b), dimensionless NO_x concentration as a function of dimensionless bed height, ($t=170$ s)

The performance of fluidized bed deNO_x reactors can also be improved by the use of small particles. Since the rate-limiting step is the mass transfer between the solids phase and the gas phase (which lumps external and internal mass transfer), not between the dense phase and the bubble phase, effort should be made to improve the mass transfer coefficient or to increase the gas-solids contact area.

As revealed in the previous section, internal mass transfer is the rate-limiting step. So it can be

approximated that $\frac{1}{k_f} \approx \frac{R_p^2}{15D_e}$. Decreasing the particle size is expected to increase the mass transfer

coefficient k_f . On the other hand, smaller particles can also increase the gas-solids contact area. Simulated curves of outlet NO_x concentrations for different particle sizes are shown in Fig. 5.7.

It is seen that there is a clear difference between the solids phase NO_x concentrations for different particle sizes. When d_p decreases by 20%, solids phase NO_x concentration increased by 12% at 170 s, greatly enhancing the adsorption performance. Correspondingly, the outlet gas phase NO_x concentration

decreases with decreasing d_p , leading to improved total NO_x abatement efficiency. The maximum NO_x capture efficiency at the start of the adsorption, which mostly corresponds to the continuous adsorption process in the i-CFB reactor with fresh catalyst, increases from 85.6% to 91.7% and 96.5% when d_p decreases to 0.8 and 0.9 times of the original size, respectively. What can be learned from this analysis is that small particles should be used in i-CFB reactors so that there are large particle surface areas for adsorption. However, one should also note that too small a particle size may create other operational problems, such as stickiness of particles, in the fluidized bed reactor.

It should be noted in the figure that the dimensionless C_s sometimes exceeds corresponding C_g . At a local point, this should not occur because NO_x cannot be transferred from the gas phase to the solids phase beyond the equilibrium. However, the results presented here are averaged values over the whole reactor. The saturation concentration given by Eq. (5.1) is not linear to the gas phase concentration. So the driving force is not linear to the gas concentration. However, all the concentrations are normalized by the feed concentration. Therefore, the higher value of dimensionless C_s than C_g is possible and does not necessarily reflect the reversal in local mass transfer.

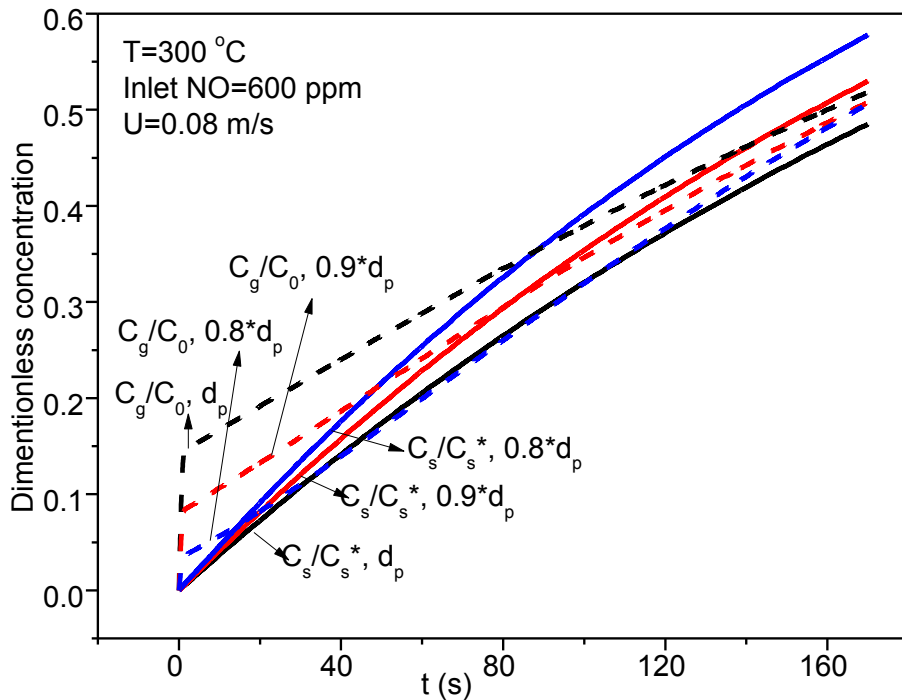


Figure 5.7 Influence of particle size on outlet NO_x concentrations

In the reactor design, gas flow rate is a very important operating parameter. So the influence of superficial gas velocity on the fluidized bed reactor NO_x adsorption is investigated by simulation with the results plotted in Fig. 5.8. Since k_f was fitted at different velocities previously, it was correlated to gas velocity U_g by Eq. (5.10). Pe_s correlation from the literature, Eq. (5.7), was used for the calculation of D_H . For the current column diameter and particles, Eq. (5.7) is corrected by the fitted Pe_s data to Eq. (5.11). It should be noted that this correlation is only applicable to the current fluidized bed reactor and the current catalyst particles.

$$k_f = 0.03 \times U_g + 0.0006 \quad R^2 = 0.964 \quad (5.10)$$

$$Pe_H = (-13.678 \times U_g + 1.6247) \times Pe_{s,literature} \quad R^2 = 0.994 \quad (5.11)$$

Fig. 5.8 illustrates that the outlet solids phase NO_x concentration increases with increasing the superficial gas velocity, because more NO_x is supplied to the reactor. However, due to the shortened contact time, the outlet gas NO_x concentration also increases, lowering the total NO_x abatement efficiency. Therefore, low gas velocity is desirable to achieve higher NO_x capture efficiency for a given reactor catalyst loading or height.

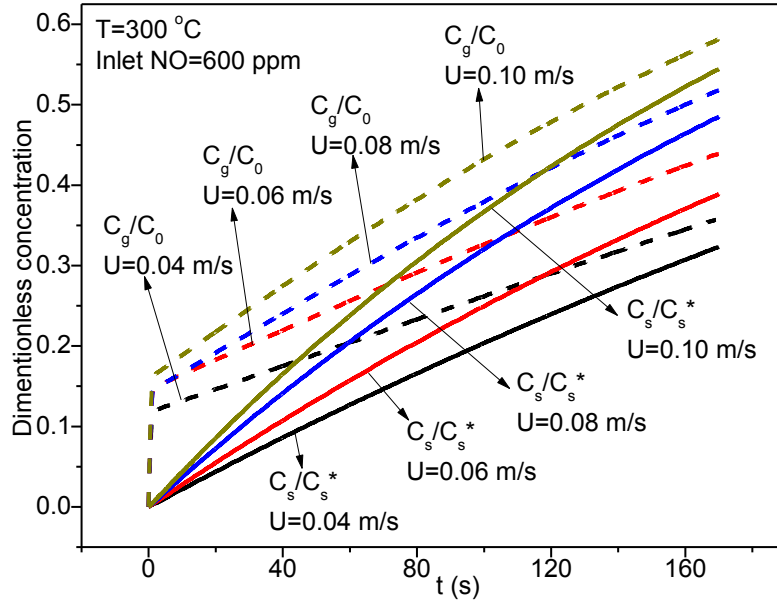


Figure 5.8 Influence of superficial gas velocity on outlet NO_x concentration

5.5.3 Simulation of adsorption zone in an i-CFB deNO_x reactor

As an important element in the i-CFB reactor, the adsorption in fluidized bed was modeled as part of a continuously operated adsorption column decoupled from the i-CFB. As shown in Fig. 5.9, different from the batch operated fluidized bed in which solids stay in the bed all the time, solids are fed to the adsorption reactor from the top and discharged from the bottom into the reduction reactor with NO_x being reduced there by reduction agent.

Two more parameters should be considered in modeling the decoupled i-CFB, solids circulation rate, G_s , and NO_x concentration on the fed solids surfaces, $C_{s,feeding}$. The solids circulation rate, G_s , represents how effectively the adsorption zone can be replaced by refreshed solids. In most cases, NO_x is not completely reduced and the NO_x concentration remaining on the solids surface leaving the reduction zone is not zero, depending on the design and operation of the reactor. This concentration will correspond

to the NO_x concentration in the feeding solids into the adsorption zone, $C_{s,feeding}$. The reduction efficiency in the reduction zone can be expressed as

$$E_r = 1 - \frac{C_{s,feeding}}{C_s^*} \quad (5.12)$$

where C_s^* is the saturated solids phase concentration at $C_{g,in}$.

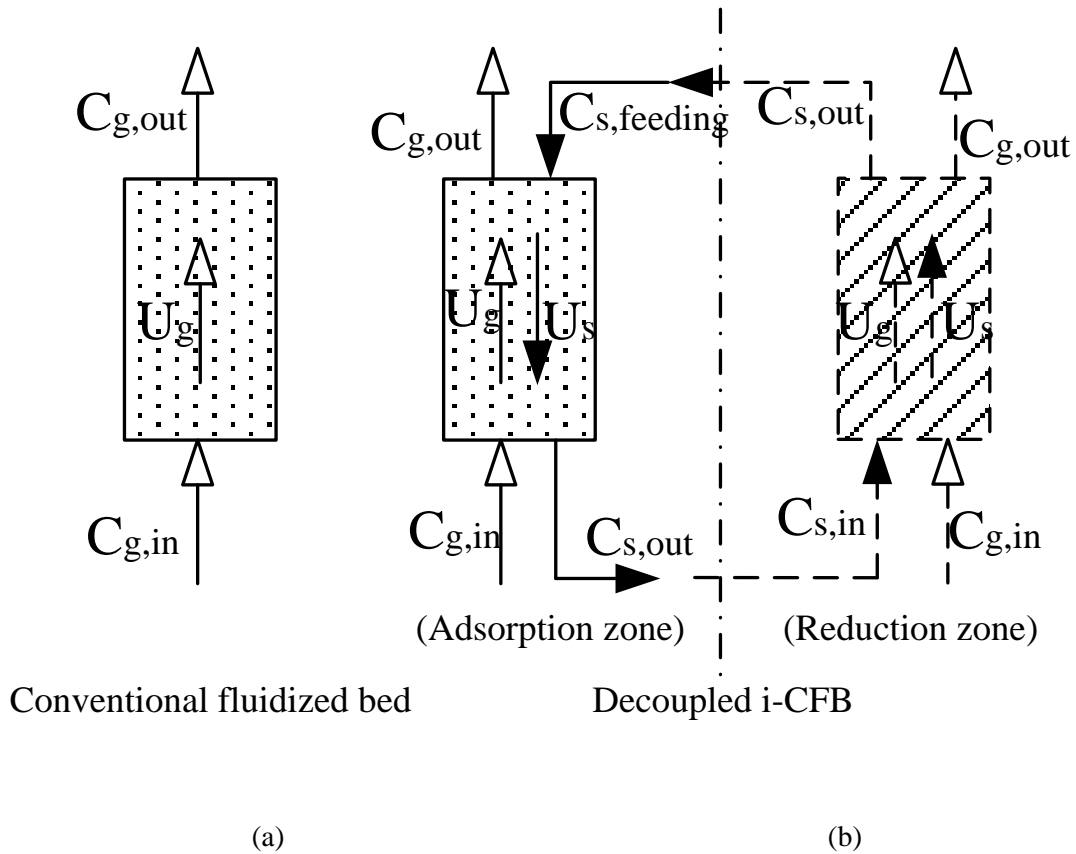


Figure 5.9 Gas and solids flow in (a) conventional fluidized bed and (b) continuous fluidized bed decoupled from the i-CFB reactor

The governing equations are still Eqs. (5.2) to (5.4) but the initial and boundary conditions become:

$$z = 0, \quad C_H = C_{gin}, \quad \frac{\partial C_s}{\partial z} = 0, \quad C_L = C_{gin}$$

$$z = H, \quad \frac{\partial C_H}{\partial z} = 0, \quad C_s = C_{s,feeding}, \quad \frac{\partial C_L}{\partial z} = 0$$

$$t = 0, \quad C_H = 0, \quad C_s = 0, \quad C_L = 0$$

Different from the dynamic breakthrough curve of the conventional fluidized bed, only the final steady state was investigated for i-CFB unit. The final stable concentration of the outlet NO_x, denoted as C_g here, also determines the overall deNO_x efficiency of i-CFB, E, by

$$E = 1 - \frac{C_g}{C_0} \quad (5.13)$$

The adsorption performance of the continuous adsorption reactor representing the decoupled adsorption zone of the i-CFB reactor was then simulated at different solids flow rate, gas velocity, C_{s,feeding} and catalyst loading M. It should be noted that the catalyst loading M represents the weight of the catalyst in the adsorption reactor, different from the total catalyst loading of the i-CFB system.

Solids circulation rate was taken as a dimensionless value.

$$G_s^* = \frac{G_s}{G_{s,0}} \quad (5.14)$$

Here, G_{s,0} is the minimum solids circulation rate calculated from

$$\frac{V_g}{V_s} = \frac{C_{s,out}^* - C_{s,feeding}}{C_{g,in} - C_{g,out}^*} \quad (5.15)$$

Where C_{s,out}^{*} and C_{g,out}^{*} are in equilibrium with C_{g,in} and C_{s,feeding}, respectively. V_s and V_g are the volume flow rate of gas and solids, respectively. G_{s,0} could then be calculated from V_s.

$$G_{s,0} = V_s \rho_s / A \quad (5.16)$$

The effect of solids circulated rate G_s on the NO_x capture efficiency was investigated and the outlet concentrations of both the solids phase and gas phase were plotted in Fig. 5.10. The feeding NO_x concentration in the solids phase was set to be 20% of the saturated concentration, which corresponds to an 80% NO_x reduction efficiency in the reduction zone of an i-CFB reactor.

It could be anticipated that both solids and gas phases will be saturated if there is no refreshed solids feeding to the reactor. So the values of both C_s/C_s^* and C_g/C_0^* are equal to 1 at $G_s=0$. If the solids are refreshed effectively enough, the adsorption bed could be filled with regenerated catalysts, with the solids phase NO_x concentration equal to the feeding NO_x concentration. With the current setting, the lowest value of C_s/C_s^* is found to be 0.2. The simulated results of C_s/C_s^* agree well with what are expected, with all the curves start from 1 at $G_s=0$ and then decrease to 0.2 when G_s increases. Similar trends are also observed for the gas phase NO_x concentration, which also starts at 1 and then stabilizes at a fixed value when G_s is high enough. But the lowest gas phase concentration is different for different values of C_s/C_s^* since it is determined by many factors such as mass transfer and contacting time.

It is noted that slopes of all the curves are very sharp when G_s is very small, usually between 0 and 2 $\text{kg/m}^2\cdot\text{s}$. After that, further increase of G_s has little effect on both solids and gas phase concentrations. The reactor is almost filled with refreshed catalysts since C_s/C_s^* values are very close to 0.2. So, for the current fluidized bed, the catalysts could be effectively refreshed when G_s is higher than 2 $\text{kg/m}^2\cdot\text{s}$. Further increasing G_s could not improve the NO_x capture efficiency substantially. In order to increase the overall NO_x abatement efficiency, other methods should be explored, such as changing the bed solids loading to increase the contacting time or NO_x reduction efficiency in the reduction zone to lower the NO_x concentration on the particles fed to the adsorption zone.

Fig. 5.10 also illustrates how the bed loading affects the solids and gas phase NO_x concentrations. Although the solids concentration curves at different bed loading are very similar, it can still be seen that the solids phase NO_x concentration is slightly higher at higher solids loadings. At a fixed G_s , there is a

larger fraction of newly refreshed solids in the adsorption zone when there is a lower solids holdup in the bed, leading to a lower overall solids phase NO_x concentration.

Contacting time between the gas and solids phases is critical for NO_x adsorption. Comparing with the solids phase NO_x concentration, gas phase NO_x concentration is more influenced by the bed loading. At a higher bed loading, the outlet gas phase NO_x concentration is much lower due to longer contacting time between the gas and solids phases. It is also found that C_g/C_0^* decreases significantly when bed loading increases from 0.5 kg to 1 kg. But further increasing the bed loading from 2 kg to 4 kg does not give such a significant improvement. The lowest value of gas phase NO_x concentration is determined by the equilibrium to the solids phase NO_x concentration. Therefore, a higher NO_x capture efficiency could be achieved by improving the reduction zone efficiency and lowering feeding solids phase NO_x concentration.

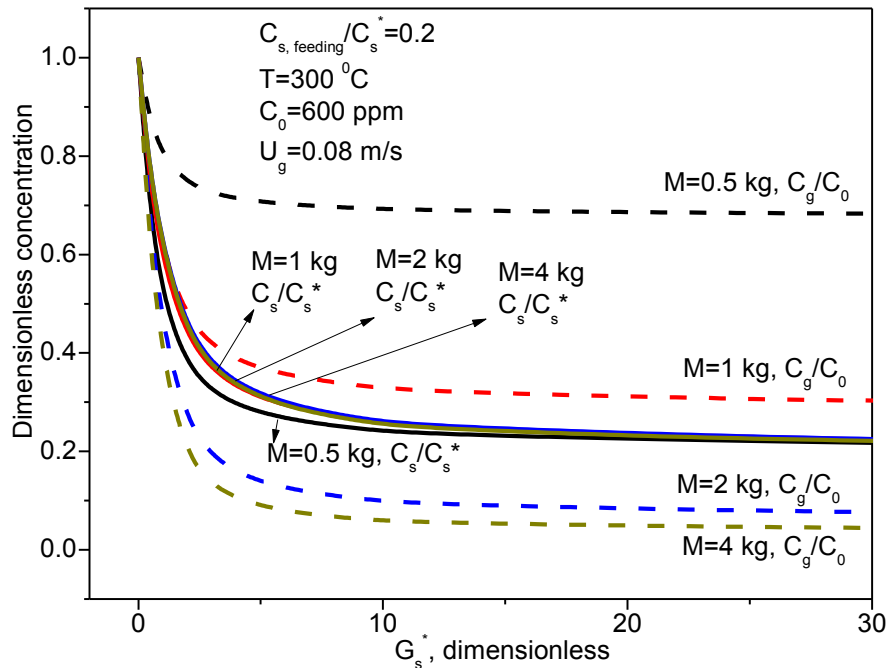


Figure 5.10 NO_x adsorption performance as a function of G_s^*

The effect of $C_{s,feeding}$ on the NO_x capture efficiency was investigated with the results plotted in Fig. 5.11. Here the X-axis is a dimensionless parameter, $C_{s,feed}/C_s^*$, where C_s^* is the corresponding saturation concentration of inlet NO_x concentration C_0 . And Y-axis is the dimensionless C_g/C_0 . It can be seen that the outlet gas NO_x concentration increases with increasing feed solids phase NO_x concentration, since less NO_x can be adsorbed onto the catalyst surface. So a good performance of the NO_x reduction zone in an i-CFB is very important to keep $C_{s,feed}$ at a low level.

Catalyst loading M also has a significant effect on the NO_x adsorption as can be seen in the figure. The NO_x adsorption performance is significantly improved at higher catalyst loadings. At $C_s/C_s^*=0.4$, the NO_x abatement efficiency can be increased from 20% to 60% when M increases from 0.5 kg to 1 kg. Further increasing M from 1 kg to 2 kg could still improve the NO_x capture efficiency. So for an i-CFB reactor, it is very important to keep sufficient catalyst in the adsorption zone to ensure the full abatement of NO_x from the gas stream.

In order to evaluate the NO_x adsorption performance, parameter C_g^* is introduced, with its definition given in Eq. (5.17). It can be considered as the limit of NO_x abatement at a given $C_{s,feed}$. Coefficient k_F is the equilibrium constant in Eq. (5.1).

$$C_g^* = (C_s / k_F)^{1/n_{NO_x}} \quad (5.17)$$

Dimensionless C_g^*/C_0 is also plotted in Fig. 5.10. It can be seen that the curve at $M=2$ kg is very close to the curve of C_g^*/C_0 , which is the limit of the NO_x capture efficiency. Thus it is not surprising that further increasing M to 4 kg has little effect on improving the NO_x abatement as shown in Fig. 5.10.

In fact, a key parameter affecting the amount of catalyst staying in the adsorption zone is the overall solids circulation rate in the i-CFB. The solids feed rate is determined by the gas velocities in both the adsorption zone and the reduction zone. However, the influence of U_g could not be fully investigated here because the hydrodynamics of an i-CFB reactor was not included in the current continuous adsorption

model. Further modeling is required to couple the hydrodynamics of i-CFB with the NO_x adsorption and reduction kinetics.

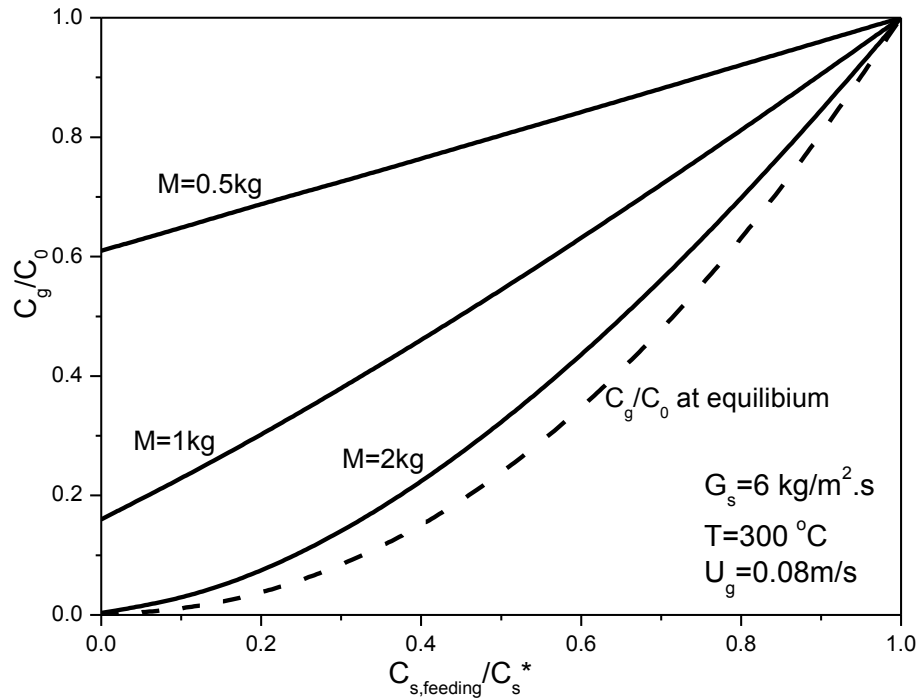


Figure 5.11 NO_x adsorption performance as a function of $C_{s,feed}/C_s^*$

5.6 Summary

A two-phase adsorption model was proposed for the NO_x adsorption in a fluidized bed reactor. The model parameters were obtained by fitting the experimental breakthrough curves. With the fitted mass transfer and gas dispersion coefficients, the model agrees well with the experimental results. Further simulation of NO_x adsorption performance suggested that small size particles and low gas velocity should be used to improve the fluidized bed performance. Simulation of the adsorption zone in a decoupled i-CFB showed that the NO_x concentration on the surface of feed catalysts could affect the NO_x abatement efficiency. At the same time, it is essential to maintain a large amount of catalyst in the adsorption zone to achieve a

high deNO_x efficiency. Since hydrodynamics of i-CFB was not included in the current model, the influence of solids feed rate and superficial gas velocity could not be fully investigated.

Chapter 6 Modeling NO_x reduction in fluidized bed reactors⁵

6.1 Introduction

In Chapter 5, NO_x adsorption in a fluidized bed reactor was modeled and simulation was conducted on the performance of adsorption zone of the i-CFB reactor. NO_x reduction zone, which is also an important part of the i-CFB reactor, is modeled in this Chapter based on the reaction kinetics developed in Chapter 4 and the fluidized bed adsorption kinetics developed in Chapter 5. The fluidized bed model is further applied to simulate NO_x reduction in the reduction zone of the i-CFB reactor.

6.2 Fluidized bed reactor model

6.2.1 Model governing equations

Similar to the fluidized bed adsorption model developed in Chapter 5, the fluidized bed reactor model consists of two phases, bubble phase and dense phase. Different from fixed beds, mass transfer of NO_x, HC and O₂ in the fluidized bed not only exists between the bubble phase and dense phase, but also between the gas phase and particle phase, as shown in Fig. 5.1. It is assumed that there are no solid particles in the bubble phase. Adsorption and reaction take places only on the particles of the dense phase.

Model governing equations for the different phases are:

$$D_s \varepsilon_s \frac{\partial^2 C_s}{\partial z^2} \pm U_s \varepsilon_s \frac{\partial C_s}{\partial z} - \frac{\varepsilon_s}{1 - \varepsilon_s} k_f \cdot (C_s - C_s^*) + R_i = \varepsilon_s \frac{\partial C_s}{\partial t} \quad (6.1)$$

for particles in the dense phase.

⁵ A version of this chapter will be submitted for publication: Xingxing Cheng and Xiaotao T. Bi, Modeling catalytic reduction of NO_x in the reaction zone of an i-CFB reactor.

$$D_H \Phi_H (1 - \varepsilon_s) \frac{\partial^2 C_H}{\partial z^2} - U_H \Phi_H (1 - \varepsilon_s) \frac{\partial C_H}{\partial z} + k_f \cdot (C_s - C_s^*) + k_{HL} a_b (C_L - C_H) = \Phi_H (1 - \varepsilon_s) \frac{\partial C_H}{\partial t} \quad (6.2)$$

for the dense phase, and

$$D_L \Phi_L \frac{\partial^2 C_L}{\partial z^2} - U_L \Phi_L \frac{\partial C_L}{\partial z} - k_{HL} a_b (C_L - C_H) = \Phi_L \frac{\partial C_L}{\partial t} \quad (6.3)$$

for the bubble phase.

Initial and boundary conditions are:

$$z = 0, \quad C_H = C_{g,in}, \quad \frac{\partial C_s}{\partial z} = 0, \quad C_L = C_{g,in} \quad (6.4)$$

$$z = H, \quad \frac{\partial C_H}{\partial z} = 0, \quad \frac{\partial C_s}{\partial z} = 0, \quad \frac{\partial C_L}{\partial z} = 0 \quad (6.5)$$

$$t = 0, \quad C_H = 0, \quad C_s = 0, \quad C_L = 0 \quad (6.6)$$

Freeboard is also included in the model. The gas in the freeboard region is considered to be in plug flow with dispersed solid particles and no bubbles in the freeboard region. Two phases are considered in the model: gas phase and solids phase, with the reaction term embedded in the solids phase. The governing equations are:

$$\frac{\partial C_s}{\partial t} - D_s \frac{\partial^2 C_s}{\partial z^2} - U_s \cdot \frac{\partial C_s}{\partial z} = -k_f (C_s - C_s^*) + R_i \quad (6.7)$$

for solids phase, and

$$\frac{\partial C_g}{\partial t} - D_g \cdot \frac{\partial^2 C_g}{\partial z^2} + U_g \cdot \frac{\partial C_g}{\partial z} = \frac{\varepsilon_s}{1 - \varepsilon_s} \cdot k_f \cdot (C_s - C_s^*) \quad (6.8)$$

for gas phase.

The inlet concentrations are obtained from the outlet concentrations of the dense fluidized bed region. Solid fraction in the freeboard is calculated by Chen and Wen's freeboard model [139], which incorporates elutriation and entrainment rates to calculate the solids hold up and solid velocity profiles in the freeboard region of a fluidized bed.

For the reduction in fluidized bed, only steady state is considered, which is assumed to be reached until $\frac{\partial C}{\partial t} < 1 \times 10^{-6}$, the same as used in the fixed bed model.

6.2.2 Model parameters

The hydrodynamic parameters, dispersion coefficients and interphase mass transfer coefficient k_{HL} , are obtained in the same way as in Chapter 5. The intraphase mass transfer coefficient k_f is determined by the properties of the catalyst. The catalyst used in the fluidized bed reaction experiment was prepared by Yang [11], which was also used for the kinetics development in Chapter 4. So the same k_f value as used in Chapter 4 is used.

6.3 Fluidized bed modeling results

6.3.1 Model verification

The model is coded in MATLAB and the differential equations are solved with a Crank-Nicolson method. The outlet concentration of the fluidized bed is calculated by Eq. (5.9). Fluidized bed reaction data, from Yang's research [11], are used to evaluate the fluidized bed reaction model. Fig. 6.1(a) presents the modeled and experimental NO_x conversions as a function of superficial gas velocity at different inlet O_2 concentrations and HC:NO ratios. It could be seen that the model could well capture the effect of inlet O_2 and HC concentration. Experimental data show that increasing HC:NO ratio has a positive effect on NO_x conversion, while increasing O_2 concentration has a negative impact on the NO_x conversion. This observation is consistent with the modeling data. At $\text{O}_2=1\%$, NO_x conversion in the fluidized bed is

predicted to increase from about 52% to 62% when HC:NO ratio increases from 1 to 2. As a comparison, NO_x conversion at O₂=1% in the fixed bed, as shown in Fig. 4.9(a), increases from 50% to 60% when HC:NO ratio increases from 1 to 2. Therefore, it could be concluded that HC shows similar effect on NO_x conversion in both the fluidized bed and fixed bed.

For O₂ effect, the model could well predict NO_x concentration at lower inlet O₂ concentration with an average error of about 4% at O₂=1%. But when inlet O₂ concentration is higher, the model tends to overestimate the NO_x conversion, especially at lower U_g. The reason may be that catalysts used in the fixed bed and fluidized bed reaction were prepared separately and slight difference in the preparation could lead to some variation in the reaction kinetics. In modeling the fluidized bed, kinetics, which was developed from the fixed bed catalyst, may lead to the under-prediction of negative O₂ effect. To further verify this assumption, experiment NO_x conversions between the fluidized bed and fixed bed were compared at HC:NO=2. In the fluidized bed experiment, NO_x conversion decreases from about 62% to 20% when O₂ concentration is increased from 1% to 8%. However, in the fixed bed experiment, as shown in Fig. 4.9(a), NO_x conversion decreases from about 60% to 40% when O₂ concentration is increased from 1% to 8%. Although the data could not be directly compared due to different catalyst loading and gas velocity, the trend clearly shows that O₂ concentration imposed a more serious negative effect in the fluidized bed than in the fixed bed, which may be attributed to the difference of the catalysts.

In terms of gas velocity, NO_x conversion is not affected noticeably by superficial gas velocity for most data points, illustrated by experimental data. This is explained by better mass-solid transfer at higher U_g. However, the modeling results couldn't well capture this trend. NO_x conversion of the modeling results clearly decreases with U_g. But overall, the modeled NO_x conversion is not very sensitive to gas superficial velocity. The differences between the experiment and modeling could be caused by the variation of reactor temperature in the fluidized bed, which fluctuated between 340°C and 360°C during the experiment.

Comparing to NO_x conversion, the model shows a very poor agreement on HC conversion, as shown in Fig. 6.1(b). Most of the measured HC conversion data ranges from 30% to 60%, while corresponding modeling data range from 65% to 100%. The difference between the experimental data and modeling results could be caused partly by experimental errors. The HC conversion was estimated based on measured CO and CO_2 concentrations by assuming that all converted HC goes to CO/ CO_2 , ignoring other possible reaction intermediates. However, in our experiment some unidentified byproducts were detected by gas chromatography, which was believed to be HCN or cyanogens [140]. This will likely cause the underestimation of HC conversion. On the other hand, the reaction kinetics fitted from fixed bed data, as shown in Fig. 4.9(b), tends to overpredict fixed bed HC conversion data. This over-prediction is then likely carried over to the fluidized bed, contributing to the overprediction of HC conversion in the fluidized bed. Although the model overpredicts the experimental data significantly, it captures the right trends of the effect of O_2 , HC:NO ratio on HC conversion. HC conversion is predicted to decrease with HC:NO ratio and increase with O_2 concentration. However, the experimental HC conversion decreases with U_g , while modeled conversion increases with U_g . The contradictory trends could also be attributed to experiment error. But overall speaking, both experimental and modeling curves are not very sensitive to U_g .

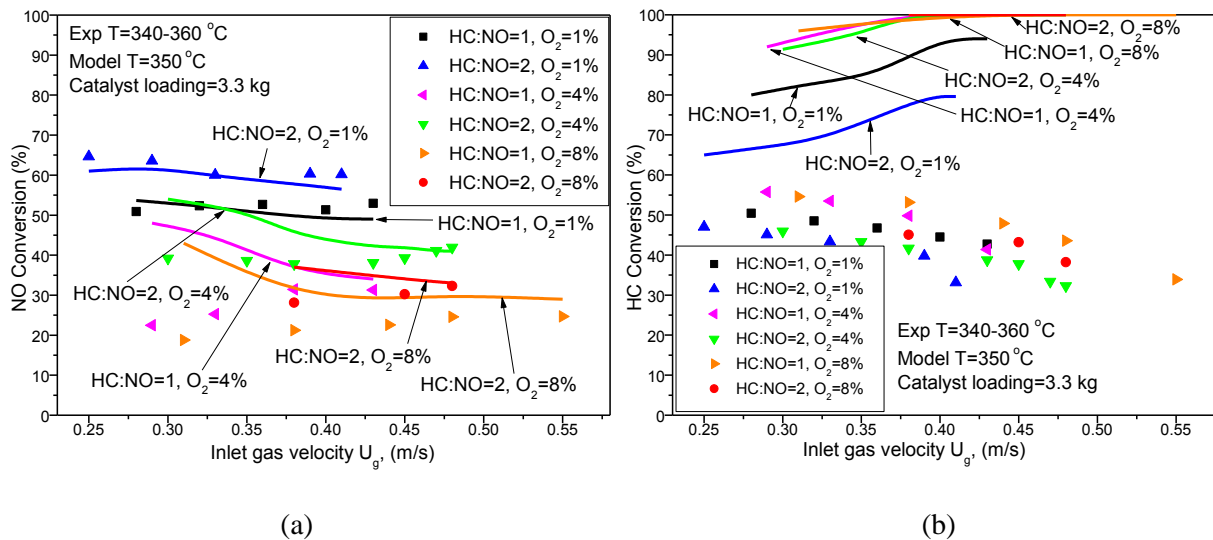


Figure 6.1 Modeled NO_x and HC conversion as a function of superficial gas velocity in the fluidized bed (Symbols: experimental data; lines: model fitting)

6.3.2 Fluidized bed simulation

To further investigate the effect of superficial gas velocity, the NO_x conversions in the fluidized bed were simulated and then compared to a fixed bed reactor, which has the same dimensions and is loaded with the same amount of catalyst. The results are shown in Fig. 6.2. NO_x conversion in the fixed bed is predicted to be higher than the conversion in the fluidized bed. This is because there is a bubble phase in the fluidized bed, where there is little catalyst inside for reaction to take place. Comparing to the fluidized bed, the absence of gas bypass in the fixed bed leads to a higher NO_x conversion. The superficial gas velocity U_g is seen to have a significant impact on NO_x conversion in the fixed bed, decreasing from 68% to 54% when U_g increases from 0.25 m/s to 0.45 m/s, due to the shortened residence time at higher superficial gas velocities. Comparing to fixed beds, NO_x conversion in fluidized beds is much less sensitive to U_g , decreasing less than 5% when U_g increases from 0.25 m/s to 0.45 m/s. The reaction taking place in the freeboard region, where there is a better mass transfer between gas and entrained particles, may also have contributed to the higher-than-expected NO_x conversions at higher U_g . This is confirmed by simulating NO_x conversion in a fluidized bed without considering the reactions taking place in the

freeboard region. As shown in Fig. 6.2, in the absence of reactions in the freeboard, the NO_x conversion in the fluidized bed is significantly affected by U_g , decreasing from 56% to 45% as U_g increases from 0.25 m/s to 0.45 m/s, which is similar to the fixed bed. Therefore, it is essential to include the freeboard region in modeling deNO_x reaction in the fluidized bed.

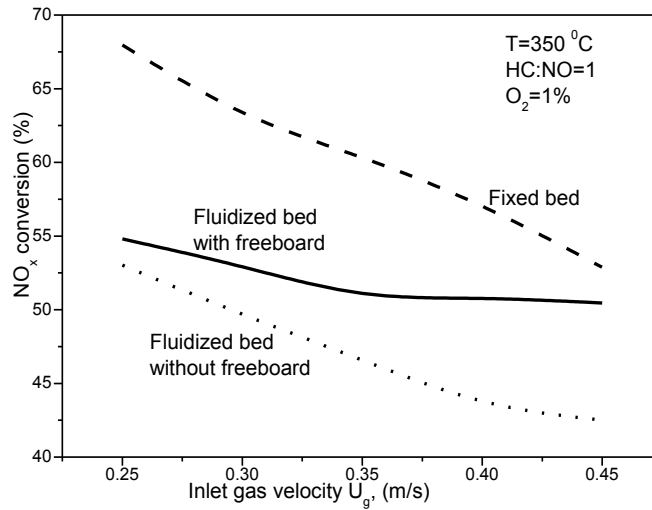


Figure 6.2 NO_x conversion at different U_g in fixed and fluidized bed reactors

Since NO_x conversion in the fluidized bed is much lower than that in the fixed bed, it is necessary to explore how to increase the NO_x conversion in fluidized beds. Simulated NO_x concentrations in different phases along the reactor length are plotted in Fig. 6.3, expressed in a dimensionless form: C_H/C_{g0} , C_L/C_{g0} , and C_s/C_{s0} , where C_{g0} is the inlet NO_x concentration and C_{s0} is the concentration in equilibrium with C_{g0} . It can be seen that NO_x concentration is almost constant in the solids phase along the bed height due to a strong back-mixing. Thus solids phase could be considered as perfectly mixed. The dimensionless NO_x concentration in the bubble phase decreases steadily from 1 to about 0.55 along the reactor since the bubble phase is modeled as in plug flow. For gas in the dense phase, the NO_x concentration profile falls between the profiles of solids phase and bubble phase. This is because NO_x in the dense phase (gas) is exchanged between both solids phase and bubble phase.

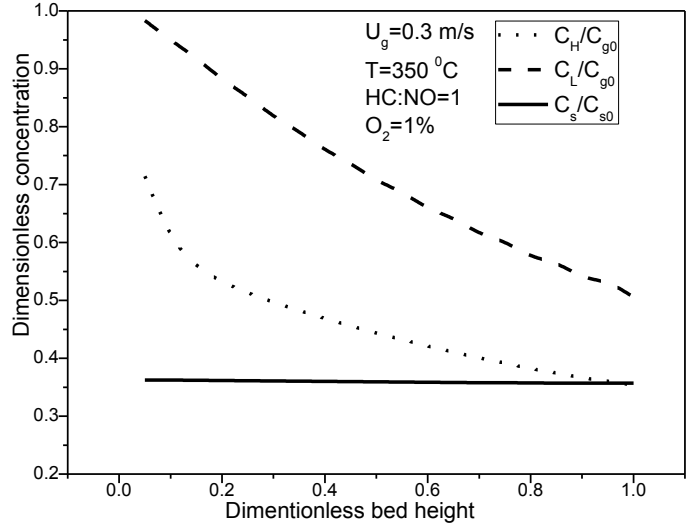


Figure 6.3 Dimensionless axial profiles of NO_x concentration in different phases

Since solids phase behaves like a CSTR in the freely bubbling fluidized bed, reducing axial solids dispersion is expected to improve the deNO_x efficiency. This is evidenced by the simulation results presented in Fig. 6.4, where the fluidized bed with D_s and D_H assumed to be 0 was simulated and compared with the normal fluidized bed. It is seen that NO_x conversion increases as the solids dispersion is reduced, especially at lower U_g . At higher U_g , the improvement is marginal since the conversion of the fluidized bed is similar to the conversion in fixed bed as indicated in Fig. 6.2. Another possible way to improve the NO_x conversion is to increase the mass transfer between bubble phase and dense phase. As shown in Fig. 6.4 which compares the performance of fluidized bed with different interphase mass transfer coefficient, k_{HL} . NO_x conversion increases as k_{HL} increases. The conversion can be further increased if dispersion coefficients D_s and D_H are zero and k_{HL} is doubled. Installing baffles in a fluidized bed can decrease solids back-mixing and reduce the bubble size which in turn can increase the interphase mass transfer between the bubble and dense phases, as suggested by equation Eq. (5.6).

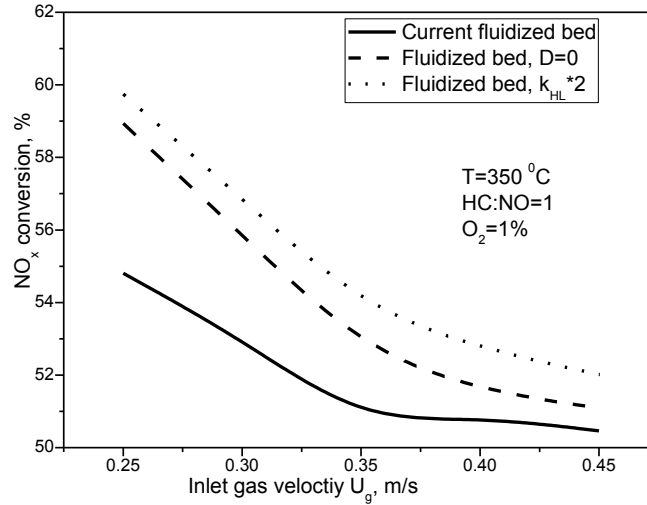


Figure 6.4 NO_x conversion at different gas dispersion and interphase mass transfer coefficient as a function of U_g

In the i-CFB deNO_x reactor, refreshed catalysts in the reduction zone will flow to the adsorption zone to adsorb NO_x in the flue gas. The NO_x concentration in the solids phase thus plays an important role in the capture efficiency of the adsorption zone because a lower NO_x concentration on the catalyst surface is desired in order to increase the NO_x adsorption to the catalyst. Although decreasing solids mixing and enhancing bubble-dense phase mass transfer could potentially improve the NO_x reduction efficiency, it is also important to understand how these improvements could affect the NO_x capture efficiency in the adsorption zone. Therefore, NO_x concentration in the solids phase is further investigated under these conditions with the simulation results plotted in Fig. 6.5.

As expected, there exists significant axial gradient of NO_x concentration on the solids surface at low or zero axial solids back-mixing (i.e. solids dispersion coefficient is 0). The dimensionless NO_x concentration in the solids phase is much lower at the outlet, which is favorable for the NO_x capture in the adsorption zone of the i-CFB.

As the interphase mass transfer increases, the figure shows that solids phase still behaves as a CSTR, with almost uniform solids phase NO_x concentration along the reactor which is also higher than that of the fluidized bed at lower k_{HL} . This is because more NO_x is transferred from the bubble phase to gas in the dense phase, increasing NO_x concentrations in the dense phase which in turn increases NO_x concentration in the solids phase.

Overall, both increasing k_{HL} and decreasing D_s could improve de NO_x efficiency in the fluidized bed. Decreasing axial dispersion could further decrease solids phase NO_x concentration at the outlet, which is favorable for NO_x capture in the adsorption zone of i-CFB. Increasing k_{HL} could lead to increased solids phase NO_x concentration at the reactor outlet, which, however, is undesired for the NO_x adsorption in the adsorption zone.

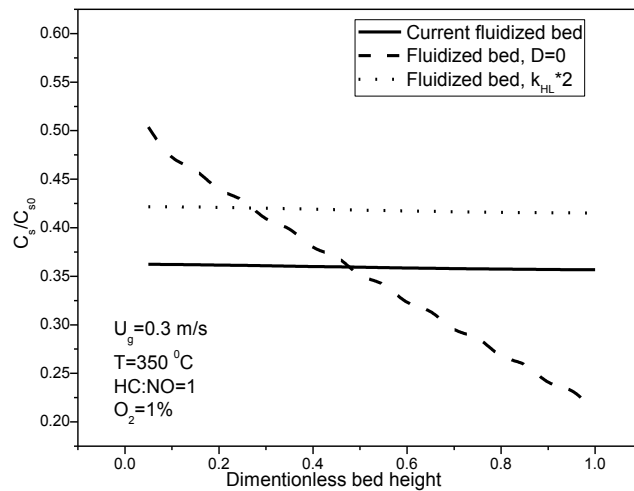


Figure 6.5 Dimensionless solids phase NO_x concentration along the reactor at different settings

6.3.3 Simulation of reduction zone of an i-CFB

As shown in Fig. 6.6, different from the fluidized bed operated with solids in the batch mode, solids move into the reduction zone of the i-CFB reactor from the bottom and overflow from the top into the

adsorption zone. The solids fed to the reduction zone are saturated with NO_x which is adsorbed from the flue gas in the adsorption zone. NO_x on the catalyst surface is then reduced by reducing agent in the reduction zone.

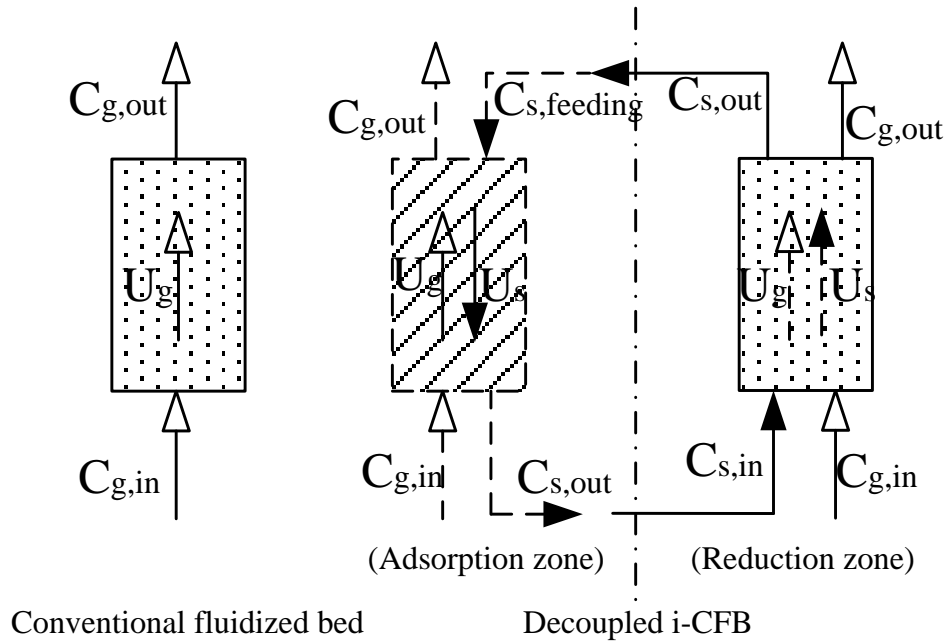


Figure 6.6 Flow diagram of fluidized bed and decoupled i-CFB

Different from conventional fluidized bed, gas fed into the reduction zone of the i-CFB contains only hydrocarbon and a small amount of O_2 , while NO_x is carried into the bottom by solids from the adsorption zone. Two more parameters should be considered in modeling the reduction zone of the i-CFB, solids circulation rate, G_s , and NO_x concentration on the fed particle surfaces, $C_{s,feeding}$. The solids circulation rate, G_s , determines how much solids are fed into the reduction zone and how long the solids could stay to have the NO_x on the surface reduced by hydrocarbon. In most cases, the catalyst is not completely saturated by NO_x in the flue gas and the NO_x concentration on the solids surface leaving the adsorption zone, defined as $C_{s,feeding}$, depends on the design and operation of the reactor.

In a conventional fluidized bed, NO_x in the flue gas is adsorbed onto the surface of the catalyst and then reduced by hydrocarbon reductant. But in the reduction zone of the i-CFB, NO_x on the surface of catalysts is directly reduced by hydrocarbon reductant. At the same time, NO_x could also desorb into the gas phase and slips out of the reactor. Therefore, different from the conventional fluidized bed, the catalytic NO_x reduction efficiency in the reduction zone of the i-CFB is given by

$$Xr = \left(1 - \frac{Q_{\text{NO}_x, \text{slip}} + Q_{\text{NO}_x, \text{d-a}}}{Q_{\text{NO}_x, \text{feeding}}} \right) \times 100\% \quad (6.9)$$

where $Q_{\text{NO}_x, \text{feeding}}$, $Q_{\text{NO}_x, \text{slip}}$ and $Q_{\text{NO}_x, \text{d-a}}$ are the amounts of NO_x fed into the reduction zone by the catalysts, escaped from the reactor with the exhaust gases, and returned to the adsorption zone with the circulating catalysts, respectively, in unit of mole/s.

Another parameter used to evaluate the performance of decoupled i-CFB is the slip ratio, defined as

$$Sl = \frac{Q_{\text{NO}_x, \text{slip}}}{Q_{\text{NO}_x, \text{feeding}}} \times 100\% \quad (6.10)$$

where $Q_{\text{NO}_x, \text{feeding}}$ is the total amount of NO_x fed to the i-CFB and the unit is also mole/s. The slip ratio, Sl , which represents the percentage of NO_x escaped from the reduction zone, is an important parameter determining the overall de NO_x efficiency in the i-CFB.

When simulating the reduction zone in the i-CFB, the governing equations are still Eqs. (6.1) to (6.3). It should be noted that the adsorption term in the governing equations accounts for NO_x desorption from the catalyst when NO_x is fed through the solids. The initial and boundary conditions now become:

$$z = 0, \quad C_H = C_{g, \text{in}}, \quad C_s = C_{s, \text{feeding}}, \quad C_L = C_{g, \text{in}} \quad (6.11)$$

$$z = H, \quad \frac{\partial C_H}{\partial z} = 0, \quad \frac{\partial C_s}{\partial z} = 0, \quad \frac{\partial C_L}{\partial z} = 0 \quad (6.12)$$

$$t = 0, \quad C_H = 0, \quad C_s = 0, \quad C_L = 0 \quad (6.13)$$

In order to evaluate the performance of the i-CFB, NO_x reduction in conventional fluidized bed (A) and reduction zone of i-CFB fed with solids saturated by NO_x (B) is directly compared. Bed catalyst loading is set to be 3 kg and the bed temperature is set as 350 °C. Inlet conditions for both gas and solids are shown in Table 6.1. The total amounts of NO_x in the feed are the same for the two reactors, although the gas carriers are different. In reactor A, NO_x is carried into the reactor by the gas feed (flue gas), while in reactor B, NO_x is supplied by the solids feed. The NO_x concentration in the fed solids of reactor B is set to be in equilibrium with the flue gas, calculated by the equilibrium of NO_x:

$$C_{s0,NO_x} = C_{s,NO_x}^* = k_{F,NO_2} C_{g0,NO_2}^{n_{NO_2}} C_{g0,O_2}^{n_{O_2}} \quad (6.14)$$

The total amount of NO_x fed into the two reactors is the same. So, the solids circulation rate in reactor B could be calculated by NO_x mass balance:

$$G_s = \frac{U_g C_{g0,NO_x} \rho_p}{C_{s0,NO_x}} \quad kg / m^2 \cdot s \quad (6.15)$$

Table 6.1 Inlet conditions for different fluidized bed used for simulation

	Reactor A: Conventional fluidized bed	Reactor B: Decoupled i-CFB fed with NO_x saturated solids
Feeding gas concentration	C _{g0,NO_x} =600 ppm C _{g0,HC} =600 ppm C _{g0,O₂} =1%	C _{g0,NO_x} =0 ppm C _{g0,HC} =600 ppm C _{g0,O₂} =1%
Superficial gas velocity	U _g =0.25 m/s ~ 0.45 m/s	Same as Reactor A
Feeding solids concentration	N/A	C _{s0,NO_x} =C _{s,NO_x} *
Solids circulation rate	0	Determined by NO _x feeding rate

NO_x reduction in the two reactors is then simulated at different superficial gas velocities. Outlet concentrations of NO_x in both the solids and gas phase are plotted in Fig. 6.7. The concentrations investigated are dimensionless values, divided by C_{g0} or C_{s0} . Reactor A shows the highest gas and solids phase NO_x concentrations. In reactor A, NO_x is transferred from gas phase to the solids phase. So, the dimensionless concentration in the gas phase is higher than the concentration in the solids phase. The superficial gas velocity, U_g , shows little influence on the outlet NO_x concentration.

When NO_x is fed through the solids phase in reactor B, outlet NO_x concentration of the gas phase is very low, because NO_x in the gas phase comes from NO_x desorption from the solids surface. A low gas phase concentration in reactor B could guarantee a low NO_x slip ratio, improving the overall performance of i-CFB. A high solids phase NO_x concentration at the outlet of reduction zone, however, implies a high NO_x concentration on the catalyst returning to the adsorption zone, imposing a negative impact on NO_x capture in the adsorption zone of i-CFB. Different from reactor A, the outlet NO_x concentration in reactor B increases substantially with increasing U_g , especially in the solids phase. Based on the equation for estimating solids circulation rate in Eq. (6.15), G_s is expected to be higher at higher U_g . Therefore, a shorter residence time of the solids at a higher U_g lead to a lower NO_x reduction and NO_x desorption, which can further lead to a higher solids phase NO_x concentration at the reactor outlet.

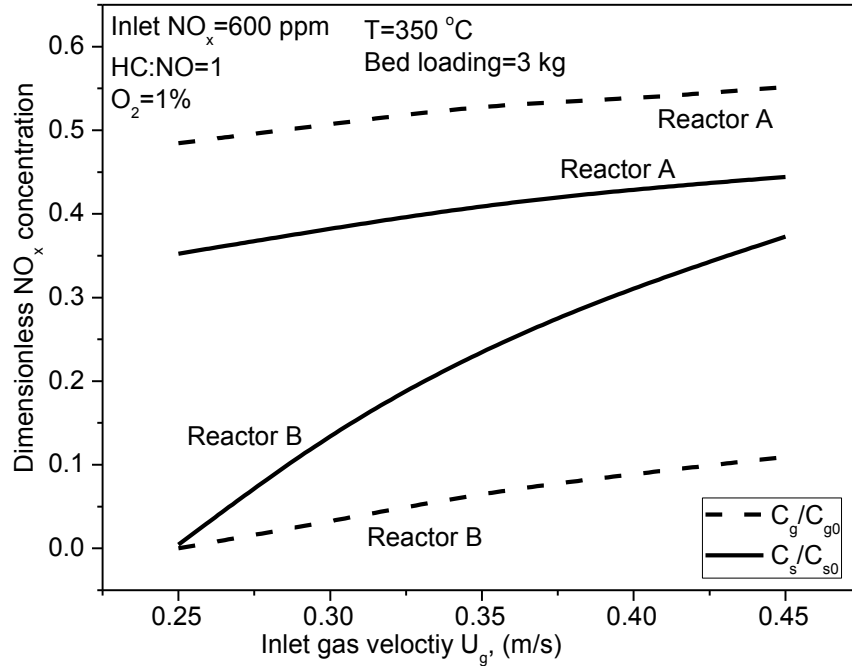


Figure 6.7 Dimensionless NO_x concentration as a function of U_g for different reactors

Fig. 6.8 shows the overall NO_x reduction efficiency, X_r, in the two reactors. NO_x conversion in reactor A is determined by the gas phase outlet concentration only since there are no solids leaving the reactor. The values are around 50%, slightly lower than the conversion simulated in the previous section due to a smaller bed catalyst loading. NO_x conversion in reactor B is determined by both gas and solids phase NO_x concentrations. The overall conversion in reactor B is much higher than the conversions in reactor A. This is anticipated since one important step in the deNO_x reaction, adsorption, is already completed before the solids enter the reactor. NO_x reduction decreases very quickly with increasing U_g, due to the shorter solids residence time at a higher solids circulation rate.

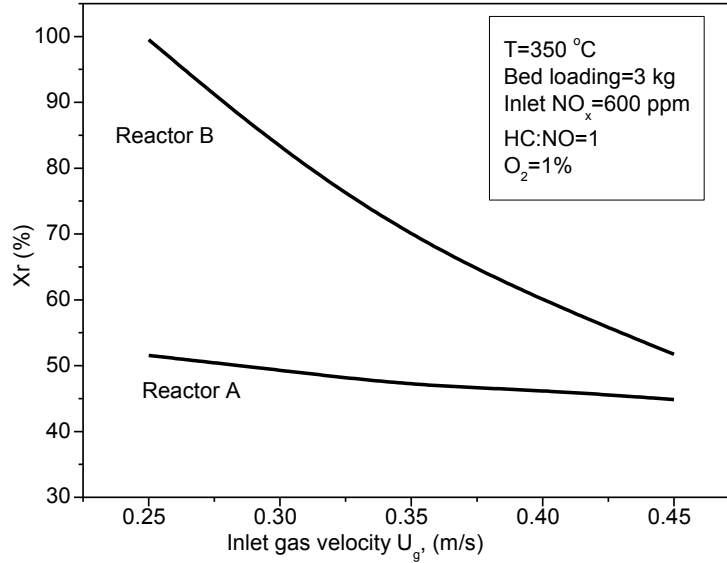


Figure 6.8 X_r as a function of U_g in different reactors

Solids circulation rate, G_s , in i-CFB is a very important operating parameter for determining both the NO_x capture efficiency in the adsorption zone and reduction efficiency in the reduction zone. It is anticipated that at a higher G_s , more solids will be re-circulated to the adsorption zone to capture NO_x , leading to a lower NO_x concentration on catalyst particles leaving the adsorption zone to the reduction zone. It is thus worth to investigate how G_s can affect the overall NO_x reduction efficiency and NO_x slip ratio in the reduction zone. The performance of an i-CFB is simulated at $U_g=0.35$ m/s with G_s changing. Other conditions remain the same as the settings for reactor B in Table 6.3. To investigate the effect of G_s on the performance of the reduction zone of the i-CFB, NO_x molar flow rate is set to be constant by decreasing the solids phase NO_x concentration at higher solids circulation rate, as shown in Eq. (6.16).

$$\frac{G_s}{G_{s0}} = \frac{C_{s0}}{C_s} \quad (6.16)$$

This is based on the assumption that the total NO_x feeding rate and capture efficiency in the adsorption zone of the i-CFB reactor remain the same. The simulated X_r and SI values are plotted in Fig.

6.9. It can be seen that the overall NO_x reduction efficiency is slightly higher at higher G_s but decreases at lower G_s , indicating that X_r is hardly influenced by G_s if inlet NO_x molar flow rate is maintained at a constant value. On the other hand, the change in NO_x slip ratio is more significant, increasing by about 10% when G_s is decreased from $2 \cdot G_{s0}$ to $0.5 \cdot G_{s0}$. This could be explained by the difference in the solids phase NO_x concentration C_s at different solids circulation rate G_s . A higher C_s at a lower G_s increases NO_x mass transfer between solids and gas phases, which leads to a higher slip ratio. Therefore, a higher solids circulation rate is preferred for the i-CFB if the total feed NO_x molar flow rate is kept constant. It should be noted that the solids phase NO_x concentration at the outlet of the reduction zone will become higher as the slip ratio is lowered, for a given overall reduction efficiency.

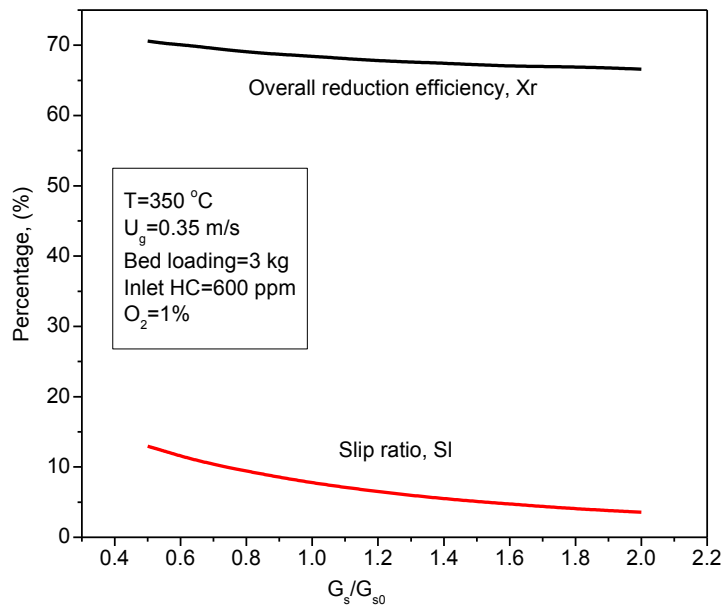


Figure 6.9 Overall efficiency, X_r , and slip ratio, Sl , as a function of G_s/G_{s0}

Another important issue for i-CFB operation is how to set the hydrocarbon concentration in the reduction zone. In the conventional fluidized bed or fixed bed reactor, hydrocarbon concentration is determined based on the given NO_x :HC ratio, since the superficial gas velocity is determined by the flow

rate of flue gas. However, gas streams of reducing agent and flue gases are fed into different zones of the i-CFB, making HC concentration and gas flow rate adjustable independently in the reduction zone.

To investigate the influence of HC concentration on the performance of the reduction zone of i-CFB, NO_x reduction at $U_g=0.35$ m/s is simulated with other conditions kept the same as those for reactor B given in Table 6.3. Solids circulation rate G_s is increased from an initial value G_{s0} , to twice of G_{s0} , $2 \cdot G_{s0}$, while solids phase NO_x concentration is kept at a constant, C_{s0} . Here both G_{s0} and C_{s0} are the same as the values used in Fig. 6.10. To keep feed $\text{HC}:\text{NO}_x=1$, either superficial gas velocity U_g or HC concentration C_{HC} is increased proportionally. The two cases are simulated with the results of X_r and Sl plotted as a function of dimensionless G_s , G_s/G_{s0} , in Fig. 6.10. X_r for either case illustrates that the overall NO_x reduction efficiency decreases when G_s increases, due to shorter residence time of solids in the reactor. NO_x slip ratio, Sl , increases at the same time. Both X_r and Sl seem to be more sensitive to the change in gas velocity, U_g , than to the change in hydrocarbon concentration, C_{HC} . It is seen that increasing U_g could lead to a lower overall NO_x reduction and more NO_x slippage, comparing to increasing the HC concentration. This is likely caused by the shorter contacting time between catalyst and gases at the higher U_g . Therefore, a reducing agent gas stream with higher HC concentrations is preferred in an i-CFB to improve the overall deNO_x performance. It should be also noted that this conclusion is valid only when other operating parameters of the i-CFB are kept at constants. In a real i-CFB, when HC concentration is higher, gas velocity in the reduction zone becomes lower, which could further change the solids circulation rate in the i-CFB and affect NO_x capture in the adsorption zone. An integral model is thus developed in next chapter to explore the performance of the i-CFB.

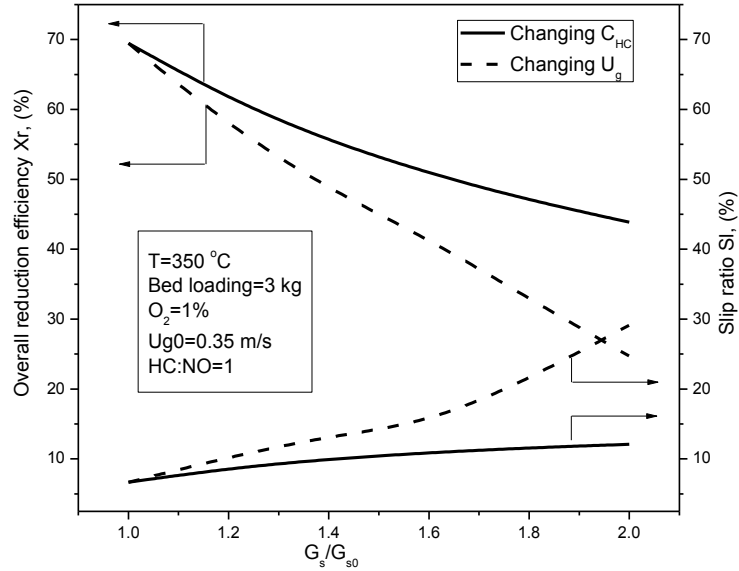


Figure 6.10 X_r and Sl values at different solids circulation rate

6.4 Summary

A model, which includes a bubble phase, gas in the dense phase and solids in the dense phase, was developed for the selective catalytic reduction of NO_x in a fluidized bed reactor and was validated by the NO_x conversion data measured in a fluidized bed reactor. The fluidized bed de NO_x model was then applied to simulate NO_x reduction in the reduction zone of the i-CFB reactor. Comparing with conventional fluidized beds, NO_x conversion could be improved if NO_x is fed through the solids phase, such as what happens in the reduction zone of an i-CFB. Also for the reduction zone of the i-CFB, a higher solids circulation rate is preferred if NO_x feed rate is kept at a constant. This is because NO_x slip ratio is lower at higher G_s , which could improve the overall NO_x reduction efficiency of the i-CFB. If NO_x feed rate is increased, HC feed rate should be increased proportionally. In this case, changing HC concentration and keeping gas velocity at a constant is preferred than changing gas velocity and keeping HC concentration at a constant. The overall NO_x conversion becomes higher and NO_x slip ratio is lower when the HC concentration is increased.

Chapter 7 Modeling catalytic NO_x reduction in i-CFB reactors⁶

7.1 Introduction

Combining the hydrodynamics model in Chapter 3, adsorption and reaction kinetics models in Chapters 4, and the fluidized bed reactor model in Chapters 5 and 6, an integrated i-CFB reactor model is developed in this chapter. Adsorption and reaction over the Fe/ZSM-5 catalyst are modeled in both the adsorption zone (annulus) and reduction zone (draft tube) of the i-CFB. The interaction of the adsorption and reduction zones is connected by the circulating catalysts between the annulus and draft tube. After being validated by the experimental data, the i-CFB reactor model is further used for optimizing the adsorption-reduction deNO_x reactor performance based on simulations.

7.2 i-CFB experiment

The deNO_x performance in an i-CFB reactor was tested by Yang [11]. The experimental set up was already described in Chapter 3. In the proposed configuration, the flue gas is passed into the adsorption zone (annulus) where NO_x is adsorbed by the catalyst particles. The NO_x-rich catalyst particles then move downward and into the reduction zone (draft tube) where NO_x adsorbed on the catalyst surface is reduced by injected hydrocarbons. The NO_x-depleted catalyst particles are then recirculated back to the adsorption zone to maintain a continuous operation. By adjusting the gas flow rates in the annulus and the draft tube,

⁶ A version of this chapter will be submitted for publication: Xingxing Cheng and Xiaotao T. Bi, Modeling catalytic reduction of NO_x in a novel i-CFB reactor.

the bypassing of the flue gas from the adsorption zone to the reduction zone can be controlled to have the O₂ concentration in the reduction zone maintained at desired levels.

In the experiment of Yang [11], 3.3 kg Fe/ZSM-5 particles were loaded into the i-CFB reactor. The reactor was first preheated by passing the preheated building air through both the annulus and the draft tube. NO from the gas cylinder was blended with preheated building air and pure N₂ to prepare the simulated model flue gas at desired NO and O₂ concentrations. At the same time, propylene was injected into the preheated N₂ to prepare the reductant gas mixture. The model flue gas was injected into the adsorption zone (annulus) through a conical distributor plate. The reductant gas mixture was injected into the reduction zone (draft tube) via a gas nozzle. The NO_x reduction performance was monitored by measuring the gas composition at the inlet and outlet of the reactor.

The model flue gas used in the experiment was a mixture prepared from a gas cylinder containing 20% NO balanced with N₂ and a liquid N₂ Dewar, with both supplied from Praxair Products Inc. Building air was used as the source of O₂. NO_x concentration in the model flue gas was controlled at 600 ppm with O₂ concentration ranging from 4 to 12%. The reducing agent used in the experiment was propylene. The gas cylinder containing 40% propylene balanced with N₂ was supplied by Praxair Products Inc. The reducing agent stream consisted of propylene + N₂, with propylene-to-NO_x molar flow ratio varied from 1 to 4. It should be noted that NO and HC were in different gas streams in the i-CFB reactor, i.e., the flue gas stream in the adsorption zone and the reductant gas stream in the reduction zone. To investigate the effect of gas velocities and other factors on the performance of the catalyst without changing HC:NO ratio, the ratio of HC:NO was defined as the molar flow rate of propylene to the reduction zone divided by the molar flow rate of NO to the adsorption zone.

$$R_{HC:NO} = \frac{C_{HC,d0}F_{d0}}{C_{NO,a0}F_{a0}} \quad (7.1)$$

The overall NO_x conversion (X_{NO_x}) was calculated by Eq. (7.2) based on the initial concentration of NO in the total gas flow of the annulus and the draft tube, and the concentration of NO_x in the gas mixture at the exit of the reactor.

$$X_{NO_x} = \frac{F_{a0} \times C_{NO,a0} - (F_a + F_d) \times C_{NO,out}}{F_{a0} \times C_{NO,a0}} \times 100\% \quad (7.2)$$

7.3 i-CFB model

The i-CFB reactor includes two reaction zones, an adsorption zone in the annulus and a reduction zone in the draft tube. Flue gas is fed into the annulus and reducing agent is fed into the draft tube. Gas bypass is considered to obtain the actual gas velocities and concentrations at the entrance of each zone. The solids flow in the annulus and the draft tube is connected by the solids circulation between them. In the modeling of i-CFB reactor, both adsorption and reaction are considered in each zone. Same as the fluidized bed deNO_x reaction model, three phases are considered for the governing equations of each zone, solids in dense phase, gas in dense phase and gas in bubble phase. Reactions take place on the surface of the catalyst. Gas leaving the annulus and draft tube enters the freeboard region, where it may continue the reaction before exits the i-CFB reactor. The schematics of the i-CFB reactor model is given in Fig. 7.1.

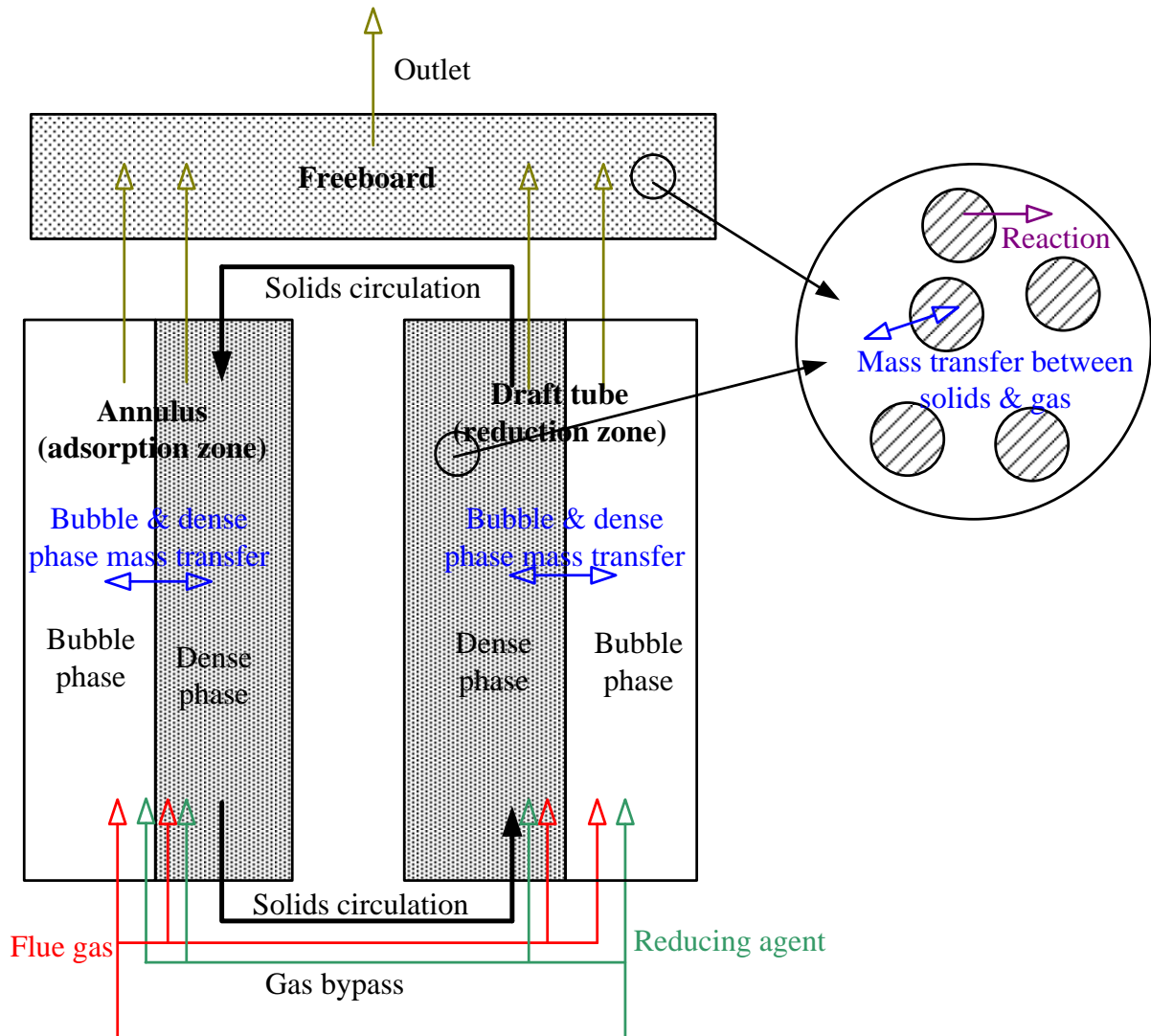


Figure 7.1 Schematics of i-CFB model

7. 3.1 Reaction zones

As discussed in Chapter 3, there are four possible flow patterns in the operation of an i-CFB: (a) no solids circulation, (b) annulus solids height lower than draft tube, (c) draft tube with a fully penetrating jet, and draft tube with an internal jet. The experimental conditions investigated in this study only covered flow patterns (b) and (c), as shown in Fig. 7.2, and thus studied in detail. For both flow patterns, the effective

bed heights in the annulus and draft tube are obtained from mass and pressure balances of the entire i-CFB, with the detailed calculation protocol being presented in Chapter 3.

As confirmed in Chapter 6, the freeboard region plays an important role for the deNO_x reaction in fluidized beds. So a freeboard region above the annulus and draft tube is considered in the model. Solids and gas flow above the dense bed reaction zone of the annulus and draft tube are very complex. For a first approximation, it is assumed for flow pattern (b) that gases in the annulus and draft tube are well mixed right above the dense bed region, which is located beneath the draft tube top. It is further assumed that the freeboard region starts right from the draft tube top as indicated by the dash red line in Fig. 7.2. For flow pattern (c), it is assumed that gases from the annulus and draft tube are well mixed above the effective bed height and the freeboard region starts from the top of the effective bed height. The solids fraction in the freeboard is treated in the same way as a regular fluidized bed, as described in Chapter 6.

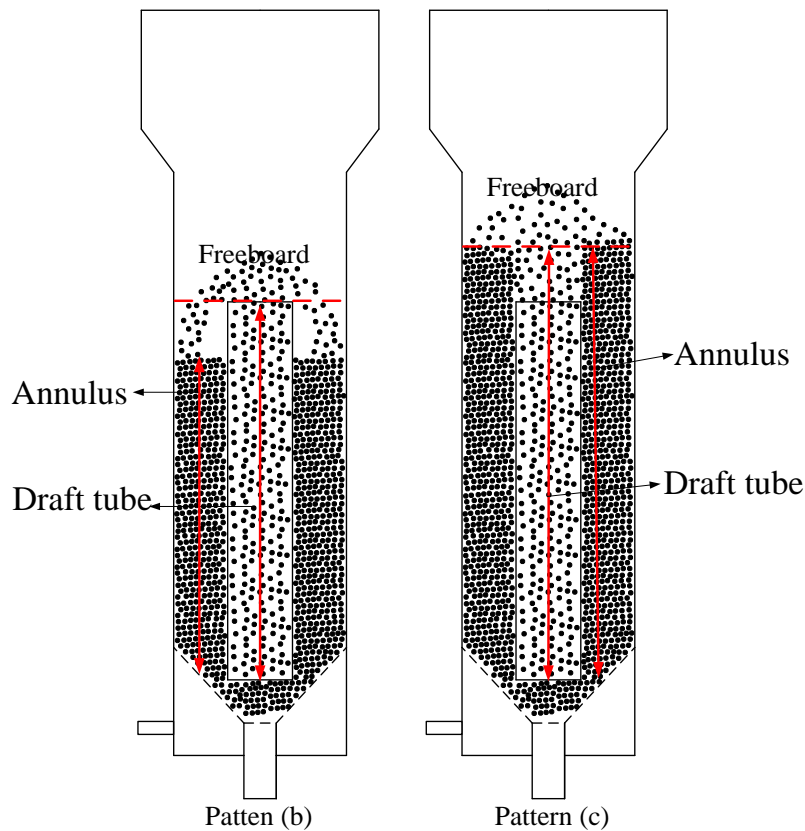


Figure 7.2 Schematics of the flow regions of i-CFB studied

7.3.2 Governing equations

As the fluidized bed reactor model developed in Chapter 6, fluidized bed consists of two phases, bubble phase and dense phase. Mass transfer of NO_x in the fluidized bed not only occurs between the bubble phase and dense phase, but also between the gas phase and particles. Adsorption and reaction take places only in the solids phase of the dense phase. In the i-CFB, the same fluidized bed reactor model is applied for both the adsorption zone (annulus) and reduction zone (draft tube). For each reaction zone, governing equations for the reactant in different phases are:

$$D_s \varepsilon_s \frac{\partial^2 C_s}{\partial z^2} \pm U_s \varepsilon_s \frac{\partial C_s}{\partial z} - \frac{\varepsilon_s}{1 - \varepsilon_s} k_f \cdot (C_s - C_s^*) + R_i = \varepsilon_s \frac{\partial C_s}{\partial t} \quad (7.3)$$

for particles in the dense phase.

$$D_H \Phi_H (1 - \varepsilon_s) \frac{\partial^2 C_H}{\partial z^2} - U_H \Phi_H (1 - \varepsilon_s) \frac{\partial C_H}{\partial z} + k_f \cdot (C_s - C_s^*) + k_{HL} a_b (C_L - C_H) = \Phi_H (1 - \varepsilon_s) \frac{\partial C_H}{\partial t} \quad (7.4)$$

for gas in the dense phase.

$$D_L \Phi_L \frac{\partial^2 C_L}{\partial z^2} - U_L \Phi_L \frac{\partial C_L}{\partial z} - k_{HL} a_b (C_L - C_H) = \Phi_L \frac{\partial C_L}{\partial t} \quad (7.5)$$

for gas in the bubble phase.

Initial conditions are:

$$t = 0, \quad C_H = 0, \quad C_s = 0, \quad C_L = 0 \quad (7.6)$$

Total number of equations and boundary conditions for each equation are listed in Table 7.1. The linkage between the adsorption and reduction zones is represented by the boundary conditions.

Table 7.1 i-CFB equations and boundary conditions

Annulus				
Gas	Equation number	Phase	Boundary condition: z=0	Boundary condition: z=H
NO	A1	Solids phase	$\frac{\partial C_{A1}}{\partial z} = 0$	$C_{A1} = C_{D1}$
	A2	High density phase	$C_{A2} = C_{NO,a}$	$\frac{\partial C_{A2}}{\partial z} = 0$
	A3	Low density phase	$C_{A3} = C_{NO,a}$	$\frac{\partial C_{A3}}{\partial z} = 0$
HC	A4	Solids phase	$\frac{\partial C_{A4}}{\partial z} = 0$	$C_{A4} = C_{D4}$
	A5	High density phase	$C_{A5} = C_{HC,a}$	$\frac{\partial C_{A5}}{\partial z} = 0$
	A6	Low density phase	$C_{A6} = C_{HC,a}$	$\frac{\partial C_{A6}}{\partial z} = 0$
O2	A7	Solids phase	$\frac{\partial C_{A7}}{\partial z} = 0$	$C_{A7} = C_{D7}$
	A8	High density phase	$C_{A8} = C_{O_2,a}$	$\frac{\partial C_{A8}}{\partial z} = 0$
	A9	Low density phase	$C_{A9} = C_{O_2,a}$	$\frac{\partial C_{A9}}{\partial z} = 0$
Draft tube				
Gas	Equation number	Phase	Boundary condition: z=0	Boundary condition: z=H
NO	D1	Solids phase	$C_{D1} = C_{A1}$	$\frac{\partial C_{D1}}{\partial z} = 0$
	D2	High density phase	$C_{D2} = C_{NO,d}$	$\frac{\partial C_{D2}}{\partial z} = 0$
	D3	Low density phase	$C_{D3} = C_{NO,d}$	$\frac{\partial C_{D3}}{\partial z} = 0$

Gas	Equation number	Phase	Boundary condition: z=0	Boundary condition: z=H
HC	D4	Solids phase	$C_{D4} = C_{A4}$	$\frac{\partial C_{D4}}{\partial z} = 0$
	D5	High density phase	$C_{D5} = C_{HC,d}$	$\frac{\partial C_{D5}}{\partial z} = 0$
	D6	Low density phase	$C_{D6} = C_{HC,d}$	$\frac{\partial C_{D6}}{\partial z} = 0$
O2	D7	Solids phase	$C_{D7} = C_{A7}$	$\frac{\partial C_{D7}}{\partial z} = 0$
	D8	High density phase	$C_{D8} = C_{O_2,d}$	$\frac{\partial C_{D8}}{\partial z} = 0$
	D9	Low density phase	$C_{D9} = C_{O_2,d}$	$\frac{\partial C_{D9}}{\partial z} = 0$
Freeboard				
Gas	Equation number	Phase	Boundary condition: z=H	Boundary condition: z= freeboard outlet
NO	F1	Solids phase	$C_{F1} = f(C_{A1} _{z=H}, C_{D1} _{z=H})$	$\frac{\partial C_{F1}}{\partial z} = 0$
	F2	Gas phase	$C_{F2} = f(C_{A2} _{z=H}, C_{A3} _{z=H}, C_{D2} _{z=H}, C_{D3} _{z=H})$	$\frac{\partial C_{F2}}{\partial z} = 0$
HC	F3	Solids phase	$C_{F3} = f(C_{A4} _{z=H}, C_{D4} _{z=H})$	$\frac{\partial C_{F3}}{\partial z} = 0$
	F4	Gas phase	$C_{F4} = f(C_{A5} _{z=H}, C_{A6} _{z=H}, C_{D5} _{z=H}, C_{D6} _{z=H})$	$\frac{\partial C_{F4}}{\partial z} = 0$
O2	F5	Solids phase	$C_{F5} = f(C_{A7} _{z=H}, C_{D7} _{z=H})$	$\frac{\partial C_{F5}}{\partial z} = 0$
	F6	Gas phase	$C_{F6} = f(C_{A8} _{z=H}, C_{A9} _{z=H}, C_{D8} _{z=H}, C_{D9} _{z=H})$	$\frac{\partial C_{F6}}{\partial z} = 0$

The kinetic model equations developed in Chapter 4 are embedded in Eq. (7.3) as the reaction term and used for the modeling of both annulus and draft tube. Coefficients of mass transfer and dispersion are calculated in the same way in Chapter 4.

7.3.3 Hydrodynamics

In the i-CFB reactor, flue gas and reducing agent bypass between the annulus and draft tube. The gas bypass ratios, R_{a-d} and R_{d-a} , are calculated using the correlations fitted in Chapter 3, Eqs. (3.28) and (3.29). The actual gas velocities in the annulus and draft tube of i-CFB with gas bypassing could then be calculated from mass balance:

$$U_a = U_{a0} - R_{a-d} \cdot U_{a0} + R_{d-a} \cdot U_{d0} \cdot (A_d / A_a) \quad (7.7)$$

$$U_d = U_{d0} - R_{d-a} \cdot U_{d0} + R_{a-d} \cdot U_{a0} \cdot (A_a / A_d) \quad (7.8)$$

Real inlet gas concentrations in annulus and draft tube could also be calculated from mass balance by Eqs. (7.9) to (7.14), assuming that there are only NO, O₂ and N₂ in the annulus inlet and only HC and N₂ in the draft tube inlet.

$$C_{NO,a} = C_{NO,a0} \cdot \frac{(F_{a0} - F_{a-d})}{F_a} = C_{NO,a0} \cdot (1 - R_{a-d}) \cdot \frac{U_{a0}}{U_a} \quad (7.9)$$

$$C_{NO,d} = C_{NO,a0} \cdot \frac{F_{a-d}}{F_d} = C_{NO,a0} \cdot R_{a-d} \cdot \frac{U_{a0}}{U_d} \quad (7.10)$$

$$C_{O_2,a} = C_{O_2,a0} \cdot \frac{(F_{a0} - F_{a-d})}{F_a} = C_{O_2,a0} \cdot (1 - R_{a-d}) \cdot \frac{U_{a0}}{U_a} \quad (7.11)$$

$$C_{O_2,d} = C_{O_2,a0} \cdot \frac{F_{a-d}}{F_d} = C_{O_2,a0} \cdot R_{a-d} \cdot \frac{U_{a0}}{U_d} \quad (7.12)$$

$$C_{HC,d} = C_{HC,d0} \cdot \frac{(F_{d0} - F_{d-a})}{F_d} = C_{HC,d0} \cdot (1 - R_{d-a}) \cdot \frac{U_{d0}}{U_d} \quad (7.13)$$

$$C_{HC,a} = C_{HC,d0} \cdot \frac{F_{d-a}}{F_a} = C_{HC,d0} \cdot R_{d-a} \cdot \frac{U_{d0}}{U_a} \quad (7.14)$$

Following the same procedure as described in Chapter 3 using Eqs. (3.4) to (3.10), solids circulation rate could be calculated based on mass and pressure balance of solids in the i-CFB. The bed expansions in both annulus and draft tube of i-CFB, as well as voidage, bubble size and bubble velocities, etc., are calculated in the same way as described in Chapter 3 using Eqs. (3.18) to (3.24), which are also used for the modeling of fluidized bed adsorption (in Chapter 5) and reaction (in Chapter 6).

7.4 Modeling results and comparison with experimental data

7.4.1 Model verification

Catalytic NO_x reduction in i-CFB reactor is simulated with the model described above. The model is coded into MATLAB with the codes shown in Appendix F. Outlet concentrations are calculated from the concentrations in both the bubble and dense phases of each reaction zone. The outlet concentration in the adsorption zone is given by:

$$C_{a,out} = \frac{\Phi_{a,H} U_{a,H} C_{a,H} + \Phi_{a,L} U_{a,L} C_{a,L}}{\Phi_{a,H} U_{a,H} + \Phi_{a,L} U_{a,L}} \quad (7.15)$$

and the outlet concentration in the reduction zone is given by:

$$C_{d,out} = \frac{\Phi_{d,H} U_{d,H} C_{d,H} + \Phi_{d,L} U_{d,L} C_{d,L}}{\Phi_{d,H} U_{d,H} + \Phi_{d,L} U_{d,L}} \quad (7.16)$$

Then the total outlet concentration of the whole i-CFB is obtained from:

$$C_{out} = \frac{C_{a,out} U_a A_a + C_{d,out} U_d A_d}{U_a A_a + U_d A_d} \quad (7.17)$$

The overall conversion could now be calculated by:

$$X = \left[1 - \frac{C_{out}U_{out}(A_a + A_d)}{C_{a,in}U_aA_a + C_{d,in}U_dA_d} \right] \times 100\% \quad (7.18)$$

NO_x and hydrocarbon conversions in the i-CFB were then modeled and compared with the experimental data at different operating conditions. Reaction in the i-CFB at O₂=4% (in the flue gas) was first modeled at different U_{a0}, U_{d0} and HC:NO ratios. The modeled results, together with the experimental data, are plotted as a function of the annulus gas velocity in Figs. 7.3 and 7.4. Fig. 7.3(a) shows the NO_x conversion at U_{d0}=0.6 m/s. The model predicts the experimental data points with an average error of about 10%. NO_x conversion decreases at higher U_{a0} due to more flue gas being fed into the reactor. But the slopes of these curves are very small. At HC:NO=2, NO_x conversion decreases from about 55% at U_{a0}=0.225 m/s to 43% at U_{a0}=0.425 m/s. So, the overall NO_x removal efficiency is not very sensitive to inlet flue gas velocities. This could be caused by the enhanced freeboard region and bubble-dense phase mass transfer at higher gas velocities, as suggested by Eq. (5.6). In terms of HC:NO ratio, NO_x conversion increases with increasing HC:NO ratio, as expected. When U_{a0} is around 0.35 m/s, NO_x conversion increases from less than 40% to more than 60% when HC:NO ratio increases from 1 to 4.

Measured and model predicted HC conversions are plotted in Fig. 7.3(b). The prediction shows an average error of about 9% with experimental data. The error for some data points is more than 15%. This is likely caused by the kinetics used in the model, which gives a poorer agreement on HC conversion for some data points than on NO_x conversion, as shown in Chapter 4. This inaccuracy is now carried on to the i-CFB model. Another possible cause is the uncertainties in the measured HC conversion. In the experiment, propylene was not directly measured but calculated from carbon balance based on the measured concentrations of CO and CO₂ in the product stream. Other possible unmeasured intermediates from incomplete oxidation of propylene could lead to the underestimation of HC conversion. Overall, HC

conversions of both modeled and experimental data fall into the same range, between 100% and 60%, and the model could well capture the effect of U_{a0} and HC:NO ratio on NO_x conversion and HC conversion.

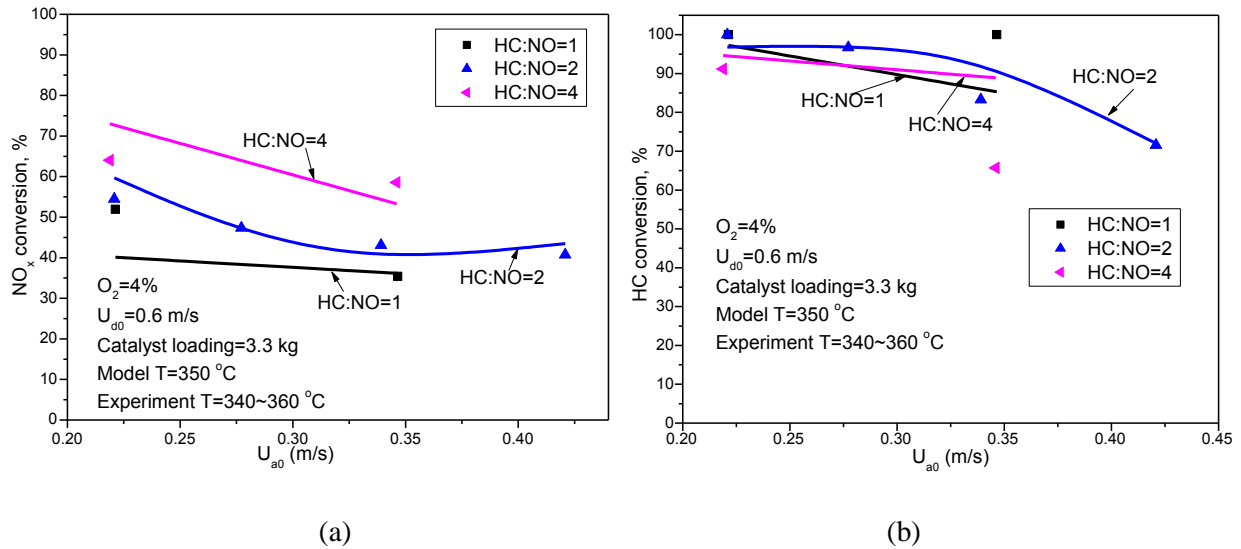


Figure 7.3 (a) NO_x and (b) HC conversion as a function of U_{a0} ($O_2=4\%$, $U_{d0}=0.6$ m/s. Symbols: experimental data; lines: model fitting)

NO_x conversion was also modeled and compared with experimental data at $U_{d0}=0.75$ m/s with the results shown in Fig. 7.4(a). Similar to Fig. 7.3(a), NO_x conversion is well predicted by the model with an average error of about 5%. NO_x conversion decreases with increasing U_{a0} and increases with increasing HC:NO ratio. A similar trend is also observed in Fig. 7.4(b) at a higher draft tube velocity of $U_{d0}=0.9$ m/s. From Figs. 7.3 and 7.4, it can be further observed that NO_x conversion increases with increasing the draft tube velocity, U_{d0} , at a given overall HC:NO molar ratio. At $U_{a0}=0.22$ m/s and HC:NO=4, NO_x conversions are 65%, 70%, and 75%, for $U_{d0}=0.6$ m/s, 0.75 m/s and 0.9 m/s, respectively. Therefore, a higher draft tube velocity is preferred for achieving a high NO_x conversion in the i-CFB.

At a higher U_{d0} , HC is more diluted in the reduction zone. de NO_x efficiency increases with increasing U_{d0} , which suggests that NO_x conversion is higher at lower HC concentration. This is contradictory to the conclusion obtained from the fluidized bed modeling, which showed that concentrated HC is preferred. Here, the higher de NO_x efficiency at a higher U_{d0} can be attributed to the

increased gas exchange from the draft tube to the annulus, R_{d-a} , as indicated by Eq. (3.28), which will be investigated in detail in the sensitivity analysis to be presented in the next section.

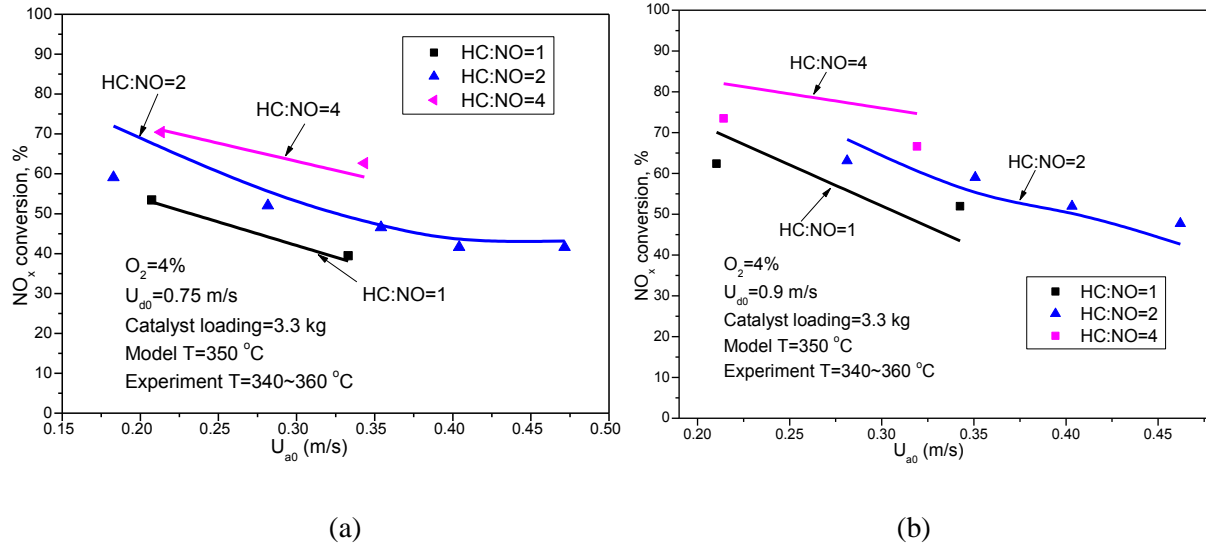


Figure 7.4 NO_x conversion as a function of U_{a0} at O₂=4%, a), U_{d0}=0.75 m/s, b), U_{d0}=0.9 m/s (Symbols: experimental data; lines: model fitting)

NO_x conversion was further modeled at different inlet O₂ concentrations. Fig. 7.5(a) shows the NO_x conversion as a function of U_{a0} at U_{d0}=0.9 m/s, HC:NO=2, and different O₂ concentrations of 4%, 8% and 12%. The average error between the modeling results experimental data is 8%. Both model and experiment show a decrease of NO_x conversion with increasing U_{a0} and flue gas O₂ concentration. The negative effect of O₂ is caused by more HC being oxidized at higher O₂ concentrations. However, this negative effect is very small in i-CFB. Modeled NO_x conversions at O₂=4%, 8% and 12% are very close to each other, confirming that i-CFB could be applied for the treatment of the flue gas containing high O₂ concentrations.

For HC conversion, both experimental and predicted results fall into the same range, between 100% and 70%, as shown in Fig. 7.5(b). Although there is a slight variation, the model could well predict the trend of i-CFB performance with an average error of 10%. Same as NO_x conversion, HC conversion

decreases at higher inlet flue gas velocities. When O_2 concentration in the flue gas increases, more HC trends to be oxidized by O_2 , leading to higher HC conversions.

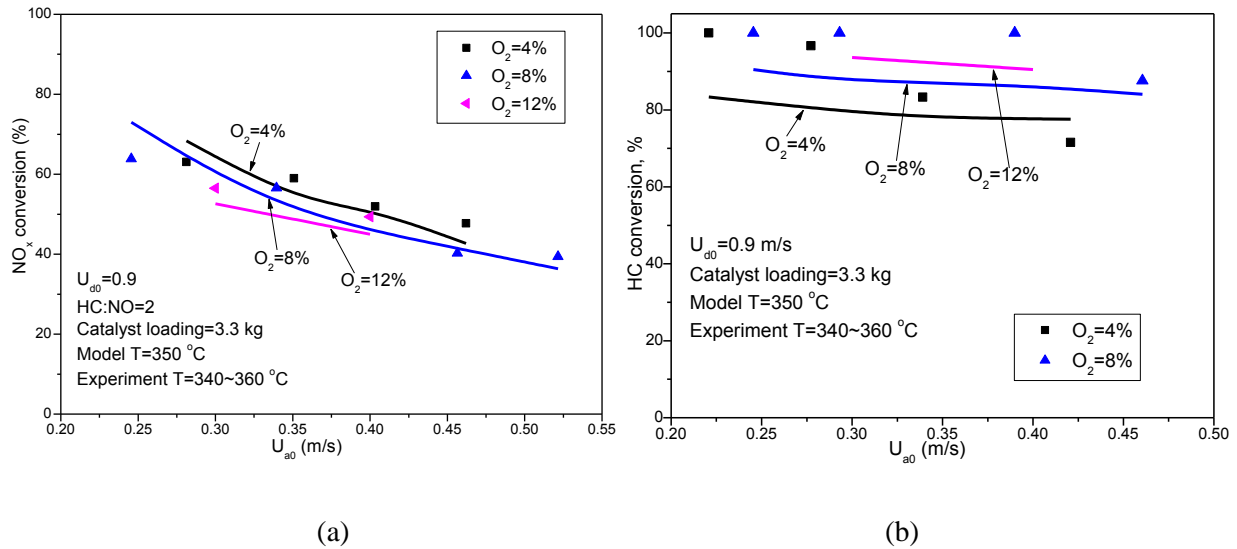


Figure 7.5 NO_x conversion as a function of U_{a0} at a), $U_{d0}=0.6$ m/s , b), $U_{d0}=0.75$ m/s (Symbols: experimental data; lines: model fitting)

The performance of i-CFB is also compared with a regular fluidized bed by modeling the de NO_x efficiency in both configurations. The same flue gas velocity, 0.4 m/s, is used, with the same HC:NO molar ratio, HC:NO=2. For i-CFB, the draft tube gas velocity is set at 0.9 m/s, because a high U_{d0} can enhance the overall de NO_x efficiency. The performance of these two configurations is compared at different inlet O_2 concentrations, ranging from 1% to 12%, with the results plotted in Fig. 7.6. It is seen that NO_x conversion in an i-CFB is higher than the conversion in a regular fluidized bed, confirming the better de NO_x performance of i-CFB. For O_2 effect, NO_x conversion in the regular fluidized bed is strongly affected by the inlet O_2 concentration, decreasing from 57% to about 33% when O_2 concentration increases from 1% to 8%. NO_x conversion in i-CFB also decreases as the O_2 concentration in the flue gas increases, but the slope of the curve is very small, especially at high O_2 concentrations, decreasing by less than 5% when the inlet O_2 concentration increases from 4% to 12%. Further increasing O_2 concentration

has little negative effect on the NO_x reduction in i-CFB, proving that the i-CFB can effectively eliminate the negative O_2 effect at high O_2 concentrations.

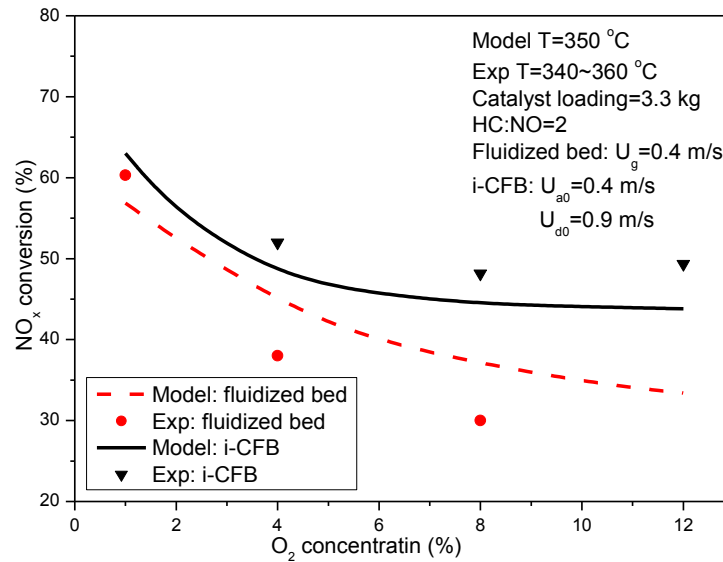


Figure 7.6 Comparison of NO_x conversion in an i-CFB and a regular fluidized bed (Symbols: experimental data; lines: model fitting)

7.4.2 Sensitivity analysis

7.4.2.1 Gas bypass

The sensitivity of the model prediction to gas bypass ratio is first examined, with predicted NO_x conversions shown in Fig. 7.7. It is seen that the model is not sensitive to gas bypass from the annulus to the draft tube, R_{a-d} , at $U_{a0} < 0.3$ m/s. However, at higher U_{a0} , NO_x conversion becomes sensitive to R_{a-d} . This is because little gas is bypassed from the annulus to the draft tube at low flue gas feed rate to the annulus. At high flow rate of flue gas in the annulus, small changes in R_{a-d} can result in significant changes of the flow condition in the draft tube, making the overall NO_x conversion more sensitive to R_{a-d} . At $U_{a0} = 0.4$ m/s, NO_x conversion decreases by about 10% when R_{a-d} is doubled, and increases by about 10% when R_{a-d} is halved. When R_{a-d} is bigger, more flue gas is bypassed from annulus to the draft tube.

O₂ concentration in the draft tube is expected to increase correspondingly. A higher O₂ concentration can lead to a lower NO_x reduction efficiency in the draft tube, and further decreases the overall deNO_x efficiency. For the same reason, deNO_x efficiency will be improved if R_{a-d} is decreased. Therefore, gas bypass from the annulus to draft tube should be well controlled during the operation of an i-CFB deNO_x reactor.

NO_x conversion is much more sensitive to gas bypass from draft tube to annulus, R_{d-a}. When R_{d-a} is halved, NO_x conversion is dramatically lowered, decreasing by more than 30%. It is expected that the deNO_x performance of i-CFB will be quite poor if there is no hydrocarbon bypassing from the draft tube to the annulus. The case with R_{d-a} doubled is not calculated because too much gas bypass from the draft tube to annulus could cause too low a gas velocity in the annulus to establish solids circulation. Instead, NO_x conversion is calculated with 10% increase in R_{d-a}. The simulated results in Fig. 7.7 show that NO_x conversion is significantly improved with only a light increase in R_{d-a}. If less gas is bypassed from the draft tube to annulus, HC concentration in the draft tube will be higher and a higher NO_x reduction is expected from the draft tube, leading to a higher overall deNO_x efficiency of the i-CFB system. However, the i-CFB modeling results tell a different story, which may be attributed to the additional deNO_x reactions in the annulus between NO_x and bypassed HC. As more HC-containing gas bypasses to the annulus, hydrocarbon concentration in the annulus is increased, which enhances the catalytic reduction of NO_x in the annulus. Correspondingly, the NO_x concentration on the catalyst surface in the annulus will be lowered, which could further improve the NO_x capture efficiency in the annulus and increase the overall deNO_x efficiency of the i-CFB.

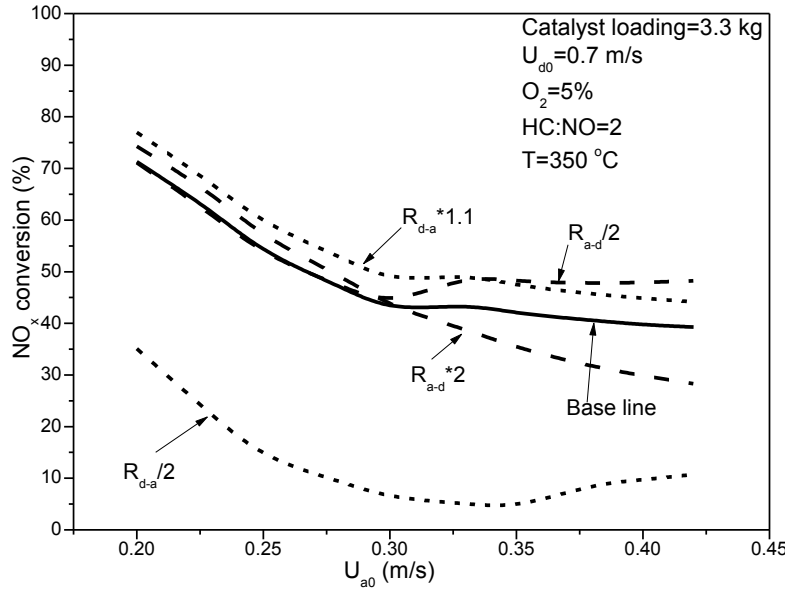


Figure 7.7 Sensitive of NO_x conversion in i-CFB to gas bypasses

7.4.2.2. Adsorption capacity and reaction rate

The sensitivity of i-CFB performance to catalyst adsorption capacity and reaction rate is investigated by model simulation. For the base line, NO_x conversion is calculated as a function of inlet flue gas velocity U_{a0} , and other conditions are set to be $U_{d0}=0.7$ m/s, $O_2=5\%$, $HC:NO=2$. As a comparison, NO_x conversions are also obtained when NO_x adsorption capacity, q_{eNO_x} , and NO_x reaction rate, R_{NO_x} , are either halved or doubled. Results in Fig. 7.8 show that NO_x conversion is not very sensitive to NO_x adsorption capacity at low flue gas velocities. This can be explained by that the NO_x adsorption capacity for the current catalyst is big enough to capture sufficient NO_x onto the catalyst surface from the annulus and carry them to the draft tube. However, when U_{a0} increases, NO_x conversion becomes more sensitive to q_{eNO_x} , with higher q_{eNO_x} leading to a higher deNO_x efficiency. Compared to NO_x adsorption capacity, the performance of i-CFB is much more sensitive to the deNO_x reaction rate. When the reaction rate constant is doubled, the overall deNO_x efficiency could reach as high as 100%. When the reaction rate is halved, NO_x conversions decrease to less than 20%. Therefore, in i-CFB, it is very important to use

catalysts of high catalytic reactivity, although NO_x adsorption capacity is also very important at high flue gas flow rate in the annulus.

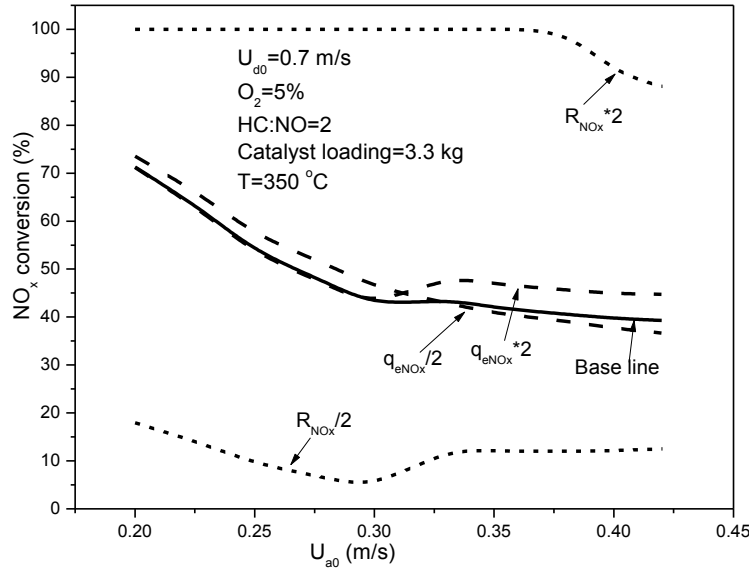


Figure 7.8 Sensitivity of NO_x conversion to variations in NO_x adsorption capacity and reduction rate constant

7.5 Simulation of i-CFB: design and optimization

7.5.1 Solids back-mixing

Solids mixing affects distributions of adsorbed NO_x in the reactor system. Fig. 7.9 presents the dimensionless NO_x concentration profile along the dimensionless bed height. For inlet condition in Fig. 7.9, i-CFB operates in the type (c) regime as shown in Fig. 7.2. So the effective bed heights of the annulus and draft tube are identical. The gas phase concentrations are calculated from NO_x concentrations in both the bubble phase and the dense phase, as indicated by Eqs. (7.15) and (7.16). These concentrations are further divided by NO_x concentration in the flue gas, C_{g0} , and plotted as dimensionless values. The NO_x concentrations in the solids phase are divided by C_{s0}^* , the equilibrium concentration of C_{g0} .

It is seen in Fig. 7.9 that the NO_x concentration in solids phase is almost uniform along the bed height. This result is consistent with the results obtained in Chapter 6 for the fluidized bed reactor, which indicates that NO_x concentration in solids phase is uniform due to strong solids back-mixing. Another interesting finding is that solids phase NO_x concentration is almost identical in the annulus and draft tube, which indicates that NO_x is sufficiently adsorbed in the annulus and circulated to the draft tube, so that the overall NO_x reduction is limited and controlled by the NO_x reduction rate in the draft tube at the simulated conditions.

The axial profiles of gas phase NO_x concentrations are quite different from the profiles of the solids phase. Gas phase NO_x concentration in the annulus decreases along the bed height since NO_x is adsorbed onto the catalyst. In the draft tube, gas phase NO_x concentration increases along the bed height because of NO_x desorption. At $H/H_0 > 0.3$, dimensionless NO_x concentration in the solids phase is higher than the gas phase dimensionless NO_x concentration in the annulus but still lower than the gas phase NO_x concentration in the draft tube. Since solids phase NO_x concentrations in the annulus and draft tube are almost the same, one may wonder how NO_x could be adsorbed from the gas phase of a lower NO_x concentration in the annulus and then desorbed to the gas with a high NO_x concentration in the draft tube. This could be interpreted by the different equilibrium concentrations in the two zones. As shown in Table 4.4, NO_x equilibrium concentration is a strong function of O_2 concentration. In the annulus with fed flue gases, O_2 concentration is higher which gives rise to a higher NO_x adsorption capacity. Gas phase NO_x concentration in equilibrium with C_{s-A} will be lower there. The dimensionless concentrations in equilibrium with C_{s-A}/C_{s0}^* and C_{s-D}/C_{s0}^* are calculated to be $C_{g-A}^*/C_{g0}=0.2$ and $C_{g-D}^*/C_{g0}=2.05$. Both equilibrium concentrations are plotted in Fig. 7.9. C_{g-D}^*/C_{g0} is not plotted proportionally to the axis since 2.05 exceeds the range. Now the driving forces of NO_x mass transfer in both adsorption and reduction zones are clear. It could also be observed from the figure that C_{g-A}/C_{g0} is very close to C_{g-A}^*/C_{g0} at the top of the reactor. It means that the solids are almost fully saturated with NO_x at the outlet of the adsorption

zone. The NO_x capture efficiency in the adsorption zone is already very high, to further improve the performance of adsorption zone the equilibrium adsorption capacity needs to be increased.

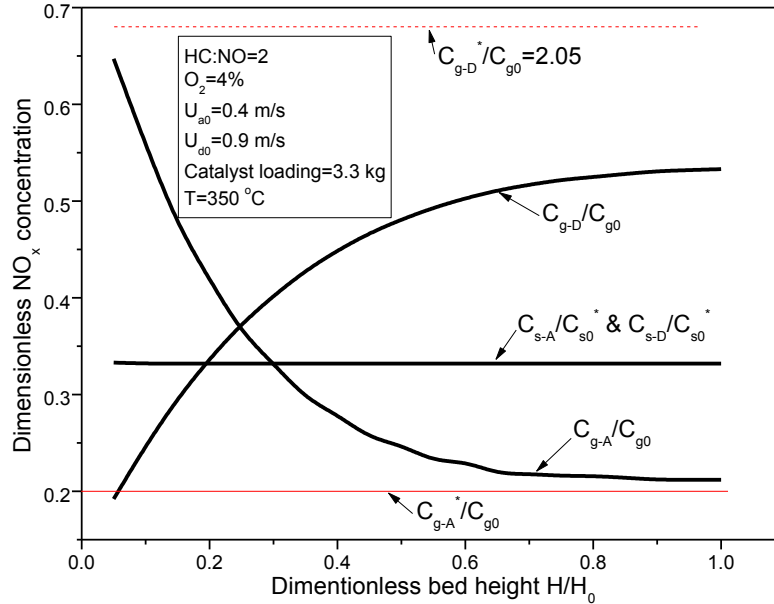


Figure 7.9 Profile of dimensionless NO_x concentration along bed height

In the Chapter 6, it was observed that decreasing solids back-mixing could significantly enhance NO_x reduction in the fluidized bed. To investigate the effect of solids back-mixing on the performance of i-CFB, both gas and solids dispersions are neglected, with both the annulus and draft tube being assumed to be operated in plug flows. With all other conditions remaining the same as the i-CFB shown in Fig. 7.9, the simulated results are found to be almost the same with those results given in Fig. 7.9. Although both zones are assumed to be in plug flow, solids phase NO_x concentrations remain constant along the bed height. This could also be explained by the fast solids circulation in the i-CFB which makes the solids phase NO_x concentration uniform along the reactor. Therefore, different from regular fluidized beds, decreasing solids back-mixing could not improve the performance of the i-CFB under the conditions simulated.

7.5.2 Solids circulation rate

The i-CFB is simulated at different solids circulation rates. Here, G_s is calculated base on the cross-sectional area in the annulus. Fig. 7.10 presents the dimensionless NO_x concentration of solids phase in both annulus and draft tube. It is observed that the concentration profile is strongly affected by solids circulation rate. Although strong back-mixing exists in fluidized beds, slopes of the concentration curves are quite big at lower solids circulation rates. The NO_x concentration is lower at the top of annulus where catalysts are returned to the annulus from the draft tube. Similarly, NO_x concentration is higher at the bottom of draft tube due to the feeding of catalyst adsorbed with NO_x from the annulus. The NO_x concentration decreases along the reactor height as NO_x is either reduced or desorbed from the catalyst surface. When the solids circulation rate increases, catalyst residence in the draft tube becomes shorter. NO_x could not be efficiently removed from the catalyst, leading to little change of NO_x concentration on the catalyst surface along the reactor. Solids phase NO_x concentrations in the annulus and draft tube also get closer at a higher G_s due to fast catalyst exchange between the two zones. At $G_s > 10 \text{ kg/m}^2 \cdot \text{s}$, there is little difference in solids phase NO_x concentration between the annulus and draft tube. Based on the discussion in the solids mixing section, it could be concluded that the axial profile of solids phase NO_x concentrations depends on solids circulation rate in i-CFBs instead of solids back-mixing. It is also confirmed that it is not useful to decrease solids back-mixing in the i-CFB.

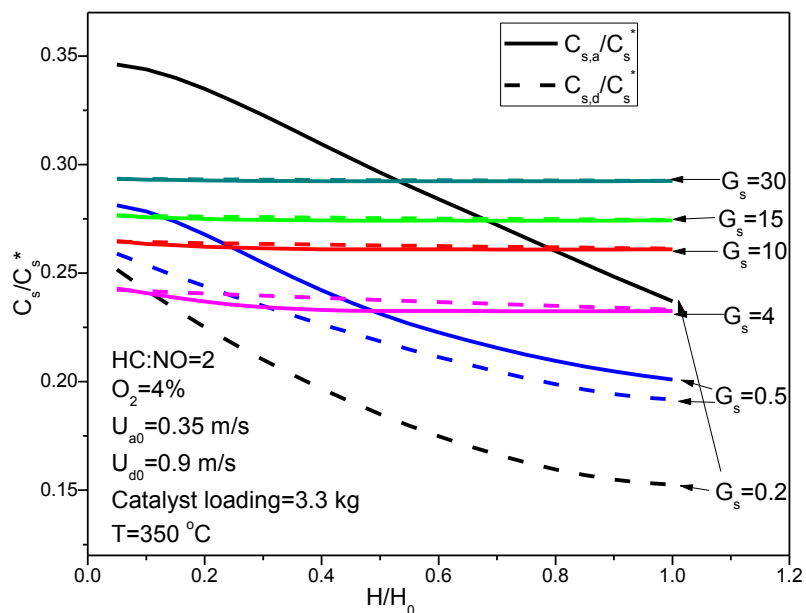


Figure 7.10 Axial profiles of dimensionless solids phase NO_x concentrations at different G_s

The overall NO_x conversion is also calculated at different solids circulation rates with the results presented in Fig. 7.10. Solids are exchanged more rapidly between the annulus and the draft tube at higher G_s , leading to effective NO_x transfer between adsorption and reduction zones. NO_x conversion in i-CFB is thus anticipated to increase with increasing solids circulation rate. The modeling result show that the conversion increases by about 5% when G_s is increased from less than $0.5 \text{ kg/m}^2\cdot\text{s}$ to $5 \text{ kg/m}^2\cdot\text{s}$. Further increasing G_s has little effect on the improvement of conversion. Although the enhancing effect of G_s is confirmed, the increase in NO_x conversion is lower than expected. The net NO_x conversion in annulus and draft tube is plotted in Fig. 7.11 to further explore the possible reason.

It is seen that among the destroyed NO_x , most is reduced in the annulus. Although draft tube is designed as the reduction zone, the converted NO_x in draft tube is only about half of the converted NO_x in the annulus. It is quite obvious that the potential of NO_x reduction in the draft tube is not fully utilized in the current i-CFB design due to the low catalyst reactivity and short contact time in the draft tube. Together with Fig. 7.10, the NO_x concentration profile shows that solids phase NO_x concentration is

higher at higher G_s . This means that sufficient amount of NO_x is passed by the catalyst from annulus to the draft tube. Instead of being efficiently consumed in the draft tube, majority of NO_x is simply returned to the adsorption zone for the next adsorption-reduction cycle. Therefore, it is suggested that longer solids residence time in the draft tube is required to further reduce NO_x in the reduction zone to fully utilize the potential of i-CFB.

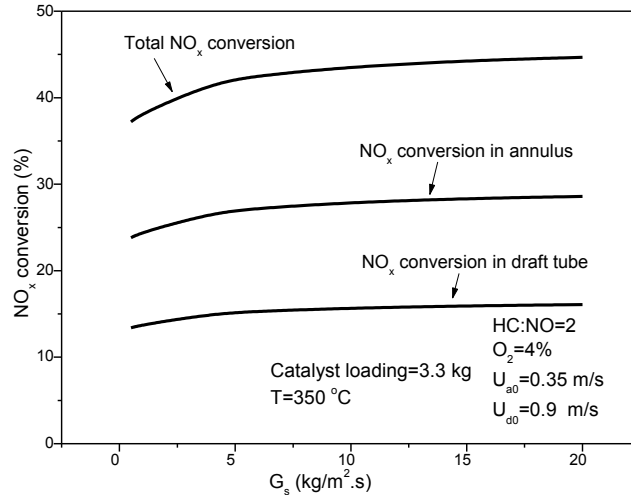


Figure 7.11 NO_x conversion as a function of solids circulation rate G_s

7.5.3 i-CFB configurations

In order to investigate the effect of solids residence time, NO_x conversion is simulated for i-CFBs with different cross sectional areas of the adsorption and reduction zones with the schematics shown in Fig. 7.12. Areas of adsorption and reduction zones are denoted as A_A and A_R , respectively. One should note that the configuration of the i-CFB may not necessarily be the same one as tested experimentally which has a draft tube and an annulus zone. Other configurations could be applied, as long as the solids could be circulated between the two zones. The total cross sectional area of the i-CFB is denoted as A_{total} , which is the sum of A_A and A_R . In the simulation, A_{total} is kept constant, the same as the total cross sectional area

of the i-CFB tested in the experiment. The fraction of the reduction zone cross area, A_R/A_{total} , is changed from 0.2 to 0.8.

To simplify the simulation and focus on the effect of A_A to A_R ratio, some other parameters are treated as simple as possible. Bed heights of the adsorption and reduction zones are assumed to be the same, determined by mass balance only. For a real i-CFB, bed height is determined by both mass and pressure balances, as well as the height of partition plate as shown in Chapter 3. Gas bypasses between the adsorption and reduction zones are not considered. The catalyst loading is set to be 3 kg. The net solids circulation flux in both annulus and draft tube is set to be constant, 0.15 kg/s, which is equivalent to about $G_s=20 \text{ kg/m}^2\cdot\text{s}$ in the experimental i-CFB. For all the cases investigated, solids are assumed to be flowing downward in the adsorption zone and upward in the reduction zone. In a real i-CFB, the direction of the solids flow depends on the pressure balance between the two zones. However, the assumption is reasonable and does not affect the simulation result. A simulation is also performed by changing the direction of solids flow manually. The results (not given here) showed that deNO_x efficiencies are the same for different solids flow directions. This is because in both zones of the i-CFB, solids back-mixing is very strong, and solids in both zones could be considered to behave like CSTR reactors. The same conclusion was also obtained in the fluidized bed adsorption (Chapter 5) and reaction (Chapter 6) modeling.

O_2 concentration in the adsorption zone is set at 8%, and O_2 is also assumed to exist in the reduction zone with a concentration of 1%. In a real i-CFB, O_2 in the reduction zone could come from the gas bypass from the adsorption zone. It could also come from the gas containing the reducing agent. However, a small portion of O_2 in the reduction zone is essential for NO_x reduction, since both Reactions (4.R3) and (4.R4) need O_2 . $\text{HC}_i:\text{NO}_x$ molar ratio is set at 2, where HC_i is the total molar flow rate of HC, which is fed into the reduction zone. Due to gas bypass, HC may also be present in the adsorption zone of the i-CFB. In Fig. 7.12, the fraction of HC passing through the reduction zone is denoted as x , and the HC fractional flow into the adsorption zone is $(1-x)$.

To evaluate the performance of i-CFB, GHSV of the reactor is set to be 5000 h^{-1} , same as the GHSV used in the fixed bed experiments. Here, GHSV of i-CFB is calculated by the flow rate of flue gas (gas in the adsorption zone) and the volume of catalyst in the whole reactor:

$$GHSV = \frac{3600F_{flue-gas}}{V_{catalyst}} \quad (7.19)$$

The volumetric flow rate of reducing agent is assumed to be half of the volumetric flow rate of flue gas. So when the cross sectional areas of both reaction and reduction zones change, the superficial gas velocity also changes.

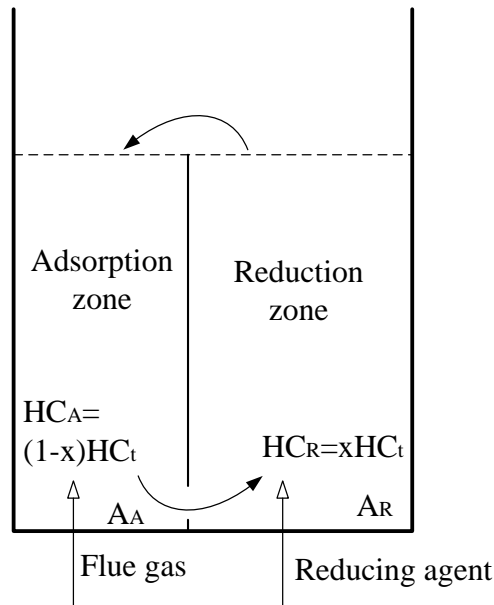


Figure 7.12 Schematics of the simulated i-CFB

The simulated NO_x conversions are plotted in Fig. 7.13 as a function of A_R/A_{total} . As expected, higher a solids residence time in the reduction zone leads to improved performance of i-CFB. When the cross-sectional area of reduction zone A_R is increased, solids velocity in this zone will be decreased, increasing the solids residence time. The curve labeled as ' $\text{HC}_R=100\% \text{HC}_t, \text{HC}_A=0$ ' corresponds to the condition with all the hydrocarbon being fed into the reduction zone. The curve clearly shows that $d\text{eNO}_x$

efficiency in i-CFB could be significantly improved at higher A_R/A_{total} , with NO_x conversion being increased from about 5% at $A_R/A_{total}=0.2$ to about 73% at $A_R/A_{total}=0.7$. Further increasing A_R will decrease the overall de NO_x efficiency. For the catalyst tested in this study, the optimum A_R/A_{total} ratio is around 0.7.

It was shown in Chapter 6 that de NO_x efficiency in the fluidized bed is lower than that in the fixed bed. This is due to gas bypassing in the bubble phase, which leads to poor contact between gas and catalyst particles. Here, the performance of de NO_x reaction is compared between the i-CFB and the fixed bed reactor. The NO_x conversion of fixed bed reactor with the same GHSV is 41%, as plotted in the figure. The performance of i-CFB is seen to be poorer than the fixed bed reactor if the cross sectional area of reduction zone is not large enough. The advantage of i-CFB could be fully explored only when the solids residence time in the reduction zone is sufficiently long. If the reactor is well designed, the i-CFB reactor could perform much better than the fixed bed reactor.

The sensitivity analysis shows that the overall de NO_x efficiency is quite sensitive to gas bypass from draft tube to annulus R_{d-a} . A possible explanation is that a higher HC concentration in the annulus lowers the NO_x concentration on the catalyst surface in the adsorption zone, which further improves the overall performance of i-CFB. Here, it is also investigated how HC distribution could affect the performance at different A_R/A_{total} ratios. NO_x conversions at different HC distributions are also plotted in Fig. 7.13. At a lower A_R/A_{total} , NO_x conversion increases when more HC goes through the adsorption zone. At $A_R/A_{total} = 0.3$, NO_x conversion increases by 5% when HC_A/HC_t increases from 0 to 10%. However, further increasing HC_A has little effect on the improvement of de NO_x efficiency. The NO_x conversion is almost the same at $HC_A=30\%HC_t$ and $HC_A=50\%HC_t$. Another interesting finding is that the positive effect of HC_A is diminishing at high A_R/A_{total} , and the trend is even reversed at $A_R/A_{total} > 0.65$. This is because HC in the reduction zone could effectively be used for NO_x reduction when A_R/A_{total} is higher and solids residence time is longer. It can also be concluded that the performance of i-CFB is less

sensitive to HC bypass at higher A_R/A_{total} ratios. Therefore, a larger cross sectional area of reduction zone is preferred for the i-CFB reactor.

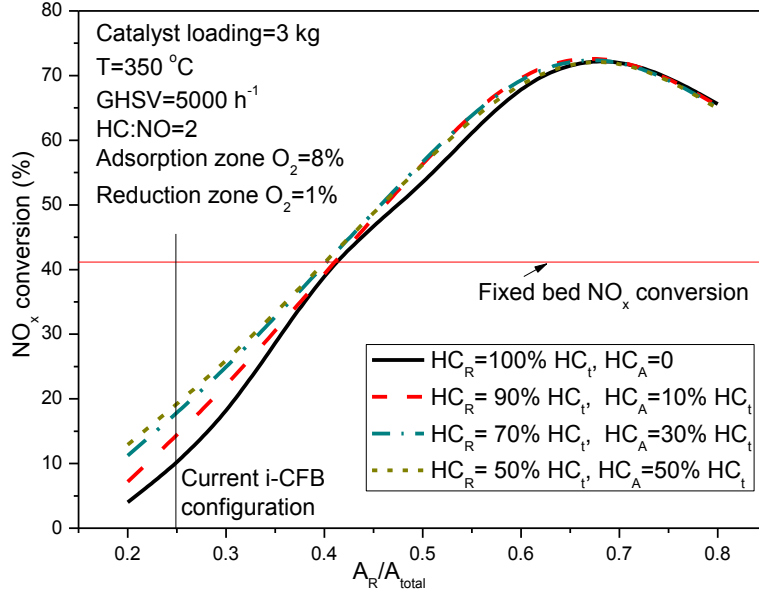


Figure 7.13 NO_x conversion as a function of A_R/A_{total}

In order to explain how A_R/A_{total} affects NO_x efficiency, NO_x concentration changes in both adsorption and reduction zones are investigated. NO_x concentration change is normalized by feeding NO_x molar flow rate, as defined by:

$$CX_{NO_x-A} = \frac{C_{in,NO_x-A} \cdot F_A - C_{out,NO_x-A} \cdot F_A}{C_{in,NO_x-A} \cdot F_A} \times 100\% \quad (7.20)$$

$$CX_{NO_x-R} = \frac{C_{in,NO_x-R} \cdot F_R - C_{out,NO_x-R} \cdot F_R}{C_{in,NO_x-A} \cdot F_A} \times 100\% \quad (7.21)$$

Positive CX values show lower NO_x concentrations at the outlet, meaning that NO_x reduction or adsorption dominates. Negative CX values indicate that NO_x concentration increases along the reactor, meaning that NO_x desorption dominates. The calculated CXs are plotted in Fig. 7.14. When A_R/A_{total}

increases, CX value in the reduction zone increases due to a longer residence time. Values of CX_{NO_x-R} increase from about -50% to about 0 when A_R/A_{total} increases from 0.2 to 0.7, which suggests more NO_x is converted by HC instead of being desorbed from the catalyst and slipping out of the reactor. CX_{NO_x-d} values close to 0 indicate that almost all NO_x on the catalyst surface is destroyed by HC and leaves little NO_x desorbed into the gas phase. At the same time, NO_x capture efficiency in the adsorption zone is increased, because NO_x concentration on catalysts returning from the reduction ozone is lowered. CX_{NO_x-a} increases from 35% to 70% when A_R/A_{total} is increased from 0.2 to 0.65. Further increasing A_R can decrease NO_x capture efficiency due to shorter solids residence time in the adsorption zone. When the improvement of NO_x reduction rate in the reduction zone cannot match the NO_x capture rate in the adsorption zone, overall $deNO_x$ efficiency in the i-CFB will get worse. This is why the optimal performance of i-CFB is around $A_R/A_{total} = 0.7$ in the simulated configuration, when the adsorption and reduction performances of the catalysts are matched.

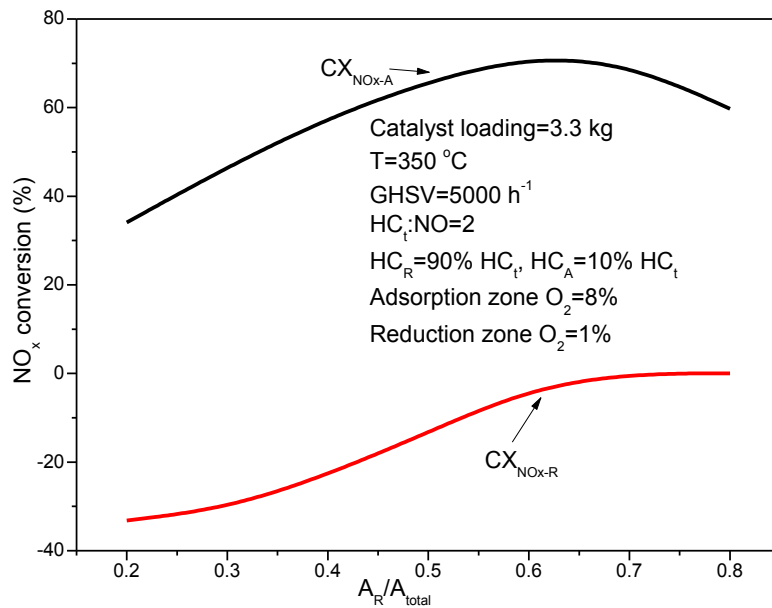


Figure 7.14 NO_x concentration change as a function of A_R/A_{total} at different zones

As discussed previously, deNO_x performance of i-CFB is not very sensitive to the catalyst adsorption capacity, q_{eNO_x} due to the insufficient solids residence time in the reduction zone, which makes NO_x reduction reaction a rate-limiting step. With the cross sectional area of reduction zone increased, NO_x reduction is no longer a rate-limiting step. Thus, there is a need to check the sensitivity to the adsorption capacity again. NO_x conversions at $HC_R=90\%HC_t$ are calculated with NO_x adsorption capacities either doubled or halved. The results are plotted in Fig. 7.15 together with the baseline. At a lower A_R , NO_x conversion is seen to be insensitive to q_{eNO_x} . q_{eNO_x} even has a negative effect on the overall deNO_x efficiency. This is explained in Fig. 7.16 based on the concentration change in the adsorption and reduction zones. At a higher NO_x adsorption capacity, NO_x capture efficiency in the adsorption zone is improved, as indicated by higher CX_{NO_x-a} values. The NO_x concentration on the catalyst surface is also expected to be higher in the adsorption zone. The NO_x concentration on the catalyst surface in the reduction zone will increase at the same time, which could lead to higher desorption of NO_x in the reduction zone. This phenomenon is indicated by the smaller CX_{NO_x-R} values in the figure. When NO_x desorption in the reduction zone exceeds adsorption in the adsorption zone, overall deNO_x efficiency decreases. At a lower A_R , little NO_x is converted catalytically in the reduction zone due to a short solids residence time, leading to serious NO_x desorption. However, with a larger A_d , more NO_x on the catalyst surface is reduced by HC, leaving less NO_x desorbed from the catalyst. More NO_x reaction in the reduction zone could also decrease the NO_x concentration on the catalyst surface and further enhance NO_x capture efficiency in the adsorption zone. Therefore, less NO_x desorption in the reduction zone and more NO_x adsorption in the adsorption zone make the overall deNO_x efficiency significantly improved at a higher A_R . In Fig. 7.15, the i-CFB performance is much more sensitive to NO_x adsorption capacity at higher A_R . NO_x conversion increases by about 25% when q_{eNO_x} is doubled at $A_R/A_{total}=0.8$. At the same time, it is observed that the optimum value of A_R/A_{total} is higher when NO_x adsorption capacity is higher. This means that a bigger reduction zone is preferred when the catalyst has a high NO_x adsorption capacity. In terms of fixed bed reactor, NO_x adsorption capacity has very little effect on the NO_x conversion, as plotted in Fig. 7.15. The positive effect of q_{eNO_x} on NO_x conversion is a unique feature of

the i-CFB reactor. It can also be concluded that a properly designed i-CFB with catalysts of sufficiently high adsorption capacity and reactivity can achieve a deNO_x efficiency of more than twice in a fixed bed reactor.

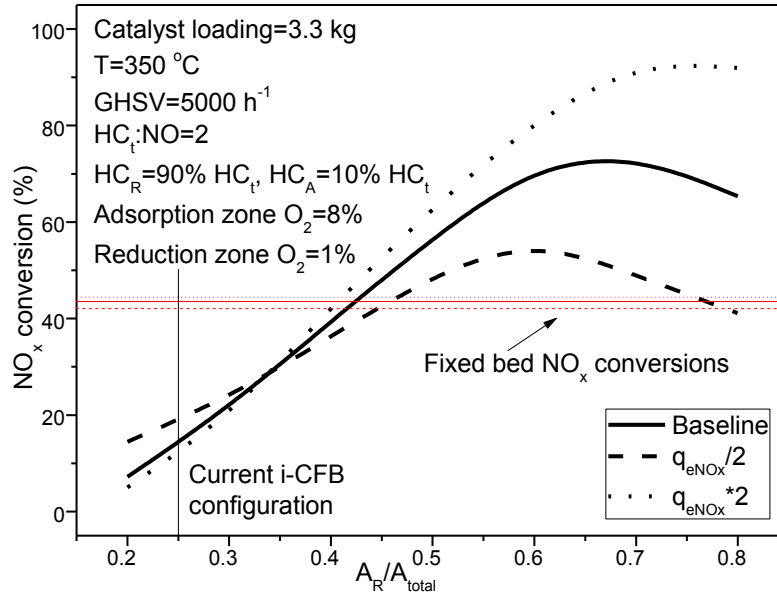


Figure 7.15 Sensitivity of NO_x conversion to NO_x adsorption capacity for i-CFBs with different configurations

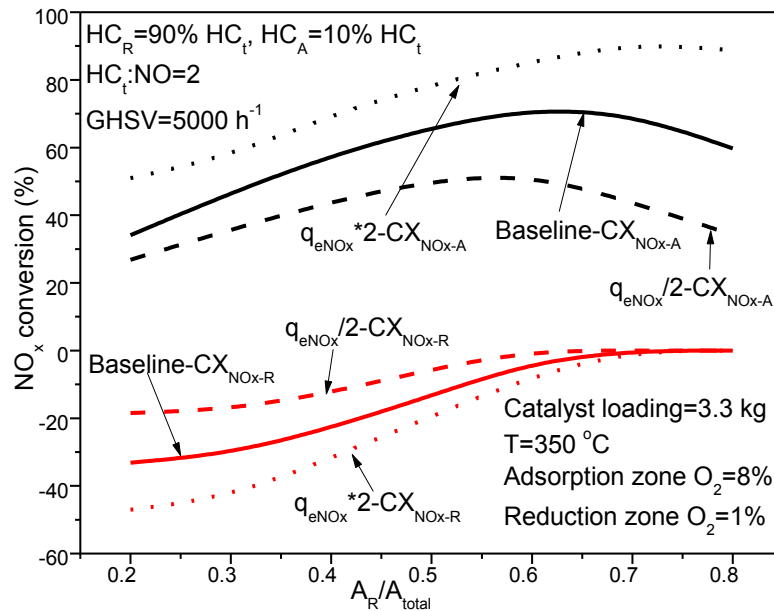


Figure 7.16 Sensitivity of NO_x concentration change to catalyst NO_x adsorption capacity

7.6 Summary

A mathematical model has been developed in this chapter to simulate the performance of the i-CFB deNO_x reactor with the intention to assist the design and optimization of the reactor. The model consists of several sub-models, including the i-CFB hydrodynamics, NO_x adsorption and reaction kinetics which were fitted and validated in previous chapters. The modeling results show a good agreement with the experimental data.

The simulation shows that deNO_x efficiency of i-CFB reactor decreases slightly with increasing the inlet flue gas velocity U_{a0} , but the negative effect of U_{a0} is expected to be much smaller than fixed bed reactor due to a better mass transfer at higher gas velocities and the contribution of the reactions in the freeboard region in the fluidized bed. For the reduction zone, deNO_x efficiency increases with increasing the inlet gas velocity U_{d0} . This is attributed to the higher R_{d-a} at a higher U_{d0} , which could significantly increase NO_x conversion as confirmed in the sensitivity analysis.

In the sensitivity analysis, it is observed that the performance of i-CFB is very sensitive to gas bypass from draft tube to the annulus, R_{d-a} , but is less sensitive to R_{a-d} . For the catalyst properties, reaction kinetics rate of the catalyst is very critical in determining the i-CFB performance, but the catalyst adsorption capacity has only marginal impact on the performance of the simulated i-CFB reactor.

Solids circulation rate G_s has little effect on the overall deNO_x efficiency. The analysis of NO_x adsorption and reaction at both the annulus and the draft tube zones revealed that solids residence time in the reduction zone is too short for the NO_x reduction reaction for the current design of i-CFB reactor. Therefore, i-CFB reactors with different cross sectional areas for adsorption and reduction zones are investigated. The simulated results showed that a large reduction zone could significantly enhance the overall deNO_x efficiency. The optimum reduction zone area fraction A_R/A_{total} should be around 0.65~0.7.

Further increases in the A_R/A_{total} ratio will decrease NO_x conversion. It is also observed that the performance of the i-CFB at higher A_R/A_{total} ratios is less sensitive to gas bypass from the reduction zone to the adsorption zone. The de NO_x efficiency of i-CFB reactor becomes more sensitive to NO_x adsorption capacity at higher A_R/A_{total} .

Chapter 8 Conclusions and recommendations for future work

8.1 Conclusions

The possible application of the integrated adsorption-reduction process was explored experimentally by Yang [11] for the selective catalytic reduction of NO_x with hydrocarbons (HC-SCR) over selected catalysts in an internal circulating fluidized bed (i-CFB). The i-CFB exhibited an ability to overcome the negative impact of excessive O_2 in the flue gas using Fe/ZSM-5(Albemarle) as the de NO_x catalyst.

The objective of this research is to model the de NO_x reaction in the i-CFB reactor in order to further optimizing the reactor design and improving its performance. The i-CFB model includes three sub-models: hydrodynamics, adsorption and reaction. Each sub-model was developed separately and validated by experimental data. An i-CFB model was then developed by integrating these sub-models and compared with i-CFB experimental data. The following conclusions can be drawn.

8.1.1 Hydrodynamics model

Hydrodynamics of the i-CFB reactor was first studied experimentally. Gas bypass was investigated by CO_2 tracer method by Yang [11], and solids circulation rate was measured in this research using an optical fibre probe at bed solids loadings of 3.3 kg and 2.275 kg. It was found that solids circulation rate was a strong function of bed loading and feeding gas velocities. At low bed loading and low draft tube gas velocity, solids circulation rate decreased as the annulus gas velocity increased. However, this trend could be reversed at high bed loadings and high draft tube velocities.

A hydrodynamic model was then developed based on mass and pressure balances. Solids discharging coefficient C_D was extracted from fitting the experimental data and an average value of 0.167

was taken for model simulation. The model could well capture the characteristics of the solids flow and gas flow distribution, and could serve as a useful tool for the design and simulation of the i-CFB deNO_x reactor system. Effective bed height and bed voidage in the draft tube and annulus could also be calculated by this model.

8.1.2 Adsorption model

The NO_x adsorption isotherm over Fe/ZSM-5 was first developed from regression of fixed bed adsorption experimental data and then applied to model fluidized bed NO_x adsorption.

To develop the adsorption kinetics, the kinetics of NO oxidation and adsorption was first proposed, following the development of Freundlich type isotherm. The isotherm parameters were fitted by adsorption capacities data obtained from fixed bed experiments. Then an axial dispersion model, which consists of a gas phase and a solids phase, was developed to simulate the breakthrough curve of NO_x adsorption. The model parameters include mass transfer coefficient and axial dispersion coefficient. The well-established mass transfer equations from literature were modified to capture the Freundlich type adsorption performance, which showed a better agreement with the experimental breakthrough curves.

A three-phase adsorption model, which includes bubble phase, solids in the dense phase and gas in the dense phase, was then proposed for the NO_x adsorption in a fluidized bed reactor. The model parameters were obtained by fitting the experimental breakthrough curves. With the fitted mass transfer and gas dispersion coefficients, the model agreed well with the experimental data. Simulations of the adsorption zone in a decoupled i-CFB showed that the NO_x concentration on the surface of feed catalysts could affect the NO_x abatement efficiency. At the same time, the large catalyst holdup in the adsorption zone is essential for achieving a high deNO_x efficiency.

8.1.3 Reaction model

Similar to the adsorption model, kinetics of deNO_x reactions was first developed with the kinetic parameters fitted from fixed bed experimental data. The kinetics was then used to model the deNO_x performance in a fluidized bed.

The kinetic model was divided into two sub-models, i), NO oxidation and adsorption, ii), NO_x reduction. The adsorption model was the same with the model developed in the adsorption section. The reduction model consists of two simplified reactions, hydrocarbon combustion and NO_x reduction. Same as the fixed bed adsorption model, two phases are included in the governing equations: solids phase and gas phase. The reaction term was embedded into the solids phase mass balance equation.

The kinetics was further applied for the fluidized bed model, which included the bubble phase, gas in the dense phase and solids in the dense phase. The model could well predict NO_x conversion in the fluidized bed. The fluidized bed deNO_x model was further applied to simulate NO_x reduction in the reduction zone of the i-CFB reactor. Comparing with conventional fluidized bed, NO_x conversion could be improved if NO_x is fed through the solids phase, as in the reduction zone of the i-CFB. Also for the reduction zone of the i-CFB, high solids circulation rates are preferred if NO_x feeding rate is set at a constant. This is because the NO_x slip ratio is lower at higher G_s, which corresponds to a better overall performance of i-CFB. If NO_x feeding rate is increased, HC feeding rate should be increased proportionally. In this case, changing HC concentration and keeping gas velocity at a constant is preferred than changing gas velocity and keeping HC concentration at a constant. The overall NO_x conversion becomes higher with a lower NO_x slip ratio when HC concentration is increased.

8.1.4 i-CFB model

The i-CFB model was developed by integrating the hydrodynamics, NO_x adsorption and reaction kinetics. The modeling results showed good agreement with the experimental data.

It is observed that deNO_x efficiency of i-CFB decreases slightly with increasing inlet flue gas velocity U_{a0} , although the negative effect of U_{a0} is much smaller than fixed bed reactors due to better mass transfer at higher gas velocities and the additional reaction in the freeboard region of the fluidized bed. For the reduction zone, deNO_x efficiency increases with increasing the inlet gas velocity of reducing agent U_{d0} . This is explained by a higher R_{d-a} at higher U_{d0} , which could significantly increase NO_x conversion, as confirmed in a sensitivity analysis.

In the sensitivity analysis, it is observed that the performance of i-CFB is very sensitive to gas bypass from draft tube to annulus R_{d-a} , while less sensitive to R_{a-d} and solids circulation rate G_s . For the catalyst properties, the reduction efficiency of NO_x adsorbed on the catalyst surface is very critical for the improvement of i-CFB performance. The simulation results showed that catalyst adsorption performance is not important for the deNO_x performance of the current i-CFB reactor configuration.

In a further simulation of i-CFB performance at different solids circulation rates, it is found that G_s has little effect on the overall deNO_x efficiency. NO_x reaction at both zones is then analyzed and it is found that the solids residence time in the reduction zone is too short in the current reactor design for the NO_x reaction. Therefore, i-CFBs with different cross sectional areas of adsorption and reduction zones are investigated. The simulated results show that a bigger reduction zone area ratio could significantly enhance the overall deNO_x efficiency. The optimum reduction zone area ratio A_R/A_{total} is determined by matching the adsorption rate in the adsorption zone with the reduction rate in the reaction zone. It is also observed that the performance of i-CFB at a higher A_R/A_{total} is less sensitive to gas bypass from reduction zone to adsorption zone.

Overall, the i-CFB model developed in this study can be used as a tool for reactor design and optimization. Simulations of deNO_x reaction in the i-CFB can provide suggestions on how to further improve its performance. For the deNO_x reaction in i-CFBs, it is possible to achieve a deNO_x efficiency higher than fixed bed reactors with the same GHSV, while maintaining a good resistance to negative O₂ effect.

8.2 Recommendations for future work

The i-CFB model developed in this study could provide some guidance for the reactor design and operation. Further research in the following aspects is still needed for the scaleup and commercialization of i-CFB deNO_x reactors:

1. The NO_x reduction efficiency of the catalyst should be tested at different temperatures. The temperature-dependent kinetics can be developed based on the experimental data, and then be used to evaluate the i-CFB performance at different temperatures.
2. As confirmed by the i-CFB model, deNO_x efficiency could be significantly enhanced at high NO_x reduction rate of the catalyst. Therefore, performance of catalyst needs to be improved, especially on the NO_x reduction rate constant. This can be achieved by introducing other metal promoters to the current Fe/ZSM-5 catalyst. Other catalyst preparation method or catalyst support could also be explored.
3. Catalyst with a better resistance to SO₂ should be developed. Catalyst deactivation due to SO₂ is one of the biggest obstacles for the wide application of HC-SCR process. It was observed in Yang's fixed bed experiment [11] that SO₂ in the flue gas feed could irreversibly decrease both the reduction efficiency and adsorption capacity of the Fe/ZSM-5 catalyst. Although effect of SO₂ was not tested in i-CFB reactor, it is anticipated that the performance of i-CFB would be negatively affected by SO₂ in the flue gas. Catalyst with a good resistance to SO₂ is strongly desired.

4. Hydrodynamics of i-CFBs with different configurations should be tested in the future. It was found from the i-CFB deNO_x simulation that a bigger cross sectional area of reduction zone could greatly increase the overall deNO_x efficiency. However, it is known that hydrodynamics of the i-CFB, either gas bypass or solids circulation rates, is quite sensitive to the reactor configuration. Hydrodynamics of other i-CFB reactor configurations should be first investigated for potential applications for deNO_x.

5. One major problem in fluidized beds is the attrition of solids, which could impact both the reaction kinetic and mechanical properties of the catalyst. Catalyst elutriation could also be a serious problem if solids are too fine. Attrition and elutriation of the selected catalyst should be tested before its application for i-CFB deNO_x reactors.

6. As discussed in Chapter 2, one benefit of fluidized beds is the convenience of catalyst regeneration. How to regenerate HC-SCR catalyst will be an important topic for investigation. Several aspects should be investigated: the deactivation rate of catalyst, rate and frequency of catalyst regeneration, the method to regenerate the catalyst, the design of regeneration system, etc.

7. CFD model could be developed for i-CFB reactors to predict and screen the hydrodynamic behaviour of the reactors with different configurations. By doing so, the number of hydrodynamic experiments will be significantly reduced.

References

- [1]. K. Wark, C.F. Warner, W.T. Davis. (1998). Air pollution: its origin and control. 3rd ed. NJ: Prentice Hall.
- [2]. K. Skalska, J.S. Miller, S. Ledakowicz. (2010). Trends in NO_x abatement: A review. *Sci. Total Environ.*, 408. 3976-3989.
- [3]. M. Radojevic. (1998). Reduction of nitrogen oxides in flue gases. *Environ. Pollut.*, 102. 685-689.
- [4]. S. Roy, M.S. Hegde, G. Madras. (2009). Catalysis for NO_x abatement. *Appl. Energy*, 86(11). 2283-2297.
- [5]. T.-S. Chou. (1995). FCC process with fines tolerant SCR reactor. Patent NO.: US 5,413,699.
- [6]. E. Hums. (1998). Is advanced SCR technology at a standstill? A provocation for the academic community and catalyst manufacturers. *Catal. Today*, 42(1-2). 25-35.
- [7]. P. Forzatti. (2001). Present status and perspectives in de-NO_x SCR catalysis. *Appl. Catal., A*, 222. 221-236.
- [8]. Z.M. Liu, J.H. Li, S.I. Woo. (2012). Recent advances in the selective catalytic reduction of NO_x by hydrogen in the presence of oxygen. *Energy Environ. Sci.*, 5(10). 8799-8814.
- [9]. Z. Liu, S.I. Woo. (2006). Recent advances in catalytic deNO_x science and technology. *Catal. Rev.*, 48. 43-89.
- [10]. T.T. Yang, H.T. Bi. (2009). A novel fluidized bed reactor for integrated NO_x adsorption-reduction with hydrocarbons. *Environ. Sci. Technol.*, 43(13). 5049-5053.
- [11]. T.T. Yang. A novel fluidized bed reactor for integrated NO_x adsorption-reduction with hydrocarbons, in Department of Chemical and Biological Engineering. 2008, University of British Columbia: Vancouver.
- [12]. H.Y. Chen, T. Voskoboinikov, W.M.H. Sachtler. (1998). Reduction of NO_x over Fe/ZSM-5 catalysts: Adsorption complexes and their reactivity toward hydrocarbons. *J. Catal.*, 180(2). 171-183.

- [13]. S.K. Park, Y.K. Park, S.E. Park, L. Kevan. (2000). Comparison of selective catalytic reduction of NO with C₃H₆ and C₃H₈ over Cu(II)-ZSM-5 and Co(II)-ZSM-5. *Phys. Chem. Chem. Phys.*, 2(23). 5500-5509.
- [14]. A. Mahecha-Betero. Comprehensive modelling and its application to simulation of fluidized bed reactors for efficient production of hydrocarbon processes, in Department of Chemical & Biological Engineering. 2009, The University of British Columbia: Vancouver.
- [15]. R.D. Toomy, H.F. Johnstone. (1952). Gaseous fluidization of solid particles. *Chem. Eng. Prog.*, 48. 220-226.
- [16]. J.R. Grace, H. Bi, M. Golriz. (2003). Circulating fluidized beds, in *Handbook of fluidization and fluid-particle systems*, W.-C. Yang, Editor. Marcel Dekker, INC.: New York. p. 485-530.
- [17]. O. Levenspiel. (1972). *Chemical reaction engineering*. 2nd ed. New York: John Wiley.
- [18]. T.C. Ho. (2003). Modeling, in *Handbook of fluidization and fluid-particle systems*, W.-C. Yang, Editor. Marcel Dekker: New York. p. 239-256.
- [19]. C.Y. Shen, H.F. Johnstone. (1955). Gas-Solid Contact in Fluidized Beds. *AIChE J.*, 1(3). 349-354.
- [20]. J.R. Grace. (1984). Generalized models for isothermal fluidized bed reactors. in *Recent Advances in the Engineering Analysis of Chemically Reacting Systems*, ed. L.K. Doraiswamy. New Delhi: Wiley.
- [21]. D. Kunii, O. Levenspiel. (1969). *Fluidization Engineering*. New York: Wiley.
- [22]. K. Kato, C.Y. Wen. (1969). Bubble assemblage model for fluidized bed catalytic reactors. *Chem. Eng. Sci.*, 24(8). 1351-1369.
- [23]. B.A. Partridge, P.N. Rowe. (1966). Chemical reaction in a bubbling gas-fluidised bed. *Trans. Inst. Chem. Engrs.*, 44(9). T335-T348.
- [24]. J.R. Grace. (1986). Fluid Beds as Chemical Reactors. in *Gas Fluidization Technology*, ed. D. Geldart. Chichester: John Wiley and Sons Ltd.
- [25]. D. Kunii, O. Levenspiel. (1991). *Fluidization Engineering*. Massachusetts: Butterworth-Heinemann.
- [26]. L. Marmo, G. Rovero, G. Baldi. (1999). Modelling of catalytic gas-solid fluidised bed reactors. *Catal. Today*, 52(2-3). 235-247.

- [27]. H.T. Bi, N. Ellis, I.A. Abba, J.R. Grace. (2000). A state-of-the-art review of gas-solid turbulent fluidization *Chem. Eng. Sci.*, 55(21). 4789-4825.
- [28]. I.A. Abba. A generalized fluidized bed reactor model across the flow regimes, in Department of Chemical and Biological Engineering. 2001, the University of British Columbia: Vancouver.
- [29]. F. Normann, K. Andersson, B. Leckner, F. Johnsson. (2009). Emission control of nitrogen oxides in the oxy-fuel process. *Prog. Energy Combust. Sci.*, 35(5). 385-397.
- [30]. P.L.T. Gabrielsson. (2004). Urea-SCR in automotive applications. *Top. Catal.*, 28(1-4). 177-184.
- [31]. F. Rahmaninejad, V.S. Gavaskar, J. Abbasian. (2012). Dry regenerable CuO/gamma-Al₂O₃ catalyst for simultaneous removal of SO_x and NO_x from flue gas. *Appl. Catal. B*, 119. 297-303.
- [32]. Y.J. Kim, H.J. Kwon, I. Heo, I.S. Nam, B.K. Cho, J.W. Choung, M.S. Cha, G.K. Yeo. (2012). Mn-Fe/ZSM5 as a low-temperature SCR catalyst to remove NO_x from diesel engine exhaust. *Appl. Catal. B*, 126. 9-21.
- [33]. R.Q. Long, R.T. Yang. (1999). Catalytic performance of Fe-ZSM-5 catalysts for selective catalytic reduction of nitric oxide by ammonia. *J. Catal.*, 188(2). 332-339.
- [34]. M.P. Ruggeri, A. Grossale, I. Nova, E. Tronconi, H. Jirglova, Z. Sobalik. (2012). FTIR in situ mechanistic study of the NH₃-NO/NO₂ "Fast SCR" reaction over a commercial Fe-ZSM-5 catalyst. *Catal. Today*, 184(1). 107-114.
- [35]. S. Brandenberger, O. Krocher, A. Tissler, R. Althoff. (2010). The determination of the activities of different iron species in Fe-ZSM-5 for SCR of NO by NH₃. *Appl. Catal. B*, 95(3-4). 348-357.
- [36]. M. Iwasaki, K. Yamazaki, K. Banno, H. Shinjoh. (2008). Characterization of Fe/ZSM-5 deNO_x catalysts prepared by different methods: Relationships between active Fe sites and NH₃-SCR performance. *J. Catal.*, 260(2). 205-216.
- [37]. S. Brandenberger, O. Krocher, M. Casapu, A. Tissler, R. Althoff. (2011). Hydrothermal deactivation of Fe-ZSM-5 catalysts for the selective catalytic reduction of NO with NH₃. *Appl. Catal. B*, 101(3-4). 649-659.
- [38]. J. Girard, G. Cavataio, R. Snow, C. Lambert. (2009). Combined Fe-Cu SCR systems with optimized ammonia to NO_x ratio for diesel NO_x control. *SAE Int. J. Fuels Lubr.*, 1(1). 603-610.

- [39]. M. Iwamoto, H. Yahiro, K. Tanda. Successful design of catalysts, in Inui, T., ed. 1988, Elsevier: Amsterdam. p. 219.
- [40]. Y. Traa, B. Burger. (1999). Zeolite-based materials for the selective catalytic reduction of NO_x with hydrocarbons. *Microporous Mesoporous Mater.*, 30(1). 3-41.
- [41]. H. He. (2008). Review of Ag/Al₂O₃-reductant system in the selective catalytic reduction of NO_x. *Catal. Surv. Asia*, (12). 38-55.
- [42]. N.W. Cant, I.O.Y. Liu. (2000). The mechanism of the selective reduction of nitrogen oxides by hydrocarbons on zeolite catalysts *Catal. Today*, 63. 133-146.
- [43]. S.Y. Joshi, M.P. Harold, V. Balakotaiah. (2010). Overall mass transfer coefficients and controlling regimes in catalytic monoliths. *Chem. Eng. Sci.*, 65(5). 1729-1747.
- [44]. M. Shelef. (1995). Selective catalytic reduction of NO_x with N-free reductants. *Chem. Rev.*, 95(1). 209-225.
- [45]. K. Lothar Riekert, B. Micheal Kotter, L. Friedrich Weyland. (1989). Method for the selective elimination of nitrogen oxides from exhaust gases. Patent NO.: US 4,867,953.
- [46]. J.R. Kittrell, D.L. Herman. (1981). Method and apparatus for reducing nitric oxide. Patent NO.: US 4,246,234.
- [47]. P.J. Jodłowski, J. Kryca, A. Rogulska, B. Gil, M. Iwaniszyn, J. Łojewska, A. Kołodziej. (2012). Advantages of a wire gauze structured reactor with a zeolite (Cu-USY) catalyst for NH₃-SCR of NO_x. *Chem. Eng. J.*
- [48]. A. Kolodziej, J. Lojewska. (2009). Experimental and modelling study on flow resistance of wire gauzes. *Chem. Eng. Process.*, 48(3). 816-822.
- [49]. A. Kolodziej, J. Lojewska, J. Tyczkowski, P. Jodlowski, W. Redzynia, M. Iwaniszyn, S. Zapotoczny, P. Kustrowski. (2012). Coupled engineering and chemical approach to the design of a catalytic structured reactor for combustion of VOCs: Cobalt oxide catalyst on knitted wire gauzes. *Chem. Eng. J.*, 200. 329-337.
- [50]. H. Sun, Y.B. Zhang, X. Quan, S. Chen, Z.P. Qu, Y.L. Zhou. (2008). Wire-mesh honeycomb catalyst for selective catalytic reduction of NO_x under lean-burn conditions. *Catal. Today*, 139(1-2). 130-134.

- [51]. F.C. Patcas, G.I. Garrido, B. Kraushaar-Czarnetzki. (2007). CO oxidation over structured carriers: A comparison of ceramic foams, honeycombs and beads. *Chem. Eng. Sci.*, 62(15). 3984-3990.
- [52]. D.S. Kalka. (1995). Integrated SCR electrostatic precipitator. Patent NO.: US 5,424,044.
- [53]. S.R. Ness, G.E. Dunham, G.F. Weber, D.K. Ludlow. (1995). SCR catalyst-coated fabric filters for simultaneous NO_x and high-temperature particulate control. *Environ. Prog.*, 14(1). 69-74.
- [54]. A.N. Hayhurst, Y. Ninomiya. (1998). Kinetics of the conversion of NO to N₂ during the oxidation of iron particles by NO in a hot fluidised bed. *Chem. Eng. Sci.*, 53(8). 1481-1489.
- [55]. S.M. Jeong, S.D. Kim. (2000). Removal of NO_x and SO₂ by CuO/gamma-Al₂O₃ sorbent/catalyst in a fluidized-bed reactor. *Ind. Eng. Chem. Res.*, 39(6). 1911-1916.
- [56]. M.F. Irfan, S.D. Kim, M.R. Usman. (2009). Modeling of NO removal over CuO/gamma-Al₂O₃ catalyst in a bubbling fluidized bed reactor. *Ind. Eng. Chem. Res.*, 48(17). 7959-7964.
- [57]. S.Q. Gao, N. Nakagawa, K. Kato, M. Inomata, F. Tsuchiya. (1996). Simultaneous SO₂/NO_x removal by a powder-particle fluidized bed. *Catal. Today*, 29(1-4). 165-169.
- [58]. K. Furuyama, Y. Ito. (1987). Reactor of moving bed type. Patent NO.: US 4,670,226.
- [59]. W. Downs, S.B. Ghorishi, R.T. Bailey, K.J. Rogers. (2010). Low-temperature, moving bed catalytic reactor for control of NO_x emissions from combustion. Patent NO.: US 7,776,293 B2.
- [60]. Y.J. Li, J.N. Armor. (1994). Selective Reduction of NO_x by Methane on Co-Ferrierites .1. Reaction and Kinetic-Studies. *Journal of Catalysis*, 150(2). 376-387.
- [61]. A. Corma, V. Fornes, E. Palomares. (1997). Selective catalytic reduction of NO_x on Cu-beta zeolites. *Appl. Catal., B*, 11(2). 233-242.
- [62]. H.-Y. Chen, W.M.H. Sachtler. (1998). Activity and durability of Fe/ZSM-5 catalysts for lean burn NO_x reduction in the presence of water vapor. *Catal. Today*, 42(1-2). 73-83.
- [63]. T.T. Yang, H.T. Bi, X.X. Cheng. (2011). Effects of O₂, CO₂ and H₂O on NO_x adsorption and selective catalytic reduction over Fe/ZSM-5. *Appl. Catal. B*, 102(1-2). 163-171.
- [64]. O.C. Snip, M. Woods, R. Korbee, J.C. Schouten, C.M. VandenBleek. (1996). Regenerative removal of SO₂ and NO_x for a 150 MWe power plant in an interconnected fluidized bed facility. *Chem. Eng. Sci.*, 51(10). 2021-2029.

- [65]. C.S. Stellema, A.W. Gerritsen, Z.I. Kolar, J.J.M. de Goeij, C.M. van den Bleek. (2001). Flow of solids in an interconnected fluidized beds system investigated using positron emission particle tracking. *Can. J. Chem. Eng.*, 79(3). 314-321.
- [66]. F.F. Snieders, A.C. Hoffmann, D. Cheesman, J.G. Yates, M. Stein, J.P.K. Seville. (1999). The dynamics of large particles in a four-compartment interconnected fluidized bed. *Powder Technol.*, 101(3). 229-239.
- [67]. H.Y. Huang, R.Q. Long, R.T. Yang. (2002). Kinetics of selective catalytic reduction of NO with NH₃ on Fe-ZSM-5 catalyst. *Appl. Catal., A*, 235(1-2). 241-251.
- [68]. Q.Q. Yu, H. Wang, T. Liu, L.P. Xiao, X.Y. Jiang, X.M. Zheng. (2012). High-efficiency removal of NO_x using a combined adsorption-discharge plasma catalytic process. *Environ. Sci. Technol.*, 46(4). 2337-2344.
- [69]. K. Yoshida, T. Kuwahara, T. Kuroki, M. Okubo. (2012). Diesel NO_x aftertreatment by combined process using temperature swing adsorption, NO_x reduction by nonthermal plasma, and NO_x recirculation: Improvement of the recirculation process. *J. Hazard. Mater.*, 231-232. 18-25.
- [70]. T. Kuwahara, K. Yoshida, Y. Kannaka, T. Kuroki, M. Okubo. (2011). Improvement of NO_x reduction efficiency in diesel emission control using nonthermal plasma combined exhaust gas recirculation process. *IEEE Trans. Ind. Appl.*, 47(6). 2359-2366.
- [71]. K. Yoshida, T. Kuroki, M. Okubo. (2009). Diesel emission control system using combined process of nonthermal plasma and exhaust gas components' recirculation. *Thin Solid Films*, 518(3). 987-992.
- [72]. D. Fissore, D.G. Tejedor, A.A. Barresi. (2006). Experimental investigation of the SCR of NO_x in a simulated moving bed reactor. *AIChE J.*, 52(9). 3146-3154.
- [73]. P. Marin, D. Fissore, A.A. Barresi, S. Ordonez. (2009). Simulation of an industrial-scale process for the SCR of NO_x based on the loop reactor concept. *Chem. Eng. Process.*, 48(1). 311-320.
- [74]. D. Fissore, O.M. Penciu, A.A. Barresi. (2006). SCR of NO_x in loop reactors: Asymptotic model and bifurcational analysis. *Chem. Eng. J.*, 122(3). 175-182.
- [75]. M. Sheintuch, O. Nekhamkina. (2004). Comparison of flow-reversal, internal-recirculation and loop reactors. *Chem. Eng. Sci.*, 59(19). 4065-4072.

- [76]. Y. Smagina, M. Sheintuch. (2011). Control of traveling solutions in a loop-reactor. *Mathematical Modelling of Natural Phenomena*, 6(1). 209-225.
- [77]. A.Y. Madai, M. Sheintuch. (2010). Reduction in greenhouse gases emission in a loop reactor adsorber: Simulations and experiments. *Chem. Eng. Sci.*, 65(19). 5392-5401.
- [78]. A.Y. Madai, M. Sheintuch. (2010). Optimal design and control of non-adiabatic loop reactors. *Chem. Eng. Sci.*, 65(1). 107-113.
- [79]. R. Sheinman, M. Sheintuch. (2009). Loop reactor design and control for reversible exothermic reactions. *Ind. Eng. Chem. Res.*, 48(11). 5185-5192.
- [80]. D.W. Agar, W. Ruppel. (1988). Extended reactor concept for dynamic deNO_x design. *Chem. Eng. Sci.*, 43(8). 2073-2078.
- [81]. A. Lindholm, H. Sjøvall, L. Olsson. (2010). Reduction of NO_x over a combined NSR and SCR system. *Appl. Catal. B*, 98(3-4). 112-121.
- [82]. T. Nakatsuji, M. Matsubara, J. Rouistenmaki, N. Sato, H. Ohno. (2007). A NO_x reduction system using ammonia-storage selective catalytic reduction in rich/lean excursions. *Appl. Catal. B*, 77(1-2). 190-201.
- [83]. J.A. Sullivan, O. Keane. (2007). A combination of NO_x trapping materials and urea-SCR catalysts for use in the removal of NO_x from mobile diesel engines. *Appl. Catal. B*, 70(1-4). 205-214.
- [84]. E.C. Corbos, M. Haneda, X. Courtois, P. Marecot, D. Duprez, H. Hamada. (2009). NO_x abatement for lean-burn engines under lean-rich atmosphere over mixed NSR-SCR catalysts: Influences of the addition of a SCR catalyst and of the operational conditions. *Appl. Catal., A: General*, 365(2). 187-193.
- [85]. Y. Li, Deeba, J.C. Dettling, J.A. Patchett, S.A. Roth. (2011). Emission treatment system with NSR and SCR catalyst. Patent NO.: US 7,919,051 B2.
- [86]. H.S. Gandhi, J.V. Cavatalo, R.H. Hammerle, Y. Chen. (2004). Catalyst system for NO_x and NH₃ emission. Patent NO.: US 2004/0076565 A1.
- [87]. L. Xu, R.W. McCabe. (2012). LNT plus in situ SCR catalyst system for diesel emissions control. *Catal. Today*, 184(1). 83-94.

- [88]. R. Bonzi, L. Lietti, L. Castoldi, P. Forzatti. (2010). NO_x removal over a double-bed NSR-SCR reactor configuration. *Catal. Today*, 151(3-4). 376-385.
- [89]. L. Castoldi, R. Bonzi, L. Lietti, P. Forzatti, S. Morandi, G. Ghiotti, S. Dzwigaj. (2011). Catalytic behaviour of hybrid LNT/SCR systems: Reactivity and in situ FTIR study. *J. Catal.*, 282(1). 128-144.
- [90]. C.K. Seo, H. Kim, B. Choi, M.T. Lim, C.H. Lee, C.B. Lee. (2011). De-NO_x characteristics of a combined system of LNT and SCR catalysts according to hydrothermal aging and sulfur poisoning. *Catal. Today*, 164(1). 507-514.
- [91]. F. Can, X. Courtois, S. Royer, G. Blanchard, S. Rousseau, D. Duprez. (2012). An overview of the production and use of ammonia in NSR + SCR coupled system for NO_x reduction from lean exhaust gas. *Catal. Today*, 197. 144-154.
- [92]. B.K. Cho. (2012). Dual bed catalyst system for NO_x reduction in lean burn engine exhaust. Patent NO.: US 8,099,951 B2.
- [93]. J.H. Jeon, S.D. Kim, S.J. Kim, Y. Kang. (2008). Solid circulation and gas bypassing characteristics in a square internally circulating fluidized bed with draft tube. *Chem. Eng. Process.*, 47(12). 2351-2360.
- [94]. B.H. Song, Y.T. Kim, S.D. Kim. (1997). Circulation of solids and gas bypassing in an internally circulating fluidized bed with a draft tube. *Chem. Eng. J.*, 68. 115-122.
- [95]. H.S. Ahn, W.J. Lee, S.D. Kim, B.H. Song. (1999). Solid circulation and gas bypassing in an internally circulating fluidized bed with an orifice type draft tube. *Korean J. Chem. Eng.*, 16. 618-623.
- [96]. S.D. Kim, Y.H. Kim, S.A. Roh, D.H. Lee. (2002). Solid circulation characteristics in an internally circulating fluidized bed with orifice-type draft tube. *Korean J. Chem. Eng.*, 19. 911-916.
- [97]. H.T. Bi, J.R. Grace. (1995). Effect of Measurement Method on the Velocities Used to Demarcate the Onset of Turbulent Fluidization. *Chem. Eng. J.*, 57(3). 261-271.
- [98]. T.D. Hadley, C. Doblin, J. Orellana, K.-S. Lim. Experimental quantification of the solids flux in an internally circulating fluidized bed, in *The 13th International Conference on Fluidization - New Paradigm in Fluidization Engineering*. 2010.

- [99]. Z. Chen. Hydrodynamics, stability and scale-up of slot-rectangular spouted beds, in Department of Chemical and Biological Engineering. 2008, The University of British Columbia: Vancouver.
- [100]. J.Z. Liu, J.R. Grace, X.T. Bi. (2003). Novel multifunctional optical-fiber probe: I. Development and validation. *AIChE J.*, 49(6). 1405-1420.
- [101]. X.Q. Song, H.T. Bi, C.J. Lim, J.R. Grace, E. Chan, B. Knapper, C. McKnight. (2004). Hydrodynamics of the reactor section in fluid cokers. *Powder Technol.*, 147(1-3). 126-136.
- [102]. C.Y. Yan, C.X. Lu, Y.S. Liu, R. Cao, M.X. Shi. (2009). Hydrodynamics in airlift loop section of petroleum coke combustor. *Powder Technol.*, 192(2). 143-151.
- [103]. W. Namkung, C. Guy, R. Legros. (2001). Prediction of solids circulation rate in the riser of an internally circulating fluidized bed (ICFB). *Chem. Eng. Commun.*, 188(1). 47-58.
- [104]. K. Svoboda, S. Kalisz, F. Miccio, K. Wiecek, M. Pohorely. (2009). Simplified modeling of circulating flow of solids between a fluidized bed and a vertical pneumatic transport tube reactor connected by orifices. *Powder Technol.*, 192(1). 65-73.
- [105]. H. Konno, S. Saito. (1969). Pneumatic conveying of solids through straight pipes. *J. Chem. Eng. Jpn.*, 2. 211-217.
- [106]. M. Kuramoto, D. Kunii, T. Furusawa. (1986). Flow of dense fluidized particles through an opening in a circulation system. *Powder Technol.*, 47(2). 141-149.
- [107]. W.Q. Zhong, M.Y. Zhang, B.S. Jin, X.P. Chen. (2006). Flow pattern and transition of rectangular spout-fluid bed. *Chem. Eng. Process.*, 45(9). 734-746.
- [108]. Q.J. Guo, G.X. Yue, J.Y. Zhang, Z.Y. Liu. (2001). Hydrodynamic characteristics of a two-dimensional jetting fluidized bed with binary mixtures. *Chem. Eng. Sci.*, 56(15). 4685-4694.
- [109]. P. Cai, G.D. Michele, A.T. Gradassi. (1993). A generalized method for predicting gas flow distribution between the phases in FBC. *Fluidized bed combustion*, 2. 991-1002.
- [110]. S.P. Babu, B. Shah, A. Talwalkar. (1978). Fluidization correlations for coal gasification materials, minimum fluidization velocity and fluidized bed expansion ratio. *AIChE Symp. Ser.*, 74. 176-186.
- [111]. T.S. Pugsley, F. Berruti. (1996). A predictive hydrodynamic model for circulating fluidized bed risers. *Powder Technol.*, 89(1). 57-69.

- [112]. A. Lindholm, N.W. Currier, J.H. Li, A. Yezerets, L. Olsson. (2008). Detailed kinetic modeling of NO_x storage and reduction with hydrogen as the reducing agent and in the presence of CO₂ and H₂O over a Pt/Ba/Al catalyst. *J. Catal.*, 258(1). 273-288.
- [113]. K. Leistner, A. Nicolle, P. Da Costa. (2012). Modelling the kinetics of NO oxidation and NO_x storage over platinum, ceria and ceria zirconia. *Appl. Catal. B*, 111. 415-423.
- [114]. N. Rankovic, A. Nicolle, P. Da Costa. (2010). Detailed kinetic modeling study of NO_x oxidation and storage and their interactions over Pt/Ba/Al₂O₃ monolith catalysts. *J. of Phys. Chem. C*, 114(15). 7102-7111.
- [115]. L. Olsson, H. Sjoval, R.J. Blint. (2009). Detailed kinetic modeling of NO_x adsorption and NO oxidation over Cu-ZSM-5. *Appl. Catal., B*, 87(3-4). 200-210.
- [116]. L. Cao, J.L. Ratts, A. Yezerets, N.W. Currier, J.M. Caruthers, F.H. Ribeiro, W.N. Delgass. (2008). Kinetic modeling of NO_x storage/reduction on Pt/BaO/Al₂O₃ monolith catalysts. *Ind. Eng. Chem. Res.*, 47(23). 9006-9017.
- [117]. B.R. Kromer, L. Cao, L. Cumarantunge, S.S. Mulla, J.L. Ratts, A. Yezerets, N.W. Currier, F.H. Ribeiro, W.N. Delgass, J.M. Caruthers. (2008). Modeling of NO oxidation and NO_x storage on Pt/BaO/Al₂O₃ NO_x traps. *Catal. Today*, 136(1-2). 93-103.
- [118]. P.S. Metkar, V. Balakotaiah, M.P. Harold. (2011). Experimental study of mass transfer limitations in Fe- and Cu-zeolite-based NH₃-SCR monolithic catalysts. *Chem. Eng. Sci.*, 66(21). 5192-5203.
- [119]. M.I. Rodrigues, C.A. Zaror, F. Maugeri, J.A. Asenjo. (1992). Dynamic modeling, simulation and control of continuous adsorption recycle extraction. *Chem. Eng. Sci.*, 47(1). 263-269.
- [120]. F. Laurent, C.J. Pope, H. Mahzoul, L. Delfosse, P. Gilot. (2003). Modelling of NO_x adsorption over NO_x adsorbers. *Chem. Eng. Sci.*, 58(9). 1793-1803.
- [121]. D. Richard, M.D.D. Nunez, D. Schweich. (2010). Adsorption of complex phenolic compounds on active charcoal: Breakthrough curves. *Chem. Eng. J.*, 158(2). 213-219.
- [122]. A. Claudino, J.L. Soares, R.F.P.M. Moreira, H.J. Jose. (2004). Adsorption equilibrium and breakthrough analysis for NO adsorption on activated carbons at low temperatures. *Carbon*, 42(8-9). 1483-1490.

- [123]. S. Dasgupta, V. Agnihotri, P. Gupta, A. Nanoti, M.O. Garg, A.N. Goswami. (2009). Simulation of a fixed bed adsorber for thiophene removal. *Catal. Today*, 141(1-2). 84-88.
- [124]. A. Gupta, V. Gaur, N. Verma. (2004). Breakthrough analysis for adsorption of sulfur-dioxide over zeolites. *Chem. Eng. Process.*, 43(1). 9-22.
- [125]. W. Whitman. (1923). The two film theory of gas absorption. *Chem. Metal. Eng.*, 29. 146-148.
- [126]. J.M.P.Q. Delgado. (2006). A critical review of dispersion in packed beds. *Heat Mass Transfer*, 42(4). 279-310.
- [127]. J.D. Seader, E.J. Henley. (1998). *Separation process principles*: John Wiley & Sons, Inc. 835.
- [128]. N. Wakao, T. Funazkri. (1978). Effect of fluid dispersion coefficients on particle-to-fluid mass-transfer coefficients in packed-beds - correlation of Sherwood numbers. *Chem. Eng. Sci.*, 33(10). 1375-1384.
- [129]. P. Menoud, L. Cavin, A. Renken. (1998). Modelling of heavy metals adsorption to a chelating resin in a fluidized bed reactor. *Chem. Eng. Process.*, 37(1). 89-101.
- [130]. T.C. Ho, N. Kobayashi, Y.K. Lee. (2002). Modeling of mercury sorption by activated carbon in a confined, a semi-fluidized, and a fluidized bed. *Waste Manage.*, 22(4). 391-398.
- [131]. K. Darkwa, A. Ianakiev, P.W. O'Callaghan. (2006). Modelling and simulation of adsorption process in a fluidised bed thermochemical energy reactor. *Appl. Therm. Eng.*, 26(8-9). 838-845.
- [132]. A.M. Hamed, W.R. Abd El Rahman, S.H. El-Eman. (2010). Experimental study of the transient adsorption/desorption characteristics of silica gel particles in fluidized bed. *Energy*, 35(6). 2468-2483.
- [133]. A. Gaikwad, S. Kale, A. Lali. (2008). Modeling of counter-current adsorption in continuous liquid-solid circulating fluidized bed adsorption chromatography. *Chem. Eng. Sci.*, 63(4). 1062-1071.
- [134]. S. Veeraraghavan, L.T. Fan, A.P. Mathews. (1989). Modeling adsorption in liquid solid fluidized-beds. *Chem. Eng. Sci.*, 44(10). 2333-2344.
- [135]. S.P. Sit, J.R. Grace. (1981). Effect of bubble interaction on interphase mass transfer in gas fluidized bed. *Chem Eng. Sci.*, 36. 327-335.

- [136]. A. Gunther, H. Helmrich, K. Schugerl. (1980). Axial-dispersion of solid and properties of gas-bubbles of a continuous fluidized-bed. *Chem. Ing. Tech.*, 52(10). 841-841.
- [137]. G. Weislehn. (1970). Determination of solid mixing coefficients in a gas fluidized bed. *Chem. Ing. Tech.*, 42(8). 524-530.
- [138]. S. Morooka, Y. Kato, T. Miyauchi. (1972). Holdup of gas bubbles and longitudinal dispersion coefficient of solid particles in fluid-bed contactors for gas-solid systems. *J. Chem. Eng. Jpn.*, 5(2). 161.
- [139]. L.H. Chen, C.Y. Wen. (1982). Model of solid gas reaction phenomena in the fluidized-bed freeboard. *AIChE J.*, 28(6). 1019-1027.
- [140]. H.Y. Chen, T. Voskoboinikov, W.M.H. Sachtler. (1999). Reaction intermediates in the selective catalytic reduction of NO_x over Fe/ZSM-5. *J. Catal.*, 186(1). 91-99.
- [141]. C. Sheindorf, M. Rebhun, M. Sheintuch. (1981). A Freundlich-type multicomponent isotherm. *J. Colloid Interface Sci.*, 79(1). 136-142.

Appendix A More discussions on solids circulation rate

Why G_s decreases when U_{a0} increases at bed loading=2.275 kg which is contradict with the observation in the literature?

Since the characteristics of gas bypass is unknown, detailed and accurate analysis could not be obtained. So here it is assumed that there is no gas bypass and the pressure drop could be analyzed quantitatively.

Following the calculated procedure in Table 3.1, most of the flow patterns of the tested points are type (b) in Fig. 3.4. The effective bed height in the draft tube equals the height of draft tube and the annulus effective bed height changes with the voidage. Since the inlet gas velocity of the draft tube does not change, the pressure drop ΔP_d is constant. For most of the data points, the annulus is operated as a fluidized bed. It can be assumed that the pressure drop in the annulus is determined by the weight of solids in the annulus.

$$\Delta P_a = g\rho_p(1 - \varepsilon_a)L_a = gM_a / A_a \quad (\text{A.1})$$

If the draft tube gas velocity is constant, voidage in the draft tube is constant, so does the amount of solids in the draft tube. Solids weight in the annulus does not change at various U_{a0} , which gives rise to a constant pressure drop across the annulus. Thus the pressure drop through the orifice, ΔP_{or} , remains constant. According to Eq. (3.10), solids circulation rate is influenced by ΔP_{or} and ε_a . At higher U_{a0} , ε_a becomes bigger, leading to lower G_s .

An attempt was made to model the solids circulation rate at bed solids loading of 2.275 kg, with the results plotted in Fig. A.1 as lines. Gas bypass was not considered since there are no data available. Therefore, the modeling results are not reliable for reactor design purpose. But they could be used to observe the trend of solids circulation rate at different conditions. It could be seen that all the modeling results fall into reasonable range of the experimental data. All the solids circulation rates decrease with annulus gas velocity, confirming the reasonability of the experiments and the explanations shown above.

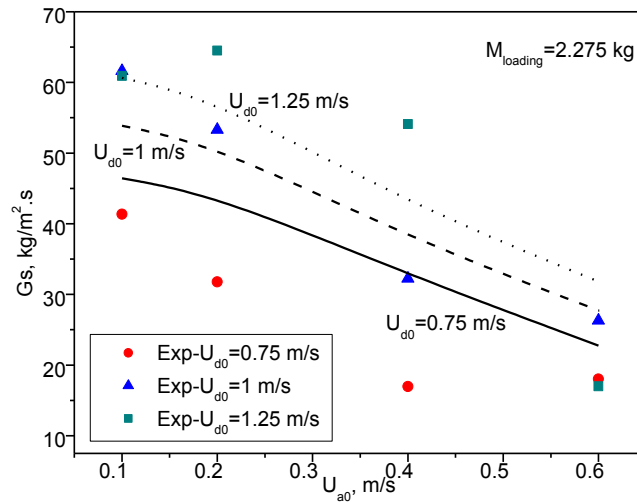


Figure A.1 Experimental and modeled solids circulation rates at a bed solids loading of 2.275 kg. (Symbols: experimental data; lines: modeling results.)

Appendix B Derivation of adsorption isotherm

The rate constants K_{O_2} and K_{NO_2} could be described with the Arrhenius expression:

$$k_i = A_i e^{-E_{ai}/RT} \quad (B.1)$$

Olsson et al. [115] observed that the desorption peak for NO_2 was broad in the NO_2 TPD on Cu/ZSM-5 catalyst, suggesting that NO_2 is adsorbed on the surface with different energy levels. Similarly, one could speculate that NO_x could also be adsorbed on the surface of Fe/ZSM-5 catalyst with different energy levels. Fitting the adsorption equilibrium to the Langmuir isotherm, which has been widely used for NO_x adsorption, it was found that the NO_x adsorption data for Fe/ZSM-5 used in this work did not fit well into the Langmuir isotherm with a single activation energy, suggesting that NO_x was adsorbed onto the surface of Fe/ZSM-5 with different energy levels. Therefore, the Freundlich isotherm, which assumes the adsorption energies follow an exponential distribution [141], was applied in this study.

$$N(Q) = \alpha \cdot \exp(-nQ/RT) \quad (B.2)$$

where $N(Q)$ is the number of sites having adsorption energy Q , and α and n are constants. It is further assumed that for each energy level, the coverage Θ follows the Langmuir isotherm. For O_2 adsorption, the coverage Θ is

$$\Theta = \frac{b \cdot C_{O_2}}{1 + b \cdot C_{O_2}} \quad (B.3)$$

The adsorption coefficient b depends on the adsorption energy in the form

$$b = b_0 \cdot \exp(Q/RT) \quad (B.4)$$

The fraction of adsorption sites occupied by adsorbate having an energy of adsorption between Q and Q+dQ is

$$d\Theta_T = \Theta(Q) \cdot N(Q)dQ \quad (\text{B.5})$$

The total coverage by the adsorbate is obtained by integration of equation (B.5) over the whole range of adsorption energies, i.e. between the limits $-\infty$ and $+\infty$. The integral after substitution of $\Theta(Q)$ and $N(Q)$ from equations (B.3)-(B.5) becomes

$$\Theta_T = \int_{-\infty}^{+\infty} \frac{b_0 \cdot \exp(Q/RT) \cdot C_{O_2}}{1 + b_0 \cdot \exp(Q/RT) \cdot C_{O_2}} \cdot \alpha \cdot \exp(-nQ/RT) dQ \quad (\text{B.6})$$

which yields

$$\Theta_T = \frac{\alpha RT b_0^n}{n} C_{O_2}^n = A C_{O_2}^n \quad (\text{B.7})$$

If the adsorption is expressed in terms of mole of adsorbate per unit volume of adsorbent q_e , the Freundlich isotherm is written in the form

$$q_e = c_m \cdot \frac{\alpha RT b_0^n}{n} C_{O_2}^n = k_F C_{O_2}^n \quad (\text{B.8})$$

For O_2 adsorption in the experiment with kinetics represented by reactions (4.R1) and (4.R2), Eq. (B.8) could still be used to calculate the O_2 adsorption. This is because the adsorbed O_2 and NO_2 contribute to only a small part of the total active sites (calculated previously as $216 \text{ mol/m}^3 \text{ cat}$), which further implies that the adsorption of O_2 is not affected by the adsorbed NO_x .

The adsorption of NO_2 could now be expressed as

$$[NO_2^*] = K_{NO_2} \cdot C_{NO} \cdot [O^*] = K_{NO_2} \cdot C_{NO} \cdot k_{FO_2} C_{O_2}^{n_{O_2}} \quad (\text{B.9})$$

An exponential distribution of adsorption energies is also assumed for K_{NO_2} . To keep consistent with equation (B.3), K_{NO_2} is replaced by b_{NO_2} . The total coverage of NO_2 could be integrated as

$$\Theta_T = \int_{-\infty}^{+\infty} b_{NO_2} \cdot C_{NO} \cdot k_{FO_2} C_{O_2}^{n_{O_2}} \cdot N(Q) dQ = k_{FO_2} C_{O_2}^{n_{O_2}} \int_{-\infty}^{+\infty} b_{NO_2} \cdot C_{NO} \cdot N(Q) dQ \quad (B.10)$$

The integration term in equation (B.10) could be calculated as

$$\begin{aligned} \int_{-\infty}^{+\infty} b_{NO_2} \cdot C_{NO} \cdot N(Q) dQ &= \int_{-\infty}^{+\infty} \frac{b_{NO_2} \cdot C_{NO}}{1 + b_{NO_2} \cdot C_{NO}} (1 + b_{NO_2} \cdot C_{NO}) \cdot N(Q) dQ \\ &= \int_{-\infty}^{+\infty} \frac{b_{NO_2} \cdot C_{NO}}{1 + b_{NO_2} \cdot C_{NO}} \cdot N(Q) dQ + \int_{-\infty}^{+\infty} \frac{b_{NO_2} \cdot C_{NO}}{1 + b_{NO_2} \cdot C_{NO}} \cdot b_{NO_2} \cdot C_{NO} \cdot N(Q) dQ \end{aligned} \quad (B.11)$$

Similar to the integration of O_2 coverage, the first term of equation (B.11) gives

$$\int_{-\infty}^{+\infty} \frac{b_{NO_2} \cdot C_{NO}}{1 + b_{NO_2} \cdot C_{NO}} \cdot N(Q) dQ = \frac{\alpha R T b_0^n}{n} C_{NO}^n \quad (B.12)$$

The second term could be integrated with the activation energy

$$\begin{aligned} \int_{-\infty}^{+\infty} \frac{b_{NO_2} C_{NO}}{1 + b_{NO_2} C_{NO}} \cdot b_{NO_2} C_{NO} \cdot N(Q) dQ &= \int_{-\infty}^{+\infty} \frac{b_0 \cdot \exp(Q/RT) \cdot C_{NO}}{1 + b_0 \cdot \exp(Q/RT) \cdot C_{NO}} \cdot \alpha \cdot \exp(-nQ/RT) \cdot b_0 \cdot \exp(Q/RT) \cdot C dQ \\ &= \frac{\alpha R T b_0^n}{n-1} C_{NO}^n \end{aligned} \quad (B.13)$$

The total NO_2 coverage, Θ_{TNO_2} , is

$$\Theta_T = \frac{\alpha R T b_0^n}{n} C_{NO}^n + \frac{\alpha R T b_0^n}{n-1} C_{NO}^n = \alpha R T b_0^n \left(\frac{1}{n} + \frac{1}{n-1} \right) C_{NO}^n = B C_{NO}^n \quad (B.14)$$

The adsorption capacity is

$$q_{eNO_2} = k_{FO_2} C_{O_2}^{n_{O_2}} \cdot \left[\alpha R T b_0^n \left(\frac{1}{n} + \frac{1}{n-1} \right) C_{NO}^n \right] \cdot c_m = k_{FO_2} C_{O_2}^{n_{O_2}} \cdot k_{FNO_2} C_{NO}^{n_{NO_2}} \quad (B.15)$$

The adsorbed O₂ and NO₂ could be expressed as:

$$q_{eO_2} = k_{FO_2} \cdot c_{O_2}^{n_{O_2}} \quad (\text{B.16})$$

$$q_{eNOx} = k_{FO_2} \cdot c_{O_2}^{n_{O_2}} \cdot k_{FNO_2} \cdot c_{NO}^{n_{NO_2}} \quad (\text{B.17})$$

Appendix C Detailed discussion on k_f

Mass transfer term $k_f(C_s - C_s^*)$ used in Eqs. (4.17) and (4.19) is slightly different with classic term $k(q^* - \bar{q})$ for mass transfer [127] as shown in Eq. (C.1).

$$\frac{\partial \bar{q}}{\partial t} = k(q^* - \bar{q}) = kK(C_g - C_g^*) \quad (\text{C.1})$$

where q^* is the adsorbate loading in equilibrium with the solute concentration, C_g , in the bulk fluid; C_g^* is the concentration in equilibrium with the average loading \bar{q} ; k is the overall mass transfer coefficient, which includes both external and internal transport resistances; and K is the adsorption equilibrium constant for a linear adsorption isotherm of the form $q = KC_g$.

For the term $kK(C_g - C_g^*)$ in Eq. (C.1), it is assumed that the adsorption follows a linear isotherm. However, the adsorption of NO_x on Fe/ZSM-5 follows the Freundlich type isotherm. The model with mass transfer treated as $kK(C_g - C_g^*)$ could not well capture the adsorption characteristics of Fe/ZSM-5. So the mass transfer term is modified to capture the Freundlich type adsorption performance. The modified model is investigated in Chapter 4 and then confirmed to fit better with the experiment than the classic model. Similar modification of the model is also adopted by Dasgupta [123] to enable the Langmuir form of isotherm to be used. But in Dasgupta's model, only intra-phase mass transfer resistance is considered.

In order to investigate the characteristics of k_f , there is a need to quote Eq. (C.1) again. Since the modified term $k_f(C_s - C_s^*)$ is comparable to the classic term $k(q^* - \bar{q})$, it is expected that characteristics of parameter k_f is similar with k . However, there is correlation in literature to calculate k directly. Eq. (C.2) is the most often used equation to calculate kK as a lumped factor.

$$\frac{1}{kK} = \frac{R_p}{3k_c} + \frac{R_p^2}{15D_e} \quad (\text{C.2})$$

where the second term on the right side represents the internal resistance and the first term represents the external mass transfer resistance, $k_c a_v$, since for a sphere the surface area/unit volume, a_v , is given by

$$4\pi R_p^2 / \left[\left(\frac{4}{3} \right) \pi R_p^3 \right] = 3 / R_p \quad (\text{C.3})$$

For the estimation of the external mass transfer coefficient k_c in fixed beds, the correlation of Wakao [128] could be used:

$$Sh = \frac{k_c d_p}{D_m} = 2.0 + 1.1 Sc^{1/3} Re^{1/2} \quad 3 < Re < 10^4 \quad (\text{C.4})$$

From Eq. (C.2), kK , as a lumped factor, is determined by the external and internal mass transfer characteristics and is independent with adsorption equilibrium K . Therefore, Eq. (C.2) could be simplified to Eq. (C.5), in which α is a constant calculated from k_c , R_p and D_e .

$$kK = \alpha \quad (\text{C.5})$$

And then it is obvious that k is linear to $1/K$, as shown in Eq. (C.6).

$$k = \alpha / K \quad (\text{C.6})$$

It could be further expected that there is a same relationship between k_f and K .

$$k_f = \alpha / K \quad (\text{C.7})$$

If there is a k_f value (k_{f0}) fitted at one condition, other k_f values could be calculated from Eq. (C.8). Here, k_c , R_p and D_e remain unchanged. It should be noted that K_i is the adsorption equilibrium of linear isotherm.

$$k_f = k_{f0} K_{i0} / K_i \quad (\text{C.8})$$

The value of K_i should be obtained according to Eq. (C.9) at each condition since the adsorption of NO_x on Fe/ZSM-5 follows Freundlich isotherm.

$$K_i = q_{ei} / C_{gi} = k_{Fi} C_{gi}^{n_i} / C_{gi} \quad (\text{C.9})$$

It is assumed that hydrocarbon is transferred from the gas phase to solids and then reacts with adsorbed NO_x on the catalyst surface. Therefore, different k_f value is used for HC mass balance equation:

$$\frac{1}{k_f} = \frac{R_p}{3k_c} + \frac{R_p^2}{15D_e} \quad (\text{C.10})$$

Appendix D Details of adsorption experiments

D.1 Experimental procedure of fixed bed adsorption

The simulated flue gas used in the experiment was a mixture prepared from several gas cylinders: 21% O₂ balanced with N₂, 0.3% NO balanced with N₂ and pure N₂ gas cylinders from Praxair Products Inc. The compositions (NO_x and O₂) of the effluent gases were analyzed by a Horiba PG-250 flue gas analyzer.

Before the start up of the experiment, the reactor was first heated to the desired temperature with pure N₂ gas passing through the catalyst bed. After the reactor temperature was stabilized, the flow of a gas mixture at a preset composition was turned on to start the experiment, with the gas mixture inlet composition determined by the same gas analyzer.

In the NO_x adsorption experiment, the model flue gas was pre-mixed with pure N₂ as the balance gas according to the preset flow rate and concentrations of NO and O₂. The composition of flue gas mixture was then measured by the gas analyzer. After stable readings of the analyzer were reached, which corresponded to the inlet model flue gas concentrations, the three way valves switched the flow to the reactor inlet and the time was recorded as the starting point of adsorption. During the adsorption process, the gas composition at the reactor's outlet was continuously monitored until the NO_x concentration became stable, with the final NO_x concentration defined as the equilibrium NO_x concentration. Thereafter, the NO and O₂ flow from the gas cylinder was turned off and, pure N₂ was used to purge the catalyst bed at 400°C for 1 hour to remove all adsorbed NO_x and O₂ from the catalyst.

Experiments on the adsorption performance of the Fe/ZSM-5 catalyst were conducted at different temperatures and NO concentrations. Each experimental condition was repeated 3 times to obtain the average adsorption capacities.

D.2 Experimental details of fluidized bed adsorption

The adsorption performance of Fe/ZSM-5 was also tested in a hot model fluidized bed. The column diameter is 108 mm (I.D.) and the height is 1092 mm. The freeboard height and diameter are 1016 mm and 260 mm (I.D.), respectively. The schematic of the fluidized bed set-up is shown in Fig. D.1. The bed catalyst loading is 0.975 kg. The adsorption performance was tested at different temperatures and inlet gas velocities. The experimental conditions are also given in Table 1.

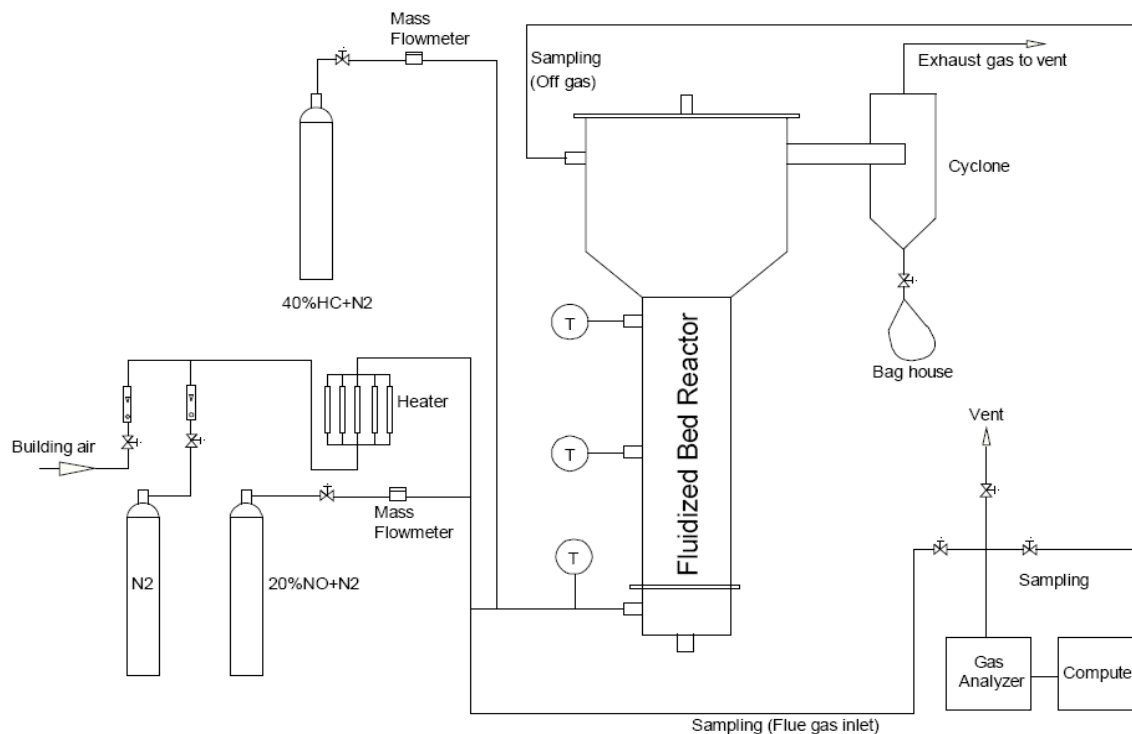


Figure D.1 Schematics of fluidized bed set-up

The model flue gas used in the experiment was a mixture prepared from 20% NO balanced with N₂ and liquid N₂ Dewar from Praxair Products. Building air was also used to provide O₂ in the feed gas. The compositions (NO_x and O₂) of the effluent gases were analyzed by a Horiba PG-250 flue gas analyzer.

In the experiment, the fluidized bed was first preheated by passing the preheated building air. After the desired temperature was reached in the reactor, the bed was purged with nitrogen for 1 hour. After the purging, 20% NO balanced with nitrogen, building air, and pure nitrogen was blended and injected to the fluidized bed after preheating. The adsorption performance was evaluated by measuring the NO_x concentration at the top freeboard region of the fluidized bed. Afterward, pure N₂ was used to purge the catalyst bed for another 1 hour to remove all adsorbed NO_x from the catalyst.

The adsorption performance was tested at different temperatures and inlet gas velocities. One experimental condition, at 300°C with an inlet NO_x concentration of 900 ppm and a superficial gas velocity of U=0.08 m/s, was tested three times to check the repeatability of the experiment.

D.3 Experimental results of fixed bed adsorption

Adsorption breakthrough curves were measured with three repeats at each experimental condition. A series of typical adsorption breakthrough curves at 250°C are shown in Fig. D.2. The results at other temperatures are not shown here.

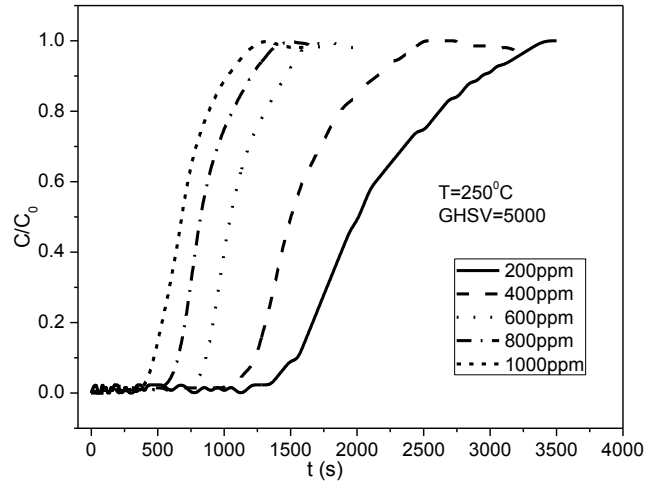


Figure D.2 Fixed bed NO_x adsorption breakthrough curves at 250 °C

D.4 Experimental results of fluidized bed adsorption

The breakthrough test of NO_x adsorption in the fluidized bed was repeated 3 times at 300 °C, an inlet NO_x concentration of 900 ppm and U=0.08 m/s. All the curves shown in Fig. D.3 are in close agreement, with small discrepancies.

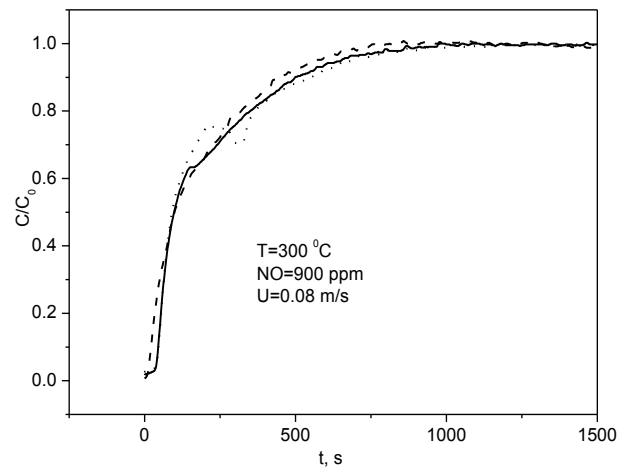


Figure D.3 Repeated breakthrough curves in the fluidized bed (T=300 °C, NO=900 ppm)

Fig. D.4 (a) and (b) are the breakthrough curves at 300°C and 350°C, respectively. Although the adsorption capacities are not calculated, it can easily be seen that the adsorption capacities are smaller at higher temperatures, with the breakthrough curves becoming steeper as the temperature increases from 300 °C to 350 °C.

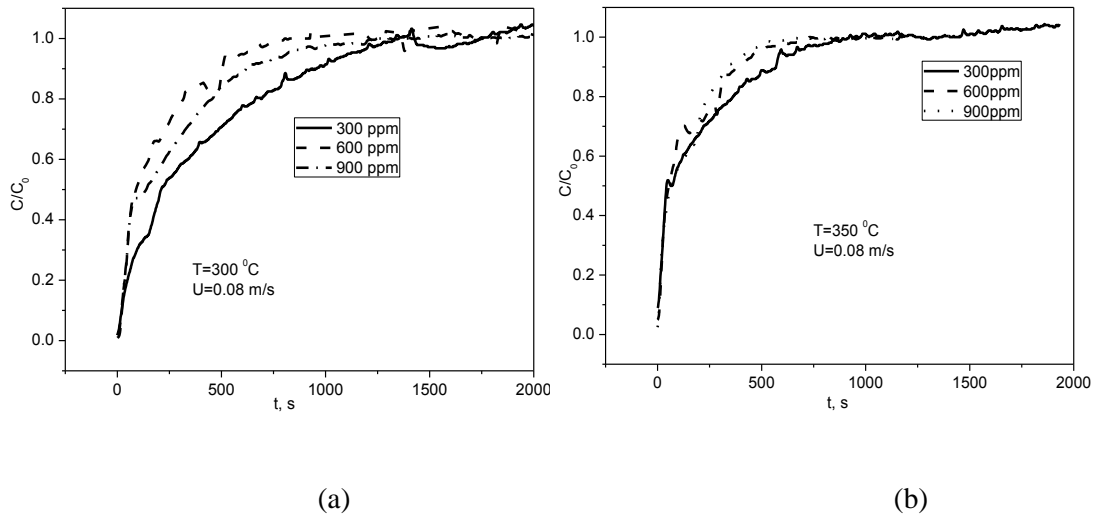


Figure D.4 Breakthrough curve of different NO_x inlet concentrations at (a) 300 °C and (b) 350 °C.

Appendix E Sensitivity analysis of fluidized bed adsorption model

The sensitivity of model to different parameters was tested with the results plotted in Fig. E.1. The breakthrough curves were modeled with parameters of mass transfer and gas dispersion either doubled or halved. These curves were then compared with original curve. It is seen that the model is most sensitive to gas-solid mass transfer coefficient, k_f . However, the breakthrough curve is not sensitive to either dense-bubbles phase mass transfer coefficient, k_{HL} , or gas dispersion coefficient D_H . This is because these parameters are already big enough.

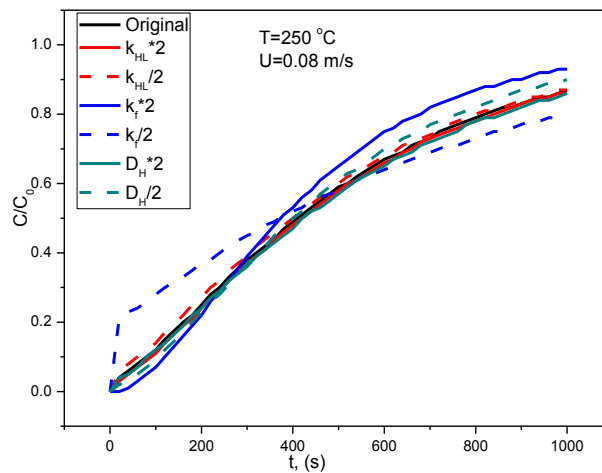


Figure E.1 Model sensitive analysis

Appendix F MATLAB codes for i-CFB model

```
%-----main function-----  
function iCFB  
% i-CFB model  
  
%-----write file, title-----  
fid = fopen ('i-CFB model.txt', 'at');  
  
fprintf (fid, '%12s\n\n', ' ');  
fprintf (fid, '%10s','Number');  
fprintf (fid, '%10s','Ua0');  
fprintf (fid, '%10s','Ud0');  
fprintf (fid, '%10s','HC:NO');  
fprintf (fid, '%10s','O2');  
fprintf (fid, '%10s','exp-XNO');  
fprintf (fid, '%10s','exp-XHC')  
fprintf (fid, '%10s','m-XNO');  
fprintf (fid, '%10s','m-XHC');;  
fprintf (fid, '%10s','f-XNO');  
fprintf (fid, '%10s\n','f-XHC');  
  
fclose all;  
  
%-----data-----  
%-----%O2=4%; HC:NO=2 -----  
% Uga =[ 0.22 0.28 0.34 0.42 ];  
% Ugd =[ 0.6 0.6 0.6 0.6 ];  
% ExpXNO=[ 54.50 47.34 43.12 40.73];  
% ExpXHC=[ 100 96.70 83.30 71.56 ];  
% O2 = ones(4)*4;  
% HCNO= ones(4)*2;  
  
%-----O2=4%-----  
% Uga=[ 0.22 0.35 0.22 0.35 ];  
% Ugd=[ 0.6 0.6 0.6 0.6 ];  
% ExpXNO=[51.93 35.41 64.04 58.53 ];  
% ExpXHC=[100 100 91.19 65.69 ];  
% HCNO=[ 1 1 4 4];  
% O2 = ones(4)*4;  
  
%-----O2=4%-----  
Uga=[ 0.21 0.33 0.19 0.28 0.35 0.40 0.47 0.23 0.34 ];  
Ugd=[ 0.75 0.75 0.75 0.75 0.75 0.75 0.75 0.75 0.75 ];
```

```

ExpXNO=[ 53.45 39.47 59.12 52.04 46.55 41.59 41.59 70.44 62.65 ];
ExpXHC=[ 93.98 80 88.50 81.42 78.58 74.51 66.73 76.64 57.88 ];
HCNO=[1 1 2 2 2 2 2 4 4 ];
O2= ones(9)*4;

%-----O2=4%-----
%Uga=[ 0.21 0.34 0.28 0.35 0.40 0.46 0.21 0.32 ];
%Ugd=[ 0.9 0.9 0.9 0.9 0.9 0.9 0.9 ];
%ExpXNO=[ 62.37 51.94 63.07 59.01 51.94 47.70 73.50 66.60 ];
%ExpXHC=[ 87.63 75.80 71.20 69.26 69.61 62.72 50.88 36.40 ];
%HCNO=[1 1 2 2 2 2 4 4 ];
%O2 = ones(8)*4;

%-----O2=12%-----
%Uga=[ 0.3 0.3 0.3 0.4 0.4 0.4 ];
%Ugd=[ 0.6 0.75 0.9 0.6 0.75 0.9 ];
%ExpXNO=[31.01 36.76 56.49 28.20 34.75 49.35];
%ExpXHC=[ 0 0 0 0 0 0 ];
%HCNO=[ 2 2 2 2 2 2 ];
%O2 = ones(6)*12;

%-----calculating-----
for number=1:9,

%-----basic setting-----
T=350+273; %temperature, K
P=1.013e5; %pressure, Pa
rou=1.29*293/T; %gas density, kg/m3

nu=(7e-5*T^2+0.0579*T-7.2566)*1e-6; %gas property, viscosity
mu=(1e-9*T^3-4e-6*T^2+0.0067*T+0.1177)*1e-5; %gas property, viscosity

Hd=1.016; %m, i-CFB configuration, draft tube height
Da=0.10; %m, i-CFB configuration, annulus diameter
Dd=0.05; %m, i-CFB configuration, draft tube diameter
Ad=3.14*Dd*Dd/4; %m2, draft tube cross area
Aa=3.14*Da*Da/4-Ad; %m2, annulus cross area

dp=150e-6; %m catalyst diameter
roubulk=979; %kg/m3, catalyst bulk density
rous=roubulk/0.55; %kg/m3, catalyst density

epss=0.45; %solids fraction at umf
epsmf=1-epss; %voidage at umf
Umf=0.01; %m/s, minimum fluidization velocity
G=3.3; %kg, bed loading

%-----feeding gas setting-----
NOa0=600e-6;
%NO concentration in flue gas, partial pressure, ppm*e-6
O2a0=1e-2*O2(number);

```

```

%O2 concentration in flue gas, partial pressure, %*e-2
HCratio=HCNO(number); %HC:NO ratio

Ua0=Uga(number); %m/s; annulus gas operation velocity
Ud0=Ugd(number); %m/s, draft tube velocity

%-----Ra-d, Rd-a-----
RAD=0.07; %Ra-d
RDA=0.01*1.039*(Ua0/Umf)^(-0.616)*(Ud0/Umf)^1.3; %Rd-a

%-----actually inlet velocities considering gas bypassing-----
Ua=Ua0-RAD*Ua0+RDA*Ud0*(Ad/Aa);
% m/s, actual inlet velocity in the annulus
Ud=Ud0-RDA*Ud0+RAD*Ua0*(Aa/Ad);
% m/s, actual inlet velocity in the draft tube

%-----actually inlet concentrations considering gas bypassing-----
mNO=NOa0*P/8.314/T;
% mol/m3, NO concentration in feeding flue gas
mO2=O2a0*P/8.314/T;
% mol/m3, O2 concentration in feeding flue gas
mHC=mNO*HCratio*(Ua0*Aa)/(Ud0*Ad);
% mol/m3, HC concentration in feeding reducing agent

mNOa=mNO*(1-RAD)*(Ua0/Ua);
% mol/m3, actual inlet concentration of NO in the annulus
mNOd=mNO*RAD*(Ua0*Aa)/(Ud*Ad);
% mol/m3, actual inlet concentration of NO in the draft tube
mO2a=mO2*(1-RAD)*(Ua0/Ua);
% mol/m3, actual inlet concentration of O2 in the annulus
mO2d=mO2*RAD*(Ua0*Aa)/(Ud*Ad);
% mol/m3, actual inlet concentration of O2 in the draft tube
mHCd=mHC*(1-RDA)*(Ud0/Ud);
% mol/m3, actual inlet concentration of HC in the draft tube
mHCa=mHC*RDA*(Ud0*Ad)/(Ua*Aa);
% mol/m3, actual inlet concentration of HC in the annulus

%-----bubble and voidage parameter in draft tube-----
Hf=Hd;
Hs=Hf/(1-epsmf); %m, parameter to calculate bubble property
Dbd=0.21*Hf^0.8*(Ud-Umf)^0.42*exp(-1.4e-4-0.25*(Ud-Umf)^2-0.1*(Ud-Umf));
if Dbd>Dd,
    Dbd=Dd;
end %m, bubble diameter in draft tube

Ubd=Ud-Umf+0.71*(9.8*Dbd)^0.5; %m/s, bubble velocity in draft tube
Y=0.108*Hs^0.26*(Ud-Umf)^0.09*dp^(-0.48)*rou^(-0.19);

if Ud<0.37,
    epsd=0.5056*Ud+0.4538;
else

```

```

    epsd=0.481 *Ud+0.5604;
end

epsbd=1-(1-epsd)/(1-epsmf);
Gd=rous*Ad*Hd*(1-epsd);    %kg, catalyst weight in draft tube
Hsd=Hd;                      %m, initial effective bed height of draft tube

%-----bubble and voidage parameter in annulus-----
Ga=G-Gd;                    %kg, catalyst weight in annulus
Hmf=Ga/Aa/roubulk;         %m, Hmf in annulus, for bubble parameter calculation
Hs=Hmf/(1-epsmf);         %m, Hs in annulus
Hf=Hmf;                    %m, Hf in annulus

Dba=0.21*Hf^0.8*(Ua-Umf)^0.42*exp(-1.4e-4-0.25*(Ua-Umf)^2-0.1*(Ua-Umf));
if Dba>Da/2-Dd/2,
    Dba=Da/2-Dd/2;
end %m, bubble diameter in annulus

Uba=Ua-Umf+0.71*(9.8*Dba)^0.5; %m/s, bubble velocity in annulus

if Ua<0.37,
    epsa=0.5056*Ua+0.4538;
else
    epsa=0.481 *Ua+0.5604;
end

epsba=1-(1-epsa)/(1-epsmf);

Ha=Ga/rous/(1-epsa)/Aa;    %m, initial bed height of annulus
Hsa=Ha;                    %m, initial effective bed height of annulus

%-----calculating effective bed heights-----
if Ha>Hd,
    Lj=0.1*11.52*(1.206/(968/0.55)*Ud^2/9.8/0.05)^0.1966;
    %m, jet height of draft tube
    for i=1:2, %iterating for effective bed heights
        if Ha<=Hd+Lj,
            Hsd=Ha;
        else
            Hsa=Ha+Lj;
            Hsd=Hsa;
        end
        Gd=rous*Ad*Hsd*(1-epsd);
        Ga=G-Gd;
        Ha=Ga/rous/(1-epsa)/Aa;
    end
end

%-----calculating solids circulation rate-----
Pa=9.8*Hsa*rous*(1-epsa); %Pa, initial pressure drop in annulus
Pd=9.8*Hsd*rous*(1-epsd); %Pa, initial pressure drop in draft tube

```

```

Gs=0; %give an initial value

for i=1:2, %iterating for solids circulation rate
Por=Pa-Pd; %Pa, initial pressure drop in orifice

fa=0.057*Gs*(9.8/0.1)^0.5; %friction coefficient in annulus
fd=0.057*Gs*3*(9.8/0.05)^0.5; %friction coefficient in draft tube
Fa=fa*Hsa-0.5*Gs^2/(968/0.55); %Pa, pressure drop due to friction in annulus
Fd=fd*Hd+0.5*9*Gs^2/(968/0.55); %Pa, pressure drop due to friction in draft tube

if Hsa>Hd,
    Fa=fa*Hd-0.5*Gs^2/(968/0.55);
end
Por=Pa-Pd-Fa-Fd;
Gs=0.17*0.146667*(2*968/0.55*(1-epsa)*Por/(1-0.021511))^0.5; %kg/m2.s, solids circulation rate
end

Usa=Gs/roubulk/(1-epsba); %m/s, solids velocity in annulus
Uzd=Gs*Aa/Ad/roubulk/(1-epsbd); %m/s, solids velocity in draft tube

%-----high-low phase mass transfer coefficient, kHL-----
Dm=zeros(3); %m2/s, molecular diffusivity
Dm=Di(T,P, 600e-6, 0, 1e-2);
DmNO=Dm(1); %m2/s, molecular diffusivity for NO
kHLa=Umf/3+2*(DmNO*epsmf*Uba/3.14/Dbd)^0.5; %m/s, kHL in annulus
kHLd=Umf/3+2*(DmNO*epsmf*Ubd/3.14/Dbd)^0.5; %m/s, kHL in draft tube

%----dispersion coefficients of solids & high phase, Ds & DH-----
gDta=(9.8*(Da/2-Dd/2))^0.5;
Pesa=19*((Da/2-Dd/2)+0.23)*Ua/gDta*(1+6.5*(Ua/gDta)^0.8);
%Péclet number of solids phase in annulus
Dsa=Ua*(Da/2-Dd/2)/Pesa;
% m2/s, dispersion coefficients of solids phase in annulus
DHa=Dsa;
% m2/s, dispersion coefficients of high phase in annulus

gDtd=(9.8*Dd)^0.5;
Pesd=19*(Dd+0.23)*Ud/gDtd*(1+6.5*(Ud/gDtd)^0.8);
%Péclet number of solids phase in draft tube
Dsd=Ud*Dd/Pesd;
% m2/s, dispersion coefficients of solids phase in draft tube
DHd=Dsd;
% m2/s, dispersion coefficients of high phase in draft tube

%-----other coefficients for governing equations-----
faHa=1-epsba; %high phase fraction in annulus
faLa=epsba; %low phase fraction in annulus
faHd=1-epsbd; %high phase fraction in draft tube
faLd=epsbd; %low phase fraction in draft tube

```

```

UHa=Umf;    %m/s; high phase gas velocity in annulus
ULa=Uba;    %m/s; low phase gas velocity in annulus
UHd=Umf;    %m/s; high phase gas velocity in draft tube
ULd=Ubd;    %m/s; low phase gas velocity in draft tube

aba=6*faLa/Dba;
% 1/m, surface area of interphase boundary per unit bed volume in annulus
abd=6*faLd/Dbd;
% 1/m, surface area of interphase boundary per unit bed volume in %
draft tube
as=6*epss/dp;
% 1/m, surface area of catalyst particle per unit bed volume in annulus

kf=0.0148*3e-6/(1-epss); % 1/s, intraphase mass transfer coefficient

%-----summary of coefficients for calculating governing equations-----
%-----governing euqation numbers:
%----annulus:  1, NO-Solids phase; 2, NO-High phase;
%              3, HC-Solids phase; 4, HC-High phase;
%              5, O2-Solids phase; 6, O2-High phase;
%              7, NO-Low phase; 8, HC-Low phase; 9, O2-Low phase;
%----draft tube: 11, NO-Solids phase; 12, NO-High phase;
%               13, HC-Solids phase; 14, HC-High phase;
%               15, O2-Solids phase; 16, O2-High phase;
%               17, NO-Low phase; 18, HC-Low phase; 19, O2-Low phase;

%----annulus:

f1c=kf*as;
f3c=f1c;
f5c=f1c;

f7c=kHLa*aba;
f8c=f7c;
f9c=f7c;

a1=Dsa;
a2=DHa;
a3=a1;
a5=a1;
a4=a2;
a6=a2;

a7=0;
a8=a7;
a9=a7;

b1= -Usa;
b2=UHa;
b3=b1;
b5=b1;

```

```

b4=b2;
b6=b2;

b7=ULa;
b8=b7;
b9=b7;

%----draft tube:

f11c=kf*as;
f13c=f11c;
f15c=f11c;

f17c=kHLd*abd;
f18c=f17c;
f19c=f17c;

a11=Dsd;
a12=DHd;
a13=a11;
a15=a11;
a14=a12;
a16=a12;

a17=0;
a18=a17;
a19=a17;

b11=Usd;
b12=UHd;
b13=b11;
b15=b11;
b14=b12;
b16=b12;

b17=ULd;
b18=b17;
b19=b17;

%-----interval set for differential equation calculation-----
t=0.01; %s,time interval
M=20; %number of length points
ha=Hsa/M; %m, length interval in annulus
hd=Hsd/M; %m, length interval in draft tube

%~~~~~
%-----matrix for differential equation calculation-----

%----annulus:
%-----matrix r1-----
r1=zeros(M,M);

```

```

for i=1:M-1;
    r1(i,i)=1+2*a1*t/ha/ha;
    r1(i+1,i)=-a1*t/ha/ha-b1*t/ha/2;
    r1(i,i+1)=-a1*t/ha/ha+b1*t/ha/2;
end

r1(M,M)=1+2*a1*t/ha/ha;
r1(M,M)=r1(M,M)+(-a1*t/ha/ha+b1*t/ha/2);

%-----matrix r3, r5-----
r3=r1;
r5=r1;

%-----matrix r2-----
r2=zeros(M,M);

for i=1:M-1;
    r2(i,i)=1+2*a2*t/ha/ha;
    r2(i+1,i)=-a2*t/ha/ha-b2*t/ha/2;
    r2(i,i+1)=-a2*t/ha/ha+b2*t/ha/2;
end

r2(M,M)=1+2*a2*t/ha/ha;
r2(M,M)=r2(M,M)+(-a2*t/ha/ha+b2*t/ha/2);

%-----matrix r4, r6-----
r4=r2;
r6=r2;

%-----matrix r7-----
r7=zeros(M,M);

for i=1:M-1;
    r7(i,i)=1+2*a7*t/ha/ha;
    r7(i+1,i)=-a7*t/ha/ha-b7*t/ha/2;
    r7(i,i+1)=-a7*t/ha/ha+b7*t/ha/2;
end

r7(M,M)=1+2*a7*t/ha/ha;
r7(M,M)=r7(M,M)+(-a7*t/ha/ha+b7*t/ha/2);

%-----matrix r8, r9-----
r8=r7;
r9=r7;

%----draft tube:
%-----matrix r11-----
r11=zeros(M,M);

for i=1:M-1;

```

```

    r11(i,i)=1+2*a11*t/hd/hd;
    r11(i+1,i)=-a11*t/hd/hd-b11*t/hd/2;
    r11(i,i+1)=-a11*t/hd/hd+b11*t/hd/2;
end

r11(M,M)=1+2*a11*t/hd/hd;
r11(M,M)=r11(M,M)+(-a11*t/hd/hd+b11*t/hd/2);

%-----matrix r13, r15-----
r13=r11;
r15=r11;

%-----matrix r12-----
r12=zeros(M,M);

for i=1:M-1;
    r12(i,i)=1+2*a12*t/hd/hd;
    r12(i+1,i)=-a12*t/hd/hd-b12*t/hd/2;
    r12(i,i+1)=-a12*t/hd/hd+b12*t/hd/2;
end

r12(M,M)=1+2*a12*t/hd/hd;
r12(M,M)=r12(M,M)+(-a12*t/hd/hd+b12*t/hd/2);

%-----matrix r14, r16-----
r14=r12;
r16=r12;

%-----matrix r17-----
r17=zeros(M,M);

for i=1:M-1;
    r17(i,i)=1+2*a17*t/hd/hd;
    r17(i+1,i)=-a17*t/hd/hd-b17*t/hd/2;
    r17(i,i+1)=-a17*t/hd/hd+b17*t/hd/2;
end

r17(M,M)=1+2*a17*t/hd/hd;
r17(M,M)=r17(M,M)+(-a17*t/hd/hd+b17*t/hd/2);

%-----matrix r18, r19-----
r18=r17;
r19=r17;

%~~~~~
%-----main calculation of differential equations-----
%---annulus
u1=zeros(M,1); %NO, solids phase
u2=zeros(M,1); %NO, gas phase
u3=zeros(M,1); %HC, solids phase
u4=zeros(M,1); %HC, gas phase

```

```

u5=zeros(M,1); %O2, solids phase
u6=zeros(M,1); %O2, gas phase
u7=zeros(M,1); %NO, bubble phase
u8=zeros(M,1); %HC, bubble phase
u9=zeros(M,1); %O2, bubble phase

uu1=zeros(M,1); %NO, solids phase
uu2=zeros(M,1); %NO, gas phase
uu3=zeros(M,1); %HC, solids phase
uu4=zeros(M,1); %HC, gas phase
uu5=zeros(M,1); %O2, solids phase
uu6=zeros(M,1); %O2, gas phase
uu7=zeros(M,1); %NO, bubble phase
uu8=zeros(M,1); %HC, bubble phase
uu9=zeros(M,1); %O2, bubble phase

ff1=zeros(M,1); %boundary, NO, solids phase
ff2=zeros(M,1); %boundary, NO, gas phase
ff3=zeros(M,1); %boundary, HC, solids phase
ff4=zeros(M,1); %boundary, HC, gas phase
ff5=zeros(M,1); %boundary, O2, solids phase
ff6=zeros(M,1); %boundary, O2, gas phase
ff7=zeros(M,1); %boundary, NO, bubble phase
ff8=zeros(M,1); %boundary, HC, bubble phase
ff9=zeros(M,1); %boundary, O2, bubble phase

%---draft tube
u11=zeros(M,1); %NO, solids phase
u12=zeros(M,1); %NO, gas phase
u13=zeros(M,1); %HC, solids phase
u14=zeros(M,1); %HC, gas phase
u15=zeros(M,1); %O2, solids phase
u16=zeros(M,1); %O2, gas phase
u17=zeros(M,1); %NO, bubble phase
u18=zeros(M,1); %HC, bubble phase
u19=zeros(M,1); %O2, bubble phase

uu11=zeros(M,1); %NO, solids phase
uu12=zeros(M,1); %NO, gas phase
uu13=zeros(M,1); %HC, solids phase
uu14=zeros(M,1); %HC, gas phase
uu15=zeros(M,1); %O2, solids phase
uu16=zeros(M,1); %O2, gas phase
uu17=zeros(M,1); %NO, bubble phase
uu18=zeros(M,1); %HC, bubble phase
uu19=zeros(M,1); %O2, bubble phase

ff11=zeros(M,1); %boundary, NO, solids phase
ff12=zeros(M,1); %boundary, NO, gas phase
ff13=zeros(M,1); %boundary, HC, solids phase
ff14=zeros(M,1); %boundary, HC, gas phase

```

```

ff15=zeros(M,1); %boundary, O2, solids phase
ff16=zeros(M,1); %boundary, O2, gas phase
ff17=zeros(M,1); %boundary, NO, bubble phase
ff18=zeros(M,1); %boundary, HC, bubble phase
ff19=zeros(M,1); %boundary, O2, bubble phase

%---parameters
CsNO=0; % mol/m3, equilibrium concentration of NOx, initial
CsO=0; % mol/m3, equilibrium concentration of O2 , initial
R=[0 0 0]; % mol/s , reaction rate, initial
RSNO2=0; % mol/s , reaction rate of NO2, initial
RHC=0; % mol/s , reaction rate of HC , initial
RO2=0; % mol/s , reaction rate of O2 , initial

KNOe=CssNO (mNO, mO2, T)/mNO;
KNOa=CssNO(mNOa, mO2a,T)/mNOa;
KNOd=CssNO(mNOd, mO2d,T)/mNOd;
KO2a=CssO(mO2a,T)/mO2a;
KO2d=CssO(mO2d,T)/mO2d;

KNOKNOea=KNOe/KNOa;
KNOKNOed=KNOe/KNOd;
KNOKO2a= KNOe/KO2a;
KNOKO2d= KNOe/KO2d;
KNOKHC= KNOe*10.12/2.18;

k=1;
XNOa=0; %initial conversion values
XNOd=0;
XHCa=0;
XNOea=0;
XNOed=0;
XHCea=0;

ERROR=3e2; %inital error value

%-----calculation-----
while ERROR>1e-6,

%-----adsorption & reaction-----
for i=1:M,

%---annulus
CsNO=CssNO(u2(i,1), u6(i,1),T);
CsO =CssO(u6(i,1),T);
R =Reaction(u1(i,1), u3(i,1), u5(i,1), T)* (1-epsa);
RSNO2=Ra(1);
RHC =Ra(2);
RSO =Ra(3);

ff1(i,1)= -f1c*KNOKNOea*(u1(i,1)-CsNO) +RSNO2; %NO, solids phase

```

ff3(i,1)= -f3c*KNOKHC*(u3(i,1)-u4(i,1)) +RHC; %HC, solids phase
 ff5(i,1)= -f5c*KNOKO2a*(2*u5(i,1)-CsO) +RSO; %O2, solids phase

ff2(i,1)= f1c*KNOKNOea*(u1(i,1)-CsNO) - f7c*(u2(i,1)-u7(i,1)); %NO, gas phase
 ff4(i,1)= f3c*KNOKHC*(u3(i,1)-u4(i,1))- f8c*(u4(i,1)-u8(i,1)); %HC gas phase
 ff6(i,1)= f5c*KNOKO2a*(u5(i,1)-CsO/2) - f9c*(u6(i,1)-u9(i,1)); %O2, gas phase

ff7(i,1)= f7c*(u2(i,1)-u7(i,1)); %NO, bubble phase
 ff8(i,1)= f8c*(u4(i,1)-u8(i,1)); %HC, bubble phase
 ff9(i,1)= f9c*(u6(i,1)-u9(i,1)); %O2, bubble phase

%---draft tube

CsNO=CssNO(u12(i,1), u16(i,1),T);
 CsO =CssO(u16(i,1),T);
 R =Reaction(u11(i,1), u13(i,1), u15(i,1), T)* (1-epsd);
 RSNO2=Rd(1);
 RHC =Rd(2);
 RSO =Rd(3);

ff11(i,1)= -f11c*KNOKNOed*(u11(i,1)-CsNO) +RSNO2;%NO, solids phase
 ff13(i,1)= -f13c*KNOKHC*(u13(i,1)-u14(i,1))+RHC; %HC, solids phase
 ff15(i,1)= -f15c*KNOKO2d*(2*u15(i,1)-CsO) +RSO; %O2, solids phase

ff12(i,1)= f11c*KNOKNOed*(u11(i,1)-CsNO) - f17c*(u12(i,1)-u17(i,1)); %NO, gas phase
 ff14(i,1)= f13c*KNOKHC*(u13(i,1)-u14(i,1))- f8c*(u14(i,1)-u18(i,1)); %HC gas phase
 ff16(i,1)= f15c*KNOKO2d*(u15(i,1)-CsO/2) - f19c*(u16(i,1)-u19(i,1)); %O2, gas phase

ff17(i,1)= f17c*(u12(i,1)-u17(i,1)); %NO, bubble phase
 ff18(i,1)= f18c*(u14(i,1)-u18(i,1)); %HC, bubble phase
 ff19(i,1)= f19c*(u16(i,1)-u19(i,1)); %O2, bubble phase

end

%---solids recirculation

u1(M,1)=(u1(M,1)*(ha-t*Usa)+t*Usa*u11(M,1))/ha;
 u3(M,1)=(u3(M,1)*(ha-t*Usa)+t*Usa*u13(M,1))/ha;
 u5(M,1)=(u5(M,1)*(ha-t*Usa)+t*Usa*u15(M,1))/ha;

u11(1,1)=(u11(1,1)*(hd-t*Usd)+t*Usd*u1(1,1))/hd;
 u13(1,1)=(u13(1,1)*(hd-t*Usd)+t*Usd*u3(1,1))/hd;
 u15(1,1)=(u15(1,1)*(hd-t*Usd)+t*Usd*u5(1,1))/hd;

%-----

%---annulus

ff1(1,1)=ff1(1,1)+(a1/ha/ha+b1/ha/2)*u1(1,1);
 ff3(1,1)=ff3(1,1)+(a3/ha/ha+b3/ha/2)*u3(1,1);
 ff5(1,1)=ff5(1,1)+(a5/ha/ha+b5/ha/2)*u5(1,1);

ff2(1,1)=ff2(1,1)+(a2/ha/ha+b2/ha/2)*mNOa;
 ff4(1,1)=ff4(1,1)+(a4/ha/ha+b4/ha/2)*mHCa;
 ff6(1,1)=ff6(1,1)+(a6/ha/ha+b6/ha/2)*mO2a;

```

ff7(1,1)=ff7(1,1)+(a7/ha/ha+b7/ha/2)*mNOa;
ff8(1,1)=ff8(1,1)+(a8/ha/ha+b8/ha/2)*mHCa;
ff9(1,1)=ff9(1,1)+(a9/ha/ha+b9/ha/2)*mO2a;

```

```
%---draft tube
```

```

ff11(1,1)=ff11(1,1)+(a11/hd/hd+b11/hd/2)*u11(1,1);
ff13(1,1)=ff13(1,1)+(a13/hd/hd+b13/hd/2)*u13(1,1);
ff15(1,1)=ff15(1,1)+(a15/hd/hd+b15/hd/2)*u15(1,1);

```

```

ff12(1,1)=ff12(1,1)+(a12/hd/hd+b12/hd/2)*mNOd;
ff14(1,1)=ff14(1,1)+(a14/hd/hd+b14/hd/2)*mHCd;
ff16(1,1)=ff16(1,1)+(a16/hd/hd+b16/hd/2)*mO2d;

```

```

ff17(1,1)=ff17(1,1)+(a17/hd/hd+b17/hd/2)*mNOd;
ff18(1,1)=ff18(1,1)+(a18/hd/hd+b18/hd/2)*mHCd;
ff19(1,1)=ff19(1,1)+(a19/hd/hd+b19/hd/2)*mO2d;

```

```
%-----
```

```
%---annulus
```

```

ff1 = u1+t*ff1;
ff2 = u2+t*ff2;
ff3 = u3+t*ff3;
ff4 = u4+t*ff4;
ff5 = u5+t*ff5;
ff6 = u6+t*ff6;
ff7 = u7+t*ff7;
ff8 = u8+t*ff8;
ff9 = u9+t*ff9;

```

```
%---draft tube
```

```

ff11 = u11+t*ff11;
ff12 = u12+t*ff12;
ff13 = u13+t*ff13;
ff14 = u14+t*ff14;
ff15 = u15+t*ff15;
ff16 = u16+t*ff16;
ff17 = u17+t*ff17;
ff18 = u18+t*ff18;
ff19 = u19+t*ff19;

```

```
%-----
```

```
%---annulus
```

```

uu1=chase(r1, ff1);
uu2=chase(r2, ff2);
uu3=chase(r3, ff3);
uu4=chase(r4, ff4);
uu5=chase(r5, ff5);
uu6=chase(r6, ff6);
uu7=chase(r7, ff7);
uu8=chase(r8, ff8);

```

```

uu9=chase(r9, ff9);

%---draft tube
uu11=chase(r11, ff11);
uu12=chase(r12, ff12);
uu13=chase(r13, ff13);
uu14=chase(r14, ff14);
uu15=chase(r15, ff15);
uu16=chase(r16, ff16);
uu17=chase(r17, ff17);
uu18=chase(r18, ff18);
uu19=chase(r19, ff19);

%-----
for i=1:M;
    if uu1(i,1)<0,
        uu1(i,1)=0;
    end
    if uu2(i,1)<0,
        uu2(i,1)=0;
    end
    if uu3(i,1)<0,
        uu3(i,1)=0;
    end
    if uu4(i,1)<0,
        uu4(i,1)=0;
    end
    if uu5(i,1)<0,
        uu5(i,1)=0;
    end
    if uu6(i,1)<0,
        uu6(i,1)=0;
    end
    if uu7(i,1)<0,
        uu7(i,1)=0;
    end
    if uu8(i,1)<0,
        uu8(i,1)=0;
    end
    if uu9(i,1)<0,
        uu9(i,1)=0;
    end

    if uu11(i,1)<0,
        uu11(i,1)=0;
    end
    if uu12(i,1)<0,
        uu12(i,1)=0;
    end
    if uu13(i,1)<0,
        uu13(i,1)=0;

```

```

end
if uu14(i,1)<0,
    uu14(i,1)=0;
end
if uu15(i,1)<0,
    uu15(i,1)=0;
end
if uu16(i,1)<0,
    uu16(i,1)=0;
end
if uu17(i,1)<0,
    uu17(i,1)=0;
end
if uu18(i,1)<0,
    uu18(i,1)=0;
end
if uu19(i,1)<0,
    uu19(i,1)=0;
end
end

```

```

%-----

```

```

u1=uu1;
u2=uu2;
u3=uu3;
u4=uu4;
u5=uu5;
u6=uu6;
u7=uu7;
u8=uu8;
u9=uu9;

```

```

u11=uu11;
u12=uu12;
u13=uu13;
u14=uu14;
u15=uu15;
u16=uu16;
u17=uu17;
u18=uu18;
u19=uu19;

```

```

k=k+1;

```

```

%-----calculation monitor-----

```

```

if rem(k,30000)==0,

```

```

    number=number

```

```

    CNOa=(u2(M,1)*faHa*UHa+u7(M,1)*faLa*ULa)/(faHa*UHa+faLa*ULa);

```

```

    CHCa=(u4(M,1)*faHa*UHa+u8(M,1)*faLa*ULa)/(faHa*UHa+faLa*ULa);

```

```

    CNOd=(u12(M,1)*faHd*UHd+u17(M,1)*faLd*ULd)/(faHd*UHd+faLd*ULd);

```

```

CHCd=(u14(M,1)*faHd*UHd+u18(M,1)*faLd*ULd)/(faHd*UHd+faLd*ULd);
CO2a=(u6(M,1)*faHa*UHa+u8(M,1)*faLa*ULa)/(faHa*UHa+faLa*ULa);
CO2d=(u16(M,1)*faHd*UHd+u18(M,1)*faLd*ULd)/(faHd*UHd+faLd*ULd);

```

```

XNOa=100*(mNOa*Ua*Aa-CNOa*Ua*Aa)/(mNO*Ua0*Aa);
XNOd=100*(mNOd*Ud*Ad-CNOd*Ud*Ad)/(mNO*Ua0*Aa);

```

```

ERROR=abs(XNOea-XNOa)/t+abs(XNOed-XNOd)/t
XNOea=XNOa;
XNOed=XNOd;

```

```

XNO=100*(mNOa*Ua*Aa-CNOa*Ua*Aa+mNOd*Ud*Ad-CNOd*Ud*Ad)/(mNO*Ua0*Aa);
XHC=100*(mHCa*Ua*Aa-CHCa*Ua*Aa+mHCd*Ud*Ad-CHCd*Ud*Ad)/(mHC*Ud0*Ad);
Xout=[XNO XHC]

```

```

end
end

```

```

%-----write data file-----

```

```

fid = fopen ('complete.txt', 'at');
fprintf (fid, '%10.4f', number);
fprintf (fid, '%10.2f', Ua0);
fprintf (fid, '%10.2f', Ud0);
fprintf (fid, '%10.2f', HCNO(number));
fprintf (fid, '%10.2f', O2(number));
fprintf (fid, '%10.2f', ExpXNO(number));
fprintf (fid, '%10.2f', ExpXHC(number));
fprintf (fid, '%10.2f', Xout);
fclose all;

```

```

%-----
%----freeboard-----
%-----inet of freeboard-----
A=3.14*Da*Da/4; % cross sectional area

```

```

Ugf = (Ua*Aa+Ud*Ad)/(Aa+Ad);

```

```

CNOf= (CNOa*Ua*Aa+CNOd*Ud*Ad)/(Ua*Aa+Ud*Ad);
CHCf= (CHCa*Ua*Aa+CHCd*Ud*Ad)/(Ua*Aa+Ud*Ad);
CO2f= (CO2a*Ua*Aa+CO2d*Ud*Ad)/(Ua*Aa+Ud*Ad);

```

```

SNOF= (u1(M,1)*Aa*(1-epsa)+u11(M,1)*Ad*(1-epsd))/(Aa*(1-epsa)+Ad*(1-epsd));
SHCF= (u3(M,1)*Aa*(1-epsa)+u13(M,1)*Ad*(1-epsd))/(Aa*(1-epsa)+Ad*(1-epsd));
SO2f= (u5(M,1)*Aa*(1-epsa)+u15(M,1)*Ad*(1-epsd))/(Aa*(1-epsa)+Ad*(1-epsd));

```

```

%-----freeboard interval-----
N=20; %number of length points
LF=0.8; %height of freeboard
hf=LF/N; %m, freeboard interval

```

```

%-----freeboard voidage-----

```

```

Hs=Hd;
Dbf=0.21*Hs^0.8*(Ugf-Umf)^0.42*exp(-1.4e-4-0.25*(Ugf-Umf)^2-0.1*(Ugf-Umf));
    if Dbf>Da,
        Dbf=Da;
    end

F0=A*Dbf*3.07e-6*rou^3.5*9.8^0.5/mu^2.5*(Ugf-Umf)^2.5; %kg/m2.s
epsF=freeb(F0, Ugf); % (20,2), (position, eps)

if Hsa<Hd,
    for i=1:N,
        if (Hsa+i*hf)<Hd,
            epsF(i,2)=1;
        end
    end
end

%-----freeboard calculation-----
%--number: 21: NO-solids phase; 22: HC-solids phase; 23: O2-solids phase;
%----- 24: NO-gas phase; 25: HC-gas phase; 26: O2-gas phase;
a21=0;
a22=a21;
a23=a21;
b21=0;
b22=b21;
b23=b21;

b24=Ugf;
b25=b24;
b26=b24;

%-----matrix-----
%-----matrix 21, r22, r23-----
r21=zeros(N,N);

for i=1:N-1;
    r21(i,i)=1+2*a21*t/hf/hf;
    r21(i+1,i)=-a21*t/hf/hf-b21*t/hf/2;
    r21(i,i+1)=-a21*t/hf/hf+b21*t/hf/2;
end

r21(N,N)=1+2*a21*t/hf/hf;
r21(N,N)=r21(N,N)+(-a21*t/hf/hf+b21*t/hf/2);

r22=r21;
r23=r21;

%-----matrix r24,25,26-----
r24=zeros(N,N);
for i=1:N-1,
    r24(i,i)=1+b24*t/hf;

```

```

r24(i+1,i)=-b24*t/hf;
r24(i,i+1)=0;
end

r24(N,N)=1+b24*t/hf;

r25=r24;
r26=r24;

%-----
u21=ones(N,1)*SNOF; %NO, freeboard, solids phase
u22=ones(N,1)*SHCF; %HC, freeboard, solids phase
u23=ones(N,1)*SO2f; %O2, freeboard, solids phase
u24=ones(N,1)*CNOF; %NO, freeboard, gas phase
u25=ones(N,1)*CHCF; %HC, freeboard, gas phase
u26=ones(N,1)*CO2f; %O2, freeboard, gas phase

uu21=zeros(N,1); %NO, freeboard, solids phase
uu22=zeros(N,1); %HC, freeboard, solids phase
uu23=zeros(N,1); %O2, freeboard, solids phase
uu24=zeros(N,1); %NO, freeboard, gas phase
uu25=zeros(N,1); %HC, freeboard, gas phase
uu26=zeros(N,1); %O2, freeboard,gas phase

ff21=zeros(N,1); %NO, freeboard, solids phase
ff22=zeros(N,1); %HC, freeboard, solids phase
ff23=zeros(N,1); %O2, freeboard, solids phase
ff24=zeros(N,1); %NO, freeboard, gas phase
ff25=zeros(N,1); %HC, freeboard, gas phase
ff26=zeros(N,1); %O2, freeboard,gas phase

%-----calculation-----
XNOe=0;
ERROR=3e4; % error, initial

while ERROR>1e-6,

for i=1:N,

CsNO=CssNO(u24(i,1), u26(i,1),T);
CsO =CssO (u26(i,1),T);
Reac=Reaction(u21(i,1), u22(i,1), u23(i,1), T)*(1-epsF(i,2));
RSNO2=Reac(1);
RHC=Reac(2);
RSO=Reac(3);

ff21(i,1)= -f1c*KNOKNOea*(u21(i,1)-CsNO) +RSNO2; %NO, solids phase
ff22(i,1)= -f3c*KNOKHC*(u22(i,1)-u25(i,1))+RHC; %HC, solids phase
ff23(i,1)= -f5c*KNOKO2a*(2*u23(i,1)-CsO) +RSO; %O2, solids phase
ff24(i,1)= f1c*KNOKNOea*(u21(i,1)-CsNO); %NO, gas phase
ff25(i,1)= f3c*KNOKHC*(u22(i,1)-u25(i,1)); %HC gas phase

```

```
ff26(i,1)= f5c*KNOKO2a*(u23(i,1)-CsO/2); %O2, gas phase
```

```
end
```

```
ff21(1,1)=ff21(1,1)+(a21/hf/hf+b21/hf/2)*SNOF;  
ff22(1,1)=ff22(1,1)+(a22/hf/hf+b22/hf/2)*SHCF;  
ff23(1,1)=ff23(1,1)+(a23/hf/hf+b23/hf/2)*SO2f;
```

```
ff24(1,1)=ff24(1,1)+(b24/hf)*CNOF;  
ff25(1,1)=ff25(1,1)+(b25/hf)*CHCF;  
ff26(1,1)=ff26(1,1)+(b26/hf)*CO2f;
```

```
ff21 = u21+t*ff21;  
ff22 = u22+t*ff22;  
ff23 = u23+t*ff23;  
ff24 = u24+t*ff24;  
ff25 = u25+t*ff25;  
ff26 = u26+t*ff26;
```

```
uu21=chase(r21, ff21);  
uu22=chase(r22, ff22);  
uu23=chase(r23, ff23);  
uu24=chase(r24, ff24);  
uu25=chase(r25, ff25);  
uu26=chase(r26, ff26);
```

```
u21=uu21;  
u22=uu22;  
u23=uu23;  
u24=uu24;  
u25=uu25;  
u26=uu26;
```

```
for i=1:N;  
  if u21(i,1)<0,  
    u21(i,1)=0;  
  end  
  if u22(i,1)<0,  
    u22(i,1)=0;  
  end  
  if u23(i,1)<0,  
    u23(i,1)=0;  
  end  
  if u24(i,1)<0,  
    u24(i,1)=0;  
  end  
  if u25(i,1)<0,  
    u25(i,1)=0;  
  end  
  if u26(i,1)<0,  
    u26(i,1)=0;
```

```

    end

end

%-----calculation monitor-----
k=k+1;

if rem(k,20000)==0,
    XNO=100*(mNOa*Ua*Aa+mNOd*Ud*Ad-u24(N,1)*A*Ugf)/(mNO*Aa*Ua0);
    XHC=100*(mHCa*Ua*Aa+mHCd*Ud*Ad-u25(N,1)*A*Ugf)/(mHC*Ad*Ud0);
    number=number
    ERROR=abs(XNOe-XNO)/t
    XNOe=XNO;
    Xoutf=[XNO XHC]
end

end

%-----write data file-----
fid = fopen ('complete.txt', 'at');
fprintf (fid, '%10.2f', Xoutf);
fprintf (fid, '%10s\n', ' ');
fclose all;

%-----
end %number

%-----end of main function-----

%-----
%-----functions-----
%-----function: equation calculation-----
function x = chase (a,b)
M=length(b);
x=zeros(M,1);
for i=2:M;
    l=a(i,i-1)/a(i-1,i-1);
    b(i,1)=b(i,1)-l*b(i-1,1);
    a(i,i-1)=0;
    a(i,i)=a(i,i)-l*a(i-1,i);
end
x(M,1)=b(M,1)/a(M,M);
for i=1:M-1;
    x(M-i,1)=(b(M-i,1)-a(M-i,M-i+1)*x(M-i+1,1))/a(M-i,M-i);
end
%-----

%-----diffusivity calculation-----
function y = Di(T,P, CNOin, CHCin, CO2in)
MNO=30;
vNO=30.419;

```

```

MO2=32;
vO2=16.6;
MHC=44;
vHC=65.34;
MN2=14;
vN2=17.9;
DNOHC=Dij(T,P,MNO,MHC,vNO,vHC);
DNON2=Dij(T,P,MNO,MN2,vNO,vN2);
DNOO2=Dij(T,P,MNO,MN2,vNO,vO2);
DHCN2=Dij(T,P,MHC,MN2,vHC,vN2);
DHCO2=Dij(T,P,MHC,MO2,vHC,vO2);
DO2N2=Dij(T,P,MO2,MN2,vO2,vN2);
CN2in=1-CNOin-CHCin-CO2in;
y=zeros(3);
y(1)=(1-CNOin)/(CHCin/DNOHC+CN2in/DNON2+CO2in/DNOO2);
y(2)=(1-CHCin)/(CNOin/DNOHC+CN2in/DHCN2+CO2in/DHCO2);
y(3)=(1-CO2in)/(CNOin/DNOO2+CHCin/DHCO2+CN2in/DO2N2);
%-----

%-----for diffusivity calculation-----
function y = Dij(T,P,Mi,Mj,vi,vj)
y=0.1013*T^1.75*(1/Mi+1/Mj)^0.5/P/(vi^(1/3)+vj^(1/3))^2;
%-----

%-----NOx adsorption capacity-----
function y = CcssNO (CNO, CO2, Te)
kNO2=-2.198*Te+1796.3;
nNO2=0.5539;
nO2=0.7356;

CSNO2=kNO2*(CO2^nO2)*(CNO^nNO2);
y=CSNO2;
%-----

%-----O2 adsorption capacity-----
function y = CcssO (CO2, Te)
kO2=-0.0206*Te+19.712;
nO2=0.7356;

CSO=kO2*(CO2^nO2);
y=2*CSO;
%-----

%-----reaction rate-----
function y = Reaction(CSNO2, CHC, CSO, Te) %T=350
K=[ 0.80  0.7  0.012  0.1  0.0  2.50  0.0155];

m1=K(1);
m2=K(2);
m3=K(3);
m4=K(4);

```

```

m5=K(5);
k3=K(6);
k4=K(7);

r3=k3*CHC^m1*CSO^m2;
r4=k4*(CSNO2^m3)*(CHC^m4)*(CSO^m5);

rNO=-2*r4;
rHC=-r3-r4;
rSO=-9*r3-5*r4;

y=zeros(3,1);
y(1)= rNO;
y(2)= rHC;
y(3)= rSO;
%-----

%-----freeboard-----
function Feps = freeb (F0, U) %F0=5; assumed, kg/m2.s
epsfree=1;
Ug=U/epsfree;
rou=0.8;
dp=155e-6;
mu=3.1e-5;
roup=1700;

Us0=20*Ug;
Hf=0.8;
NH=500;
NU=500;
h=Hf/NH;
Fi=zeros(NH,4);
% 1, height; 2, Fi0; 3, velocity; 4, solids hold up, kg/m3

Fi(:,1)=linspace(0,Hf,NH);
Fi(:,2)=F0*exp(-6.4*Fi(:,1));

Ne=1;
for nU=2:NU,
    y=Us0*nU/NU;

    dy=0;
    i=1;

    while y>0,
        if y==Ug;
            y=y+0.01;
        end
        NRe=rou*dp*abs(y-Ug)/mu;
        CDs=24/NRe*(1+0.15*NRe^0.687)+0.42/(1+4.25e4*NRe^1.16);
        CD=CDs*epsfree^(-4.7);

```

```

dy=-((roup-rou)*9.8/roup/y-0.75*CD*rou*(y-Ug)*abs(y-Ug)/roup/dp/y;
if dy>0,
    dy=-0.001;
end
y=y+dy*h;

if y>0.00001,
    Fi(i,3)=y;
end
end

i=i+1;
Fi0=Fi(Ne,2)-Fi(i-1,2); % current flux

for j=1:i-2,
    if Fi(j,3)>0,
        Fi(j,4)=Fi(j,4)+Fi0/Fi(j,3);
    end
end

Ne=i-1; %number of ex point

end

for i=1:NH,
    Fi(i,4)=Fi(i,4)+Fi(i,2)/(0.8-Ug); %downflow particles
end

Feps=zeros(20,2);
for i=0:19;
    Feps(i+1,1)=mean(Fi(i*25+1:i*25+25,1));
    Feps(i+1,2)=1-mean(Fi(i*25+1:i*25+25,4))/roup;
end
%-----

```